Fermi National Accelerator Laboratory

Vadim V. Kashikhin

Design and optimization of superconducting accelerator magnets

Doctoral Thesis

Advisors: Dr. A.V. Zlobin (FERMILAB)

Prof. V.A. Glukhikh (NIIEFA)

2002

TABLE OF CONTENTS

INTRODUCTION

Researches in the particle physics require construction of high-energy accelerating systems. One of possibilities to obtain necessary interaction energy is colliding particles of oppositely directed beams. The machines utilizing this principle are traditionally called colliders. They fall into two major groups: linear colliders and storage rings. Beams in linear colliders are accelerated and transported to a collision point and then discarded after the single collision. In storage rings, particle of two beams recirculate along closed orbit and continuously interact in points of intersection. They can be stored in two separate rings or in a single ring if the beams consist of oppositely charged particles.

The idea of colliding beams in storage rings was originally proposed in 1956 [1]. The first accelerators utilizing this principle were: 250 MeV (here and after is given energy per beam) single e^+e ring AdA at Frascati (Italy, 1962), 140 MeV double e^-e^- ring VEP-1 at Novosibirsk (Russia, 1963) and 500 MeV double e^-e^- ring CBX machine at Stanford (USA, 1963) [2]-[3]. The first hadron collider was 31 GeV double pp^- ring ISR at CERN (Switzerland, 1971) [4].

Further development of accelerating systems was on the way towards higher interaction energies. In terms of collider subsystems, it requires increasing of magnetic field strength in bending dipoles or a machine circumference. Both ways lead to the cost and operating expenses grows. Therefore, optimization of the machine parameters plays an important role for its development and operation.

One of the major elements driving the cost of a storage ring is a bending dipole magnet. Earlier accelerators utilized superferric bending dipoles, where magnetic field, created by resistive coils, was shaped by iron poles in the magnet aperture. However, superferric magnets were ineffective for fields above 2 T due to the iron yoke saturation, leading to suffering of magnet performance. Also considerable amount of electrical energy losses in resistive coils made operation of such systems rather costly.

Discovery of superconductivity by a Dutch physicist H. Kamerlingh Onnes in 1911 made it possible to tremendously increase the current density in a bulk of material. However, practical implementation of superconducting windings in accelerator magnets happened after extensive study and development of superconducting cables and cryogenic technique in late 70th. Largest operating accelerators, based on superconducting magnets are [5]-[7]:

- Tevatron - 0.9 TeV single pp^- ring with 4.4 T field at FNAL (USA, 1987);
- HERA - 0.82 TeV double $e^{\pm}pp$ ring with 4.7 T field at DESY (Germany, 1992);
- RHIC - 0.5 GeV double pp ring with 3.5 T field at BNL (USA, 1999).

Among colliders being under development at the meantime are: UNK - 3 TeV double pp ring with 5.1 T field at IHEP (Russia) and LHC - 7 TeV double pp ring with 8.4 T field at CERN.

Further increase of the operating field is possible with the help of Nb_3Sn, which is class A15 intermetallic compound. This type of superconductor is considered for implementation in the second stage of Very Large Hadron Collider (VLHC), being investigated at several US laboratories [10]. The shell type Nb_3Sn dipole models manufactured at CERN, University of Twente and LBNL reached central fields of 9.5 T, 11.3 T and 12.8 T respectively at 4.3 K [11]-[13]. The Nb_3Sn common coil magnet, developed recently at LBNL, reached 14.6 T field in 10 mm bore [14], thanks to the excellent performance of modern Nb_3Sn superconductors.

Development and testing of the accelerator magnets made from high temperature superconductors (HTS) is also in progress at different institutions [15]-[16]. However, HTS cost and performances are the major factors, limiting its implementation in large-scale applications.

There is a fundamental difference between the superconducting accelerator magnets and other superconducting magnets (like large solenoids for particle detectors and toroids for nuclear fusion machines), making their design and construction a very special brunch of technology [17]:

- Necessity to use very high current densities for economical generation of high fields.
- Extreme precision of the magnetic field distribution in small apertures.
- Complex and non-uniform pattern of electromagnetic forces in coil and iron yoke.
- Large number of magnets in accelerator.
- High degree of reproducibility and reliability.

These characteristics make the development of superconducting accelerator magnets singularly complex and difficult and assume solving a wide range of non-trivial design and fabrication problems, including:

- Field quality in the magnet aperture must be within specification (typically 10^{-4}) during beam injection, acceleration and collision periods that requires:
  - optimization of the coil cross-section in order to minimize geometrical field errors;
  - optimization of the iron yoke cross-section in order to reduce harmonic deviations due to the iron saturation effect;
  - correction of the persistent current effect leading to hysteretic behavior of harmonics in accelerating cycle;
  - minimization of the dynamic effects due to eddy currents in conductive elements of magnetic system;
  - 3D optimization of the coil end-parts to minimize integral multipoles along magnet length.

7

- A magnet of minimum cost must be able to reach the nominal field at given ramp rate and remain there for prolonged periods without irreversible transitions to the resistive state (quenches). It implies:
  - optimization of the coil volume, copper to non-copper ratio and critical current density in superconductor;
  - 3D optimization of coil ends to reduce the peak field in the coil end below acceptable value;
  - minimization of coil inductance and stored energy;
  - minimization of the heat generation due to eddy current losses in the cable and surrounding elements.

Therefore, consequent study of the mentioned above problems, development and verification methods of their solution based on numerical and experimental models is an important issue for the progress in accelerator magnet physics and technology.

Goals of the performed work. The dissertation work had the following goals:

- Study and development of the Nb_3Sn shell type dipole magnet with single aperture on the field of 11-12 T, including:
  - optimization of the coil and yoke cross-section;
  - development of the magnet short models;
  - experimental investigation of the magnetic field quality in the short models.
- Parametric study of field quality in dipole and quadrupole magnets and methods of its improvement.
- Development of reliable and cost effective designs of Nb_3Sn dipole and quadrupole magnets with horizontal and vertical bore separation for the second stage VLHC.
- Study of the persistent current effect in Nb_3Sn magnets and methods of its correction, including.

Scientific novelty and the results to be defended. The following new results are presented in the thesis:

- Developed magnetic design of single aperture Nb_3Sn shell type dipole with a peak field of 11-12 T. Two short magnet models have been manufactured according to the developed design and tested. Obtained experimental data most comprehensively describe field quality in Nb_3Sn magnets. Magnetic measurements gave possibility to quantitatively characterize distribution of geometrical harmonics in magnet aperture, influence of superconductor magnetization on the field quality, dynamic effects related to eddy currents in elements of construction and harmonics drift at the injection plateau. Comparison with calculations allowed experimental verification of numerical models and development recommendations

on improvement of magnet parameters.

- Proposed and numerically evaluated design of a <u>single-layer</u> common coil dipole magnet, meeting VLHC requirements. One has demonstrated possibility of obtaining the necessary field level and quality using only one coil layer with 3 blocks per quadrant that has never been done before. The proposed design has certain advantages with respect to traditional block type magnets, providing better field quality within operating range and reduced manufacturing time.

- Performed optimization of shell type dipole with "cold" iron yoke and horizontal bore separation, meeting VLHC requirements. Proposed and numerically verified possibility of making cuts along flux lines, minimizing field sensitivity to gap variations.

- Proposed an effective design of the shell type dipole with "warm" iron yoke and horizontal bore separation. In process of numerical optimization, the magnet outer dimension has been reduced by factor of 2 and "cold" block weight by factor of 3-4, with respect to the "cold" yoke magnet, while meeting VLHC requirements. The coil inductance is by 23 % smaller that reduces voltages, generated during quench and allows increasing the magnet length.

- Considered shell type dipole with "cold/warm" iron yoke and vertical bore separation, meeting VLHC requirements. Performed optimization demonstrated possibility of reduction the magnet size by ~30 % with respect to the entirely "cold" yoke design.

- Developed effective designs of quadrupole magnets with different functions and aperture separations intended to work together with the proposed dipole magnets. All of them meet VLHC requirements.

- Proposed and numerically evaluated shell and block type coils with a <u>minimum inductance</u>. They allow achieving a better field quality by a precise control of every cable position, increasing the magnet length without complication of the quench protection system, reduction of time and quantity of materials, necessary for the magnet production.

- Numerically and experimentally verified method of simulation the coil magnetization effect based on finite-element code, which takes into account precise (measured) properties of superconductor and other magnetic elements. Based on this method, there was performed numerical simulation of the coil magnetization effect in different designs of Nb_3Sn dipole magnets. Evaluated impact of the magnet design on the coil magnetization effect.

- Proposed and numerically verified cheap and effective methods of correction the coil magnetization effect based on iron shims. They allow reduction of field distortions in Nb_3Sn magnets by factor of 3-5. Demonstrated that performance of the passive correctors can be enhanced by factor of 2 using small adjustment of coil geometry. Performed experimental investigation and verification of the proposed passive correctors, installed inside aperture of Nb_3Sn dipole magnet.

Thus, developed magnet designs, proposed methods of field correction, results of numerical and experimental simulations are to be defended.

Practical value. Results and methods described in the dissertation were implemented during:

- Conceptual design study of second stage VLHC. Proposed single-layer dipole magnet with common coils and quadrupole magnet with FF functions were used as the base-line designs for 100 TeV collider with 233 km circumference.
- Development, manufacturing and test of Nb_3Sn short dipole models at Fermilab.
- Development, production and test of passive correctors of the coil magnetization effect, together with Nb_3Sn short dipole models.

Publicizing of the results. Major results of dissertation have been reported during meetings of the High Field Magnet Group at Fermilab, VLHC meetings and workshops, Accelerator Physics and Technology Seminar at Fermilab, Budker seminar at Fermilab, Fermilab preprints, international conferences PAC99, MT16, ASC2000, PAC2001, MT17 and presented in publications [40]-[42], [44], [46]-[47], [49], [50], [53]-[56], [78], [93]-[96], [98]-[101], [103]-[105], [108]-[114], [118], [132], [134], [138], [141]-[143], [146], [147], [150], [151], [156], [157].

Volume and structure of dissertation. The dissertation consists of introduction, five chapters, conclusion, two appendixes and list of references. Every chapter contains a separate introduction and a summary. Major results, obtained during R&D are summarized in the conclusion to the dissertation.

CHAPTER 1. STUDY AND OPTIMIZATION OF SUPERCONDICTING COILS

1.1 Introduction

The early accelerators and colliders were based on the iron-dominated (or superferric) magnets. Magnetic flux produced by resistive (copper) coils in these magnets was transported by means of ferromagnetic yoke into the magnet aperture, where pole tip profile and ferromagnetic shims formed necessary field distribution. However, such approach became costly and ineffective with demand of higher magnet strength. Ferromagnetic yoke in such magnets could effectively (without considerable losses on fringe fields) transport magnetic flux until it is saturated. Since the best material (iron-cobalt alloy) for the pole tips had saturation magnetization of 2.35 T, it limited the operating field in the iron-dominated magnets at a level of 2 T.

The yoke saturation effect causes field distortions, which could acceptably be controlled by the "crenellation" or "two current" techniques up to 3 T field [18]. Apart from that, reasonable restrictions on the magnet size drove current density in resistive coils to an extent imposing water-cooling to extract the energy dissipations that made operation of accelerator highly energy consuming. One of the last machines, built with the resistive magnets was Main Injector into Tevatron at FERMILAB [19].

However, using of superconducting coils instead of resistive may reanimate the superferric magnet concept. One of the possible options is the transmission line magnet [20], where the magnetic flux is created by a single superconducting cable, carrying 100 kA current and surrounded by ferromagnetic yoke with two horizontal gaps for the counter-rotating beams. Using of the iron yoke limits operating field in the magnet at 2-3 T that requires digging up a long tunnel in order to attain the next level of beam energies. Nevertheless, simplicity of the transmission line magnet and low manufacturing cost allow increasing the tunnel length without cost grows of accelerator. This idea was used in the first stage VLHC, which has the same energy and cost as SSC, but 2.7 times longer tunnel [10].

Modern superconductors with high current densities allow reaching of much higher fields than can be produced by superferric magnets. Meeting the field quality target makes it necessary to get rid of ferromagnetic yoke as the magnetic flux transporter from the coil to magnet aperture. Magnets utilizing this concept (called "conductor-dominated") consist of superconducting coil adjacent to the beam pipe that surrounded by iron yoke from outside, which plays a role of the flux return and magnetic screen. Necessary field distribution is usually provided by optimized geometry of superconducting coil.

1.1.1 Definition of the field harmonics

The field quality in magnet aperture is convenient to describe in terms of a limited set of harmonic (multipole) coefficients. From definition of the magnetic field vector potential in Cartesian coordinates:

$$\vec{B} = curl\vec{A} = \vec{i}\left(\frac{\partial A_z}{\partial y} - \frac{\partial A_y}{\partial z}\right) + \vec{j}\left(\frac{\partial A_x}{\partial z} - \frac{\partial A_z}{\partial x}\right) + \vec{k}\left(\frac{\partial A_y}{\partial x} - \frac{\partial A_x}{\partial y}\right)$$

and considering two-dimensional problem that is the case for field inside long magnets, one can find:

$$B_x = \frac{\partial A_z}{\partial y} \ , \ B_y = -\frac{\partial A_z}{\partial x} \qquad (1.1.1)$$

Taking into account that the field can be also expressed as a gradient of its scalar potential in non-current region:

$$\vec{B} = -\mu \cdot grad(U)$$

or

$$B_x = \mu\frac{\partial U}{\partial x}, \ B_y = \mu\frac{\partial U}{\partial y} \qquad (1.1.2)$$

one can define an analytic complex potential function:

$$P(x, y) = A_z(x, y) + \iota U(x, y),$$

since equations (1.1.1) - (1.1.2) satisfy the Cauchy-Riemann conditions for analytic functions. The complex potential function can be further expanded into the power series around the center of coordinates:

$$P(x, y) = \sum_{n=0}^{\infty}(B_n + iA_n)(x + iy)^n , \qquad (1.1.3)$$

where B_n, A_n are called normal and skew multipole coefficients.

Taking the derivatives of (1.1.3) one can find multipole expansion of the flux density components in Cartesian coordinate system, which in European convention [21] writes:

$$B_y(x, y) + iB_x(x, y) = B_{ref} \sum_{n=1}^{\infty} (b_n + ia_n) \left(\frac{x+iy}{r_{ref}} \right)^{n-1},$$

where r_{ref} is a reference radius, B_{ref} is a reference field - magnitude of the main field component at the reference radius, $a_n = A_n/B_{ref}$, $b_n = B_n/B_{ref}$ are normal and skew multipole coefficients, related to the main field component.

The same equation can be written in trigonometric form that is more convenient to use in polar coordinate system:

$$B_\theta(r, \theta) = B_{ref} \sum_{n=1}^{\infty} \left(\frac{r}{r_0} \right)^{n-1} [b_n \cos(n\theta) - a_n \sin(n\theta)]$$

$$B_r(r, \theta) = B_{ref} \sum_{n=1}^{\infty} \left(\frac{r}{r_0} \right)^{n-1} [b_n \sin(n\theta) + a_n \cos(n\theta)]$$

This definition of the field multipoles will be further used in the content of to describe the field quality. Calculation of the relative multipole coefficients can be done according to Euler formulas [22] for known distribution of radial field component along a circle with radius r_{ref}:

$$a_n = \frac{1}{B_{ref} \pi} \int_0^{2\pi} B_r(r_{ref}, \theta) \cos(n\theta) d\theta, \ b_n = \frac{1}{B_{ref} \pi} \int_0^{2\pi} B_r(r_{ref}, \theta) \sin(n\theta) d\theta$$

1.1.2 Generation of pure multipole fields

The ways to produce pure magnetic fields by a current-carrying media are known for a long time. The simplest case is two parallel, flat, infinitely high and long conductors with current flowing in opposite directions that produces a uniform dipole field in between. This case, however, does not have a practical value due to the infinite conductor volume.

Another possibility is a so-called cosine-theta current distribution: a layer of current distributed at the surface of a cylinder with radius r_0 according to functions:

$$I(\theta) = -\frac{2B_{ref} r_0^{\ n}}{\mu_0 n} \cos(n\theta) \ \text{ or } \ I(\theta) = -\frac{2B_{ref} r_0^{\ n}}{\mu_0 n} \sin(n\theta),$$

produces correspondingly pure normal or skew multipole field of the order n [23].

If to approximate such current carrying-layer by a cylindrical conductor with a wall of finite thickness – the current density in the wall should follow cosine or sine distribution given above.

Practically it is easier to achieve a uniform current density. In this case, approximation of the required current distribution renders the coil wall thickness to follow the cosine or sine pattern. Geometrically this requirement means that the coil shape should follow two intersecting circular or elliptical conductors, carrying currents in opposite directions.

Field inside of a single circular or elliptical conductor with an origin at the center of coordinates can be expressed in complex form as:

$$B_{cir}(x, y) = \mu_0 \frac{J}{2}(x - iy), \ B_{ell}(x, y) = \mu_0 \frac{J}{a + b}(bx - iay),$$

where J is a current density in the conductor, a and b are horizontal and vertical half-axes of the ellipse. In case of two intersecting conductors field in the region of intersection can be found by superposition. If they carry currents of equal densities but opposite signs – the conducting media can be removed from the region of intersection, opening free space for the beam. It is easy to see that the field at any point inside of the intersection region is real, uniform and constant, meaning existence of the dipole component only:

$$B_{cir}(x, y) = \mu_0 J \Delta, \ B_{ell}(x, y) = 2\mu_0 J \frac{b\Delta}{a + b}, \tag{1.1.4}$$

where conductors are horizontally shifted by $\pm\Delta$ from the center of coordinates.

Two ellipses with a common center but rotated by 90 degrees one with respect to another (with interchanged a and b) produce following field in the region of intersection:

$$B_{ell}(x, y) = \mu_0 J \frac{b - a}{b + a} \cdot (x + iy).$$

Taking derivatives from real and imaginary parts along X and Y directions, one gets constant gradient:

$$G(x, y) = \frac{d \, \mathrm{Re}(B_{ell}(x, y))}{dx} = \frac{d \, \mathrm{Im}(B_{ell}(x, y))}{dy} = \mu_0 J \frac{b - a}{b + a} = const. \tag{1.1.5}$$

Thus two oriented by 90 degrees ellipses generate a pure quadrupole field.

Direct approximation of the intersecting circular or elliptical cylinders is possible if the coil is wound from a wire with much smaller dimensions than the size of the supporting cylinder. It

results in a large number of turns and inductance of the coil and used to be implemented in supplementary accelerator magnets (multipole correctors), working at low field levels and current ramp rates.

Main accelerator magnets has to have a lowest inductance possible due to the quench protection issues. Therefore, using of low number of turns in the coil, wound from multistrand cable with a large cross-section is a must. In most of the main accelerator magnets, the cable width is comparable to the aperture size, making it difficult to directly reproduce the cosine current distribution.

1.1.3 Coil configurations

There are two major types of cable arrangements with respect to the coil aperture used in the conductor dominated superconducting magnets. The first and most commonly used one is a so-called shell type coil. It is wound on a surface of a circular or elliptical cylinder and consists of one or more current-carrying layers (shells). Ideally, the cable should have trapezoidal cross-section in order to match appropriate sectors of the current shells (keystoned cable), which is practically achievable for coils with a large bore diameter (TEVATRON, HERA, RHIC). In this case, all the cables are positioned radially that simplifies winding and ensures that both inner and outer coil surfaces follow circular or elliptical pattern [21]. However, the radial turn position is difficult to achieve for smaller coils since the cable compaction ratio at the narrow edge $f_c = t_i/2d_s$ should stay above a tolerable limit of 0.75 (here t_i is the cable thickness at the narrow edge and d_s is the strand diameter) [21].

The second approach is a block type coil, which consists of a cable with rectangular cross-section. Cross-section of the coil blocks is also rectangular that makes it possible to build a so-called common coil configuration [24]. In this case, the cable is wound into the racetrack shape that requires only two (multilayer) coils to generate dipole fields of opposite signs in two apertures.

1.1.4 Coil design techniques

In dipole and quadrupole magnets with big apertures based on the shell type coils, the cable keystoning angle can be adjusted within tolerable limits in order to match with the radial lines. Every conductor block in such configuration matches with an arc sector, shown in Figure 1.1.1.
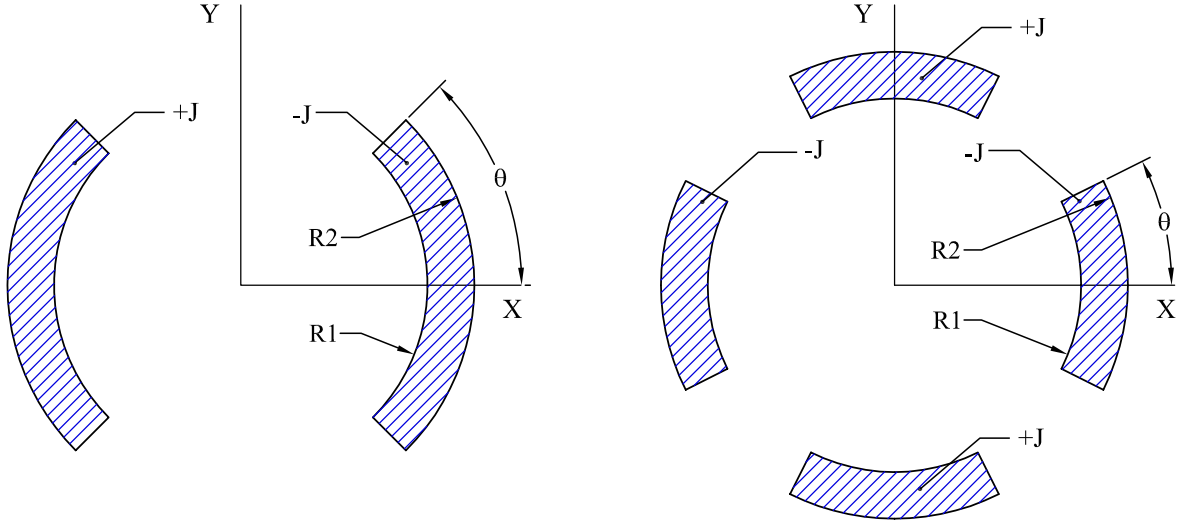
Figure 1.1.1 Shell type coils (left – dipole, right - quadrupole).

Magnetic field generated by the shell conductors can be analytically expressed in terms of multipole coefficients as:

$$B_1 = \frac{2\mu_0 J}{\pi}(R_2 - R_1)\sin(\Theta),$$

$$B_n = \frac{2\mu_0 J}{\pi}\frac{(R_2^{\,2-n} - R_1^{\,2-n})}{n(2-n)}\sin(n\Theta),$$

$$n = 2k+1, \ \ k \in \text{Real}$$

for the dipole and

$$B_2 = \frac{2\mu_0 J}{\pi}\ln\!\left(\frac{R_2}{R_1}\right)\sin(2\Theta),$$

$$B_n = \frac{4\mu_0 J}{\pi}\frac{(R_2^{\,2-n} - R_1^{\,2-n})}{n(2-n)}\sin(n\Theta),$$

$$n = 4k+2, \ \ k \in \text{Real}$$

for the quadrupole coil configurations [17].

It is easy to see that by choosing dipole shells with a limiting angle of 60 degrees per quadrant, one can eliminate first allowed by the coil symmetry multipole coefficient (after dipole) – sextupole (B_3). Similarly, choosing 30 degrees shells for quadrupole one can eliminate the first

allowed dodecapole (B_6). Two current shells can therefore simultaneously eliminate both sextupole and decapole in the dipole magnet. Such principle was implemented first in Tevatron magnets by choosing the limiting angle of about 72 degrees in the inner and 36 degrees in the outer layer [5].

The above formulas do not take into account the current density variations across the shell due to the cable keystoning as well as insulation between cables, which can only be neglected for relatively large coil radii. For smaller ones (SSC, LHC, VLHC) these effects must be taken into account along with the block shape that in this case does not match with an arc sector. Nevertheless, it is possible to compute the field analytically as a superposition of fields from single strands by the Biot-Savar low and use an optimization algorithm to find the required solution.

This approach is implemented in ROXIE (Routine for the Optimization of magnet X-sections, Inverse field computation and coil End design) code created by S. Russenschuck at CERN for the design and optimization of the LHC superconducting magnets [25], [26]. The coil and iron yoke modeler modules of the code allow generation of a magnet geometry by meaningful engineering design parameters, such as the number of conductors and blocks, radii of block supporting cylinders, inclination and positioning angles of the blocks, conductor dimensions and properties. The field is evaluated analytically by the Biot-Savar low in case of yoke with constant permeability and infinite outer boundary (image current method) or numerically, using reduced vector potential formulation in case of the yoke with real dimensions and properties. All evaluated field quantities can be addressed as objectives for the numerical optimization.

Most of the optimization problems include multiple conflicting objectives that must be considered simultaneously, a so-called vector optimization problem [27]. The solution process of vector optimization problems consists of three steps: decision-making methods [28]-[29], methods to treat non-linear constrains [30]-[32] and minimization algorithms [33].

Mathematical optimization techniques have been applied in computational electrophysics for relatively long time [34]-[36]. These attempts were, however, application specific. Only in late 80th optimization routines were incorporated in multipurpose numerical computation codes (ANSYS).

The wide range of applied methods proves that there is no general method developed so far to solve the nonlinear optimization problems in a similar way as it can be done for the linear problems [37]. There are many different applications of computational electrophysics and every one has a preferable solving procedure. Some methods used for optimization of the conductor-dominated magnets are provided with ROXIE code [27].

1.2 Study of the coil design parameters

All the superconducting accelerator magnets built by present time utilize shell type dipole coils with the apertures of 50 mm and more. In addition, there is a clear correlation between nominal beam energy and coil aperture – dipole magnets with smaller apertures are used to transport higher energy beams. The major reason of this is economical as a part of the main magnet price in overall collider cost increases rapidly with the operating field. It is obviously important to determine and use a minimum magnet aperture, which can satisfy requested accelerator parameters.

One of unknown contributions into the physical magnet aperture is the <u>dynamic aperture</u> – maximum amplitude of a particle, which can survive for a given number of turns. Usually the dynamic aperture is determined after extensive run of beam-tracking programs with input data of accelerator lattice and expected field errors [38]. The field errors must be computed for a known coil configuration, with some initial aperture approximation. Therefore, in general, optimization of the coil geometry is contingent with the beam track calculation that makes it extremely time consuming. However, using of the beam tracking programs can be avoided at an initial stage of magnet design, by imposing of magnet field to satisfy field error table for a machine with close beam parameters. Then the coil optimization should be performed in order to determine a most economical coil configuration (with a minimum aperture size) that satisfies the field quality criteria.

As preliminary criteria of the field quality there were taken tolerances on systematic and random field errors, developed for SSC [9], as it had closest center-mass energy to any future collider.

1.2.1 Idealized optimum dipole coil

Simulation of the coil configuration, required for generation of the uniform dipole field B within aperture of the given radius $r,$ in many cases involves numerical optimization of multiple conductor positions around the aperture. A theoretical limit for optimum coil configuration (with minimum cross-section area and cost) can be, however, derived semi-analytically.

Let us find a coil configuration based on two intersecting ellipses that generates uniform magnetic field with the flux density B inside aperture with radius r (Figure 1.2.1) and has a minimum possible cross-section area. The current-carrying superconducting material is assumed to have critical current density in the non-copper fraction J_c at the field B_0 and some temperature, while being uniformly distributed together with copper stabilizer within the ellipses.

Copper to non-copper ratio is also uniform and equals to K_{cusc}. The critical current density of Nb$_3$Sn superconductor can be expressed as a function of applied field B, according to [39]:

$$J_c(B) = \frac{C}{\sqrt{B}}\left(1 - \frac{B}{B_{c2}}\right)^2,$$

where B_{c2} is the upper critical field of superconductor. The constant C is defined as:

$$C = \frac{J_c(B_0)\sqrt{B_0}}{\left(1 - \frac{B_0}{B_{c2}}\right)^2},$$

where B_0 is some reference field at which the critical current density is known.
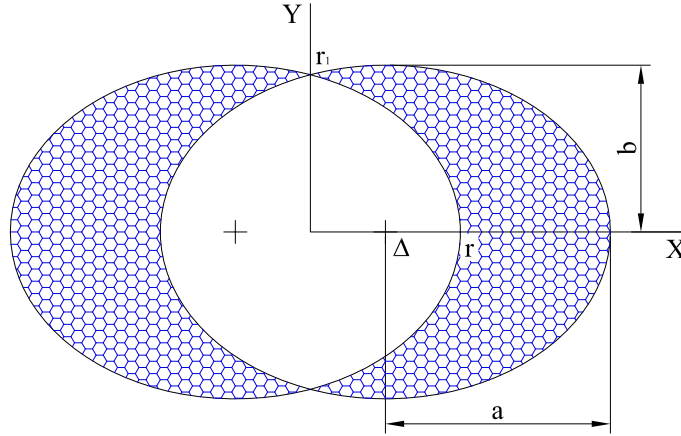
Figure 1.2.1. Naming convention of the dipole coil.

The effective (mean) current density in a conductor containing copper and non-copper fractions is:

$$J(B) = \frac{J_c(B)}{1 + K_{cusc}}. \tag{1.2.1}$$

Cross-section area of the two ellipses with taken out region of intersection can be written as:

$$S = 2\left\{\pi ab - 2\left[ab \cdot \arccos\left(\frac{\Delta}{a}\right) - \Delta r_1\right]\right\}. \tag{1.2.2}$$

Using the equation of field produced by two intersecting ellipses (1.1.4) and taking into account that:

19

$$\Delta = a - r \qquad (1.2.3)$$

one can express flux density as:

$$B = 2\mu_0 J(B) b \frac{a - r}{a + b}$$

that allows to derive one of ellipse half-axis as a function of another and applied field

$$b = \frac{Ba}{2\mu_0 J(B)(a - r) - B}. \qquad (1.2.4)$$

The y-position of intersection point of two ellipses can be derived form the ellipse's equation as:

$$r_1 = b\sqrt{1 - \left(\frac{\Delta}{a}\right)^2}. \qquad (1.2.5)$$

Combining (1.2.3)-(1.2.5) with (1.2.2) one can find the coil cross-section area as a function of one unknown parameter *a:*

$$S = \frac{2aB}{2\mu_0 J(B)(a - r) - B} \left\{ \pi a - 2 \left[a \cdot \arccos\left(1 - \frac{r}{a}\right) - (a - r)\sqrt{1 - \left(1 - \frac{r}{a}\right)^2} \right] \right\}$$

A minimum of the given above function corresponds to the optimum parameter *a* that can be calculated from its derivative. It is simpler to find solution of the resultant transcendent equation numerically for a given set of parameters. Assuming $J_c(12 \text{ T}) = 2000 \text{ A/mm}^2$, $K_{cusc} = 0.85$, $r = 20$ mm and target field $B = 12$ T, one can plot the coil area as a function of *a* (Figure 1.2.2). The dependence turns complex if:

$$a < r/2$$

and has an asymptote at:

$$a = \frac{B}{2\mu_0 J} + r.$$

There is only one unambiguous minimum on the curve at $a = 35.52$ mm that allows to find the rest of geometrical parameters from (1.2.3)-(1.2.5). Thus b = 14.12 mm, $\Delta = 15.52$ mm and $r_1 = 12.70$ mm for the minimum coil area $S = 17.0 \text{ cm}^2$. Figure 1.2.3 shows the idealized optimum coil configuration that satisfies the given set of parameters.
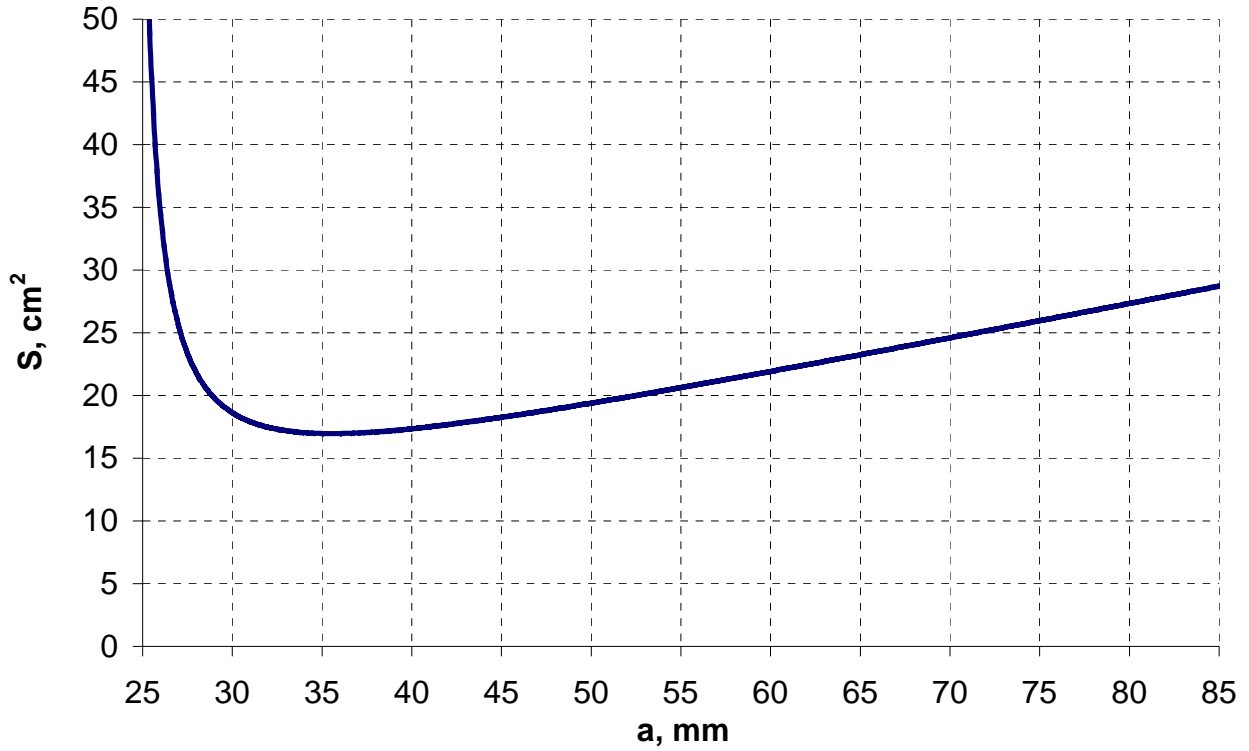
Figure 1.2.2. Coil area as a function of the ellipse's horizontal half axis.
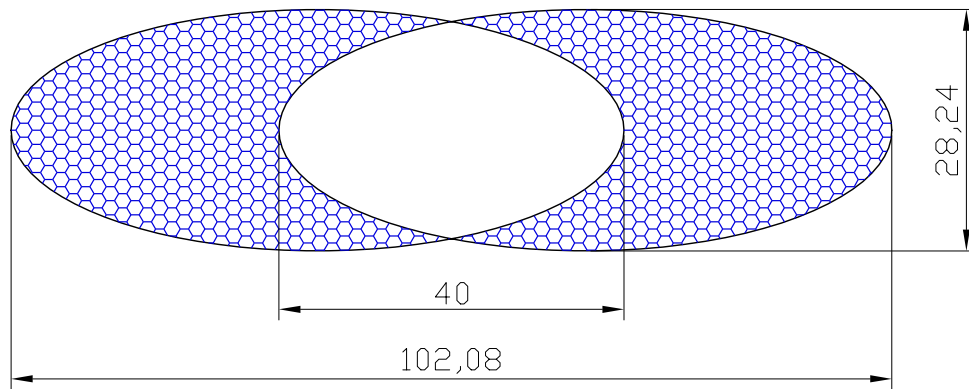
Figure 1.2.3. Idealized optimum coil configuration

It is noticeable that the physical aperture of such coil is close to an elliptical shape with a ratio of ellipse axes $r_1/r = 0.63$. Since most of the magnets should have a circular aperture by technological reasons, it is necessary to apply constrain for fitting a circle with radius r inside the aperture.

A distance from the origin to a point on the ellipse with coordinate x is determined as:

$$r_b(x) = \sqrt{x^2 + y^2} = \sqrt{x^2 + b^2\left(1 - \frac{(x-\Delta)^2}{a^2}\right)}.$$

Taking derivative is easy to find x corresponding to a minimum $r_b(x)$:

$$x_{min} = \frac{b^2\Delta}{b^2 - a^2}.$$

So the constrain to be satisfied for the circle with radius r to fit inside the coil aperture should be:

$$r_b(x_{min}) = r.$$

Now one can determine the minimum coil area that satisfies this constrain. It implies solving the system of equations:

$$\begin{cases} 2\left\{\pi ab - 2b\left[a \cdot \arccos\left(\frac{\Delta}{a}\right) - \Delta\sqrt{1 - \frac{\Delta^2}{a^2}}\right]\right\} = S \\ 2\mu_0 J(B)b\frac{\Delta}{a+b} = B \\ b\sqrt{\left(\frac{b\Delta}{b^2 - a^2}\right)^2 - \frac{1}{a^2}\left(\frac{b^2\Delta}{b^2 - a^2} - \Delta\right)^2 + 1} = r \end{cases} \qquad (1.2.6)$$

The number of unknown variables in the system exceeds the number of equations, meaning that there are multiple sets of variables, simultaneously satisfying the system. However, there is only one set of variables for every aperture size, field and critical current density, corresponding to the minimum coil area. It was found using the Levenberg-Marquardt minimization method implemented in MathCad program package under condition $S \to 0$.

The minimum coil area that satisfies all the conditions and constrains is $S = 18.68$ mm^2 and the coil geometrical parameters are $a = 30.3$ mm, $b = 23.6$ mm and $\Delta = 10.1$ mm. The coil geometry is presented in Figure 1.2.4. Thus meeting the condition of the circular aperture requires 10 % larger coil area with respect to the case without the circular constrain.

It was interesting to analyze dependence of the minimum coil area and corresponding geometry on the target field and superconductor properties for a given bore size. Since there is no simple analytical solution for the coil parameters, it was convenient to take the considered earlier coil

configuration with the circular aperture as the origin case and determine normalized parameters. Minimizing the system of equations at different B and $J_c(12\ T)$ one obtains the minimum coil area and relevant geometrical parameters (Figures 1.2.5-1.2.6).
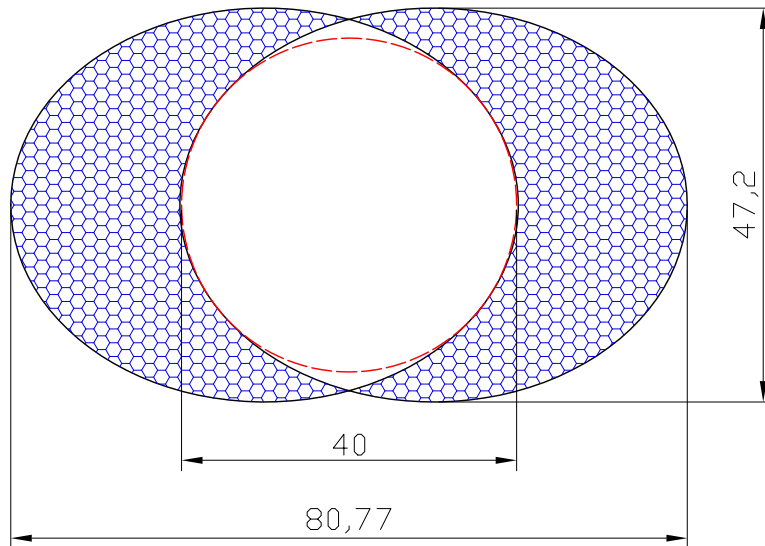

Figure 1.2.4. Idealized optimum coil configuration with a circular aperture.
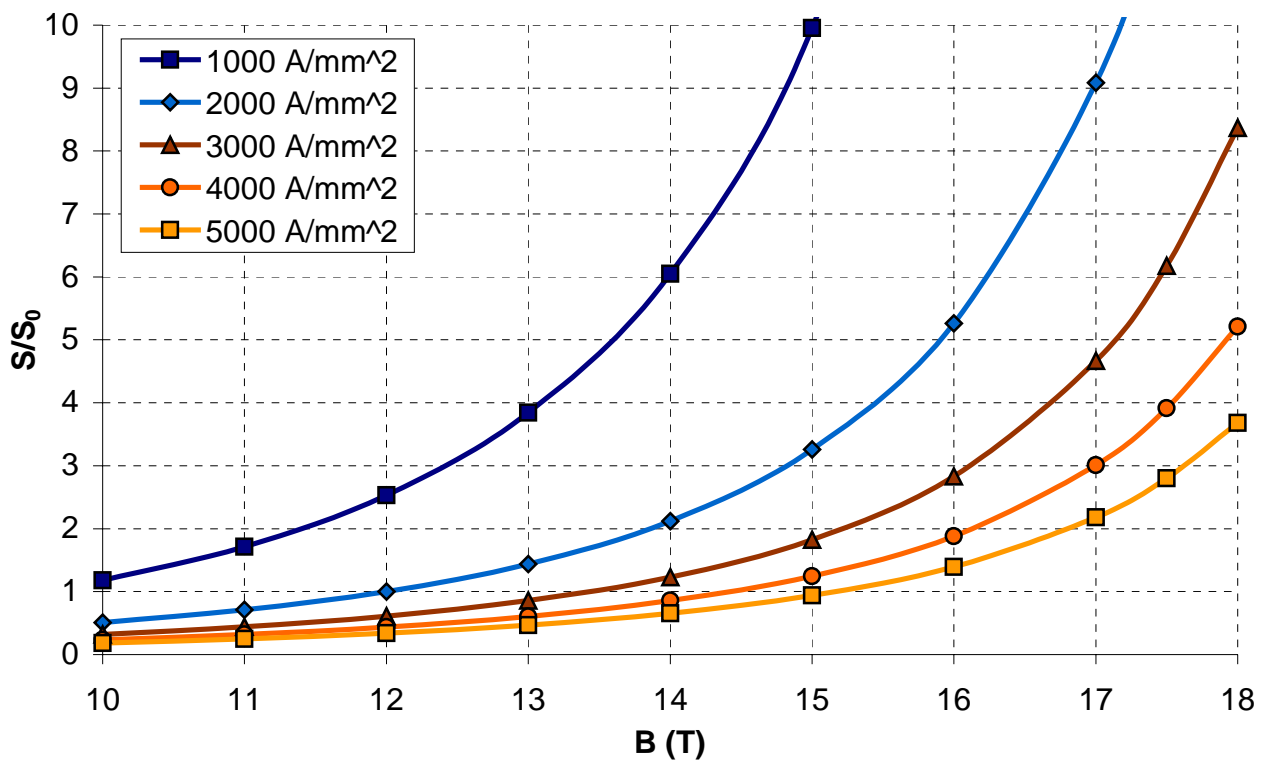

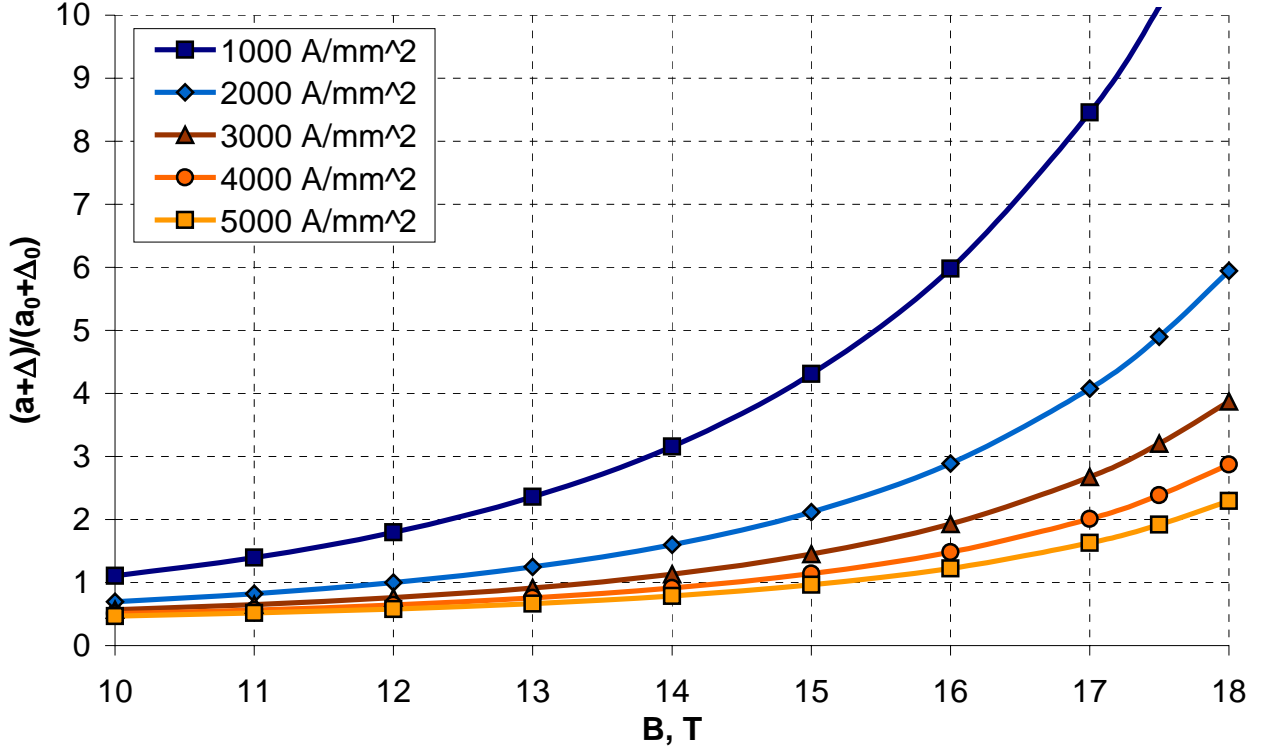Figure 1.2.5. Normalized coil area as a function of the bore field.

Figure 1.2.6. Normalized coil horizontal size as a function of the bore field.

It is possible to see that the coil area approximately doubles for every 2 T in the field range of 10-13 T. At higher fields it increases even more rapidly. Thus, 2.2 times and 5.3 times higher coil areas are required to obtain 14 T and 16 T fields correspondingly with respect to the origin case, assuming the same critical current density and coil bore size. A superconductor with higher critical current density can dramatically improve the magnet performance in the high field region. For example, superconductor with $J_c(12 \text{ T}) = 5000 \text{ A/mm}^2$ allows reaching 15 T field at the same coil area as the origin case needs to reach 12 T field. The coil horizontal size changes less rapidly – it approximately doubles for every 3 T. Using of superconductor with higher J_c allows reducing of the coil size by approximately the same extent as the coil area.

One of important implications of the derived analytical expressions is the ability to precisely evaluate the minimum coil area (and cost) for any given properties of superconducting material, operating field and aperture size without running of complicated and time consuming numerical simulations. It therefore gives possibility to determine scaling laws for the coil and magnet cost and eventually optimum parameters of a whole collider.

Using the derived expressions there was performed a cost analysis and optimization of a hadron collider, described in Appendix A and [40], [41], which allowed making important conclusions on the optimum machine parameters.

1.2.2 Idealized optimum quadrupole coil

Similarly to the considered dipole case, one can find an optimum quadrupole coil configuration. Total area of the four shells produced by two intersecting ellipses (Figure 1.2.7) is:

$$S = 4ab \cdot \arcsin\left(\frac{a^2 - b^2}{a^2 + b^2}\right).$$

The field gradient from (1.1.5) equals:

$$G = \mu_0 J(B_{max})\frac{b - a}{b + a}, \tag{1.2.7}$$

where $J(B_{max})$ is the current density in the conductors according to (1.2.1) at the maximum field in the conductors B_{max}. Unlikely to the idealized dipole coil, the maximum field is not equal to the bore field and therefore must be found separately.
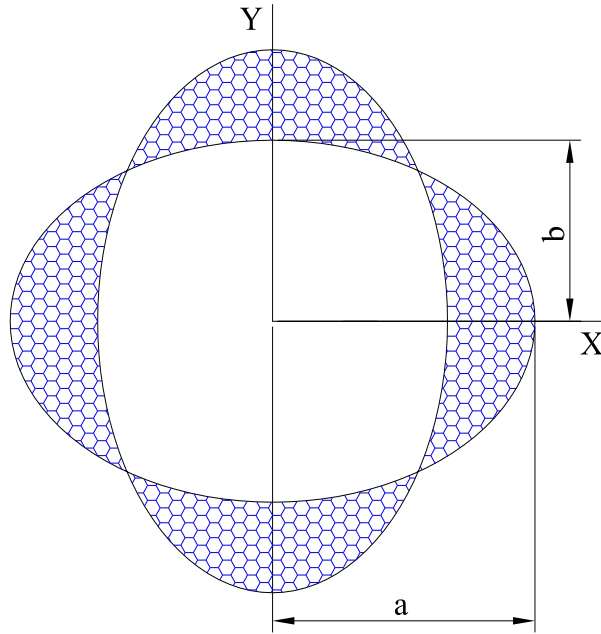

Figure 1.2.7. Naming convention for the quadrupole coil.

The absolute field value in the region of intersection equals:

$$B_{tot}(x, y) = \mu_0 J(B_{max})\frac{b - a}{b + a}\sqrt{x^2 + y^2} .$$

The total field on the surface of the ellipse with horizontal half-axis a and vertical half-axis b can be found as a function of one parameter using the ellipse equation:

$$B_{tot}(x) = \mu_0 J(B_{max}) \frac{b-a}{b+a} \sqrt{x^2 + b^2 \left(1 - \frac{x^2}{a^2}\right)}.$$

Point of the two ellipses intersection equals to:

$$x' = y' = \frac{ab}{\sqrt{a^2 + b^2}}.$$

Now it is possible to find the maximum and minimum fields on the ellipse surface:

$$B_{max} = B_{tot}(x') = \mu_0 J(B_{max}) \frac{b-a}{b+a} \cdot ab \sqrt{\frac{2}{a^2 + b^2}},$$

$$B_{min} = B_{tot}(0) = \mu_0 J(B_{max}) \frac{b-a}{b+a} \cdot b,$$

which in terms of the field gradient equals:

$$B_{min} = G \cdot b, \ B_{max} = G \cdot ab \sqrt{\frac{2}{a^2 + b^2}}. \tag{1.2.8}$$

It is interesting to find the ratio between the maximum and minimum fields, which depends only on the ellipse geometrical parameters:

$$\frac{B_{max}}{B_{min}} = a \sqrt{\frac{2}{a^2 + b^2}} = \sqrt{\frac{2}{1 + \frac{1}{k_{ell}^2}}},$$

where $k_{ell} = a/b$ is the ellipticity ratio ($a \geq b$). Thus for $k_{ell} = 1$ the ellipses turn into circles and the field ratio turns to 1. This case does not have a practical interest since at the same time the field turns to zero. For $k_{ell} \to \infty$ the ratio turns to $2^{1/2}$, which is not of a practical interest as well, since the coil area goes to infinity. Therefore, for any feasible quadrupole coil geometry, ratio of the maximum to the minimum field on the inner coil surface is within:

$$1 < \frac{B_{max}}{B_{min}} < \sqrt{2}.$$

Combining (1.2.7)-(1.2.8) into the system of equations:

26

$$
\begin{cases}
G = \mu_0 J(B_{max}) \dfrac{b-a}{b+a} \\[3mm]
B_{max} = G \cdot ab \sqrt{\dfrac{2}{a^2+b^2}}
\end{cases}
, \qquad (1.2.9)
$$

one can determine the geometrical parameters a and b. Since the quadrupole geometry is explicitly described by the two unknown parameters within two equations (unlikely to the dipole coil), there is only one idealized quadrupole configuration for a given gradient and superconductor properties. Therefore, there is no optimum quadrupole coil configuration in terms of the coil area.

Due to complexity of the current density function, it is easier to resolve the system numerically for a given set of parameters. The maximum (quench) gradient of 450 T/m, coil bore radius $r = b$ = 20 mm and the critical current density $J_c(12\ T) = 2000$ A/mm^2 were assumed as the origin parameters. Corresponding coil geometry is presented in Figure 1.2.8 and the normalized ratios of the coil area and parameter a are shown in Figures 1.2.9-1.2.10 for different current densities. It is noticeable that the coil area approximately doubles for every 50 T/m in the region of 400-500 T/m. Using of superconductor with a higher critical current density increases gradient. Thus a critical current density $J_c(12\ T) = 5000$ A/mm^2 allows to reach 580 T/m at the same coil area (and geometry) as in the origin case. Figure 1.2.11 shows the coil area and ellipticity ratio as functions of the bore radius, for the gradient and the superconductor properties set at the origin case values. The obtained analytical expressions for the quadrupole coil area can be used for a collider cost optimization along with expressions for the dipole magnets.
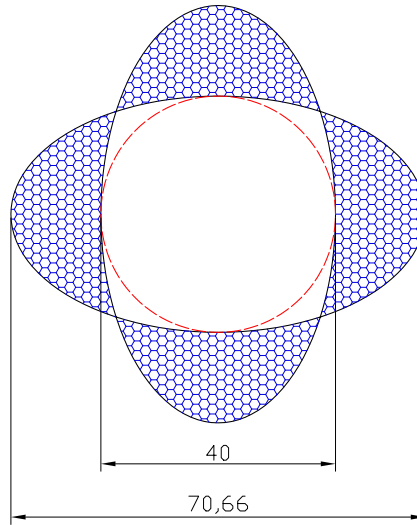

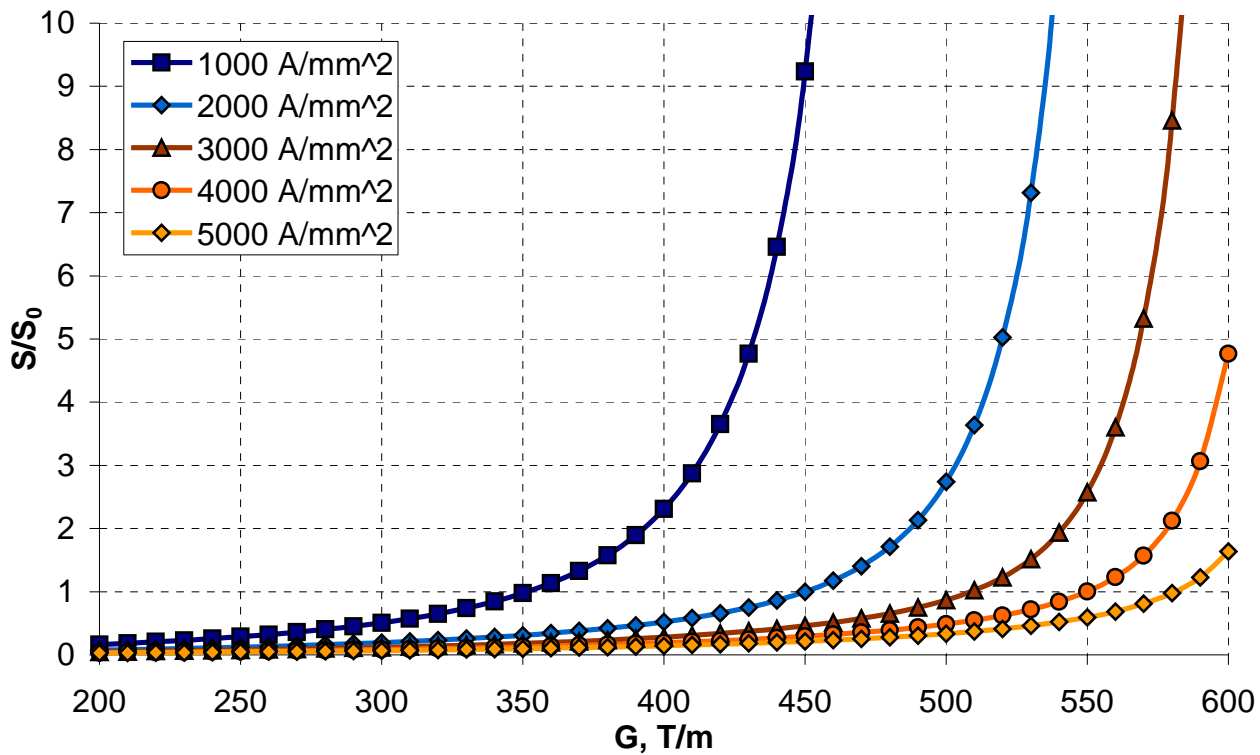Figure 1.2.8. Idealized quadrupole coil configuration.

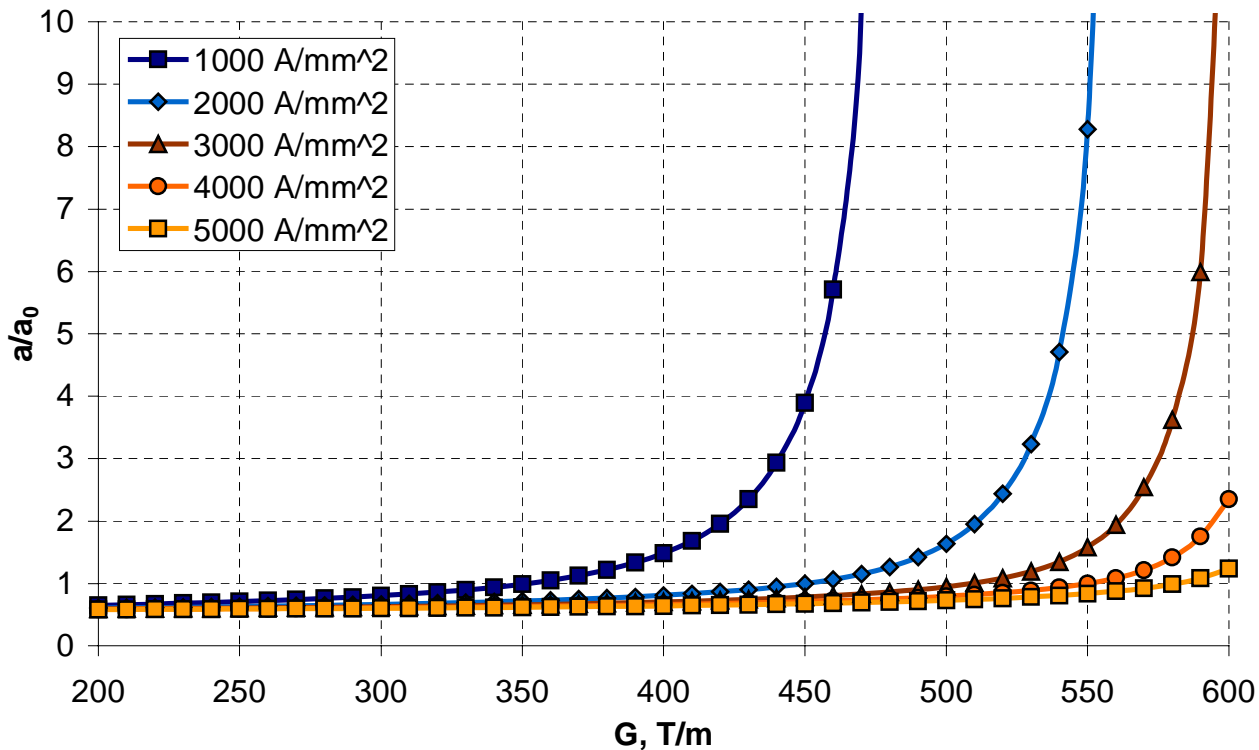Figure 1.2.9. Normalized coil area as a function of the bore gradient.

Figure 1.2.10. Normalized horizontal coil size as a function of the bore gradient.
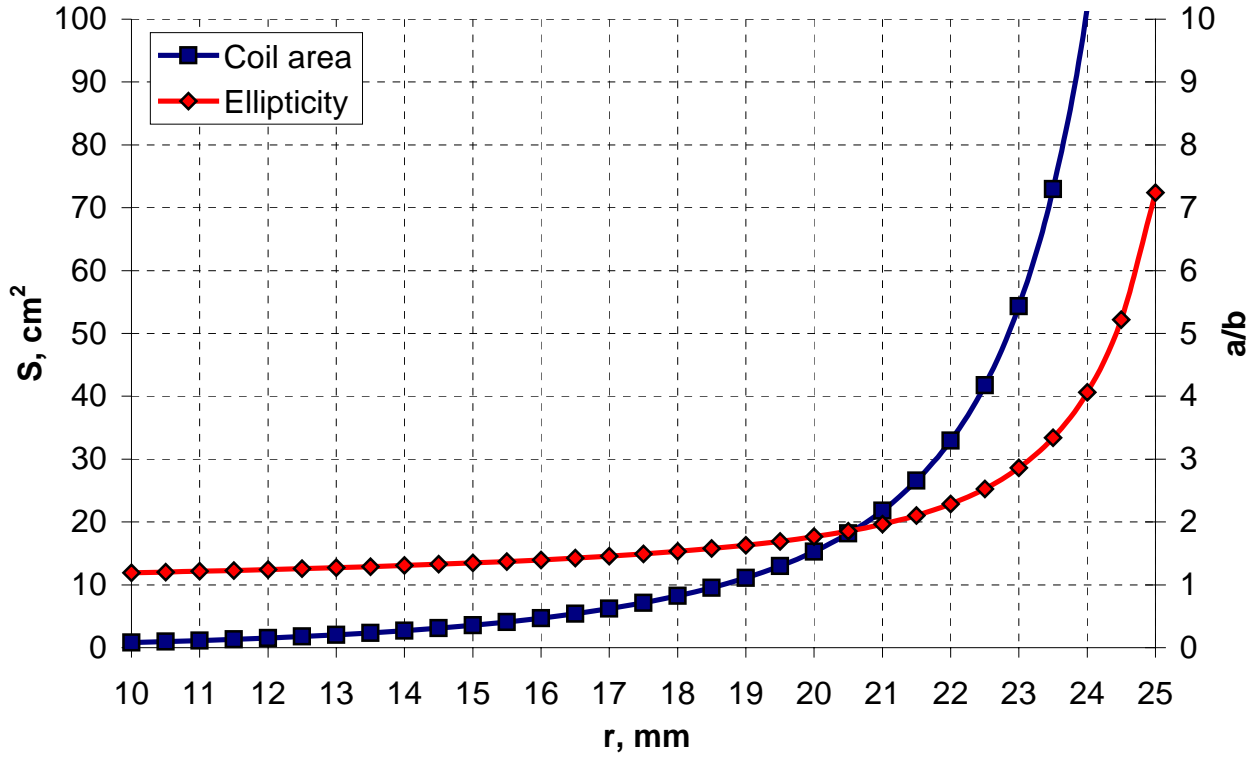
Figure 1.2.11. Coil area and ellipticity ratio as a function of the bore radius.

1.2.3 Scan of the real coil design parameters

A set of real coil configurations with bore sizes within 30-45 mm range was analyzed in order to determine practically achievable field quality and required tolerances on block positions. Only two layer coils with several blocks in the inner and outer layer were considered. The iron yoke was analytically simulated by a circular cylinder (center of the iron yoke coincides with the coil bore center) with final inner and infinite outer radii and constant permeability, which was chosen equal to 1000 during the multipoles minimization and 4.5 during the quench field calculations. The number of coil blocks, number of cables in a block, block positioning and inclination angles, wire dimensions, number of strands per cable and strand diameter were included in the list of design parameters and varied during optimization process to obtain a minimum of the objective function. In addition, three cases of the coil shape were considered – shell type coils with circular and elliptical apertures and block type coils. In the second case, the ellipticity ratio was used as one of design parameters for optimization. The objective function comprised systematic field multipole errors with a set of weight factors, changed at the different steps of optimization. Another parameter fixed in this part of the optimization was the quench field in the coil bore center of 12.0 T that along with a conservative safety margin of 20 % would provide close to the optimum (Appendix A) nominal field of 10 T.

The critical current density in superconducting wire was assumed 2000 A/mm^2 at 12.0 T field and 4.2 K temperature. Copper to non-copper ratio in the wire was chosen 0.85 that is considered high enough for stabilization of micro-quenches and quench protection of a short model by a dump resistor [42]. However, for a very conservative quench protection approach of a long magnet by quench heaters one has to increase the copper to non-copper ratio in order to limit the current density in copper fraction of a wire at about 1000 A/mm^2 after quench [43]. It requires increasing of copper to non-copper ratio to about 2. In this case, reduction of the superconductor area is supposed to be compensated by future enhancement of the critical current density.

The total number of 12 coils was optimized using ROXIE code with the absolute accuracy on the block position of 1 µm. The coil cross-sections with diagrams of field quality inside the bore and coordinates of the coil blocks in each case are summarized in Appendix B. Table 1.2.1 shows geometrical parameters of the optimized designs.

Table 1.2.1. Geometrical parameters of different coil designs.

Coil design	Bore diam., mm	Bare cable width, mm	Bare cable middle thickness, mm	Strand diam., mm	N of strands/ cable	N of cables/ coil quadrant	Bore ellipticity (b/a)
circular shell	30	13.865	1.067	0.6	46	32	1
	35	12.657	1.245	0.7	36	32	1
	40	12.858	1.422	0.8	32	30	1
	45	12.657	1.600	0.9	28	29	1
elliptical shell	30	13.865	1.067	0.6	46	32	1.04
	35	12.657	1.245	0.7	36	32	1.017
	40	12.858	1.422	0.8	32	30	1.036
	45	12.657	1.600	0.9	28	29	1.02
block	30	13.544	1.056	0.6	44	34	∞
	35	14.364	1.232	0.7	40	30	∞
	40	14.774	1.408	0.8	36	28	∞
	45	14.775	1.584	0.9	32	28	∞

Blocks position and ellipticity ratio were varied in the optimization process to obtain minimum of the objective function. Every optimized circular coil served as an initial approximation for the elliptical coil with the same horizontal bore size. Table 1.2.2 presents systematic relative harmonics in 10^{-4} evaluated at the reference radius of 1 cm. Shaded cells indicate unacceptably high values, exceeding the target harmonics (SSC specification). It is noticeable that high order harmonics are smaller in the block type coil with respect to the shell type coil that explains by a larger than the physical aperture effective bore diameter (that determines the field) in the block type coil. It is particularly confirmed by the fact that introduction of ellipticity into the shell type

coil (increasing the effective aperture) provides a noticeable reduction of the high order harmonics. For example, b_{11} in a block type coil with the bore size D_b is close to the same multipole in the shell type coil with the bore size $D_b + 5$ mm, which means the effective aperture of the block type coil is by ~ 5 mm larger than its physical aperture.

For the same reason, the larger effective bore diameter decreases efficiency of the block type coil, resulting in larger coil area for generation of the same field within the same physical aperture as in the shell type coil and consequently larger inductance and stored energy.

Table 1.2.2. Systematic relative multipoles in different coil designs.

Coil design	Bore diameter, mm	Relative multipoles, 10^{-4}				
		b_3	b_5	b_7	b_9	b_{11}
circular shell	30	0.0111	0.2481	1.2453	-2.2034	2.6288
	35	-0.0006	0.0307	0.0699	-0.1990	0.7371
	40	0.0004	0.0129	0.0349	-0.1134	0.2021
	45	0.0003	-0.0024	0.0020	-0.0002	0.0751
elliptical shell	30	0.0000	-0.0004	0.0053	-0.0862	2.0715
	35	-0.0003	0.0118	0.0571	0.0023	0.6683
	40	0.0000	-0.0016	0.0008	-0.0048	0.1626
	45	0.0001	-0.0008	-0.0010	0.0013	0.0702
block	30	0.0007	0.0021	0.0007	0.0005	0.9394
	35	-0.0004	0.0024	0.0030	-0.0008	0.2491
	40	-0.0003	-0.0003	-0.0012	0.0032	0.0751
	45	-0.0011	0.0048	0.0072	-0.0734	0.0166
Target		0.0076	0.018	0.040	0.089	0.19

Along with the systematic field harmonics, random field multipoles depending on the coil manufacturing tolerances were taken into account. The elliptical coil, being a transient case between circular and block type coil in terms of the field quality was excluded from the analysis. The random displacements in the shell type coil were applied for the azimuthal and radial block position, when for the block type coil they were applied for the horizontal and vertical block position. The standard harmonic deviations were derived from 500 cases of randomly positioned (within specified limits) blocks according to:

$$\sigma = \sqrt{\frac{1}{n}\sum_{i=1}^{n}(x_i - \bar{x})^2} \ ,$$

where n is the number of cases, x_i is the random value and $\bar{x}$ is the mean value of a multipole. Tables 1.2.3-1.2.4 summarize the standard deviations of the multipoles due to +/-50 μm random block displacement from the nominal positions and the target values (SSC specification).

Table 1.2.3. Standard deviations of the normal multipoles.

Coil design	Bore diam., mm	Standard deviation, 10^{-4}							
		b_2	b_3	b_4	b_5	b_6	b_7	b_8	b_9
shell	30	1.87	1.26	0.75	0.33	0.11	0.21	0.11	0.11
	35	1.40	0.81	0.43	0.15	0.06	0.08	0.03	0.02
	40	1.19	0.64	0.28	0.08	0.03	0.04	0.01	0.01
	45	0.82	0.39	0.18	0.05	0.01	0.01	0.01	0.00
block	30	1.98	0.87	0.30	0.15	0.09	0.07	0.05	0.04
	35	1.63	0.64	0.19	0.08	0.04	0.03	0.02	0.01
	40	1.33	0.46	0.12	0.05	0.02	0.01	0.01	0.00
	45	1.10	0.37	0.09	0.03	0.01	0.01	0.00	0.00
Target		0.7	2	0.3	0.7	0.1	0.2	0.2	0.1

Table 1.2.4. Standard deviations of the skew multipoles.

Coil design	Bore diam., mm	Standard deviation, 10^{-4}							
		a_2	a_3	a_4	a_5	a_6	a_7	a_8	a_9
shell	30	0.96	0.81	0.57	0.53	0.38	0.11	0.07	0.06
	35	0.69	0.55	0.34	0.27	0.16	0.03	0.02	0.01
	40	0.6	0.39	0.24	0.16	0.08	0.01	0.01	0.00
	45	0.43	0.24	0.12	0.08	0.04	0.01	0.00	0.00
block	30	0.73	0.76	0.51	0.3	0.15	0.08	0.04	0.02
	35	0.57	0.54	0.32	0.16	0.07	0.03	0.01	0.01
	40	0.48	0.4	0.21	0.09	0.04	0.01	0.00	0.00
	45	0.39	0.28	0.14	0.06	0.02	0.01	0.00	0.00
Target		0.7	0.6	0.7	0.2	0.2	0.03	0.2	0.05

One can see that none of the considered designs meets the target parameters, which means the assumed tolerance on block positions was too large. In order to determine what tolerance would allow meeting the target parameters, the block type coil design with 30 mm bore diameter was analyzed at several different tolerances (Tables 1.2.5-1.2.6). The results show that the standard deviations are directly proportional to the values of tolerances used during analysis. This fact can be used to scale tolerances for different coil bore sizes and shapes, which meet specified values of the standard deviation. Since the first allowed harmonic - quadrupole b_2 has a largest off-target value, it was used as a criterion for acceptable tolerance. Figure 1.2.12 shows derived tolerances on the block positions as functions of the bore diameter for the shell and block type coils. The shell type coil requires approximately 5% less stringent tolerances than the block type coil in the 30-40 mm range of bore sizes. A bigger difference at the bore diameter of 45 mm is explained by one additional block per coil quadrant in the shell type design. Apart from that, the block positioning accuracy depends on the bore diameter in nearly similar way for both coil types. Thus, coil blocks must be positioned with better than +/-20 μm accuracy for the coil bore

diameter of 30 mm that can be achieved by constraining of every block in a rigid, precisely manufactured (stamped) mechanical structure. A traditional way of the coil manufacturing involves "floating" spacers between the blocks and consequently 1.5-2 times larger deviations, which are suitable for the coils with bigger than 50 mm bore. Table 1.2.7 presents parameters of magnets based on the optimized coils.

Table 1.2.5. Standard deviations of the normal multipoles.

Tolerance, μm	Standard deviation, 10^{-4}							
	b_2	b_3	b_4	b_5	b_6	b_7	b_8	b_9
50	1.98	0.87	0.3	0.15	0.09	0.07	0.05	0.04
25	0.99	0.44	0.15	0.07	0.046	0.035	0.024	0.018
10	0.29	0.13	0.05	0.03	0.018	0.013	0.009	0.007

Table 1.2.6. Standard deviations of the skew multipoles.

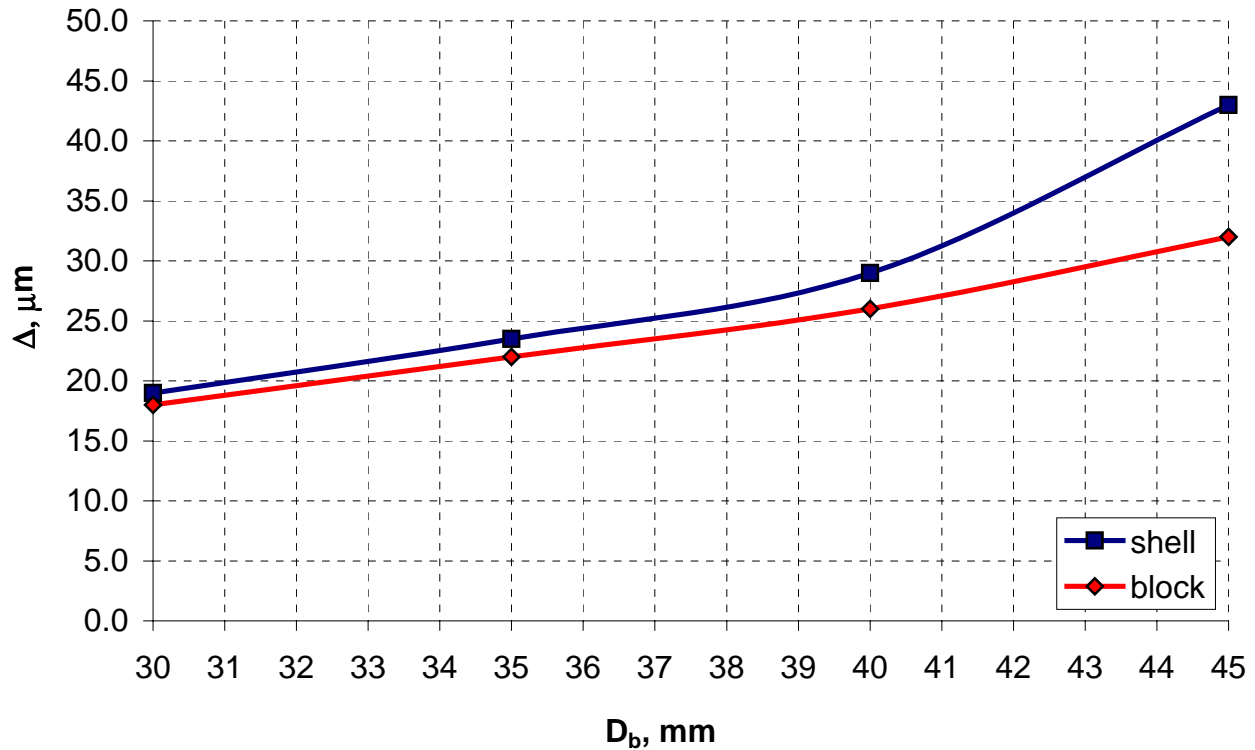| Tolerance, μm	Standard deviation, 10^{-4}							
	a_2	a_3	a_4	a_5	a_6	a_7	a_8	a_9
50	0.73	0.76	0.51	0.3	0.15	0.08	0.04	0.02
25	0.36	0.38	0.25	0.15	0.08	0.04	0.02	0.01
10	0.14	0.13	0.083	0.048	0.026	0.014	0.008	0.004

Figure 1.2.12. Tolerance on the blocks positioning versus the bore diameter.

Table 1.2.7. Magnet parameters.

Coil design	Bore diam., mm	Quench field, T	Peak field/ bore field	Current, kA	Induct., mH/m	Stored energy	Forces/I coil quadrant		Yoke IR, mm	Cond. area, cm^2
							F_x, MN/m	F_y, MN/m		
shell	30	11.96	1.040	12.93	2.30	192.26	2.06	-0.99	52	16.65
	35	11.97	1.044	13.59	2.38	219.78	2.25	-1.08	52	17.73
	40	11.97	1.050	15.55	2.09	252.68	2.45	-1.18	55	19.30
	45	11.95	1.055	17.09	1.98	289.15	2.65	-1.28	57	20.66
block	30	11.97	1.016	13.03	2.48	210.53	2.25	-1.04	54	16.92
	35	11.95	1.019	16.09	1.95	252.42	2.49	-1.12	57	18.47
	40	11.95	1.022	18.77	1.72	302.99	2.74	-1.24	61	20.27
	45	12.04	1.036	20.08	1.76	354.82	3.02	-1.32	63	22.80

The maximum field slightly varies among these designs due to the geometry discretization (+/- one cable per coil quadrant or two strands per cable), so to make a correct efficiency comparison it was necessary to bring them to one field. Due to a high cable compaction in the inner layers of all the designs and a large effect of the inner layer to the harmonics, it looked only feasible to adjust number of conductors in the outer layer. It was numerically determined that an addition of one conductor to the outer layer increases the maximum field by ~ 0.1 T, which made it possible to bring all the designs to one field by changing number of conductors in the outer layer.

Figure 1.2.13 shows the coil area adjusted for 12 T bore field as a function of bore diameter. As expected, the block type coil design has higher conductor area than the shell type. The difference is relatively small at the bore diameter of 30 mm (1.4 %), but increases up to 7.5 % at the bore diameter of 45 mm.

Figure 1.2.14 presents stored energy and Figures 1.2.15-1.2.16 show horizontal and vertical force components as functions of the bore diameter at 12 T field. Thus, the difference between the two designs in stored energy increases from 9 % to 20 % and the difference in horizontal forces increases from 9 % to 12 % correspondingly for the bore sizes range from 30 mm to 45 mm. The difference in vertical force is smaller and virtually does not depend on the bore size.
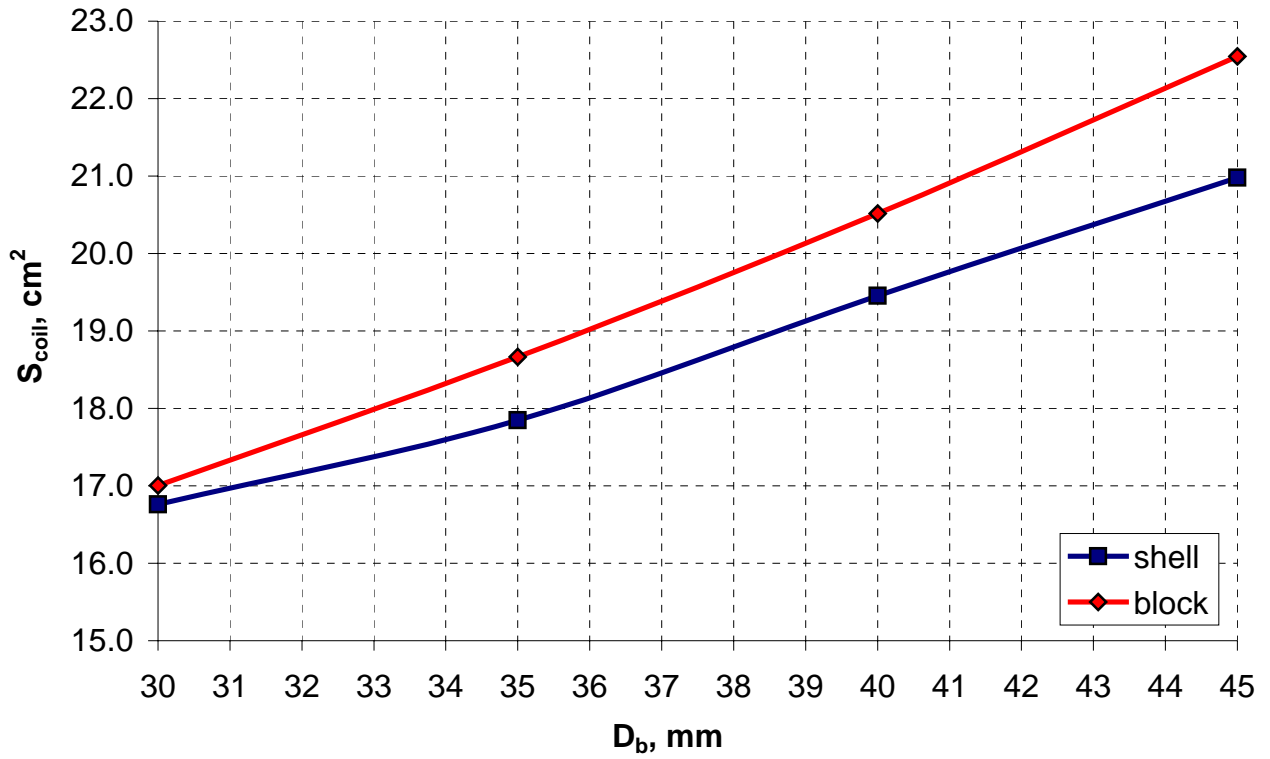
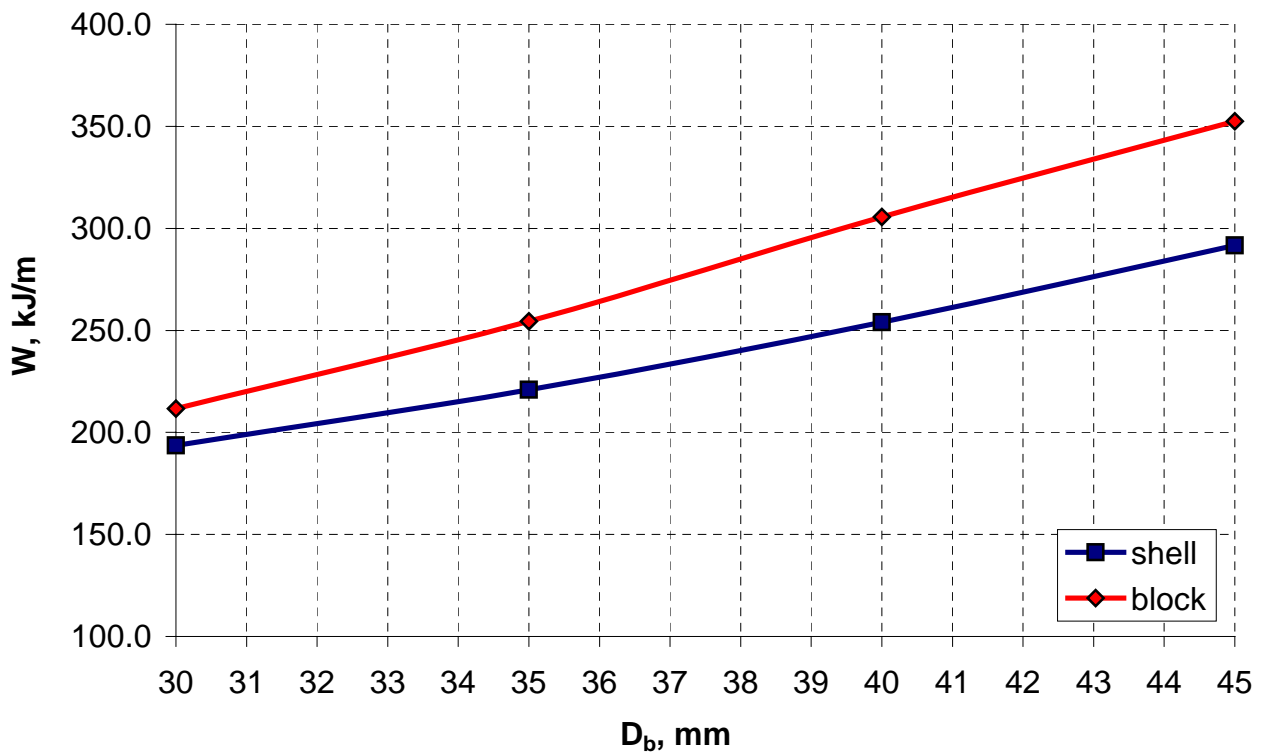Figure 1.2.13. Coil (strands) area as a function of bore diameter.

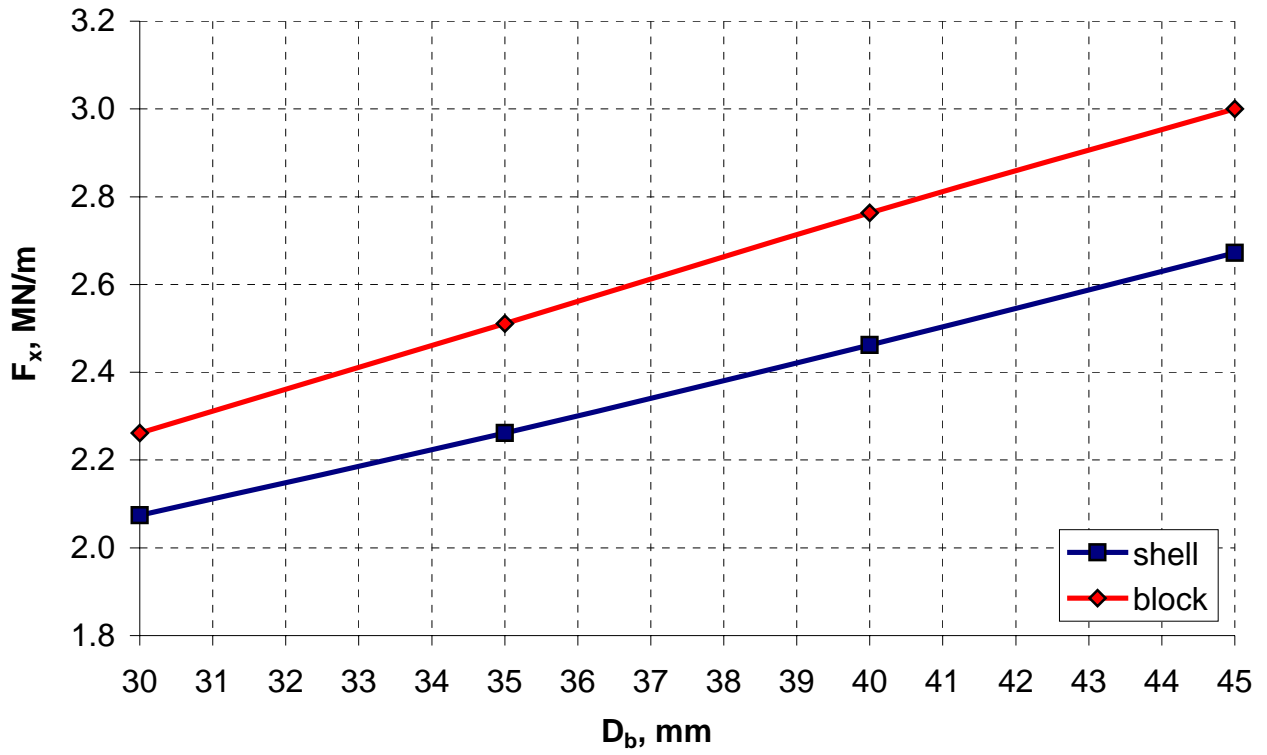Figure 1.2.14. Stored energy as a function of bore diameter.

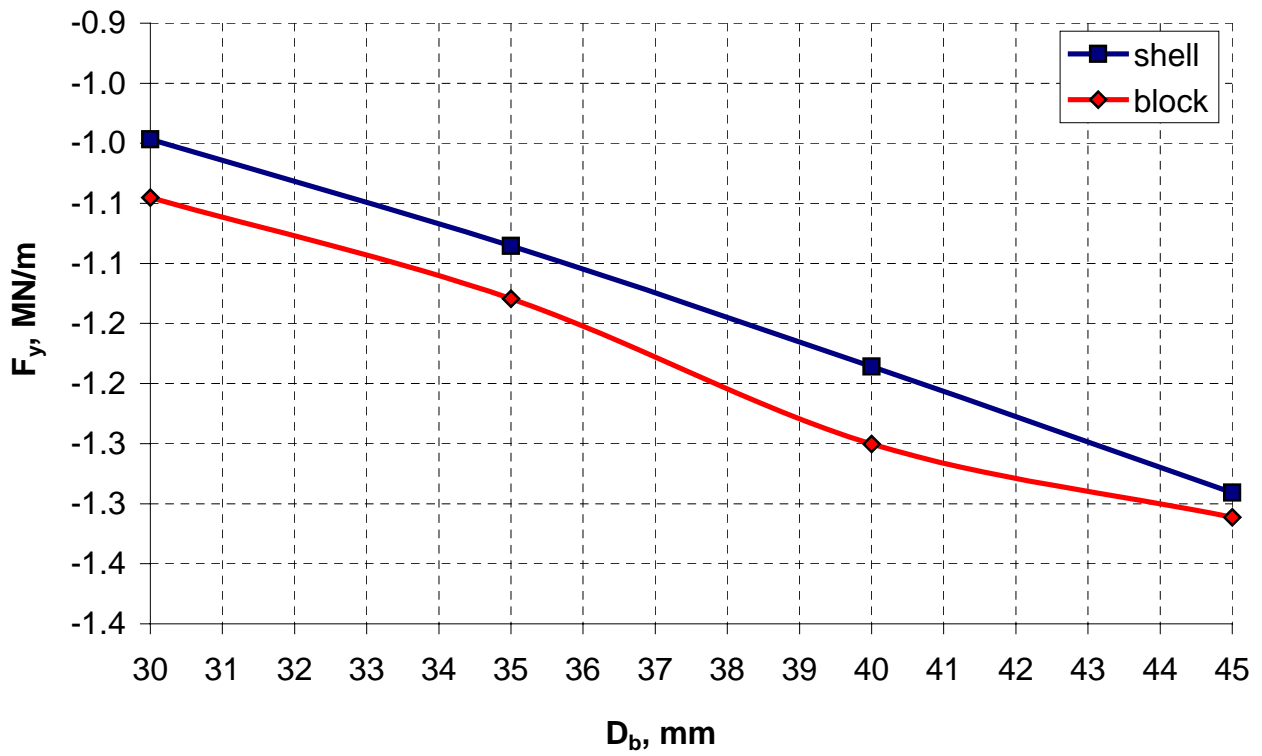Figure 1.2.15. Horizontal force in I coil quadrant as a function of bore diameter.

Figure 1.2.16. Vertical forces in I coil quadrant as a function of bore diameter.

1.3 Coil optimization for VLHC

The data described in the previous paragraph provided enough information about the coil bore size needed for satisfaction of the preliminary field quality criteria. It allowed fixing of the coil bore size and performing a final coil optimization. The superconductor properties were chosen the same as during the study of coil bore size. However, peculiarities of manufacturing the shell and block type magnets imposed using of different coil design approaches.

1.3.1 Shell type dipole coil

A small bending radius of the pole turn in the shell type coils required using of a so-called "wind and react technique" [42], [44]. According to this technique the Nb_3Sn cable gets wound into the proper coil shape first and reacted at high temperature (650 C during 2-3 weeks) afterwards for the chemical reaction, turning mixture of niobium and tin into A15 intermetallic composition, to occur. The cable becomes brittle after reaction making it difficult to impossible to perform any mechanical operations. It requires that all the necessary technological procedures, like cable insulation, to be done before reaction. The high reaction temperature does not allow any of the widely used in NbTi coils organic insulations. Fortunately during R&D at Fermilab, there was found an acceptable inorganic insulation [45], which could withstand both high reaction temperatures and considerable mechanical stresses. It consists of ceramic tape that can be used in regular insulating machines and ceramic binder, applied after the coil winding (before reaction), which increases the insulation mechanical and electrical strength. The total insulation depends on the tape thickness, percentage of overlap, amount of the binder and applied pressure. It was chosen 0.25 mm per side of the cable [46]. The coil bore size was fixed at 43.5 mm that satisfies the random multipole specifications with the tolerance on block position of 35-40 μm. The cable dimensions and number of turns were optimized to have a minimum inductance, while keeping the quench current close to the upper edge of the available current supply (25 kA).

Cross-section of the shell type coil optimized by ROXIE code is presented in Figure 1.3.1 along with the field quality (non-uniformity ΔB/B) diagram. Tables 1.3.1-1.3.3 show the relative systematic harmonics and geometrical parameters of the coil. It was possible to increase the strand diameter by 15 % with respect to the above cases, while keeping the field quality within specification. It resulted in a smaller number of turns and a substantially smaller inductance. The coil geometry was optimized in assumption of a circular yoke with the inner radius of 60 mm and constant magnetic permeability of 1000, which was a correct assumption at low field. The non-linear magnetization effects will be considered in chapters on the finite-element analysis.
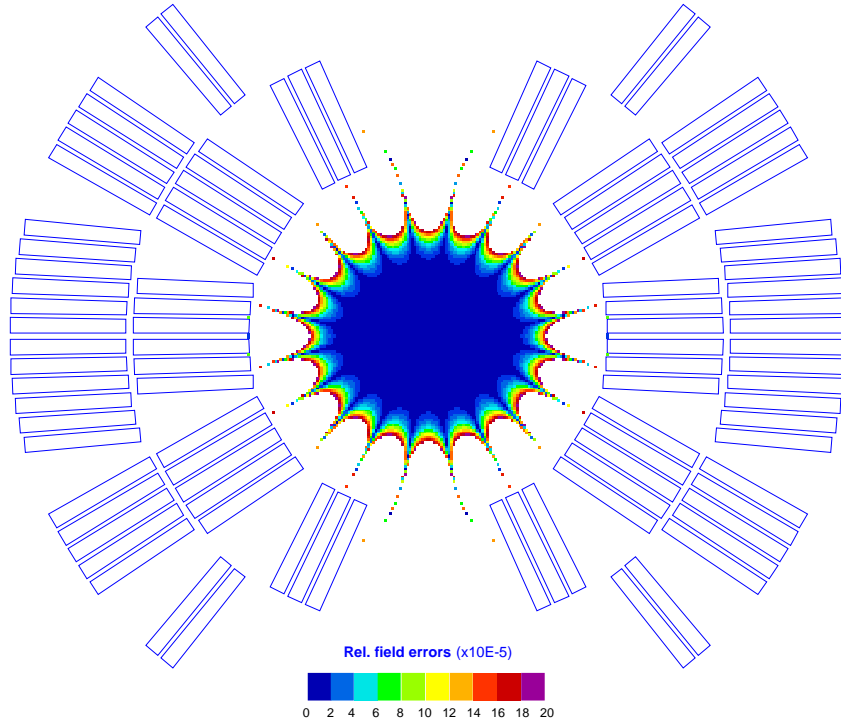
Rel. field errors (x10E-5)

0 2 4 6 8 10 12 14 16 18 20

Figure 1.3.1. Optimized shell type coil cross-section with the field quality diagram.

1.3.2 Block type dipole coil

The plain rectangular geometry of the block type coils makes it well suited for the common-coil configurations that simplifies the coil design and manufacturing with respect to complicated spatial shape of the shell type coils. Another advantage of the common-coil is by factor of ~10 larger minimum bending radius of the cable than in the shell type coil that makes it possible to implement a so-called "react and wind" manufacturing technique. According to this technique, a bare cable is reacted on a spool of large radius (comparable with the bending radius), then insulated and wound into the coils. Obviously all the operations with the reacted cable have to be done with an utter care to avoid a large critical current degradation. There was found a straight correlation between the strand diameter and a minimum bending radius for a fixed bending degradation. Thus the strand and cable tests conducted at Fermilab determined the optimum strand diameter of 0.7 mm for the minimum bending radius of the Rutherford type cable of 90 mm [47]. These constrains were used as a starting point for the coil optimization.

Keeping of the large cable bending radius made it difficult to implement the auxiliary turns above/below the aperture (similar to ones shown in the coil design study) in order to create the necessary spatial current distribution. It would require bending them in the horizontal plane that

38

would not be acceptable due to the small bending radius or to bend them both ways in the vertical plane, as proposed in [48] that would considerably increase the magnet dimensions.

Along with the goal of minimizing the coil inductance, these considerations had led to the idea of a single-layer coil without the auxiliary turns [49]. Keeping the bore field at the same level as in the two-layer design requires increasing the cable width and therefore aspect ratio by ~ 40 %. However, the plane racetrack coil geometry can adopt such cables without running into the cable stability problems. Maximum cable width in this case is limited only by the capability of the available cabling machine.

The required current distribution was created by a small horizontal shift towards vertical axis in the outer coil blocks. Figure 1.3.2 shows coil cross-section optimized using ROXIE code along with the field quality diagram. Tables 1.3.1-1.3.3 present systematic and random (+/-50 μm displacement) field harmonics and coil geometrical parameters.
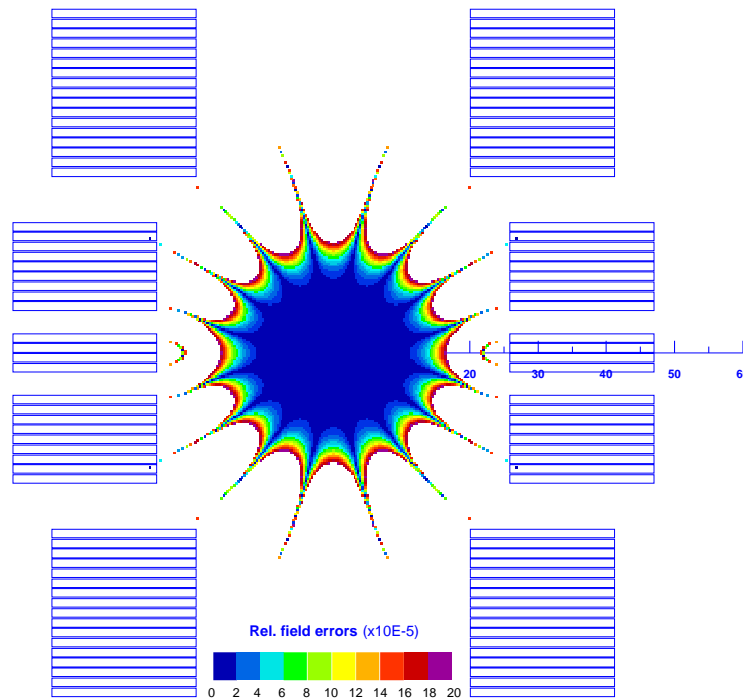

Figure 1.3.2. Optimized block type coil cross-section with the field quality diagram.

Table 1.3.1. Cable parameters in the shell and block type designs.

Coil design	Bare cable		Strand diameter, mm	Cabling angle, deg.	N strands
	Width, mm	Midthickness, mm			
shell	14.232	1.800	1.012	14.5	28
block	21.095	1.245	0.700	14.5	60

39

Table 1.3.2. Systematic and random harmonics, 10^{-4}.

n	Shell		Block	
	b_n	$\max(\sigma_{an}, \sigma_{bn})$	b_n	$\max(\sigma_{an}, \sigma_{bn})$
2	-	1.20	-	1.04
3	0.000	0.56	-0.002	0.36
4	-	0.28	-	0.14
5	0.000	0.10	0.000	0.05
6	-	0.05	-	0.02
7	-0.000	0.02	0.014	0.01
8	-	0.01	-	0.00
9	-0.091	0.00	-0.048	0.00
10	-	0.00	-	0.00
11	0.099	0.00	0.001	0.00

Table 1.3.3. Magnet design parameters.

Parameter		Coil type	
		Shell	Block
Physical aperture, mm		43.5	40.0
Geometrical aperture, mm		43.5	55.1
Number of turns		48	56
Maximum field, T		12.01	10.82
Maximum current, kA		21.52	24.18
Transfer function, T/kA		0.558	0.447
Inductance, mH/m		1.33	1.43
Maximum stored energy, kJ/m		308.9	419.2
Maximum force per I coil quadrant	F_x, MH/м	2.77	2.93
	F_y, MH/м	-1.27	-1.34
Yoke inner radius, mm		60.0	100.0
Conductor cross-section area, cm^2		22.33	26.71

The geometrical field multiplies are within specification in spite there are only three block per coil quadrant. The cable utilized 60 strands, which was the upper limit of the cabling machine (available from LBNL). The circular iron yoke used in this optimization had the inner radius of 100 mm and constant permeability of 1000. However, the mechanical analysis [47] shown a necessity of flat iron yoke surface, that required relevant coil re-optimization. It is presented in chapter on the finite element analysis.

1.4 Minimum inductance dipole coils

The above coil optimization was constrained by limitation of the maximum current 25 kA at the test facility. It imposed the number of conductors that generates the required field and therefore

the coil inductance, which for the chosen coil bore size and field was within 1.5-2.5 µH/m. This inductance was determined to be safe enough for the quench protection of ~15 m long magnet [50]. However the tends to increase a collider circumference and to minimize a number of active elements in the system make it necessary to use a maximum possible length of the dipole magnets, suitable for manufacturing, transportation and installation procedures.

Taking into account a considerable and developing success in high temperature superconducting current leads [51] and compact, high current power converters [52], limitation of the maximum magnet current at 20-30 kA vanishes in a long term of the collider development. This allows minimization of the coil inductance by decreasing the number of turns. Obviously, there should be a coil configuration with a minimum number of turns, based on the cable with constant area and shape, which generates field of the required quality and strength.

It was made a continuous iterative minimization of the number of turns with help of ROXIE code. Figure 1.4.1 presents cross-sections of the shell and block type coils that have minimum possible number of turns, based on the Rutherford type cable yet. Table 1.4.1 summarizes systematic and random field multipoles (+/-50 µm random cable displacement) for the optimized coils, which exceed the field quality requirements.

The upper coil block has only one cable in the Design I, which is the minimum element of the coil discretization. Attempts to remove one cable from any of the three blocks would violate badly the necessary spatial current distribution, which therefore allows considering this design as a coil with the minimum number of turns or the minimum inductance coil.
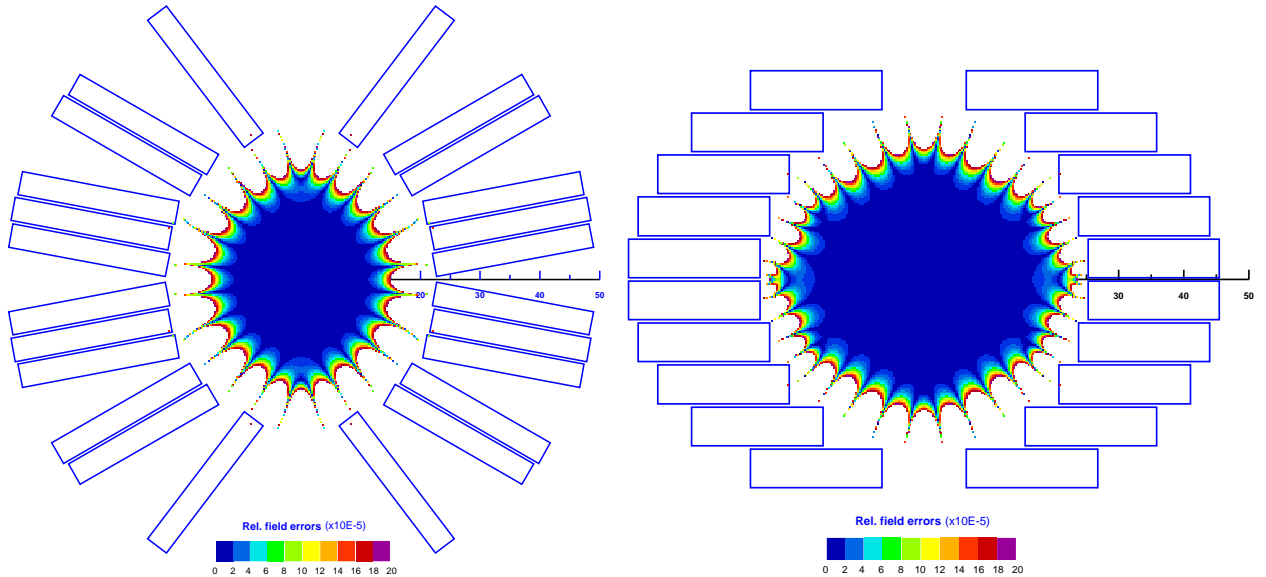

Figure 1.4.1. Minimum inductance coils (Design I – left, Design II - right).

Table 1.4.1. Systematic and random field multipoles, 10^{-4}.

n	Design I		Design II	
	b_n	max(σ_{an}, σ_{bn})	b_n	max(σ_{an}, σ_{bn})
2	-	1.02	-	1.07
3	-0.0001	0.47	0.0005	0.49
4	-	0.22	-	0.19
5	0.0011	0.10	0.0003	0.08
6	-	0.04	-	0.03
7	0.0019	0.02	0.0005	0.01
8	-	0.01	-	0.00
9	-0.0035	0.00	0.0008	0.00
10	-	0.00	-	0.00
11	-0.0219	0.00	-0.0013	0.00

The number of turns is not so strictly fixed in the Design II coil, which approximates geometry of two intersecting ellipses. Nevertheless, five cables per coil quadrant are required to achieve the necessary field quality, while the cable still has a reasonable thickness. In addition, accommodation of thick cables required aligning them on elliptical cylinder in Design I coil.

The minimum number of turns in both designs makes it attractive to wind such coils into a mechanical structure (similar to those used in the stators of electrical motors). This forced implementation of rectangular cables in both designs for simplification of the winding technology. The collar structures and winding considerations for such coils are described in [53].

Parameters of the Rutherford type cables used in the Design I and II coils are summarized in Table 1.4.2. Both cables have small aspect ratio that ensures a good cable mechanical stability. However, the cables are based on quite large strands 2-3.5 mm in diameter that is by factor of 2-3 larger than those currently used in Nb$_3$Sn cables. Consequently, such cables would have rather high mechanical rigidity that may create some problems during coil winding. In addition, in case of the react and wind technique, suitable for the Design II coil, the large strand diameter would require a significantly larger bending radius than in the developed common-coil. In order to avoid these problems, a multistage cable with sub-strands shown in Figure 1.4.2 can be used. Those allow decreasing the sub-strand diameter to a level of 0.45-0.7 mm, comfortable for the strand production.

Table 1.4.2. Cable parameters.

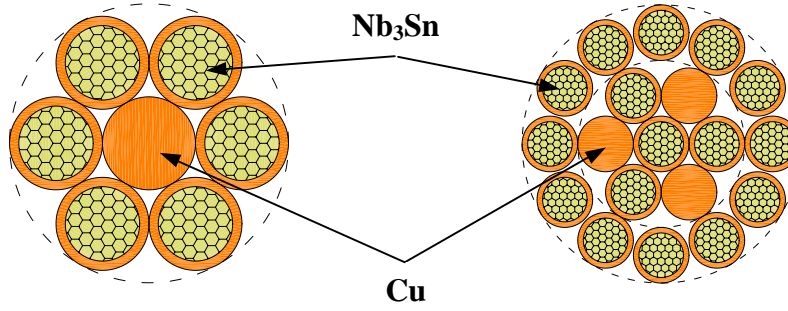| Coil design	Bare cable		Strand diameter, mm	Cabling angle, deg.	N strands
	Width, mm	Midthickness, mm			
Design I	26.717	3.942	2.200	14.5	24
Design II	20.233	5.935	3.350	14.5	12

Figure 1.4.2. Examples of combined strand structures made of copper and Nb₃Sn strands.

Combination of the Nb_3Sn strands having minimum copper to non-copper ratio, necessary for the strand production and cryogenic stabilization with pure copper strands, allows achieving the copper to non-copper ratio in the final strand, required for the quench protection at a lower strand cost [53]. Table 1.4.3 presents the major magnet parameters. Those were calculated at 11 T bore field with a round inner surface of the iron yoke and low constant iron permeability μ~5 chosen such to represent the yoke saturation.

Table 1.4.3. Magnet parameters.

Parameter		Unit	Design I	Design II
Physical aperture		mm	45.0	45.0
Geometrical aperture		mm	45.0	50.0
Number of turns			12	10
Maximum field		T	11.79	11.84
Maximum current		kA	87.203	99.297
Transfer function		T/kA	0.1352	0.1192
Inductance		mH/m	0.076	0.057
Maximum stored energy		kJ/m	289.0	281.0
Maximum force per	F_x	MN/m	3.01	3.03
I coil quadrant	F_y	MN/m	-1.23	-1.28
Yoke inner radius		mm	60	55
Conductor cross-section area		cm²	22.61	22.84

Minimum distance of 8 mm between the outer coil and the inner yoke surfaces was the same as in the two-layer shell-type dipole model. The quench field was calculated for J_c(12 T, 4.2 K) = 2000 A/mm² and copper to non-copper ratio of 0.85. Both designs have nearly the same physical apertures, coil areas and quench fields. The coils can be accommodated inside "cold" or "warm" iron yokes in case of the horizontal bore arrangement and in the common-coil configuration with "cold/warm" iron yoke in case of the vertical bore arrangement [54]. A minimum number of turns in both designs leads to low transfer functions and high current, which is nevertheless smaller than 100 kA – a nominal current of the first stage VLHC magnets [10]. However, due to small number of turns the magnets have exceptionally low inductance per unit of length, which is

43

by factor of ~20 smaller than in any other high field dipole magnet. It allows increasing the magnet length well above the currently used limit of 15-20 m that reduces manufacturing expenses and improves the collider reliability.

1.5 Shell type quadrupole coil

The arc quadrupole magnets usually comprise a small part of the collider magnets that makes implementation of the main dipole cable in quadrupole coils economically reasonable at the same bore size [8]. Based on this consideration, the quadrupole coil bore diameter was fixed at 43.5 mm and the cable choice was similar to the one used in the shell type dipole coil. Thick collars were used in order to provide the radial coil prestress and constrain electromagnetic forces, unlikely to the dipole magnets, where prestress was provided by the outer skin. It was determined that a 20 mm thick stainless steel collar serves this purpose well [55]. Geometrical field multipoles have been optimized using ROXIE code in assumption of constant yoke permeability of 1000. Figure 1.5.1 shows the coil geometry after optimization and Tables 1.5.1-1.5.2 summarize the systematic and random (+/-50 μm random blocks displacement) field multipoles and coil parameters.
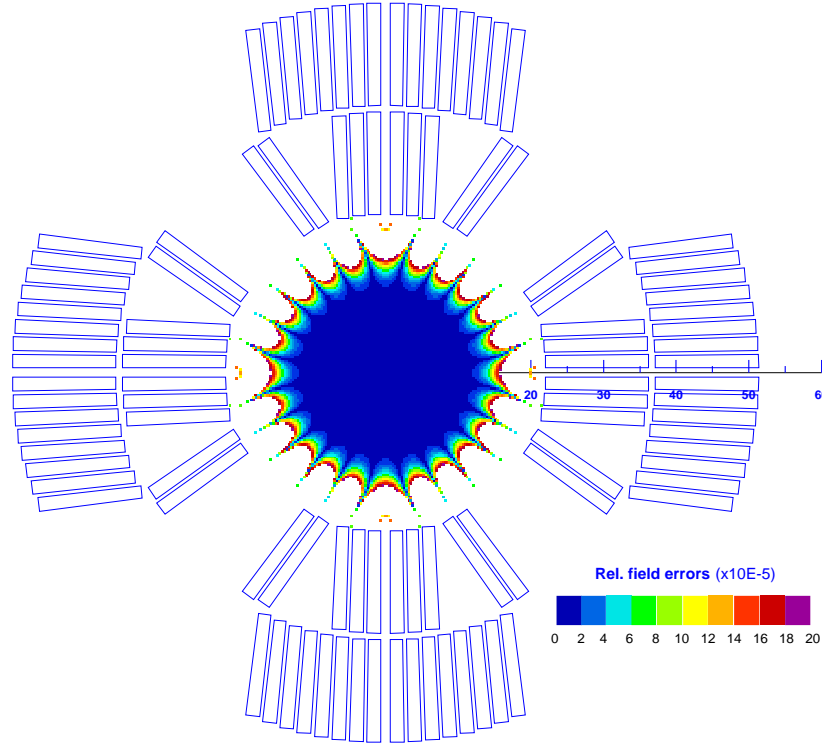
Figure 1.5.1. Quadrupole coil cross-section with the field quality plot.

The maximum field gradient achievable in presented configuration is 438 T/m at a current of 29.5 kA that is by factor of 1.3 larger than in the shell type dipole magnet. It requires a separate powering of the quadrupole magnets. The systematic field multipoles are within specification, while the random multipoles are twice higher than in the shell type dipole.

However, they were normalized by the amplitude of the main (quadrupole) field component, and have to be adjusted for the dipole field level to make a correct comparison. The maximum amplitude of the quadrupole component is 4.4 T at 1 cm radius, which occurs at the maximum dipole field of 12 T. Therefore the quadrupole harmonics must be normalized by a factor of $12/4.4 = 2.7$, which brings them down to the level of the dipole harmonics. It is quite explicable since both magnets have the same coil aperture and close number of turns. The coil inductance is twice smaller than in the shell type dipole due to a negative coupling between half of the turns, while the stored energy is about the same. The quadrupole magnet parameters, based on the considered coils are described in [56].

Table 1.5.1. Systematic and random multipoles.

n	b_n	$\max(\sigma_{an}, \sigma_{bn})$
1	-	7.48
3	-	1.82
4	-	0.83
5	-	0.38
6	-0.0003	0.19
7	-	0.07
8	-	0.03
9	-	0.01
10	-0.0039	0.00

Table 1.5.2. Magnet design parameters.

Parameter		Unit	Value
Physical aperture		mm	43.5
Geometrical aperture		mm	43.5
Number of turns			52
Maximum gradient		T/m	438.0
Maximum current		kA	29.51
Transfer function		T/m/kA	14.842
Inductance		mH/m	0.567
Maximum stored energy		kJ/m	246.8
Maximum forces per	F_x	MN/m	1.24
I coil octant	F_y	MN/m	-1.56
Yoke inner radius		mm	72
Conductor cross-section area		cm^2	24.19

1.6 Summary

The results obtained during study and optimization of the coil design parameters can be summarized as follows:

- The idealized optimum coil configurations has been found for a set of parameters, close to the requirements being considered for the high field option of 100 TeV collider. The coil area drastically increases with the bore field for a fixed superconductor critical current density. However, using of superconductor with increased critical current density can improve the situation. Derived expressions give possibility of analytical scaling the coil area for any operating field, bore size and superconductor properties.

- Study of various coil designs made it possible to determine limitations of coil bore size and tolerances on block positioning:
  - the coil bore size, which satisfies a reasonable criteria of systematic field errors must be higher than 40 mm for both shell and block type designs;
  - the target of the random field errors dictates tolerance on the coil blocks positioning to be better than 30 μm and 25 μm for the shell and block type designs respectively with 40 mm bore that may look too stringent for the available production technology. It sets another limitation on the coil bore size at about 45 mm, unless a precise manufacturing technology is developed;
  - the block type magnets yield efficiency to the shell type magnets at the same aperture size, field and superconductor properties. The reason is in essentially better approximation of the necessary spatial current distribution by the shell type coils rather than by the block type coils.

- There was developed the two-layer shell type coil with 43.5 mm bore, used for the construction of the single bore dipole magnets at Fermilab. It was demonstrated that 6 block per coil quadrant make it possible to achieve the target specification on geometrical field quality. Reduced coil volume, stored energy and inductance with respect to existing shell type designs (LHC dipole).

- There was developed the single-layer block type design, which can be used in the common-coil configuration. It was demonstrated that the field of required quality and strength can be achieved with only three blocks per coil quadrant. A small, horizontal shift of the outer blocks is used for the necessary field tuning. It eliminates the auxiliary turns in the coil aperture that essentially simplifies design and production technology.

- There were proposed designs of the minimum inductance coils based on the Rutherford type cable. It was shown that 12 turns in the shell type coil and 10 turns in the block type coil are necessary and enough for generation the field of required strength and quality. It imposes the

minimum inductance, which is by factor of ~25 smaller than in existing shell and block type magnets with the same field level and aperture size. Exceptionally low inductance allows a cardinal improvement of the coils mechanical structures and removes limitations on the maximum magnet length. Considered combination of the Nb_3Sn and copper sub-strands reduces the conductor cost by 15-20 %.

- There was developed shell type quadrupole coil with the same bore size and cable as for the shell type dipole coil. It was shown that the necessary gradient and field quality can be reached in the two-layer configuration with three blocks per octant.

CHAPTER 2. STUDY OF THE YOKE DESIGN PARAMETERS

2.1 Introduction

Coils in all of the accelerator magnets, operating of being building at present time for large accelerators, were made from NbTi superconductor. It allows reaching the maximum field in dipole magnets of about 10 T at 1.9 K [8]. However, due to the practical and economical reasons, operating field in the NbTi magnets was chosen well below this limit. Table 2.1.1 presents parameters of the main dipole and quadrupole magnets in these machines.

Table 2.1.1. Parameters of superconducting dipole and quadrupole magnets.

Laboratory	FNAL	DESY	IHEP	SSCL	BNL	CERN
Machine	Tevatron	HERA	UNK	SSC	RHIC	LHC
Circumference, km	6.3	6.3	21	87	3.8	27
Particle type	pp$^-$	e$^\pm$p	pp	pp	ions/pp	pp
Energy/proton beam, TeV	0.9	0.82	3	20	0.5	7
Operating temperature, K	4.6	4.5	4.6	4.35	4.6	1.9
Arc dipole magnets						
Nominal field, T	4.4	4.68	5.1	6.79	3.46	8.36
Coil bore diameter, mm	76.2	75	80	50	80	56
Magnetic length, m	6.1	8.8	5.8	15	9.7	14.2
Quantity	774	416	2168	7944	264	1232
Arc quadrupole magnets						
Nominal gradient, T/m	75.8	91.2	96.1	194	71.8	223
Aperture, mm	88.9	75	80	50	80	56
Magnetic length, m	1.7	1.9	3.0	5.7	1.1	3.1
Quantity	216	256	322	1696	276	386

The first superconducting accelerator built, Tevatron has still the most compact magnets. The iron yoke is at the room temperature that allows a very compact cryostat but makes the field quality sensitive to the location of the "cold" coil within the "warm" iron yoke. In case of misalignment, the field quality deteriorates as well as eccentricity forces between coil and yoke create stresses in the coil support structure. The self-centering coil support system utilizing spring-loaded bolts was implemented in order to provide the nominal coil position. Many features of the Tevatron set the style for those to follow, particularly using of precision punching techniques to produce collar laminations. Collars of alternating pattern, fitted around the coil are pressed to a precise dimension using a hydraulic press and then welded together. Thus, it is possible to benefit from the economies of mass production, while retaining precision of the punching process [5].

Aluminum alloy collars are used in HERA magnets, giving a better match to the transverse contraction of the coils. The iron is placed immediately around the collars at low temperature providing precise centering of the coil. Being closer to the coil, the iron contributes more to field level, however its saturation causes deterioration of the field quality. The cold mass is more rigid, requiring fewer supports from room temperature, but the cryostat is bigger and heavier [6].

Similar in many aspects to HERA, SSC used "cold" iron and stainless steel collars, however larger field and thus electromagnetic forced during excitation required strong iron participation in support of the forces. The design was based on slim collars that are elastically deformed by the pre-compressed coil but forced into the design shape by very rigid iron yoke. In this type of design, the interface between the collar and yoke is very critical and particular attention has to be paid to the different thermal shrinkage of the coil, stainless steel collar and iron yoke [9].

Perhaps the simplest and most economical design so far, RHIC dipole uses a single-layer coil. Despite this simplification, the field quality is at least as good as in HERA and better than in Tevatron. The iron yoke is used as the force-supporting collar being separated from the coil by a precision molded phenolic spacer, which also serves as an excellent electrical insulator. The disadvantage of unfavorable differential thermal shrinkage and loss of prestress during cooling down remains but creates no problem for moderate field levels in RHIC [7].

Since it is intended to reach the highest possible energy in the existing tunnel, magnets for LHC must achieve high fields. After an initial assessment of Nb_3Sn, it was decided that NbTi cooled to 1.9 K provides a more economical and reliable solution. Cooling NbTi from 4.2 K to 1.9 K offers an extra 3 T field at the same reference current density. To minimize cost and space required in the tunnel, the magnets use an elegant "two in one" design. As disadvantage, non-linear magnetic coupling between the two coils causes unallowed by dipole symmetry even multipole terms, providing an extra load to the active correcting system [8]. It complicates magnet design and requires precise numerical simulation and optimization for providing the necessary field quality.

Methods of magnetic field simulation described in previous chapter are suitable for magnetic systems with linear properties and simple geometry. They are convenient to use at an initial step of a magnet design, when fast estimation is required. In reality superconducting magnet systems contain materials with non-linear magnetic properties and have complicated shape, which cannot be precisely described by an exact analytical expression. Simulation of magnetic field within such systems requires implementation of numerical methods. Within a large variety of algorithms used for numerical field simulations there are two major branches: differential and integral methods.

2.1.1 Solution of non-linear magnetostatic problems

The magnetostatic field can be explicitly described by the Maxwell differential equations [57]:

$$curl\vec{H} = \vec{J} \qquad (2.1.1)$$

$$div\vec{B} = 0 \qquad (2.1.2)$$

together with the constitutive magnetic media properties:

$$\vec{B} = \mu\vec{H} \; . \qquad (2.1.3)$$

Magnetic field analysis is usually based on the vector potential formulation. The equation to be solved for the static magnetic field is derived by combination:

$$\vec{H} = \frac{1}{\mu}\vec{B} = \frac{1}{\mu}curl\vec{A}$$

from definition of the vector potential:

$$\vec{B} = curl\vec{A}$$

and (2.1.3) in (2.1.1):

$$curl\left(\frac{1}{\mu}curl\vec{A}\right) = \vec{J} \; . \qquad (2.1.4)$$

In two-dimensional case the differential equation (2.1.4) transforms into the equation with respect to one longitudinal component of vector potential:

$$curl\left(\vec{i}\,\frac{1}{\mu}\frac{dA_z}{dy} - \vec{j}\,\frac{1}{\mu}\frac{dA_z}{dx}\right) = J_z$$

that can be solved using the finite-element (FEM) method. This approach used in many FEM codes, like POISSON [58], OPERA2D/PE2D [59] and ANSYS2D [60], provides reliable results and moderate computation time.

Another possibility is based on the scalar potential formulation. Within the non-current regions:

$$curl\vec{H} = 0$$

and therefore the field can be described as the gradient of a scalar potential function U:

$$\vec{H} = -grad(U). \qquad (2.1.5)$$

Substituting (2.1.5) and (2.1.3) in (2.1.2) one can write:

$$div\big(\mu(gradU)\big) = 0$$

or in the two-dimensional case:

$$div\left[\mu\left(\vec{i}\,\frac{dU}{dx} + \vec{j}\,\frac{dU}{dy}\right)\right] = 0.$$

The differential equation can be solved by the FEM method, but only applicable to the system driven by permanent magnets or by boundary conditions. It is explicitly described in [61]. Due to this restriction, it has a limited implementation in numerical codes, however some of them like OPERA2D offer the scalar potential formulation as an extra option.

Limitation of the scalar potential formulation can be overcome if to define a function $\vec{T}$ as:

$$curl\vec{T} = \vec{J}. \qquad (2.1.6)$$

Then:

$$curl\vec{H} - curl\vec{T} = curl(\vec{H} - \vec{T}) = 0$$

and therefore a reduced scalar potential function U_r can be introduced as [62]:

$$\vec{H} - \vec{T} = -grad(U_r). \qquad (2.1.7)$$

The expression (2.1.7) automatically satisfies the first Maxwell equation (2.1.1) and only the second equation (2.1.2) remains to be solved. Taking into account (2.1.2)-(2.1.3) it can be written in the form:

$$div\big(\mu\big(\vec{T} - grad(U_r)\big)\big) = 0$$

or:

$$div\big(\mu \cdot grad(U_r)\big) = div(\mu\vec{T}), \qquad (2.1.8)$$

which is the generalized Laplace-Poisson equation. There are several options for the choice of function $\vec{T}$, satisfying its definition. The most straightforward way is to define $\vec{H}_s$ according to the Biot-Savart low:

$$\vec{H}_s(P) = \frac{1}{4\pi} \int_{V_c} \frac{\vec{J}(Q) \times \vec{R}}{|\vec{R}|^3} dV_c, \qquad (2.1.9)$$

where V_c is the current-carrying volume, P is the field observation point, Q is the source point and $\vec{R}$ is the vector pointing from Q to P. Obviously:

$$curl\vec{H}_s = \vec{J} \qquad (2.1.10)$$

that satisfies (2.1.6) and therefore $\vec{H}_s$ is the valid choice for $\vec{T}$. In highly permeable media the magnitude of $\vec{H}$ is often much less than that of $\vec{H}_s$, which leads to high cancellation errors when using $\vec{H}_s$ as $\vec{T}$ in (2.1.7). Also, the space variations of $\vec{H}$ and $\vec{H}_s$ will be quite different if the one is represented using derivatives of a finite-element form function (low-order polynomial) and the other one using the direct analytical evaluation (2.1.9), which results in magnification of computational errors.

These difficulties can be avoided if there are no currents flowing in the magnetic materials. The regions with zero current density can be represented using the total magnetic scalar potential U (2.1.5). By combination the total and reduced scalar potential, the cancellation difficulties disappear [61]. Such algorithm is implemented in the Vector Fields code OPERA3D/TOSCA for simulation of spatial magnetic fields [59]. Its minimal combination consists of using the reduced potential only inside volumes where the currents flow and the total potential everywhere else. This has a practical limitation since the reduced potential volume may have a complicated shape and cutting surfaces would have to be specified in the total potential space to maintain a single-valued potential. On the other hand, the scalar potential formulation of the spatial magnetostatic fields offers the most economic description in terms of unknown functions. Also the current carrying regions in this formulation do not have to be modeled by finite elements that significantly simplifies building of the finite-element model and extremely helpful in 3D simulations.

One should notice that using of $\vec{H}_s$ as $\vec{T}$ is not the only possibility. For example, $\vec{T}$ can be defined as vector normal to a shell of arbitrary shape spanned by a current [63], [64]. This approach is used in KOMPOT package of 3D magnetostatic field simulations [65]. Some useful options concerning the finite-element implementation can be found in [66]-[68].

The total vector potential formulation described above has disadvantage with respect to the reduced scalar potential since shape of the current regions has to be exactly modeled by the finite

elements. If this is not the case, precision of the calculations becomes very low. This disadvantage can be avoided by introduction a reduced vector potential $\vec{A}_r$ as:

$$\vec{B} = \mu_0 \vec{H}_s + curl\vec{A}_r, \tag{2.1.11}$$

where $\vec{H}_s$ is the Biot-Savart field defined by (2.1.9) [71]. Obviously $\mu_0 \vec{H}_s$ is magnetic field due to currents in a free space and $curl\vec{A}_r$ is the field resulting from the presence of iron. The choice (2.1.11) automatically satisfies the second Maxwell equation (2.1.2) since the divergence of current-generated field is zero. Then only the first equation remains to be solved. Taking into account (2.1.3) and (2.1.10):

$$curl\left(\frac{1}{\mu} curl(\vec{A}_r)\right) = curl\left[\vec{H}_s\left(1 - \frac{\mu_0}{\mu}\right)\right].$$

This second order partial differential equation is similar to (2.1.4), however the right side does not contain current density and therefore an exact modeling of conductors shape by finite elements is not required. Similarly to the reduced scalar potential method, the calculation accuracy is lower with respect to the total potential formulation. This approach is used in ROXIE FEM module for the field simulations and yoke design of LHC magnets [71].

Although the finite element method is most commonly used, it is not the only method of solving the field differential equations. For instance, there are various publications on the method of final differences to solve the scalar and vector potential formulated problems [68]-[70].

Function $\vec{T}$ in the generalized Laplace-Poisson equation (2.1.8) can be also defined using the integrated magnetic material properties – magnetization $\vec{M}$ as:

$$\vec{M} = \vec{B} - \mu_0 \vec{H}.$$

Then the reduced scalar potential can be derived by integration the equation (2.1.8) over the magnetic volumes V_m [73]:

$$U_r = \frac{1}{4\pi\mu_0} \int\limits_{V_m} \frac{\vec{M} \cdot \vec{R}}{|\vec{R}|^3} dV_m.$$

It is clear that neither the potential U_r nor the magnetization $\vec{M}$ is known at this stage. Combining this equation with (2.1.7) and known material properties $\vec{M}(\vec{H})$ one can derive the field strength as:

$$\vec{H}(P) = \vec{H}_s(P) - \frac{1}{4\pi\mu_0} \, grad \int\limits_{V_m} \frac{\vec{M}(\vec{H},Q) \cdot \vec{R}}{|\vec{R}|^3} dV_m,$$

where $\vec{H}_s(P)$ is the field from conductors defined by the Biot-Savart low (2.1.9), P is the field observation point, Q is the source point and $\vec{R}$ is the vector pointing from Q to P.

This method was first adopted in GFUN code and later in DIAMOND and other codes, which were successfully used in several laboratories [74]-[77]. The codes use a piece-wise constant magnetization. Therefore, discontinuities of $\vec{M}$ on the element boundaries can cause problems by allowing some non-physical solutions and making difficult accurate calculations inside the iron. Another disadvantage is that the number of unknowns is by factor of three higher than for the scalar potential formulation, requiring significantly larger computing resources.

Due to these reasons, the method of integral equations did not find a wide implementation in the field analysis of electromagnetic devices, while the differential methods are commonly used. However, in some specific applications, especially containing small iron and large conductor volumes, at uniform field in the iron and for simulation of spatial fields far from the sources, the method of integral equations can give certain advantages with respect to the finite-element method.

2.1.2 The iron saturation effect and its correction

At relatively small field levels in the conductor-dominated magnets, the iron can be considered as a material with linear magnetic properties. It means the iron contribution into the central field grows proportionally with the coil contribution. With a good power of accuracy the iron magnetization can be represented as a function of field, containing two parts: with a constant slop and plateau.

Figure 2.1.1 shows magnetization curve measured at Fermilab for a low-carbon steel used in High-Gradient Quadrupole magnet [78] and the relevant relative permeability. Steel with the same magnetic properties is being used in iron yokes of the Fermilab high field dipoles and therefore considered in all the numerical calculations. One can see that the iron magnetization is virtually linear up to the field $B = 2.12$ T, which is called <u>saturation field</u> and becomes constant for higher fields, having value of the <u>saturation magnetization.</u> Most of the steels used in magnetic systems have saturation magnetization and saturation field within 1.8-2.2 T. Due to a non-uniform field distribution within iron yoke of accelerator magnet, different parts of the yoke work in different regions of the magnetization curve.
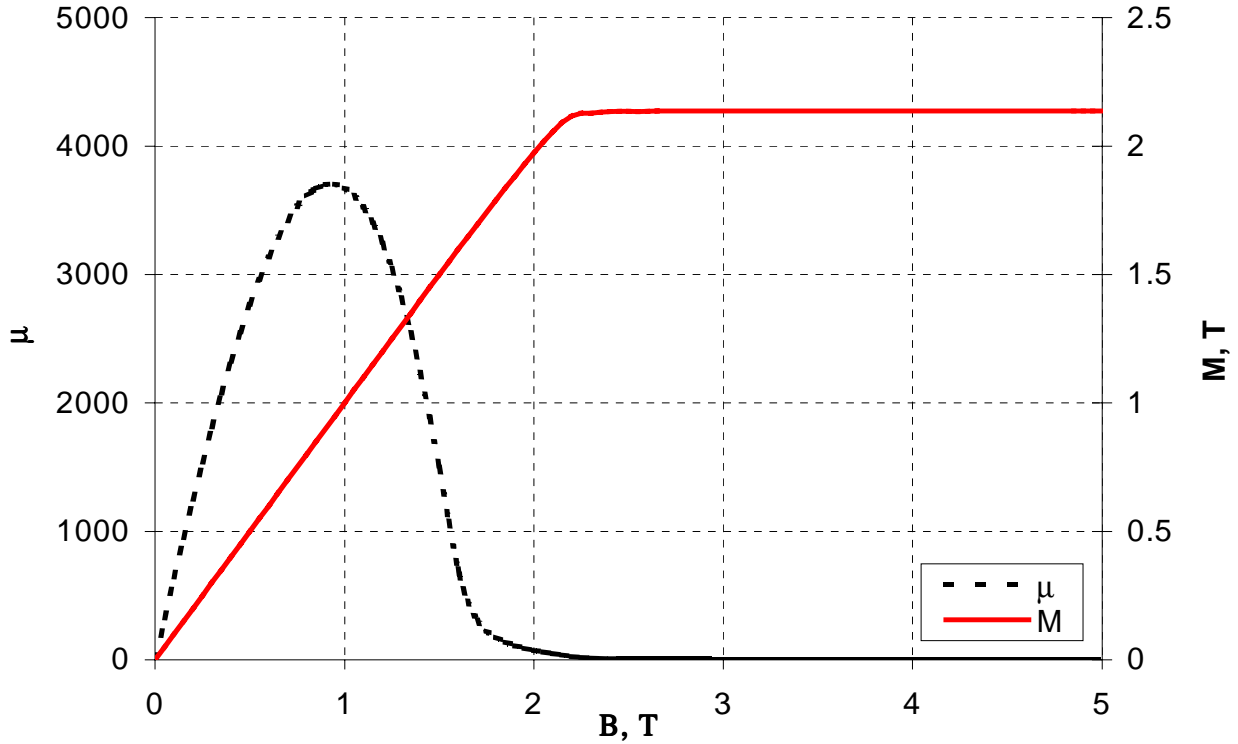
Figure 2.1.1 Iron relative permeability and magnetization as functions of the field.

It is clear that due to a non-uniform field distribution within iron yoke of accelerator magnet (the maximum field is in the pole region and the minimum is in the middle plane), different parts of the yoke work in different regions on the magnetization curve. It produces non-linear effects in the field harmonics, which are complex functions of the yoke geometry and field level.

Table 2.1.2 contains the amplitudes of multipole deviations due to the yoke saturation effect in superconducting magnets built for different machines [8], [9], [79]-[85] (at the reported reference radii). Only the Tevatron magnets utilizing the "warm" iron have negligibly small yoke saturation effect. The low order harmonic deviations in the rest of the magnets are by two orders of magnitude higher than the field errors typically acceptable without correction (Table 1.2.2). It requires implementation of correcting systems in order to eliminate the errors during machines operation.

Table 2.1.2 Multipole deviations due to the iron yoke saturation in different dipole magnets.

Machine	Tevatron	HERA	UNK	SSC	RHIC	LHC
Yoke type	warm	cold	cold	cold	cold	cold
Δb_2, 10^{-4}	-	-	-	-	-	2.0
Δb_3, 10^{-4}	0.0	2.0	0.7	1.2	2.5	0.8
Δb_4, 10^{-4}	-	-	-	-	-	0.2
Δb_5, 10^{-4}	0.0	0.2	0.8	0.05	0.4	0.1

A beneficence of the passive correction of the yoke saturation effect has been recognized a long time ago. There are various publications available describing different techniques [86]-[90]. Most of them employ the idea of creating a region within the iron yoke that has opposite (to the iron saturation) effect on the field distribution. Then the yoke contribution remains constant during the operation cycle, having no effect on the field distribution (the transfer function *B*/*I* is not constant though, since the flux is partially conducted by the non-linear magnetic material).

Technically this may be achieved by optimization of the inner and outer yoke surfaces. The method of reduction the saturation harmonics by iron ellipticity [88] was implemented in LBNL NbTi magnet D19 and showed a noticeable field quality improvement [91]. Optimization of the outer yoke surface can further improve the field quality, however this way is less preferable and can be used to a certain extent, until it starts to violate the skin/helium vessel stability.

Another possibility is based on keeping the inner and outer yoke surfaces round and introduction holes inside the yoke body. Since there is a necessity of holes inside the yoke for assembly, cooling, electrical buses and instrumentation, their position and size can be (to a certain extent) optimized for the field qualify improvement. Most of the superconducting dipole and quadrupole magnets built since Tevatron employ this principle of the passive correction.

2.2 Study of the yoke design parameters in single aperture magnets

The first generation of superconducting accelerator magnets was based on the single aperture concept, where the coil package is installed inside its own yoke. Thus it requires two physically separated bending magnets at every point of the tunnel for steering two equally charged beams. The idea of two coils for the counter-rotating beams installed within a single yoke structure – the so-called double aperture magnet was implemented in LHC and proven to be more economical solution with respect to the single aperture magnets [8]. However, the single aperture magnets still find implementation in special accelerator areas, like the utility straight sections, where a large beam separation is required. In addition, the single aperture magnets are no doubt simpler to design, manufacture and test that is beneficial in the initial stage of a magnet R&D program.

In order to determine the quantity of multipole deviations coming from the yoke saturation effect, simple models of the shell dipole and quadrupole magnets, shown in Figure 2.2.1 have been analyzed using OPERA2D code. The models consisted of optimized coils with 43.5 mm bore (Chapter 1) and yokes with parametrically variable geometry. The yoke magnetic properties were modeled by the measured magnetization curve (Figure 2.1.1). The yoke saturation effect as a function of the bore field and yoke geometry was studied for the allowed low order harmonics – sextupole and decapole in the dipole and dodecapole in the quadrupole magnet.
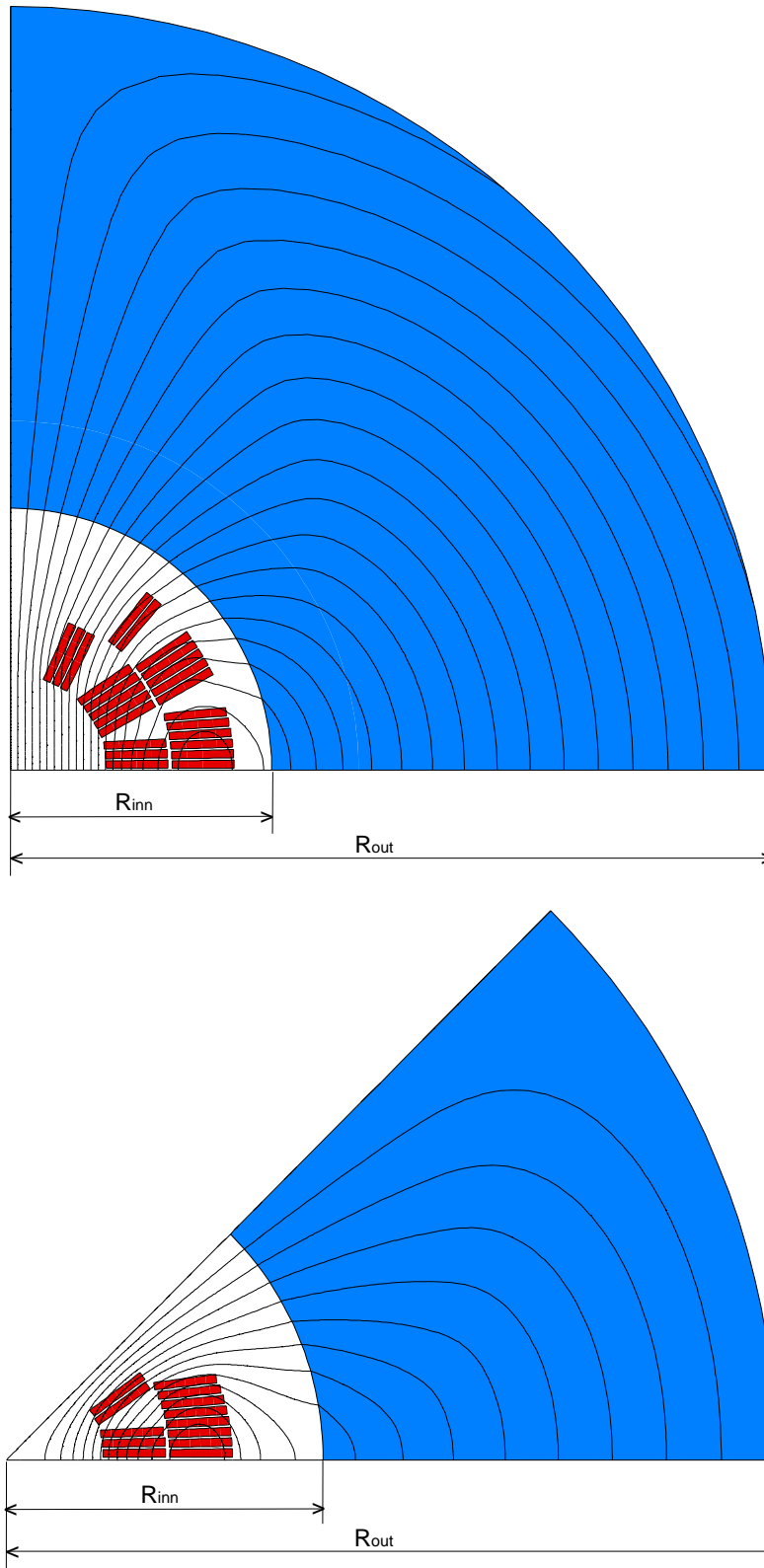
Figure 2.2.1. The dipole (upper) and quadrupole (lower) FEM models.

2.2.1 Variation of the yoke outer radius

A circular inner yoke surface for the dipole and quadrupole models was set at the minimum distance (Chapter 1) from the coils of 8 mm and 20 mm for the dipole and quadrupole respectively. The radius of the outer circular surface was varied within 100-400 mm range. Figures 2.2.2 – 2.2.3 present sextupole and decapole components deviation in the dipole model as functions of the bore field for different outer yoke radii.

It is noticeable that the radius variation within 400-250 mm does not significantly change the multipole deviations. Further decreasing of the yoke radius forces the sextupole curve to cross the horizontal axis at a smaller field. It leads to a partial compensation of the yoke saturation effect that quantitatively confirms by Figure 2.2.4, presenting maximum sextupole deviations from the initial (zero) level within 0-12 T and 0-20 T fields range.

There is a clear minimum at the yoke outer radius of 175 mm for the field variation range from 0 to 12T. For the wider 0-20T range there is a minimum as well at the yoke outer radius of 200 mm, though the sextupole variation in this case is by 1.3 units higher.

The decapole deviations due to the yoke saturation effect are by factor of 20 smaller than for the sextupole and can be virtually neglected.
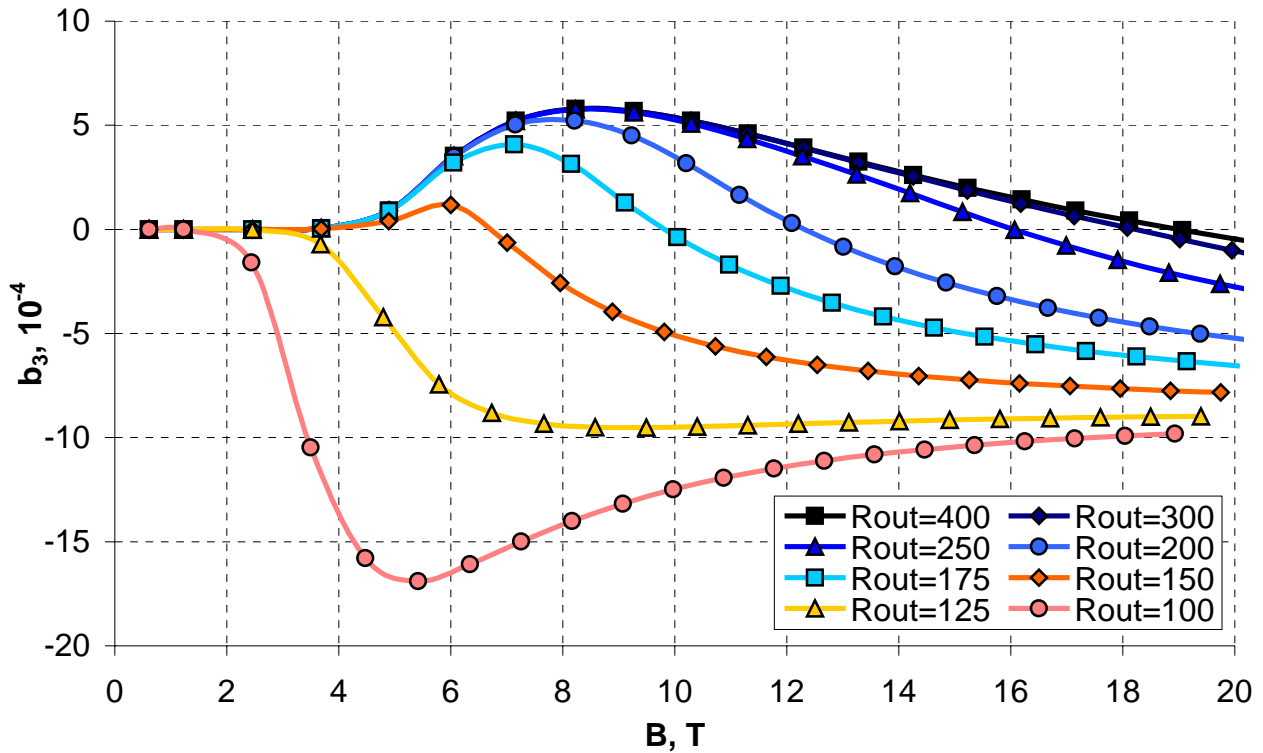
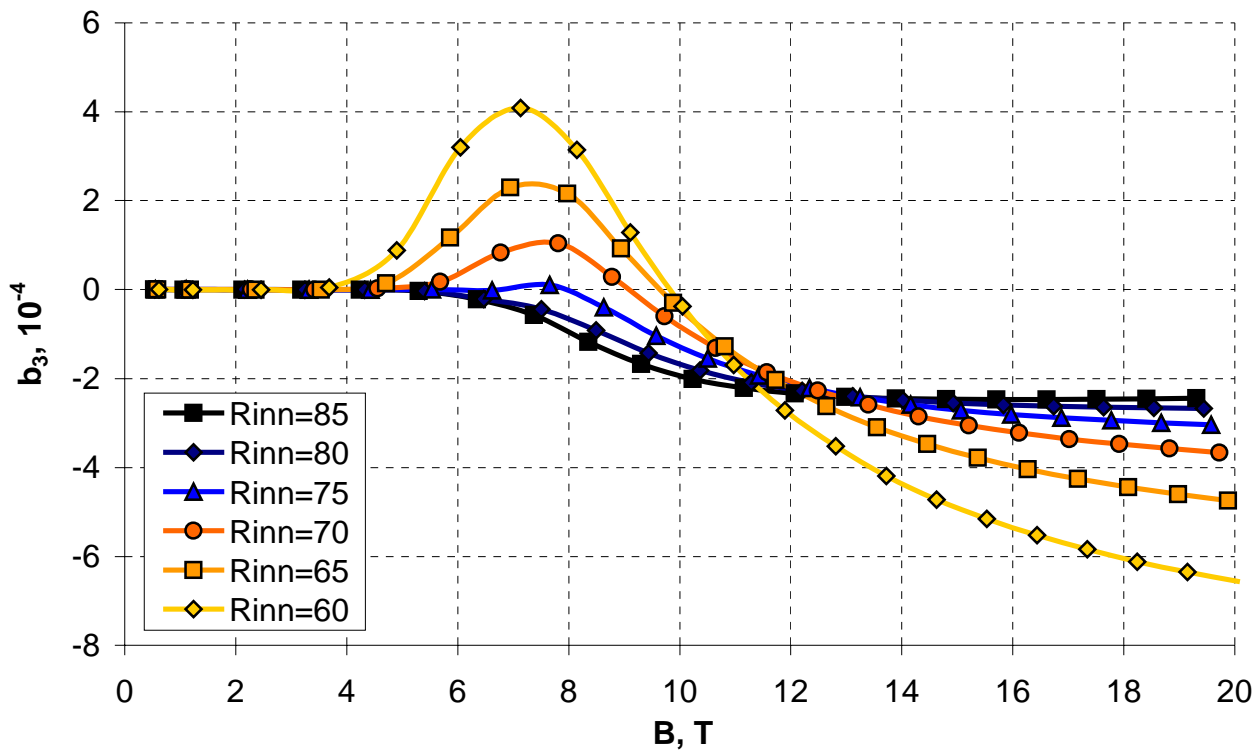Figure 2.2.2. Sextupole deviations as functions of the bore field.
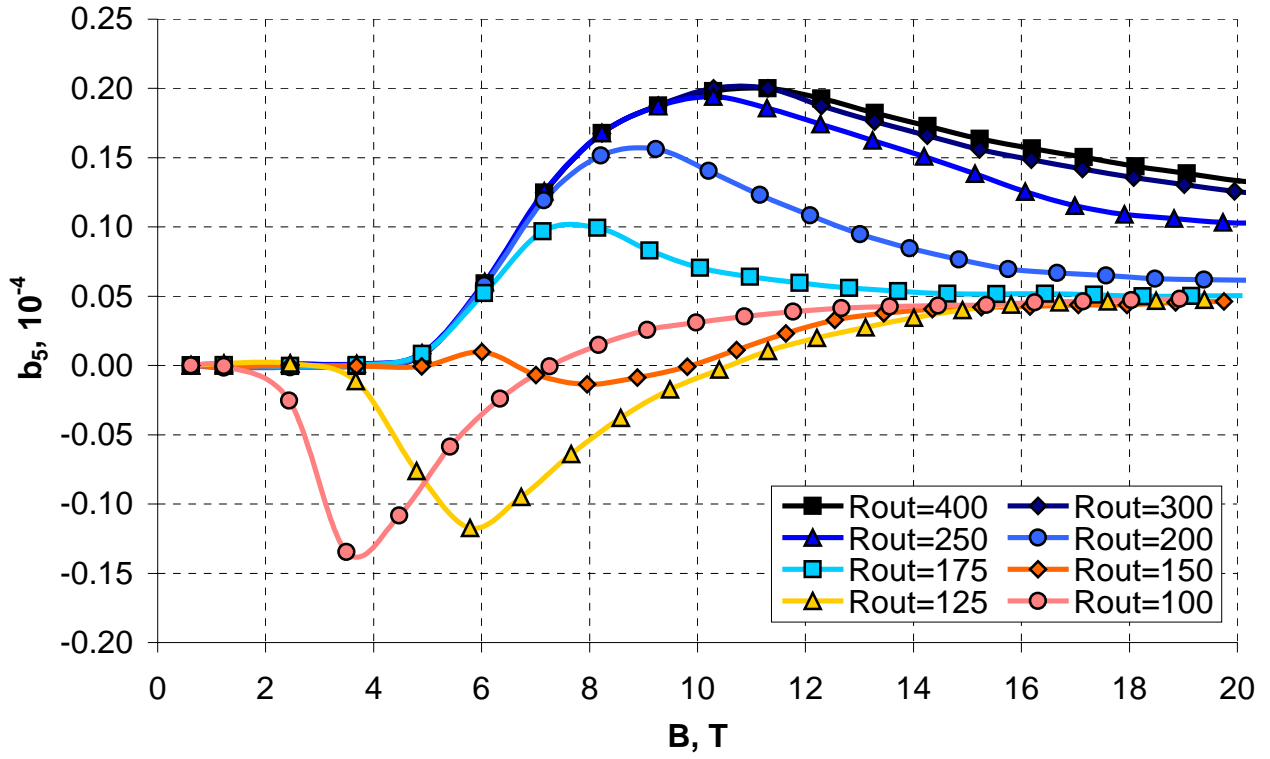
Figure 2.2.3. Decapole deviations as functions of the bore field.
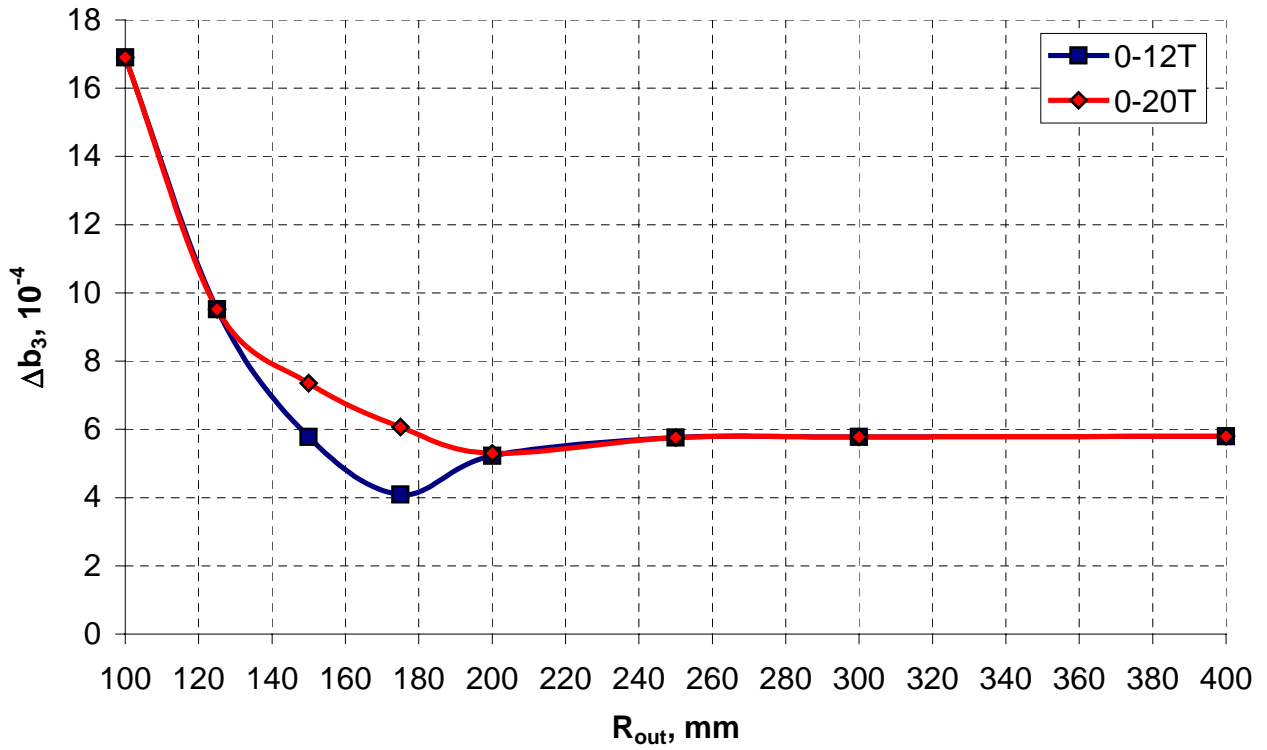
Figure 2.2.4. Maximum sextupole deviations as functions of the yoke outer radius.

The quadrupole magnet has an essentially better performance in terms of the yoke saturation effect. Although the flux flowing through the yoke saturates it virtually to the same extent as in the dipole magnet at equal peak fields, the first allowed by quadrupole symmetry multipole – dodecapole b_6 decays much faster than the sextupole in the dipole magnet and presumably acceptable without any correction (Figure 2.2.5). Thus, the choice of the outer yoke dimension in quadrupole magnet has to be governed by some other than field quality considerations, like fringe field at the outer yoke surface.
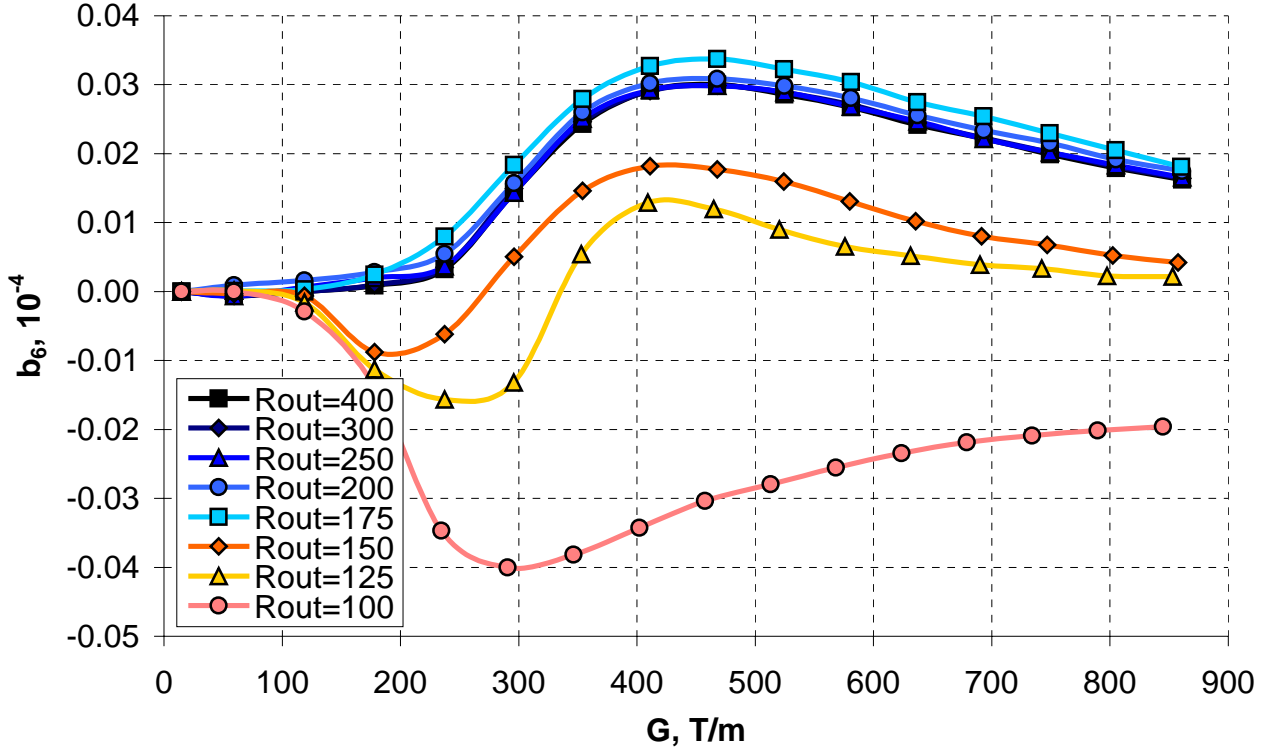
Figure 2.2.5. Dodecapole deviations as functions of the gradient.

Figure 2.2.6 shows the fringe field defined as the maximum field at the radius (R_{out} +1) cm for both dipole and quadrupole magnets at the bore field and gradient of 12 T and 500 T/m respectively. The fringe field changes by 4-5 orders of magnitude within investigated radii range. The fringe field is about 200 mT in the dipole magnet for the optimum yoke outer radius of 175 mm. Such field level is, for example, acceptable at CERN for the whole working day exposure in terms of biological effects [92]. Moreover, keeping in mind that the field significantly reduces by the cryostat space and the outer iron shell, the actual fringe field outside of the magnet can be made by an order of magnitude smaller. Thus, fixing the fringe field in the quadrupole at 200 mT also, one finds the yoke outer radius of 125 mm that is by 40 % smaller than for the dipole.

Figures 2.2.7-2.2.8 show the yoke contribution to the bore field and gradient as functions of the bore field and gradient in the dipole and quadrupole magnets.
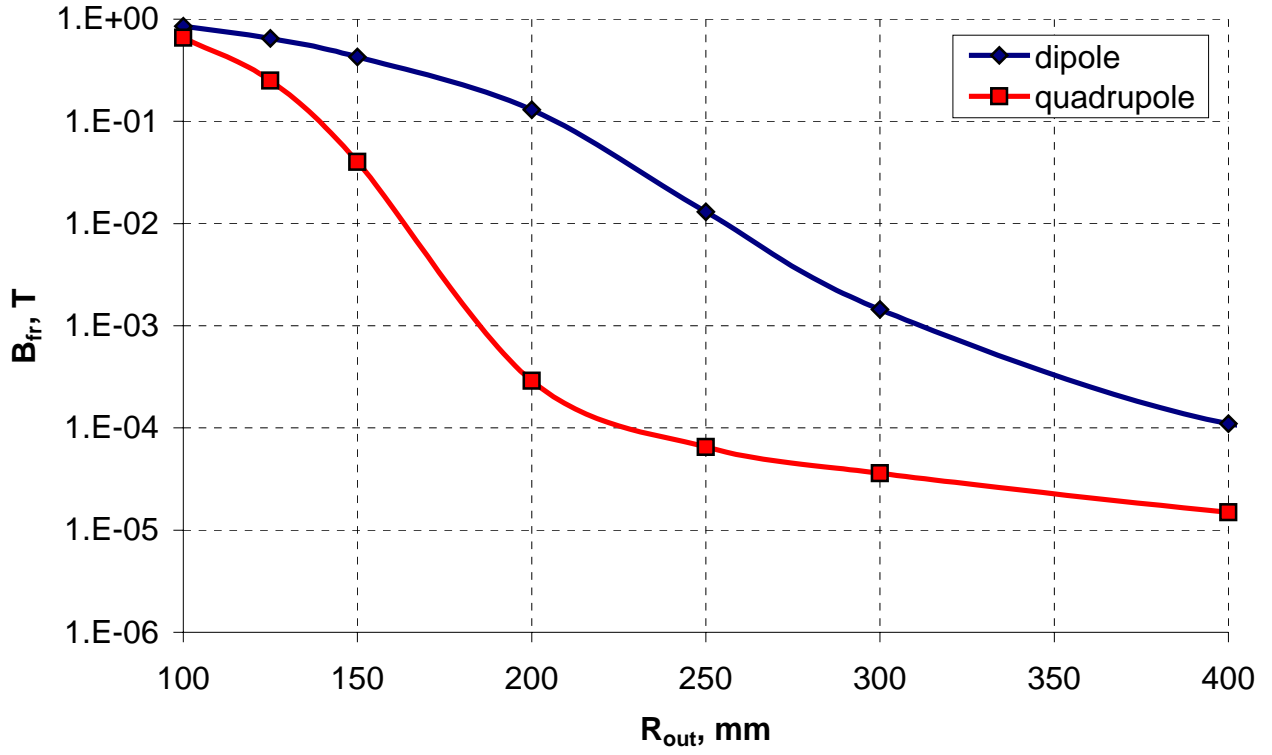
Figure 2.2.6. Fringe fields at the outer yoke surface.
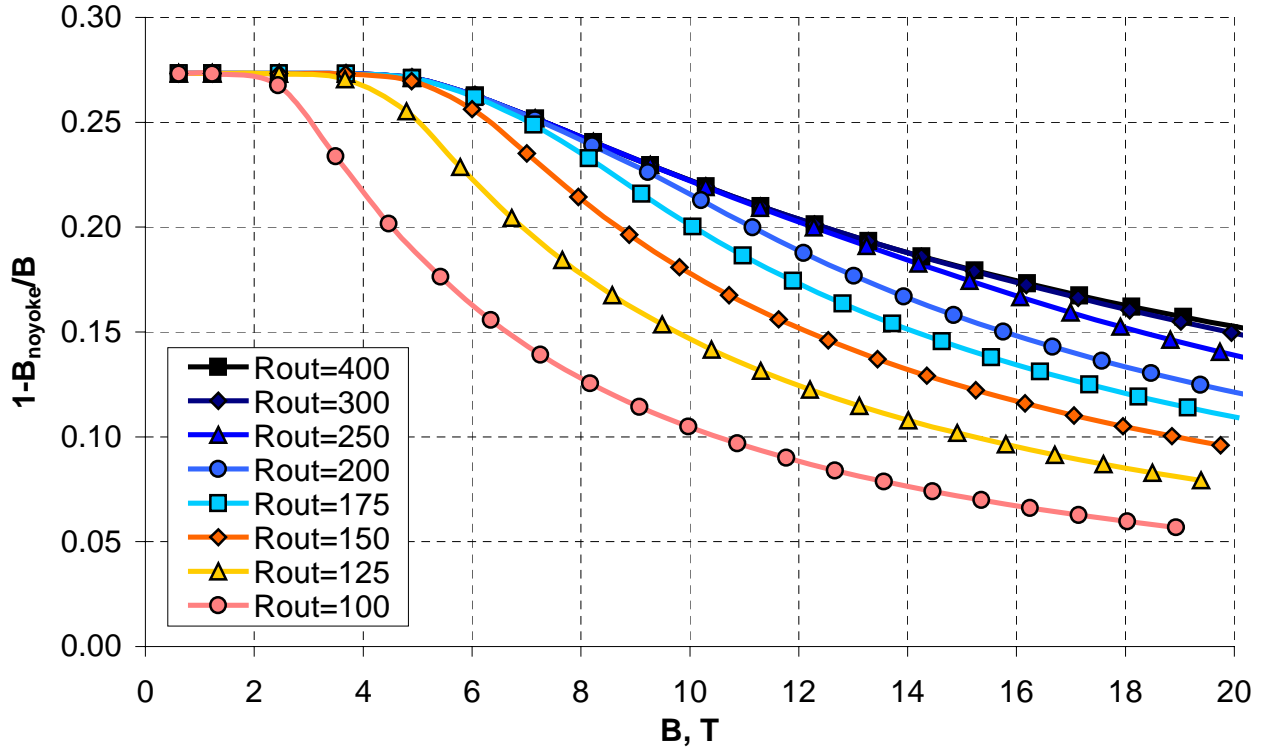
Figure 2.2.7. Yoke contributions to the bore field in dipole magnet.
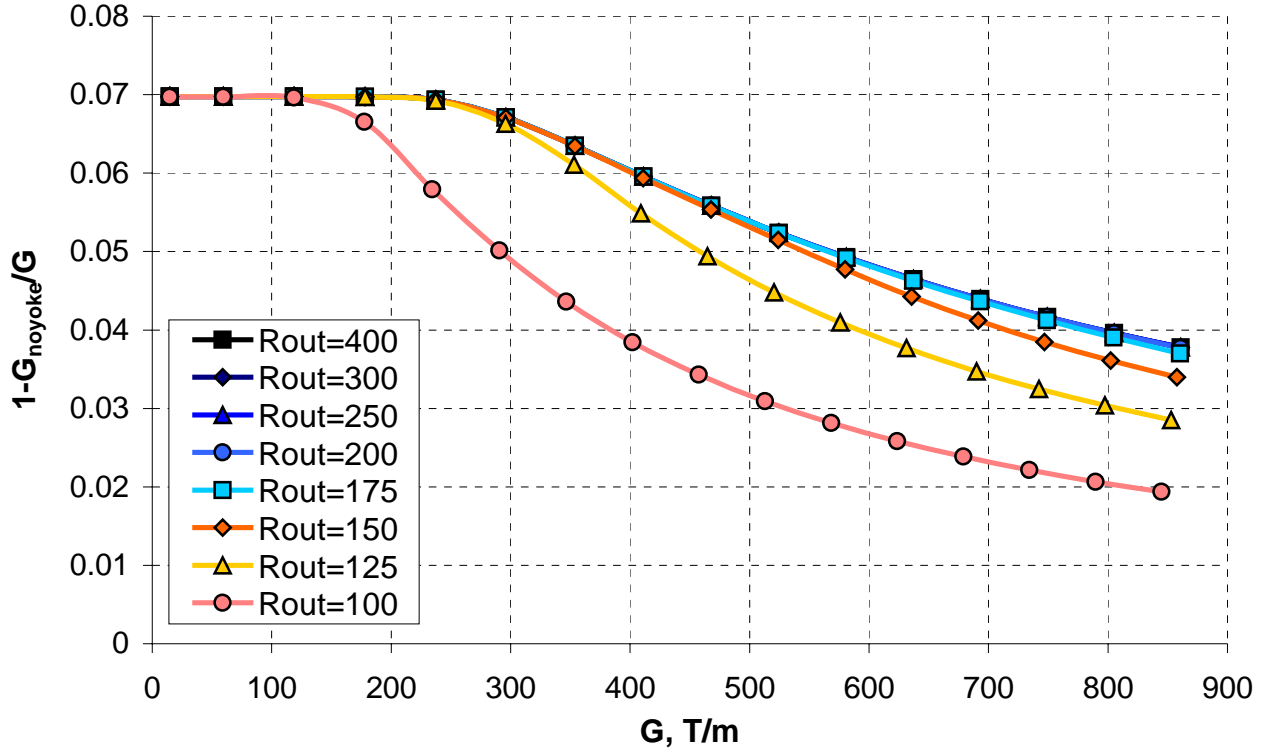
Figure 2.2.8. Yoke contributions to the bore field in quadrupole magnet.

It is notable that the yoke contribution is already small at low fields, but drops even more when the iron starts to saturate. Thus the maximum yoke contributions in the dipole and quadrupole magnets are only 27 % and 7 % respectively. These values drop to 17 % and 5 % at 12 T field in the dipole and 450 T/m gradient in the quadrupole magnets. A very low efficiency of the iron yoke in the quadrupole magnet explains by a significant space between coil and the yoke spanned by the stainless steel collar. Reduction of the collar thickness would increase the yoke efficiency, then however, the issue of the coil prestress in two orthogonal planes by means of the yoke would have to be addressed.

2.2.2 Variation of the yoke inner radius

The circular yoke inner boundary was varied in several steps within range of 60-85 mm in the dipole magnet. Since the quadrupole magnet did not possess any problems with the field quality at the considered yoke radius, its increase might only improve the situation. Due to this reason, the single aperture quadrupole was removed from the further analysis. The yoke outer radius of the dipole magnet was fixed at an optimum value of 175 mm, determined in previous paragraph.

Figure 2.2.9 shows the sextupole distributions for different inner yoke radii and Figure 2.2.10 – the maximum sextupole deviations from the initial value for the two field ranges.
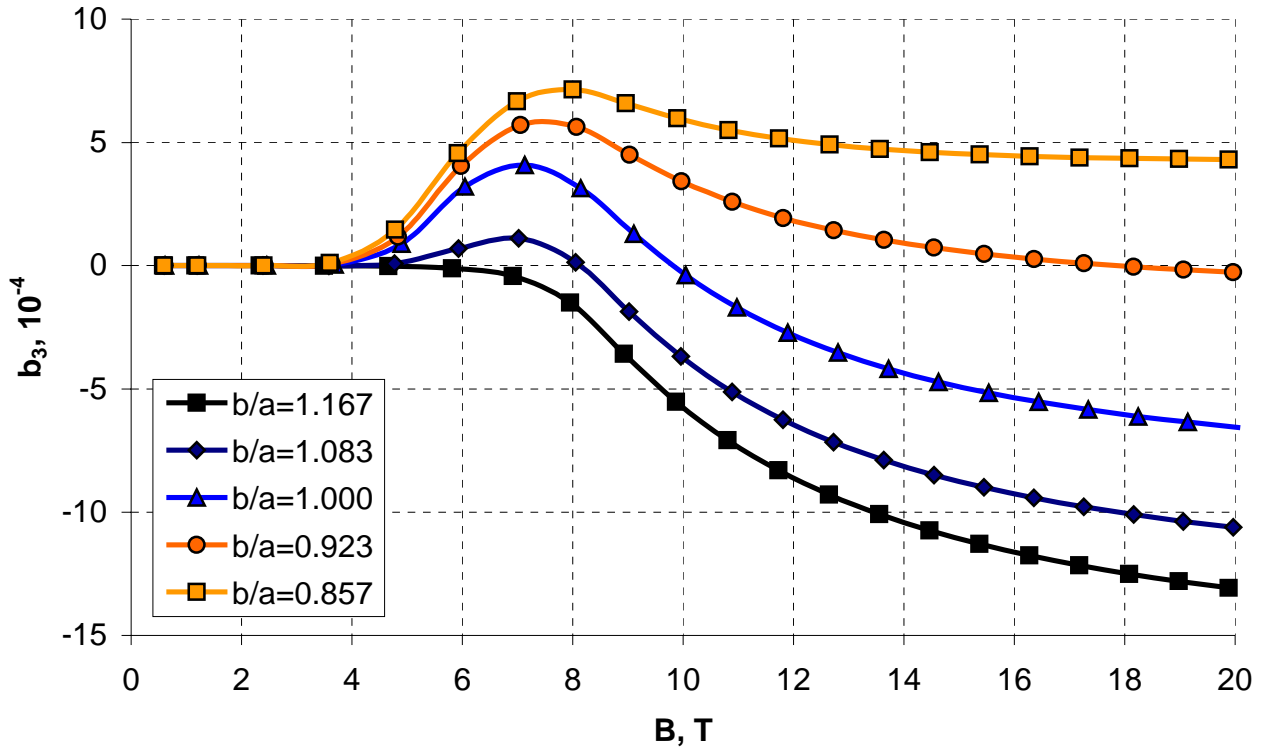
Figure 2.2.9. Sextupole deviations as functions of the bore field.
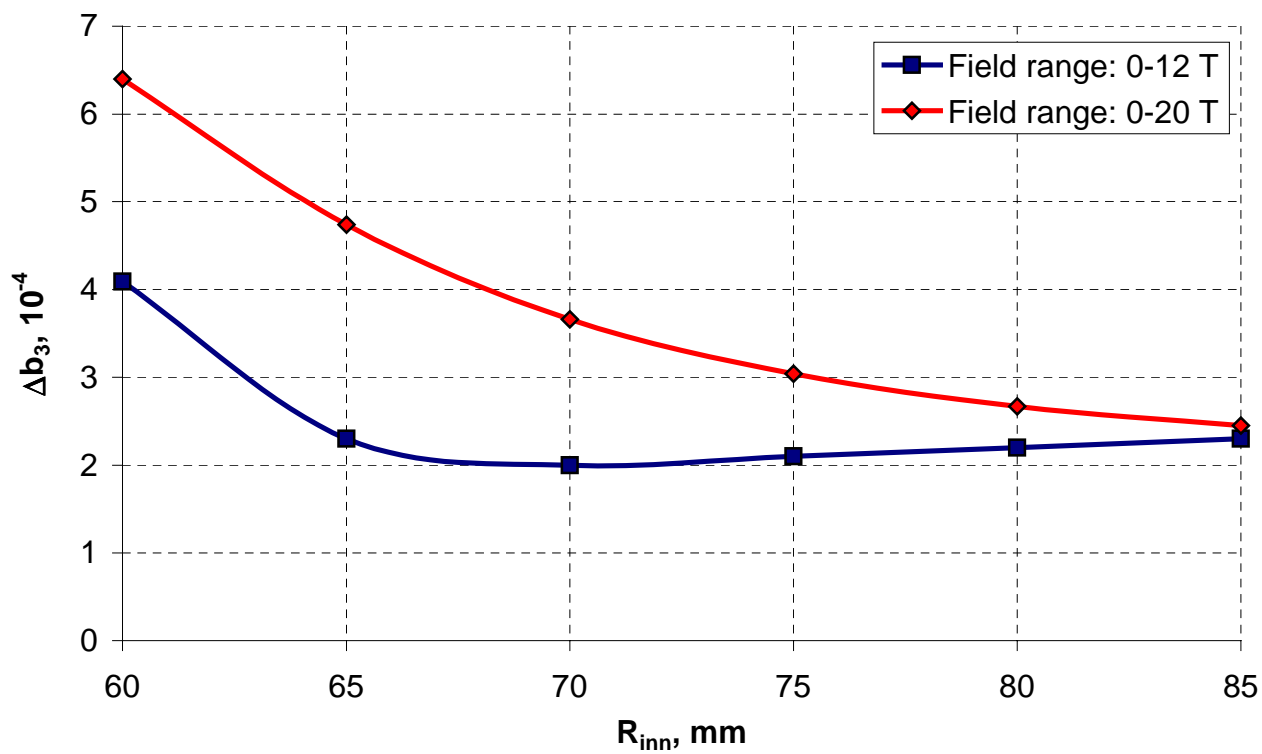
Figure 2.2.10. Maximum sextupole deviations as functions of the yoke inner radius.

Since changes of the yoke inner boundary introduce disturbances in the geometrical multipoles at low fields, the curves were adjusted vertically in order to obtain zero level at low field (in this case the curves represent pure yoke saturation effect). The decapole deviations were not considered due to their small value.

The plots clearly indicate that increasing of the yoke inner radius reduces the positive sextupole component at intermediate fields as well as the negative component at high fields and so it is generally beneficial for improving the field quality. There is an optimum yoke inner radius of 70 mm in the 0-12 T field cycle, but the optimum yoke radius for the 0-20 T cycle is off the considered range. However, the two curves virtually converge to each other at the yoke inner radius of 85 mm.

It is obvious that increasing of the yoke inner radius reduces the yoke efficiency, which is quantitatively confirmed in Figure 2.2.11. The yoke contribution drops from 27 % to 16 % at low fields after increasing of the yoke inner radius from 60 mm to 85 mm. However, the difference in the yoke efficiency becomes smaller at higher field levels due to the saturation, giving possibility of adjusting the yoke inner radius for the field quality correction with only small efficiency losses.
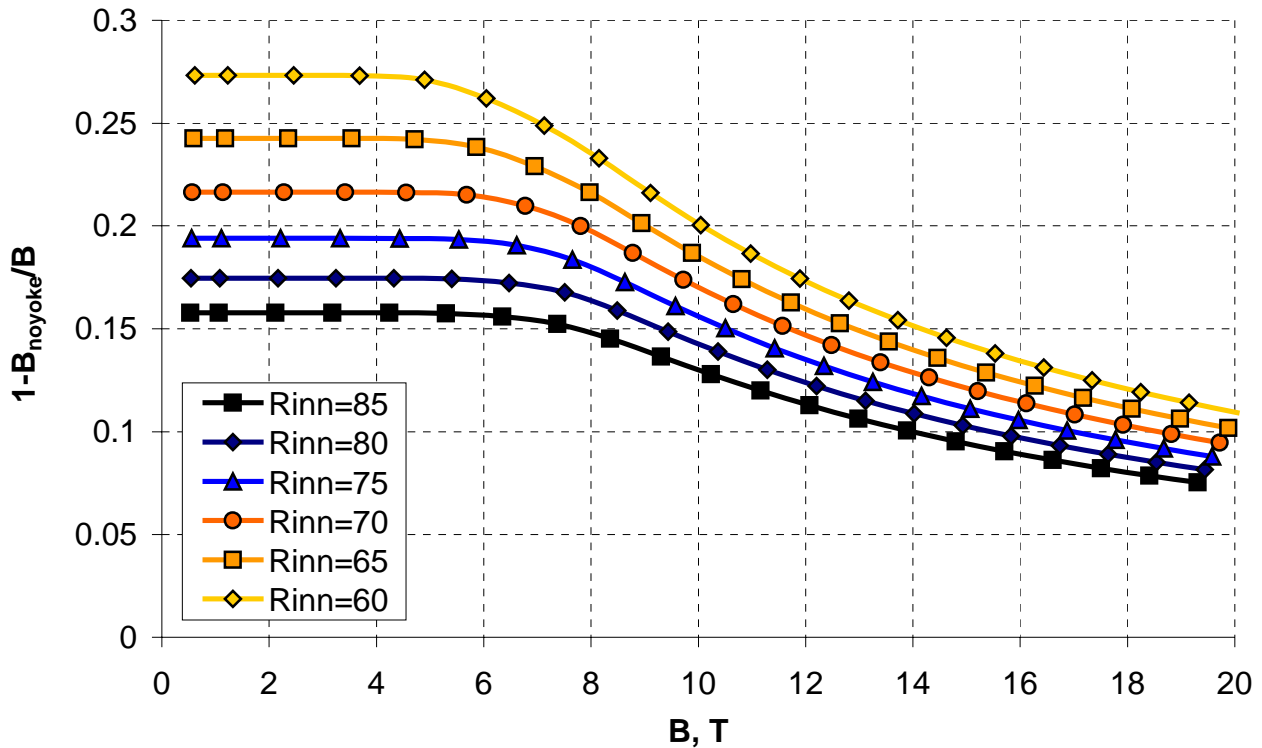
Figure 2.2.11. Yoke contribution to the bore field.

2.2.3 Variation of the yoke inner surface ellipticity

The inner yoke boundary in dipole magnet was made elliptical in order to determine its effect on the field quality. One of the ellipse half-axes was set equal to the minimum yoke radius – 60 mm and another one was varied within 60-70 mm, that provided the ellipticity *b/a* variation within 0.857-1.167 range. The circular yoke outer boundary had the optimum radius of 175 mm.

Figure 2.2.12 presents the sextupole deviations, adjusted to zero at low field level and Figure 2.2.13 shows the maximum sextupole component deviations within two cycles. Implementation of the "vertical ellipticity" (b/a>1) for the inner yoke boundary allows effective reduction of the sextupole deviations within 0-8 T field range. However, the vertical ellipticity at higher fields results in a large negative sextupole component giving worse results than the circular case.

The "horizontal ellipticity" (b/a<1) helps to reduce a large negative sextupole at high field levels. Thus, the inner yoke surface ellipticity of *b/a* = 0.923 eliminates the sextupole component at 18 T field, making only a small sextupole buildup at an intermediate field. This can be a useful approach of the field quality correction in the very high field magnets.

Figure 2.2.14 shows the yoke contribution into the bore field at for different ellipticity ratios. The vertical ellipticity *b/a*=1.167 gives the maximum drop in the yoke contribution, which is, however, relatively small – 5 % at low fields.

Figure 2.2.12. Sextupole deviations as functions of the bore field.
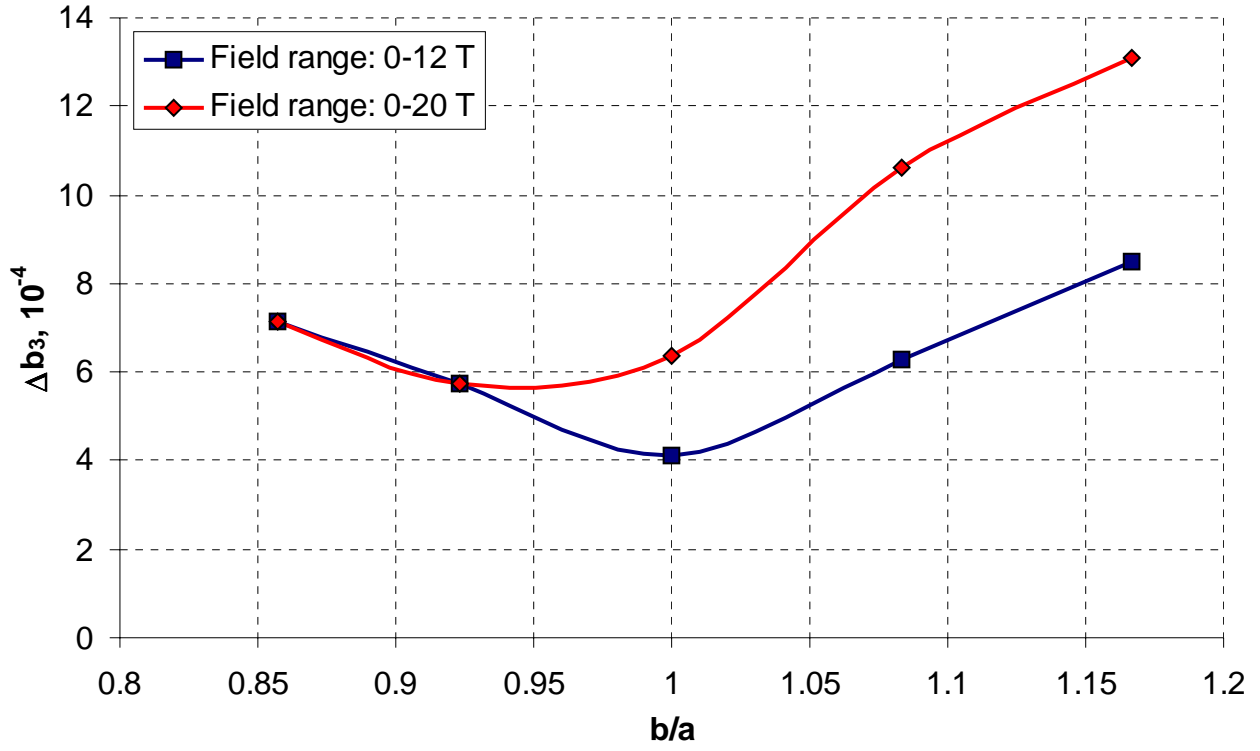
Figure 2.2.13. Maximum sextupole deviations as functions of the yoke ellipticity.
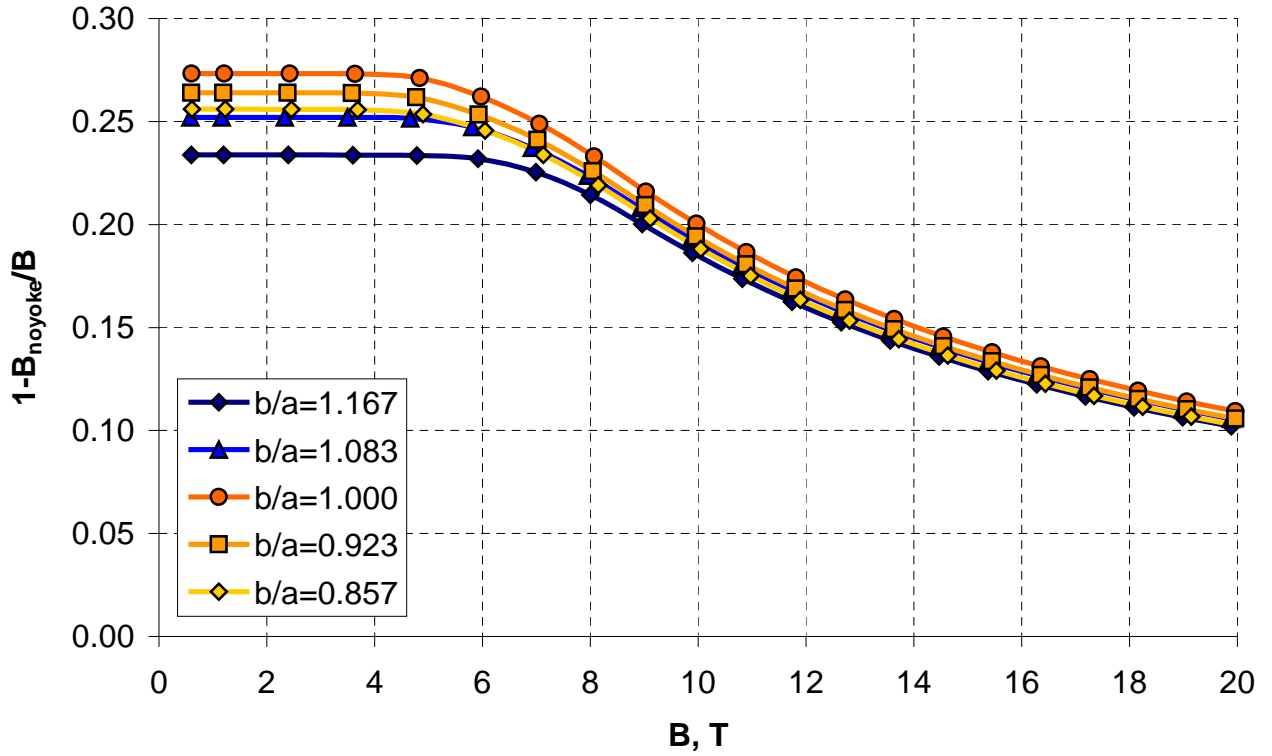
Figure 2.2.14. Yoke contribution to the bore field.

2.3 Double aperture magnets

Double aperture magnet concept reduces the number of magnets in a machine by factor of two with respect to the single aperture option and thus accelerates the magnet manufacturing, testing and installation procedures, which is vitally important for the machines with large number of magnets. However, large magnetic coupling of two coils within one yoke causes violation of the field symmetry that implies certain difficulties in the magnet design. To understand peculiarities of the double aperture magnet, several simple models of the dipole and quadrupole magnets have been analyzed for different sets of design parameters.

2.3.1 Dipole magnet with horizontal bore arrangement

Two shell type dipole coils, described in Chapter 1 were horizontally accommodated within the common iron yoke. Figure 2.3.1 shows the corresponding OPERA2D model. For the equally charged particles to rotate in opposite directions, the main field components have to be of the opposite signs in the adjacent apertures. In terms of the boundary conditions, it means zero normal derivative of vector potential in the magnet vertical plane of symmetry (flux lines are normal to the plane). Such boundary condition implies the positive coupling (or mutual inductance) between the coils – each coil increases magnetic field in the other one. The coil-to-yoke distance was set to the minimum (8 mm), determined in Chapter 1. The yoke did not contain any holes and technological cutouts, which might affect the field distribution.

Initially, the beam-to beam distance was fixed at $S = 200$ mm and the yoke outer radius was varied within 200-400 mm. Figures 2.3.2-2.3.3 present quadrupole and sextupole components at different outer yoke radii, coming from the yoke saturation effect. The quadrupole component deviations grow up with decreasing of the yoke outer diameter. It explains by the fact that part of the magnetic flux returning through the yoke, expels from outside of the coils to the inter-coil space with decreasing of the outer yoke radius. Such flux redistribution leads to left-right flux imbalance within every aperture and therefore to the negative quadrupole component for any of the considered yoke outer radii. The sextupole curve exhibits obviously the same behavior as in the single aperture magnet as it is generally non-sensitive to the left-right field asymmetry within the aperture.

For the complete picture of the yoke design parameters influence on the field quality, it was necessary to find out how the quadrupole component depends on the bore separation distance at the fixed yoke outer radius. It was chosen according to the fringe field of ~0.1 T, shown in Figure 2.3.4, corresponding to the yoke outer radius of 250 mm.

$\partial A/\partial n = 0$, positive coupling

S/2

R_{out}
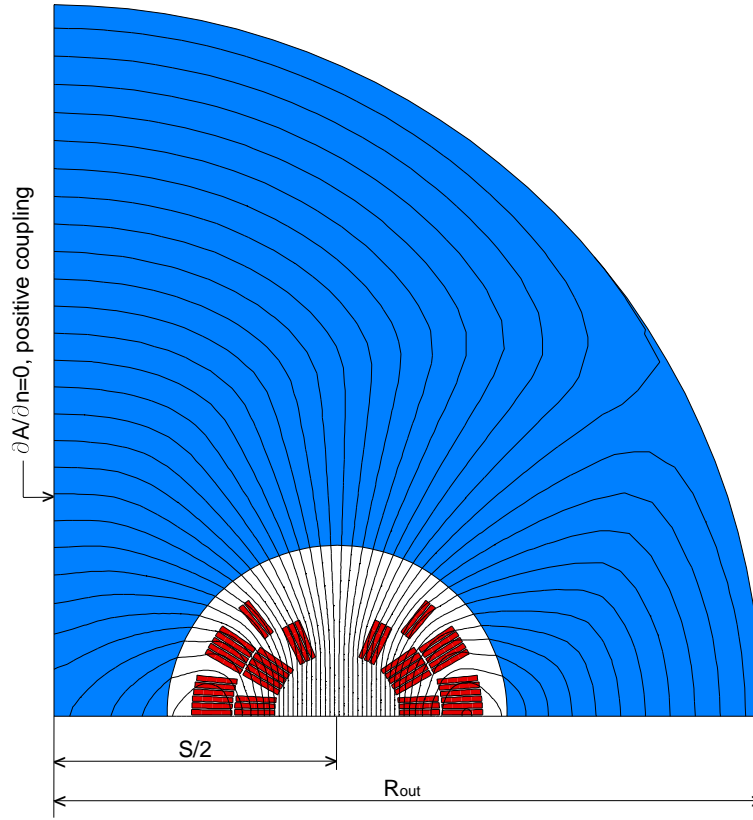
Figure 2.3.1. Dipole model with horizontal bore separation.
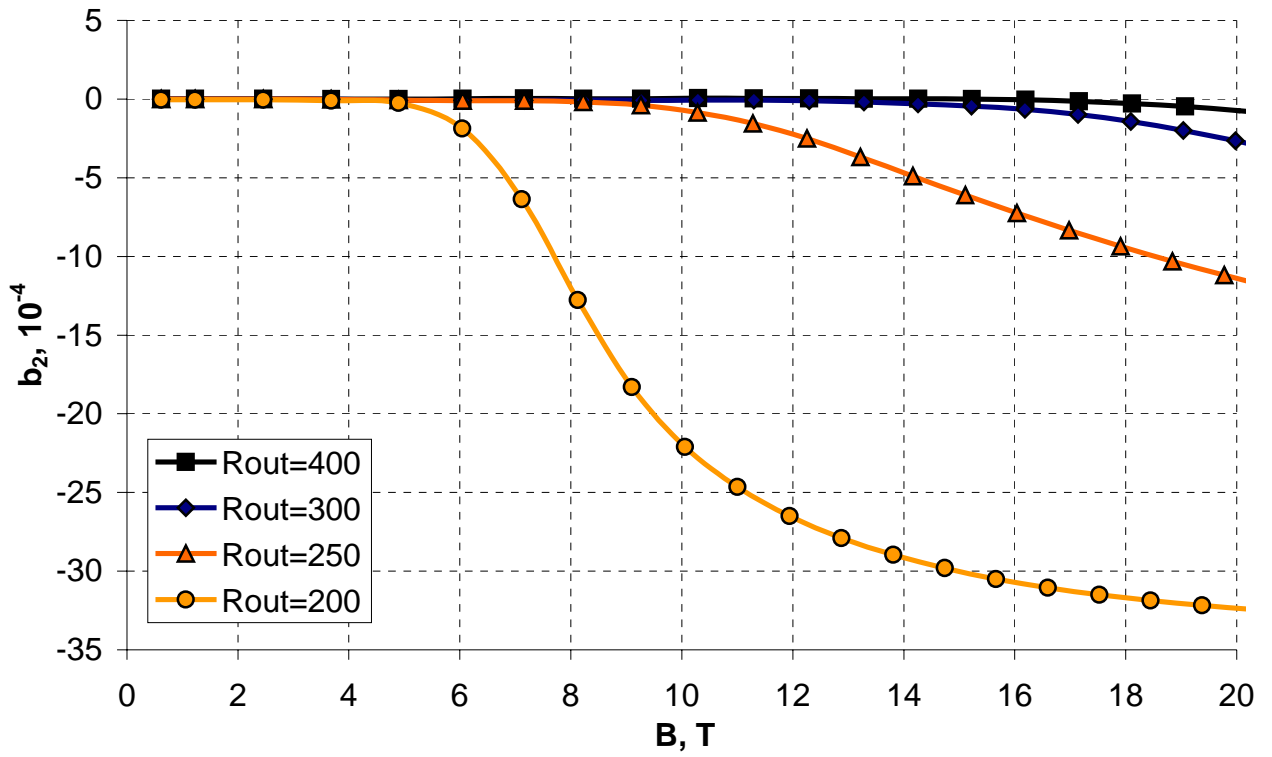
Figure 2.3.2. Quadrupole components as functions of the bore field.
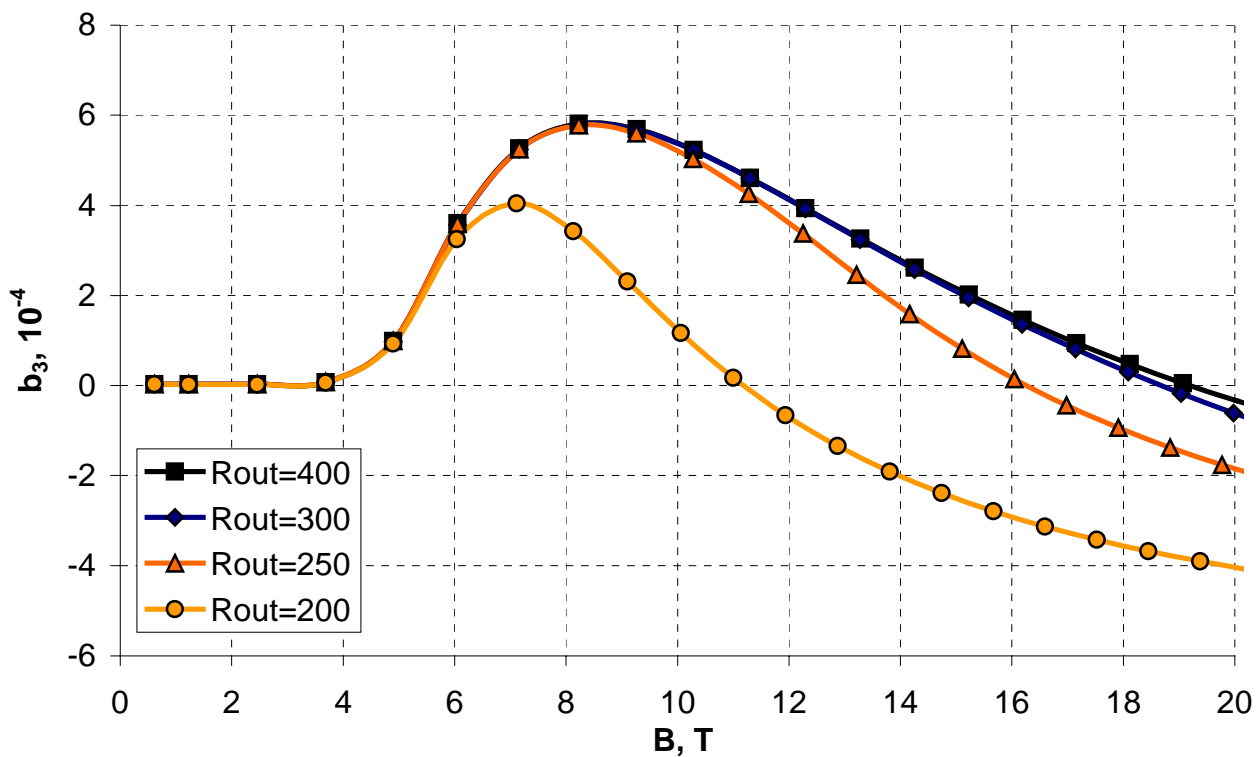
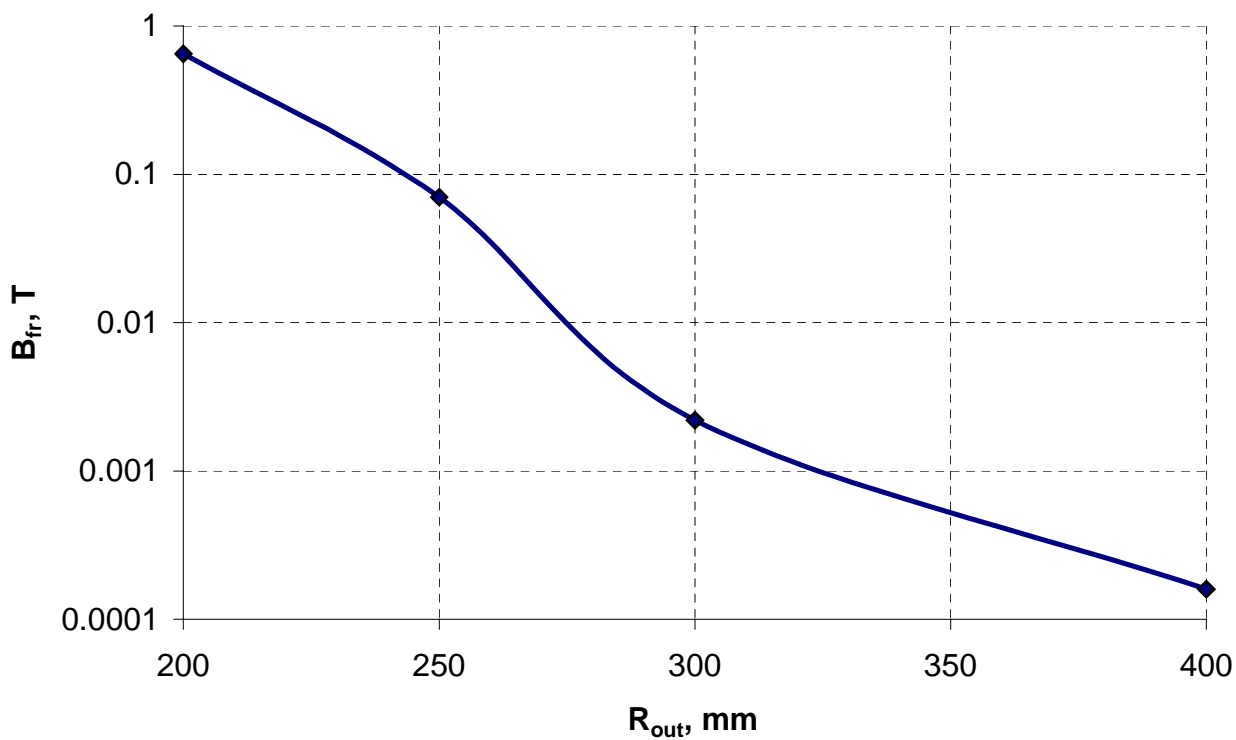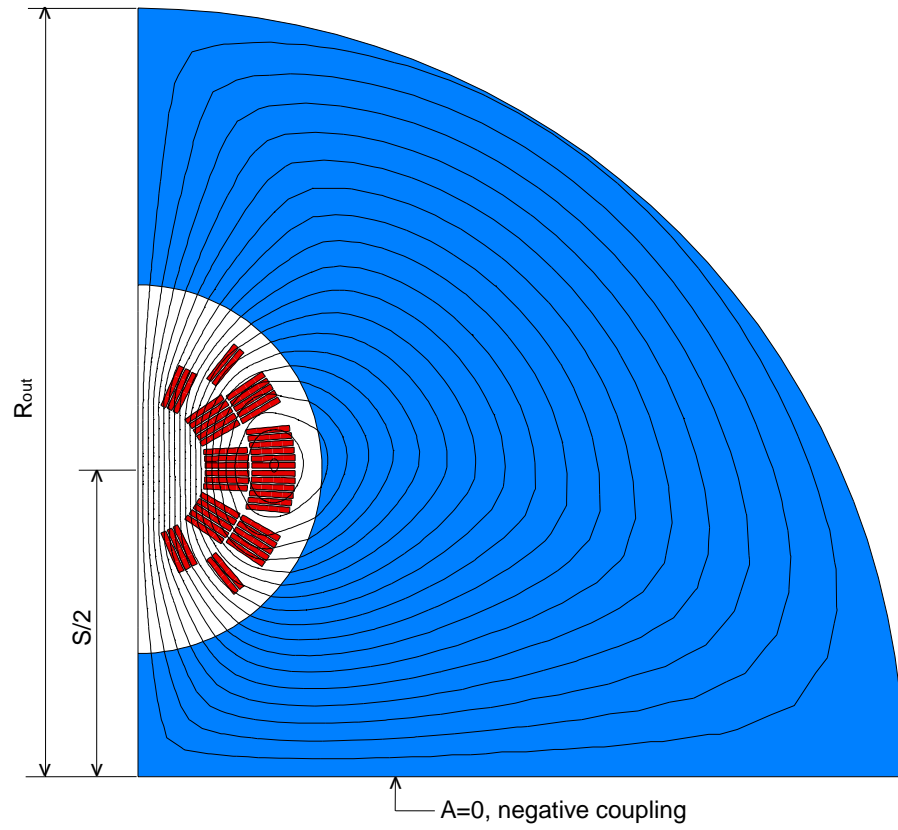Figure 2.3.3. Sextupole components as functions of the bore field.

Figure 2.3.4. Fringe field as a function of the yoke outer radius.

Figure 2.3.5 presents the quadrupole component distribution for different beam separation distances and Figure 2.3.6 – maximum quadrupole deviations within two field ranges. There are minimums on the quadrupole curves at the bore separation distances of 170 and 200 mm for the field ranges of 0-12 T and 0-20 T correspondingly. Existence of the optimum bore separation distance in the dipole magnet with horizontal bore separation explains by following considerations:

- When the bore separation distance is small – the positive coupling between two coils is large, which produces a large negative quadrupole component.
- Making the bore separation distance larger decreases the coupling. However, when the coils are close to the fixed outer yoke surface – the flux expels from outside of the coils into the inter-coil region, increasing the positive coupling and therefore negative quadrupole component. Thus, there is a certain bore separation distance at which sum of both effects is minimum.

One can notice that the minimum on the quadrupole curve is pretty shallow that gives possibility to determine the optimum the bore separation range of 160-200 mm for 0-12 T fields range and allows certain freedom in choosing the bore separation distance. Having a small bore separation is preferable for easier beam shuffling, however it may be limited at larger values by the beam instrumentation devices, such as the beam position monitors.
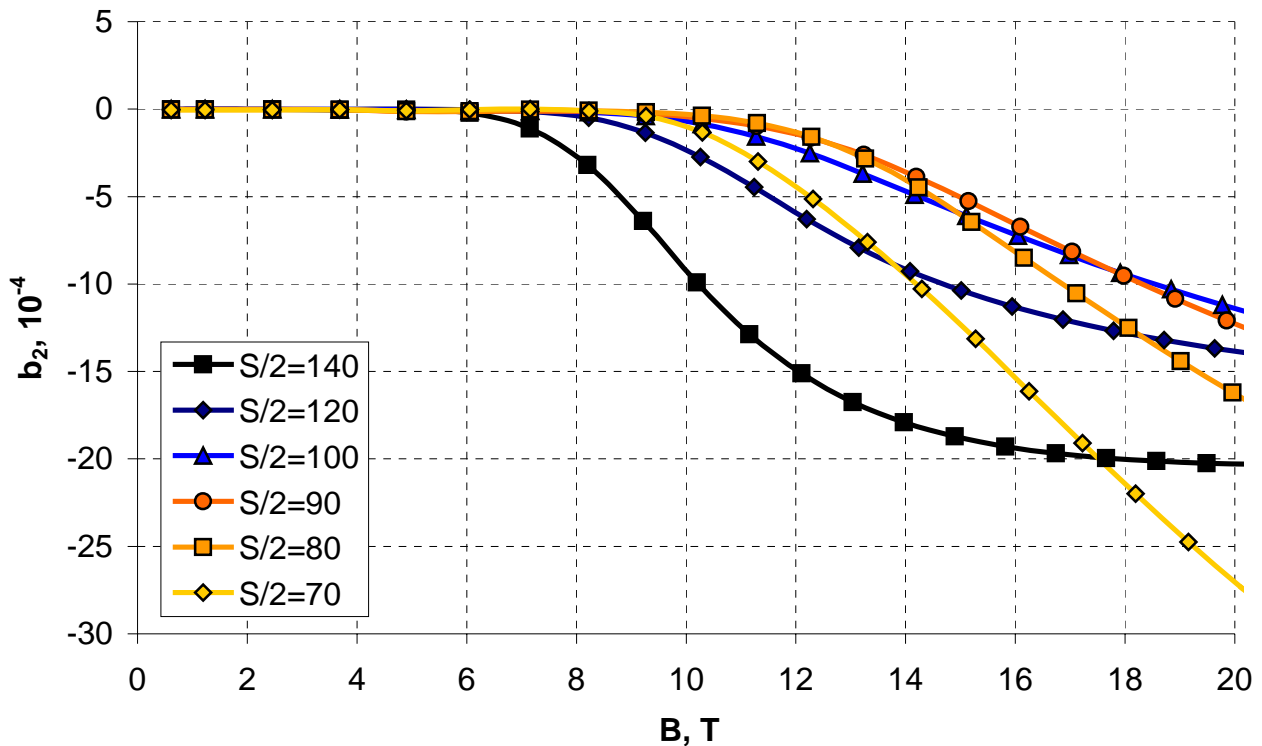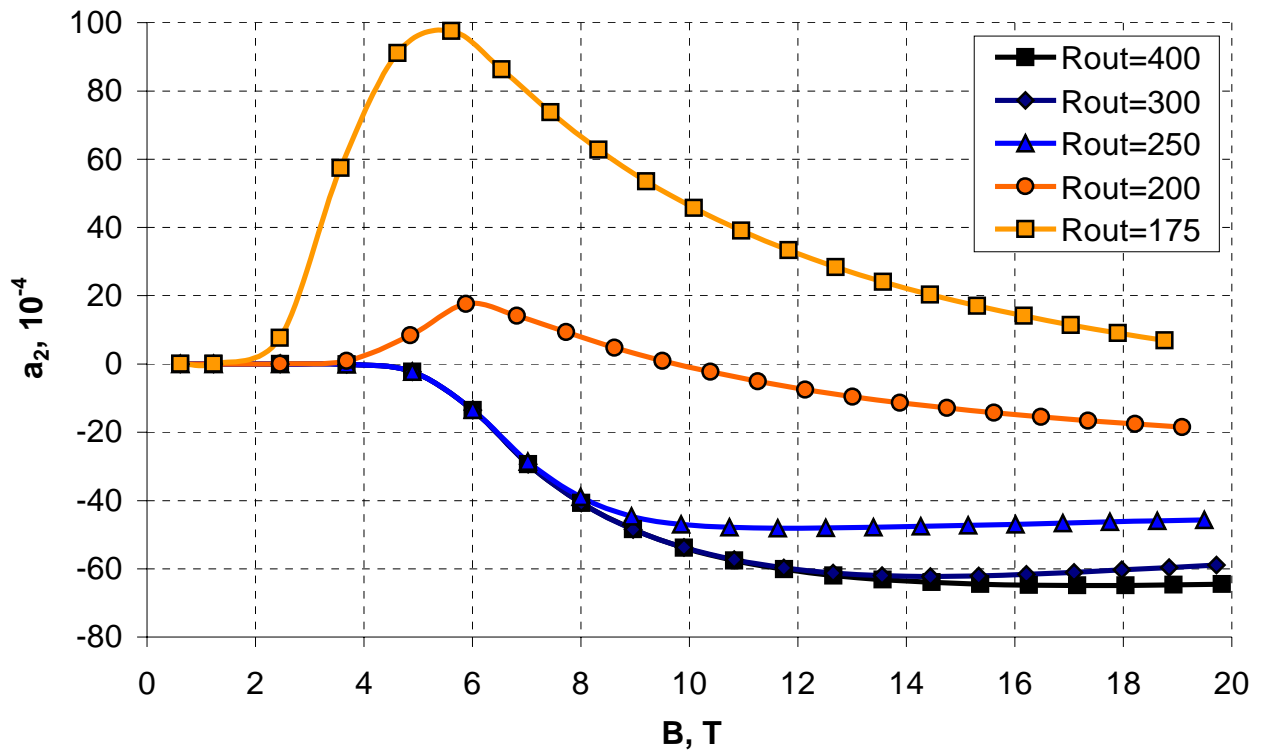

Figure 2.3.5. Quadrupole component as a function of the bore field.
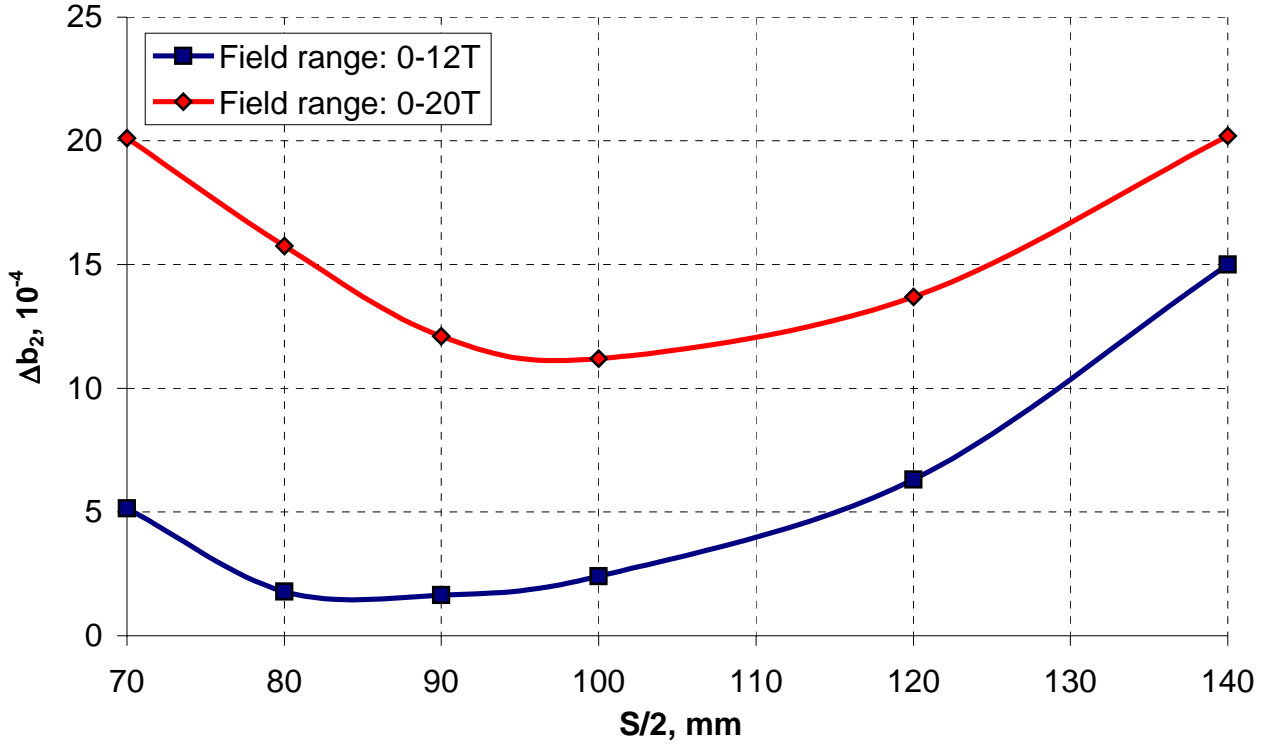
Figure 2.3.6. Maximum quadrupole deviations as functions of the half bore separation distance.

2.3.2 Dipole magnet with vertical bore arrangement

The vertical coil arrangement within a common yoke is another possibility of the double aperture concept. The common coil magnet has the inherent vertical bore separation. Shell type dipole coils can be arranged this way as well. In either case, the coils are to generate the field of opposite signs in two apertures. It implies a boundary condition of constant vector potential in the magnet horizontal plane and therefore the negative coupling between two apertures (the flux lines are tangential to the plane). To understand peculiarities of this case in terms of the field quality, the OPERA2D model similar to the one described in the previous paragraph was built. It is shown in Figure 2.3.7.

At first, the bore separation distance was fixed at 200 mm and the yoke outer radius was varied within the range of 175-400 mm. Figure 2.3.8 shows the skew quadrupole component coming from the yoke saturation effect. Small yoke outer radius leads to a large positive skew quadrupole component, since the flux expels form the outside to the inter-coil region. On the other hand, increasing of the yoke outer radius forces the flux to outside, turning the skew quadrupole component negative. Obviously, there should be an optimum yoke outer radius, illustrated in Figure 2.3.9.

Figure 2.3.7. Dipole model with vertical bore separation.
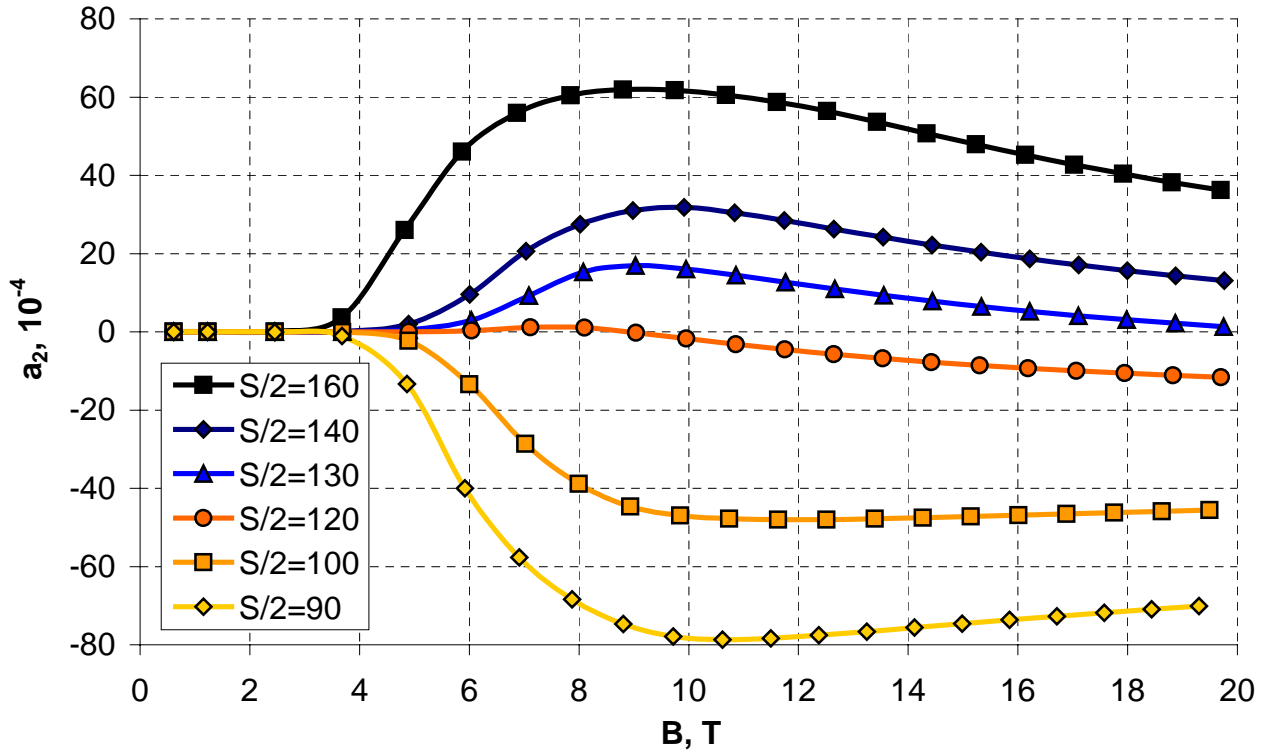

Figure 2.3.8. Skew quadrupole component as a function of bore field.
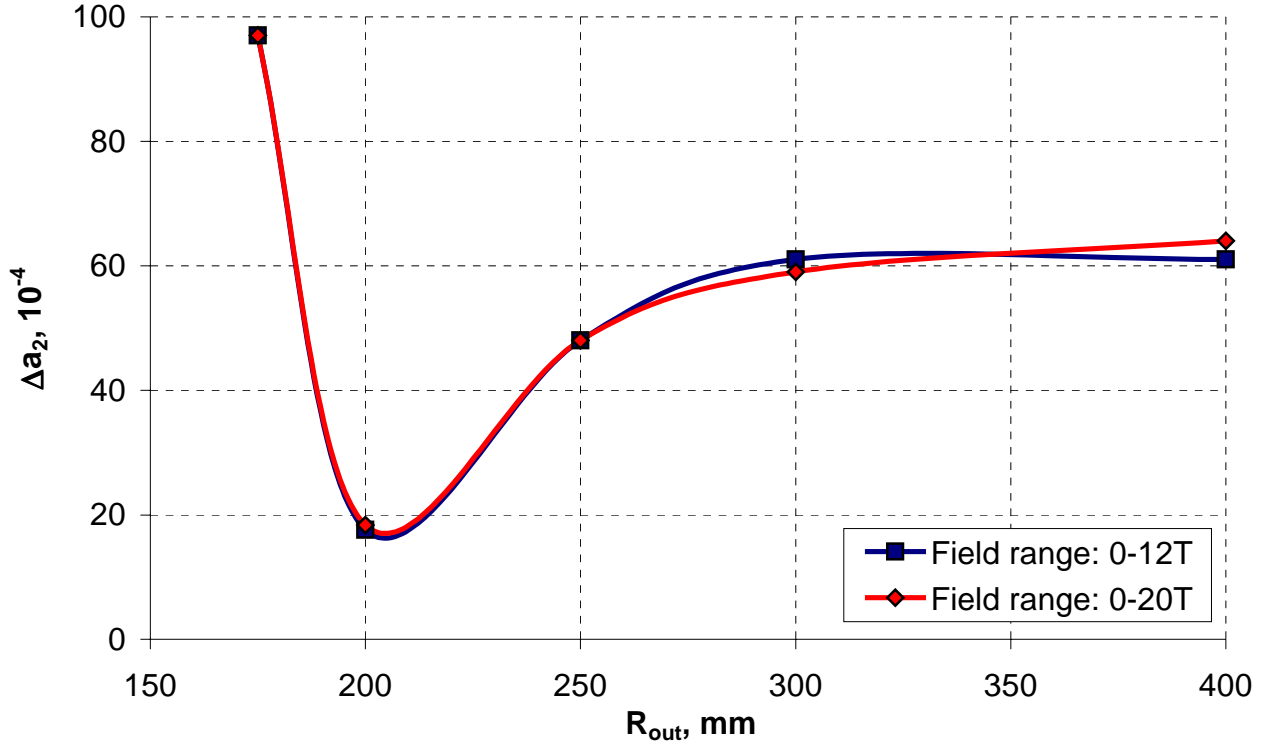
Figure 2.3.9. Maximum skew quadrupole deviations as functions of the yoke outer radius.

Thus the quadrupole deviations are minimum for the yoke outer radius of ~ 210 mm. There is virtually no difference between two curves because maximum deviations of the harmonic happen below 12 T field, as the yoke saturation effect is stronger than in the magnet with horizontal bore arrangement. It quantitatively confirms by a relatively high fringe field at the outer yoke surface (Figure 2.3.10). Thus, the fringe field is by factor of three larger than in the magnet with horizontal bore arrangement at the same yoke radius of 250 mm. It in general demands stronger shielding of the magnet with vertical bore arrangement at comparable yoke sizes.

Figure 2.3.11 presents the quadrupole distributions for different bore separation distances and Figure 2.3.12 shows the maximum quadrupole deviations in two field ranges. There are clear minimums on the curves at the bore separation distance of ~250 mm for both field ranges, which was the same as the yoke outer radius. This "coincidence" explains by two magnetic boundaries, defining the flux distribution within the yoke. One boundary is the magnet horizontal plane with geometrically imposed condition of a constant vector potential. Another boundary is the iron-to-air interface with a "weakly" imposed condition of constant vector potential. Both boundaries expel the flux with nearly equal force and the top-bottom symmetry occurs when the coil is at approximately equal distances from them. Therefore, the optimum bore separation distance for the dipole magnet with vertical coil arrangement is by ~40 % larger than for the magnet with horizontal coil arrangement at equal yoke outer radius.
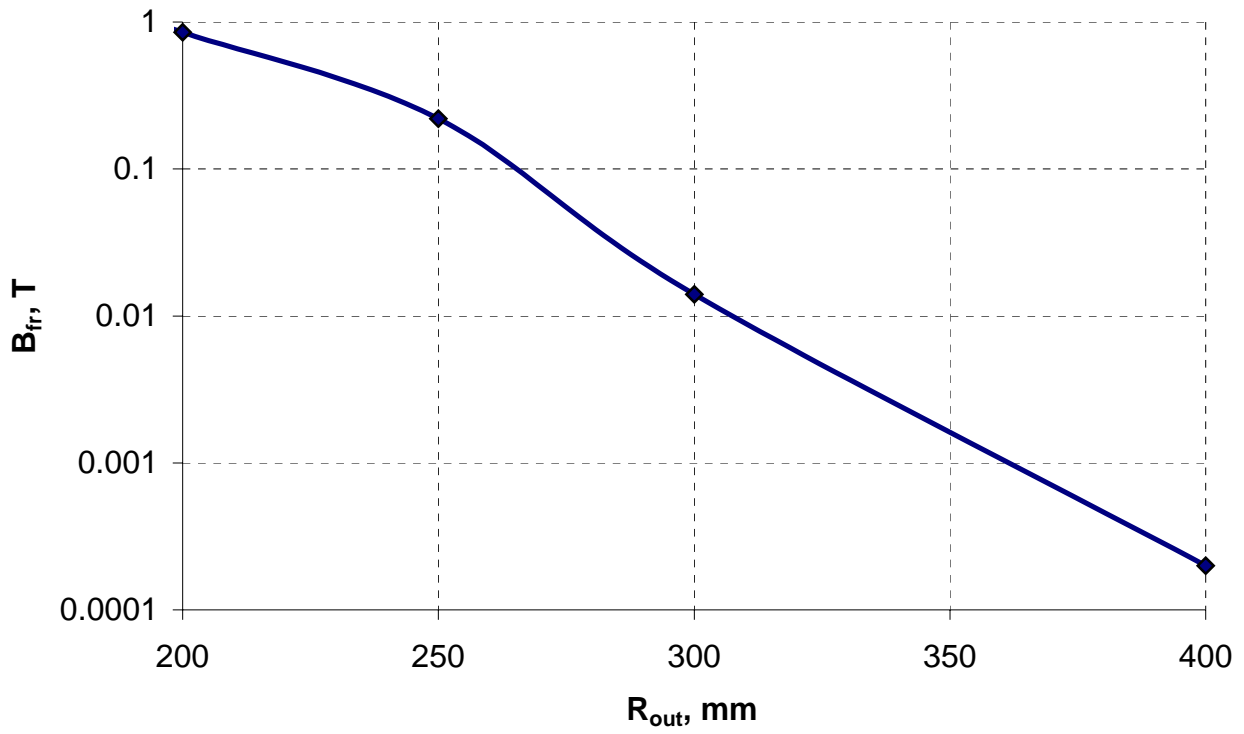
Figure 2.3.10. Fringe field as a function of the yoke outer radius.

Figure 2.3.11. Skew quadrupole component as a function of the bore field.
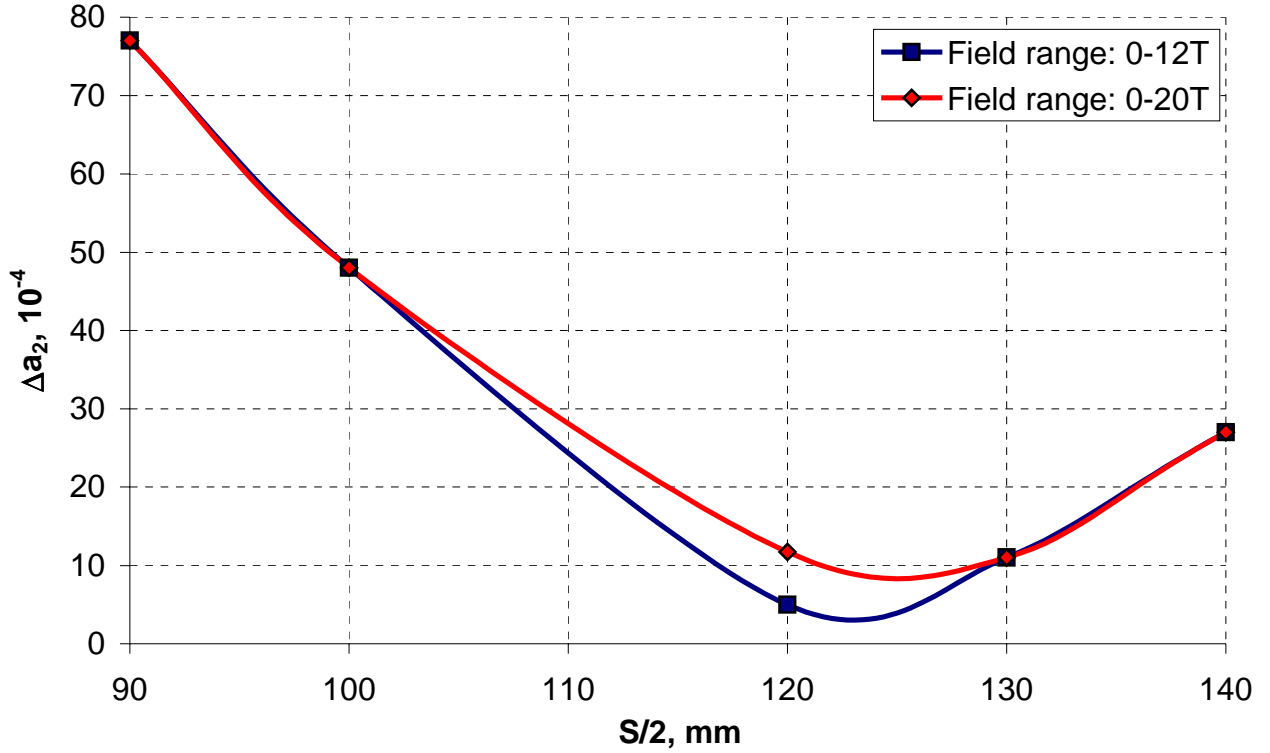
Figure 2.3.12. Maximum skew quadrupole deviations as functions of the bore separation distance.

2.3.3 Quadrupole magnets

The double aperture quadrupole magnet is a logical extension of the idea of two magnets in one yoke, similar to the dipole magnet design. Unlikely to the dipole magnets, where horizontal or vertical coil arrangement makes a considerable difference in magnetic design, double aperture quadrupole magnets are independent on the arrangement. It explains by the fact that the quadrupole field is explicitly described by 0-45 degrees sector of symmetry. Thus, rotation of the coil by 90 degrees turns the normal quadrupole into the normal quadrupole of opposite sign, unlikely to the dipole magnet, where such transformation turns the normal dipole into the skew dipole.

Presence of the second aperture causes multipoles, unallowed by the quadrupole symmetry. In case of horizontal bore separation, the left-right asymmetry generates normal odd harmonics (dipole, sextupole, decapole, etc.), when in case of vertical separation they turn into odd skew multipoles (skew dipole, skew sextupole, skew decapole, etc.).

Unlikely to the dipole magnet, there are two options for arranging functions of two quadrupole coils within common yoke, depending on the accelerator lattice - they can produce equal or

opposite effects on the relevant beams. In case of the equal effect, they simultaneously have either focusing or defocusing effect (that will be referred to as FF), when in the case of opposite effects one is focusing and another one is defocusing (FD). These two cases correspond to different boundary conditions in the plane of symmetry separating two apertures. Figure 2.3.13 shows coils for the possible cases with the flux lines and boundary conditions.

The FF magnet function occurs when the flux lines are tangential to the symmetry plane and therefore the boundary condition of a constant vector potential implies. The FD magnet function occurs when the flux is normal to the symmetry plane that implies the boundary condition of zero normal derivative of vector potential in the plane. The magnetic coupling between two apertures is negative in the first case and positive in the second that makes a big difference in terms of magnetic design. To study peculiarities of these cases, two simple OPERA2D models were built and shown in Figure 2.3.14.
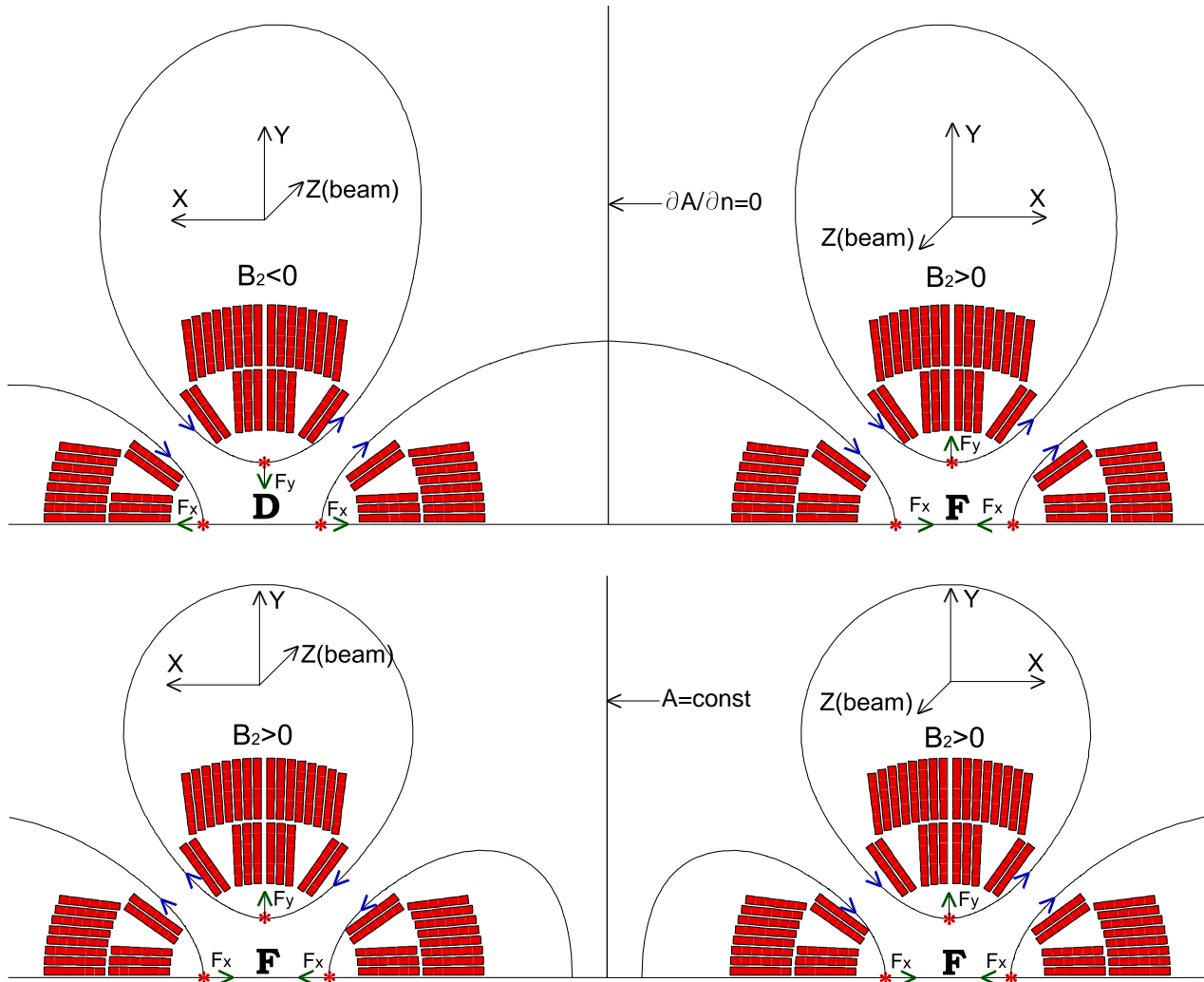
Figure 2.3.13. FD (upper) and FF (lower) quadrupole functions within one yoke.

76

R_{out}

$S/2$

$\partial A/\partial n=0$, positive coupling

R_{out}

$S/2$

A=0, negative coupling
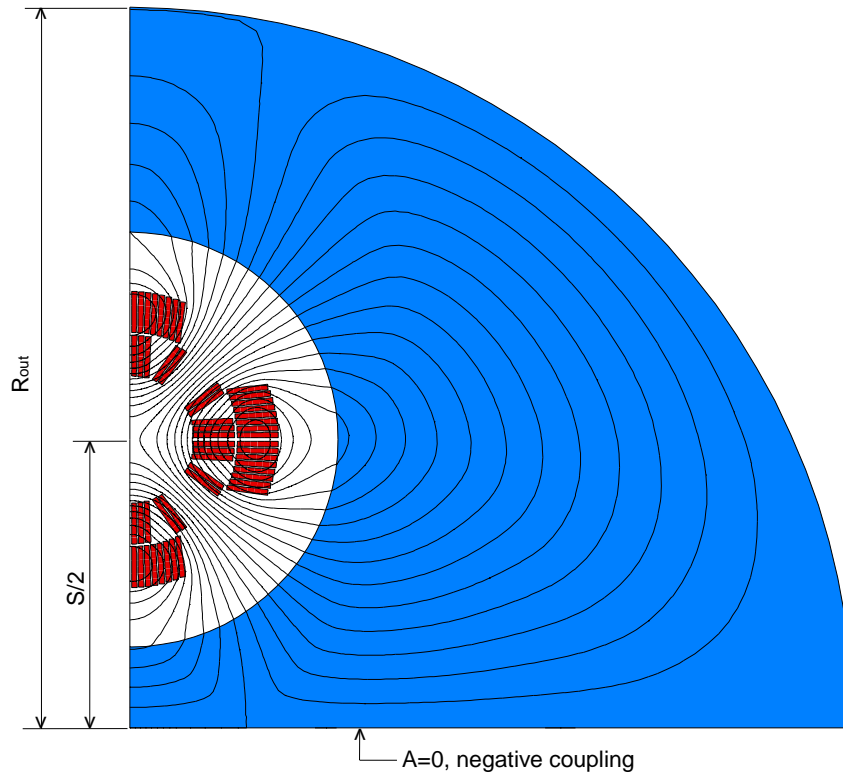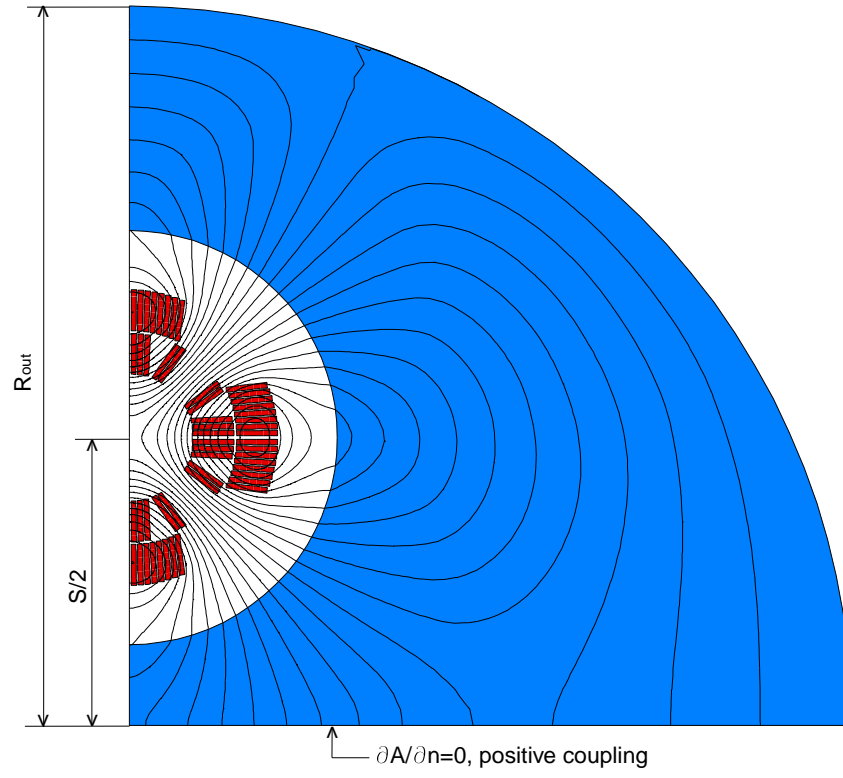
Figure 2.3.14. FD (upper) and FF (lower) quadrupole models.

Initially, the bore separation distance was fixed at 200 mm and the dependence of the yoke outer radius on the field quality was analyzed. Figures 2.3.15-2.3.18 present deviations of the skew dipole and sextupole components coming from the yoke saturation as functions of the bore gradient for FF and FD cases.

It is possible to see that the skew dipole component drops in the FF magnet with increasing of the yoke outer radius, when the skew sextupole component has a minimum at ~220-230 mm for the field range of 0-400 T/m. However, taking into account relatively small skew sextupole level, it should not drive the yoke radius choice.

Both skew dipole and sextupole simply drop with increasing of the yoke outer radius in the FD magnet. From the fringe field plot shown in Figure 2.3.19, one can notice an essentially smaller fringe field level than in either of the dipole magnets at the same outer yoke radius. Thus, it was convenient to fix the yoke outer radius at the same value as in the dipole magnets – 250 mm and study the field quality dependence on the bore separation distance.

Figures 2.3.20-2.3.23 present the skew dipole and skew sextupole components as functions of the gradient for different bore separation distances, and Figures 2.3.24-2.3.25 show maximum deviations of the skew dipole component within two cycles.
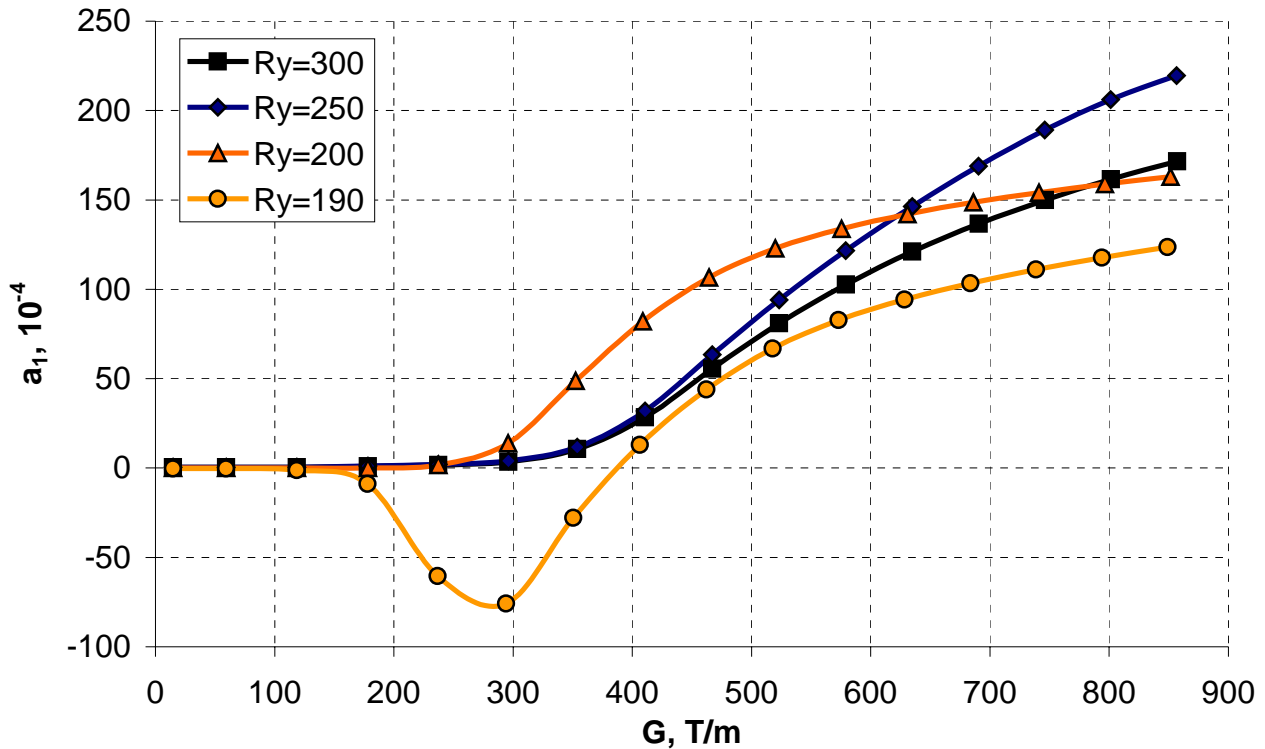
Figure 2.3.15. Skew dipole component in FF magnet as a function of the bore gradient.
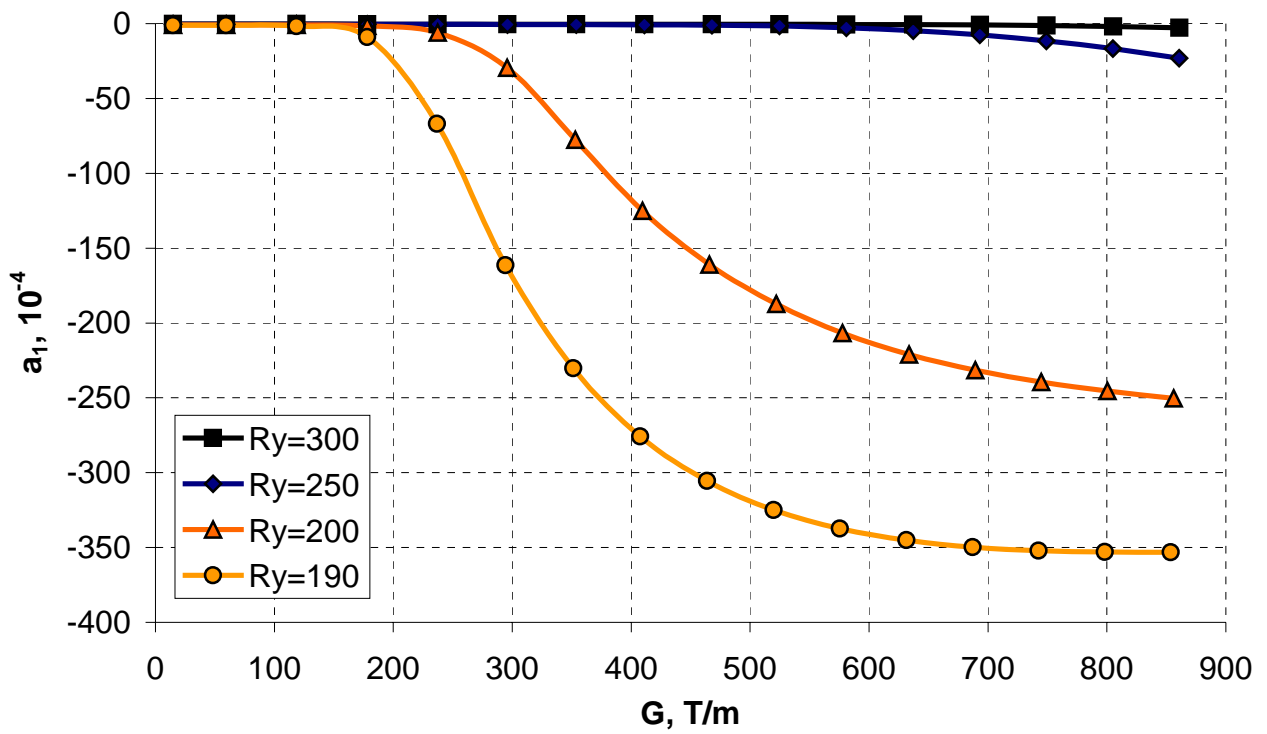
Figure 2.3.16. Skew dipole component in FD magnet as a function of the bore gradient.
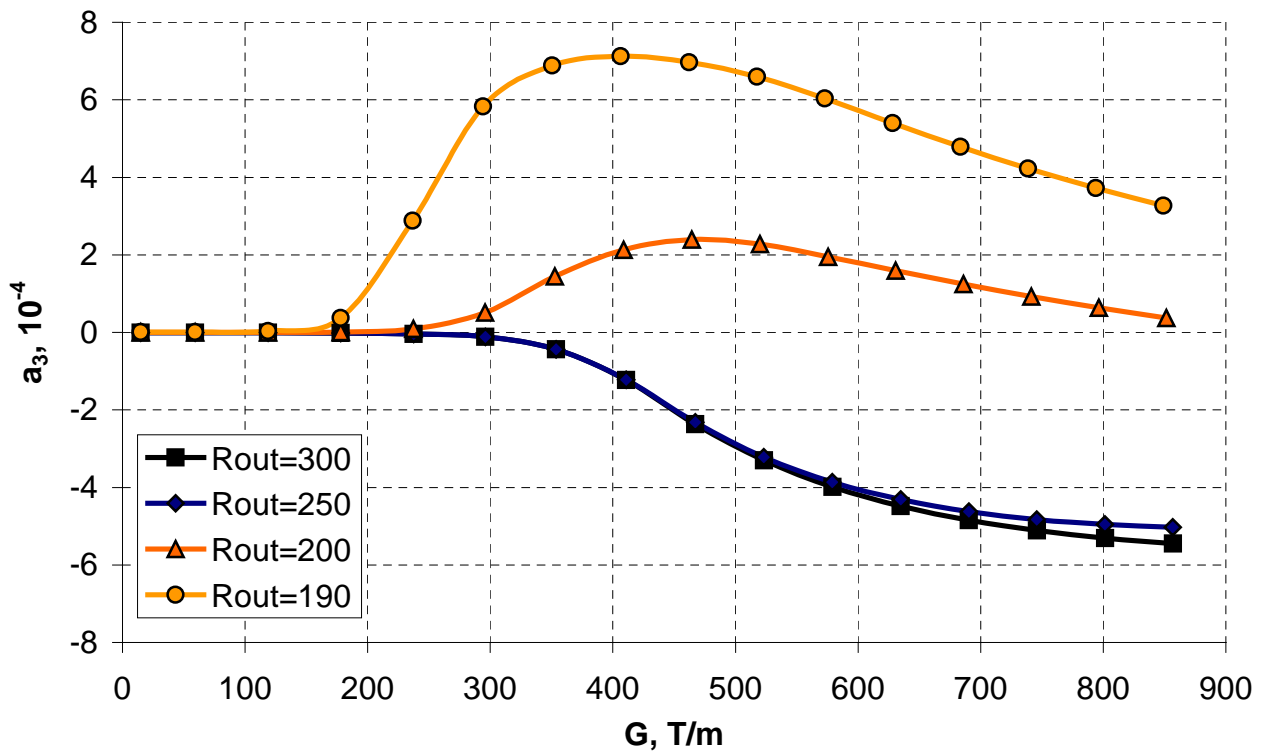
Figure 2.3.17. Skew sextupole component in FF magnet as a function of the bore gradient.
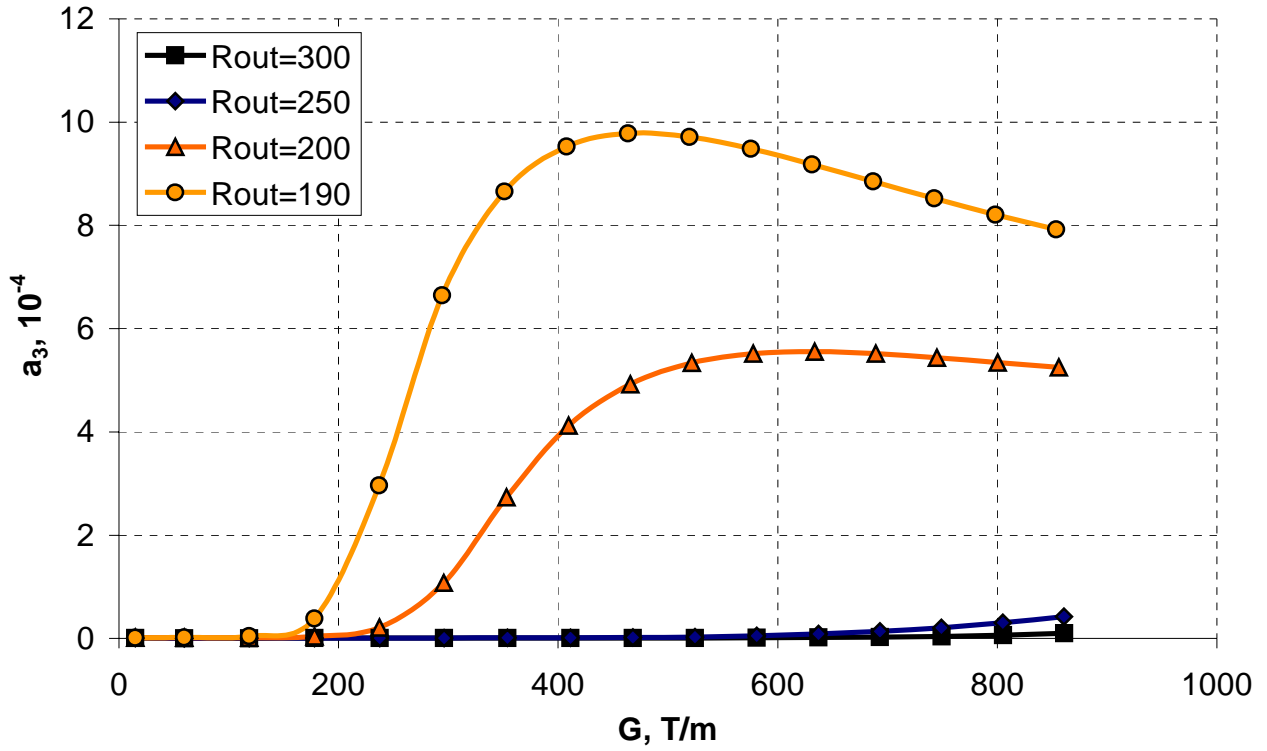
Figure 2.3.18. Skew sextupole component in FF magnet as a function of the bore gradient.
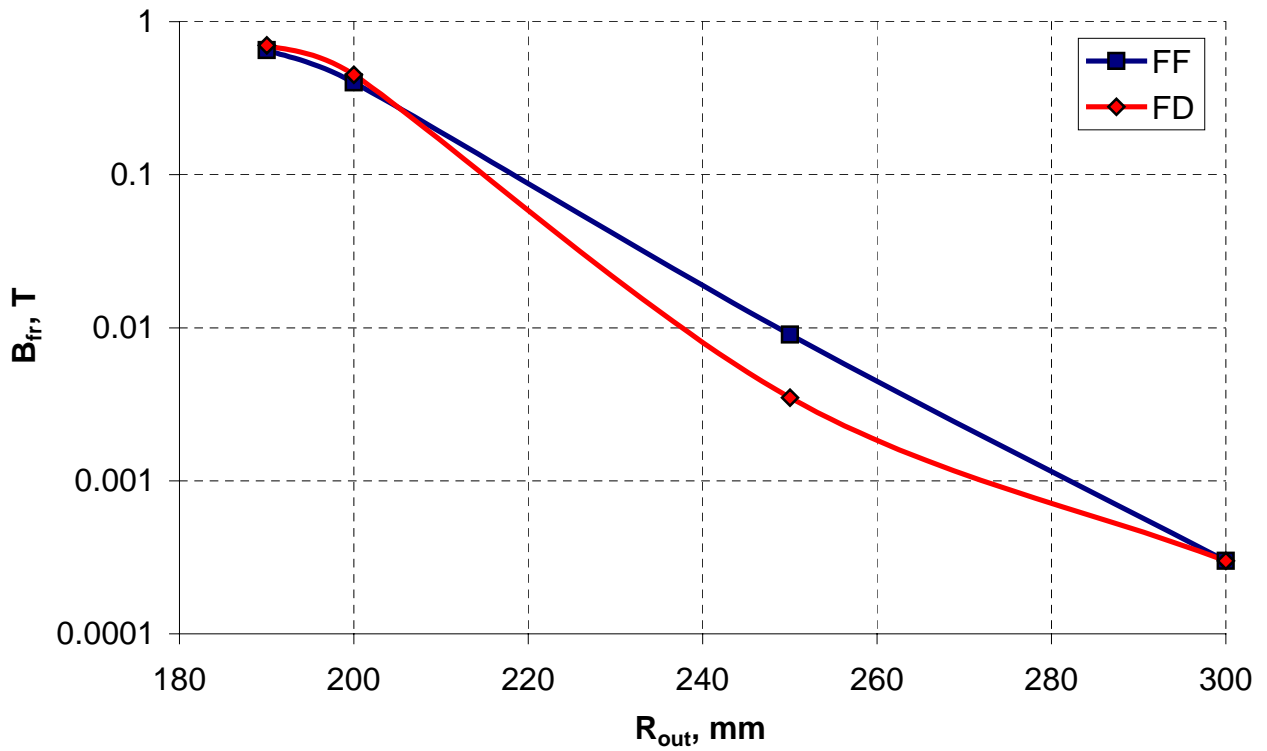

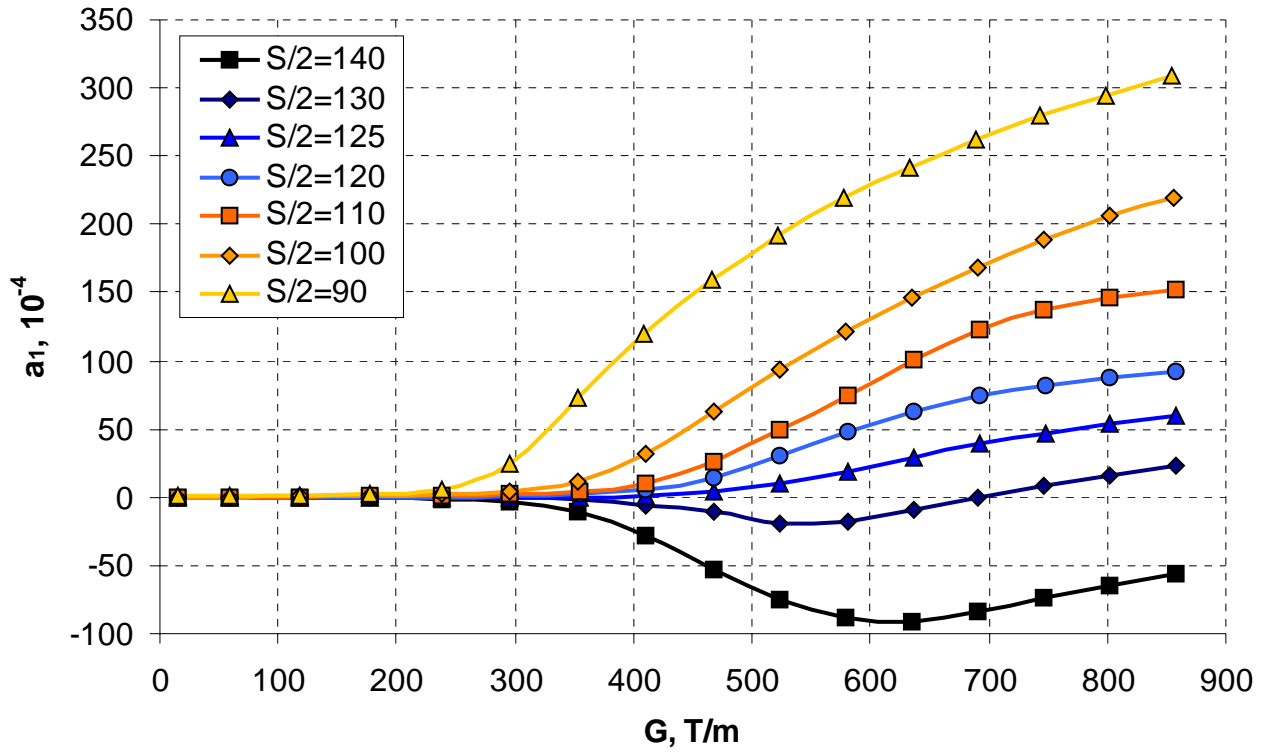Figure 2.3.19. Fringe fields as functions of the yoke outer radius.

Figure 2.3.20. Skew dipole components in FF magnet as functions of the bore gradient.
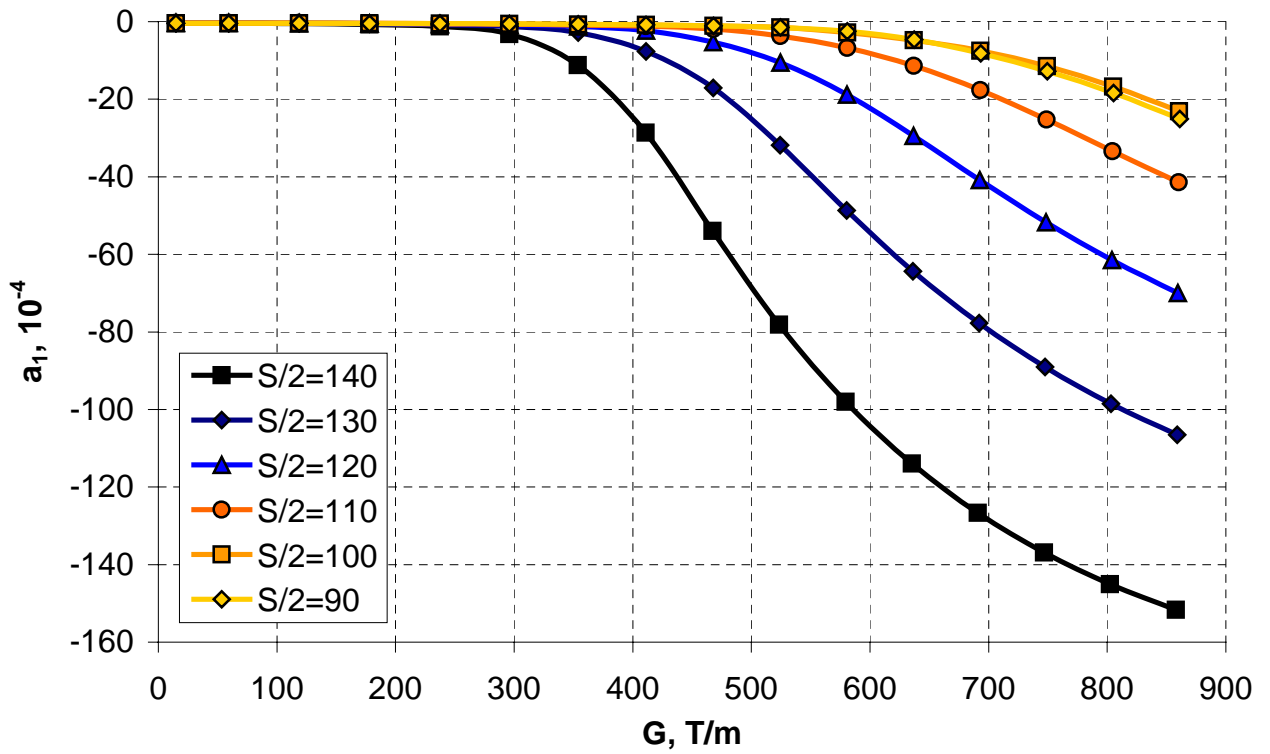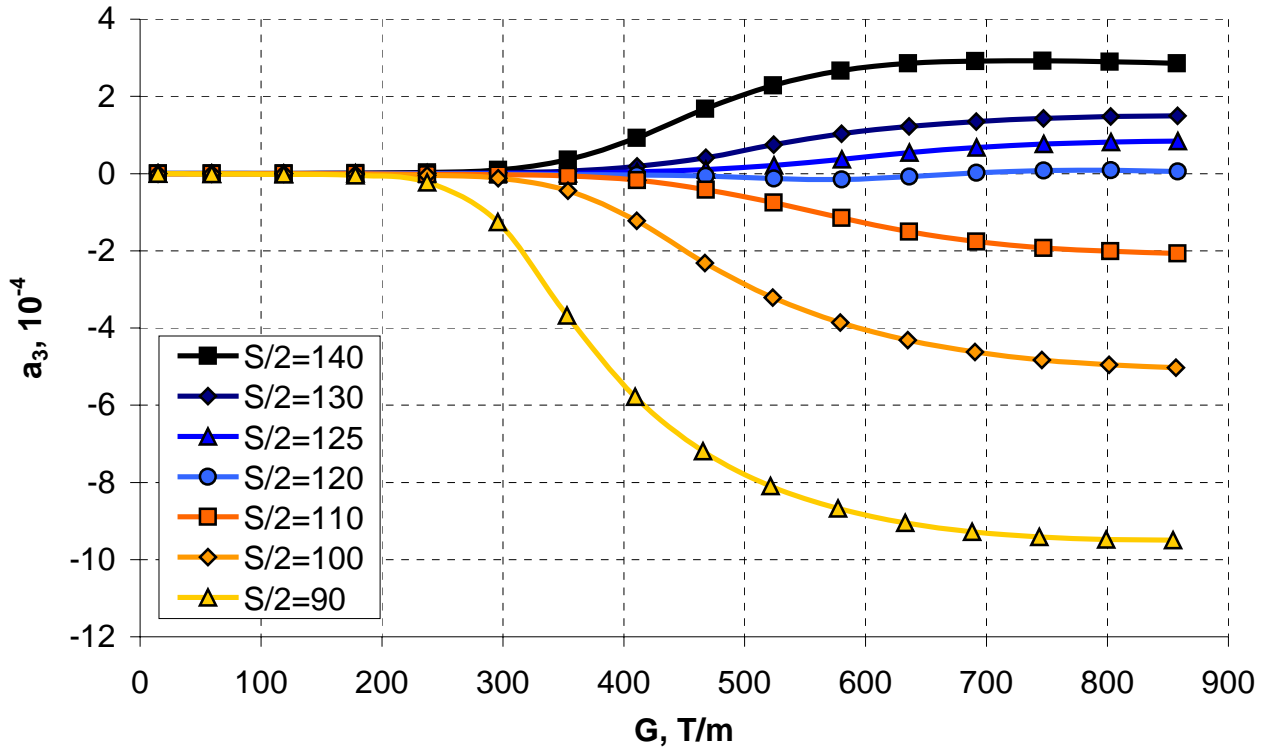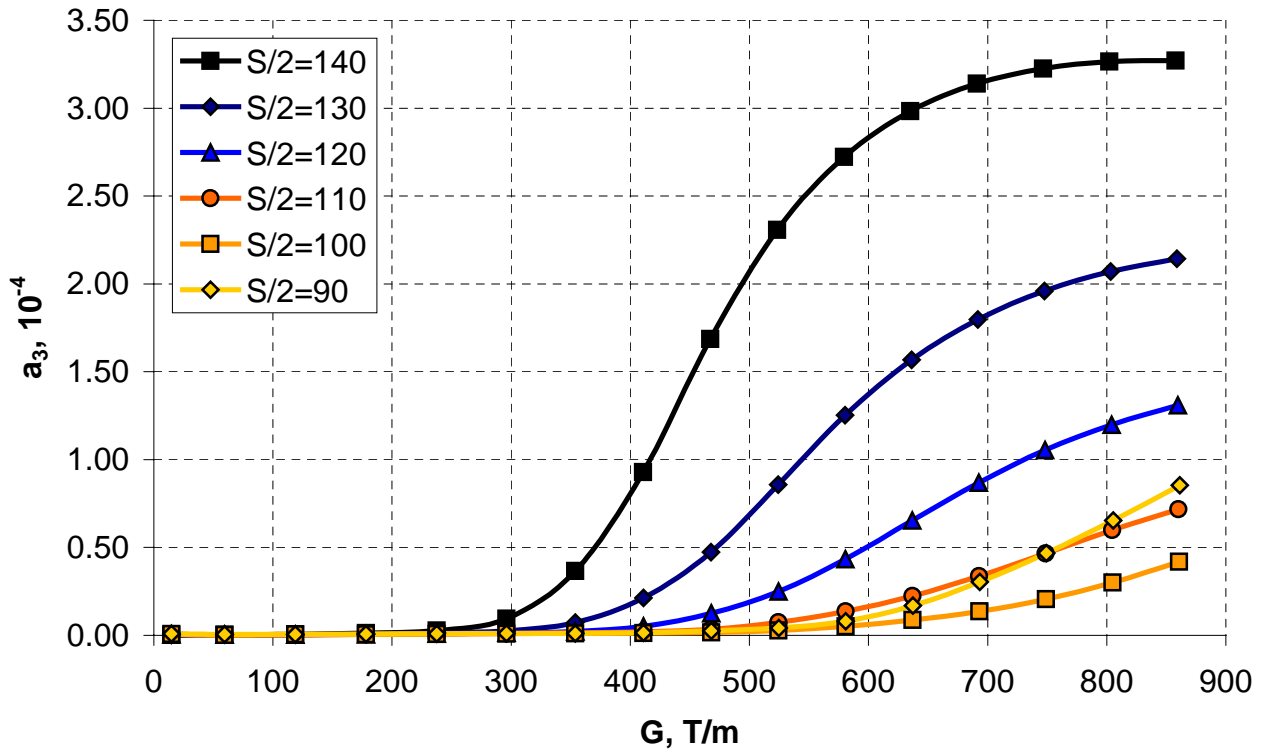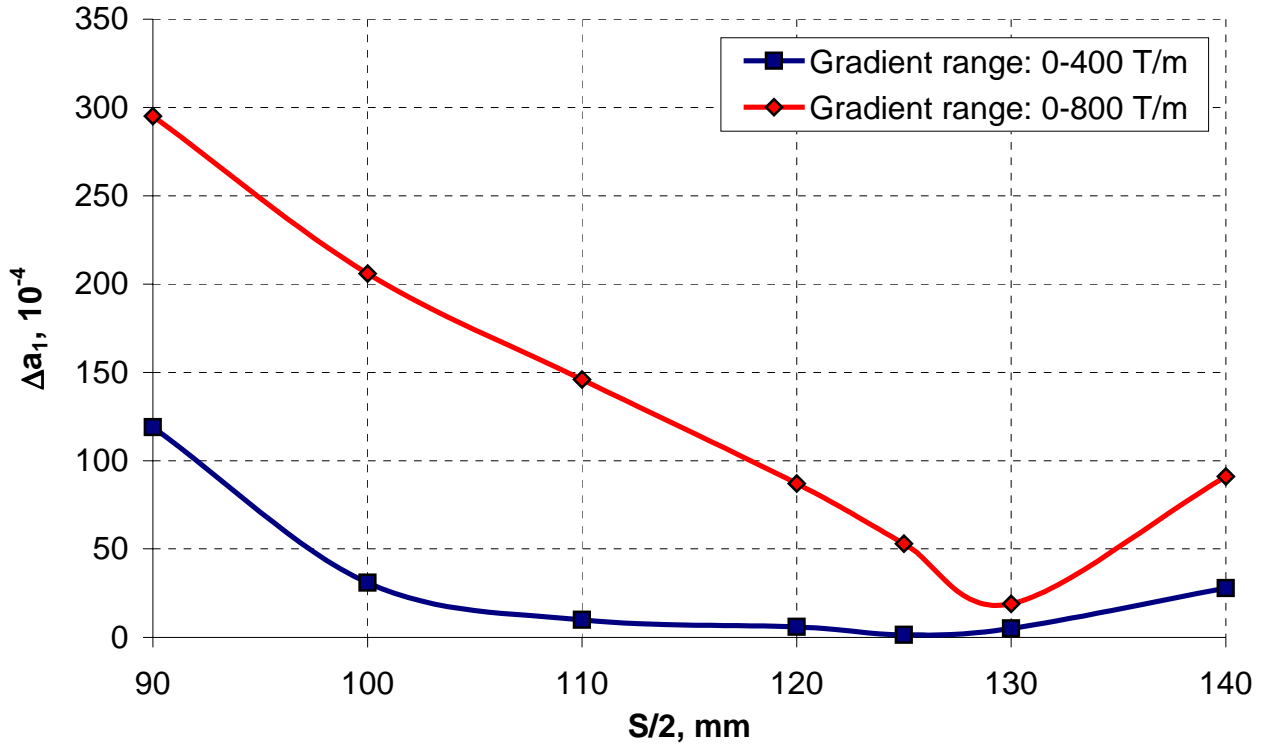

Figure 2.3.21. Skew dipole components in FD magnet as functions of the bore gradient.

Figure 2.3.22. Skew sextupole components in FF magnet as functions of the bore gradient.

Figure 2.3.23. Skew sextupole components in FD magnet as functions of the bore gradient.

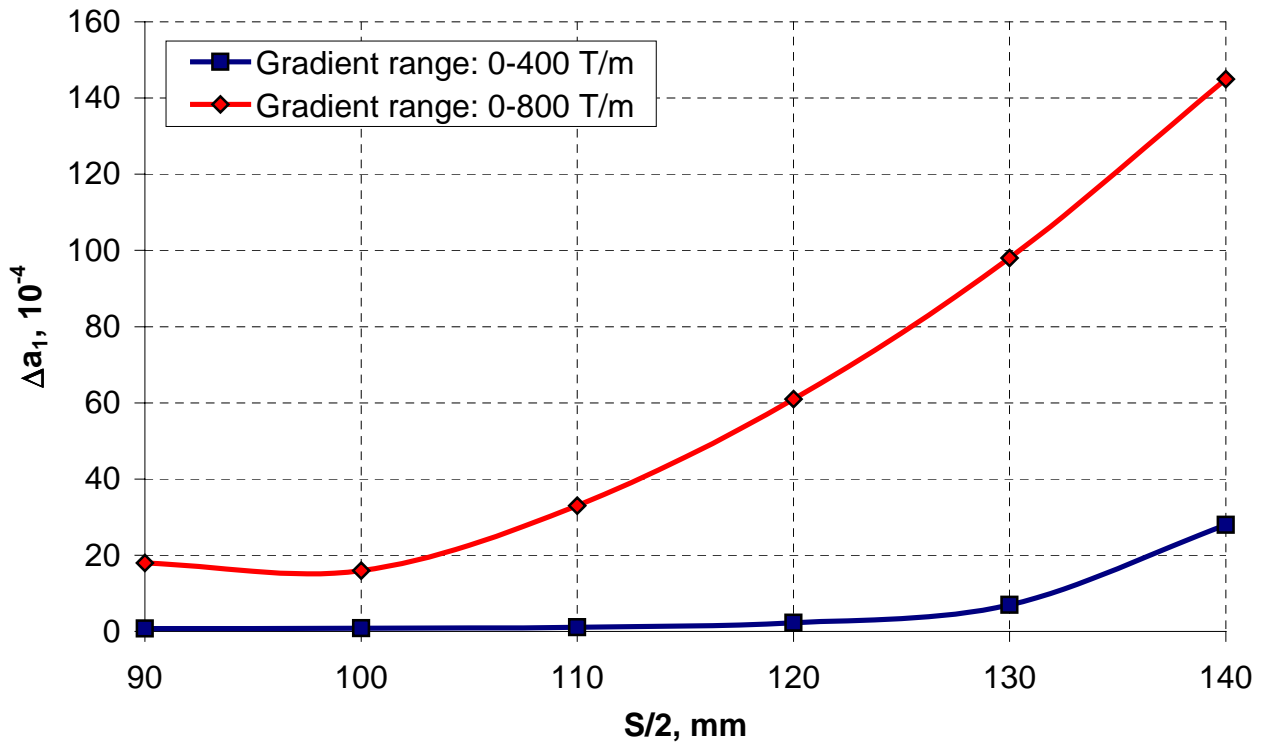Figure 2.3.24. Skew dipole deviations in FF magnet as functions of the bore separation distance.

Figure 2.3.25. Skew dipole deviations in FD magnet as functions of the bore separation distance.

There is a clear optimum of the bore separation distance at around 255-260 mm for the FF magnet and around 200 mm for the FD magnet in either 0-400 T/m or 0-800 T/m gradient cycle. The skew sextupole has a minimum in the FF magnet at the same bore separation distance, as for the skew dipole. There is no sextupole minimum for the FD magnet, which is however small enough to be neglected.

Based on the obtained results and the fact that the quadrupole magnet has to have the bore separation distance exactly equal to the bore separation distance of the main dipole, one can make the following conclusions:

- The dipole magnets with horizontal bore arrangement have the optimum bore separation distance of 160-200 mm, that is essentially the same as for the quadrupole magnet with FD functions. Therefore, using of the FD quadrupole magnets together with the dipoles having horizontal bore separation is natural. It requires the minor changes in magnet geometries to achieve a good field quality. This approach is used in the LHC magnets.
- The dipole magnets with vertical bore arrangement have the optimum bore separation distance approximately equal to the yoke outer radius, which is the case for the FF quadrupole magnets (those have the boundary conditions similar to the dipoles). Therefore, it is preferable to use the dipole magnets with vertical bore arrangement together with the FF quadrupoles.

If there is a necessity of unpreferable combinations, there are the following options:

- The dipole magnet with horizontal bore separation has to have the bore separation (and obviously the yoke outer radius) larger than the optimum in order to work together with the FF quadrupole magnet. This way is not cost-effective since the dipole magnet is the major cost driver. An alternative reduction of the optimum bore separation distance in the FF quadrupole can only be done to a relatively small extent without significant field quality deterioration. Taking the iron out of the high field region (making it "warm") may help to solve this problem, although asymmetrical quadrupole coils has to be used.

- Using of the FD quadrupole along with the dipole having the vertical bore separation creates fewer problems since in this case the quadrupole bore separation distance can be increased in order to match the dipole bore separation for the expense of increasing the yoke outer size in the quadrupole magnet. Doing so does not make a significant cost impact due to a relatively small number of quadrupole magnets.

2.4 Passive correction of the yoke saturation effect by holes

Analysis of the simple magnet configurations described in previous paragraphs has demonstrated that optimization of the inner/outer yoke surfaces and beam separation distances alone does not provide satisfactory results of the field quality. There were several units of low order harmonics remaining in most of the optimized cases, which must be further reduced. Introduction of obstacles to the magnetic flux in form of holes allows flux redistribution between different parts of the yoke that may be used for correction of the yoke saturation effect. In order to understand the effect of the holes on the field multipoles, a simple OPERA2D model shown in Figure 2.4.1 was analyzed.
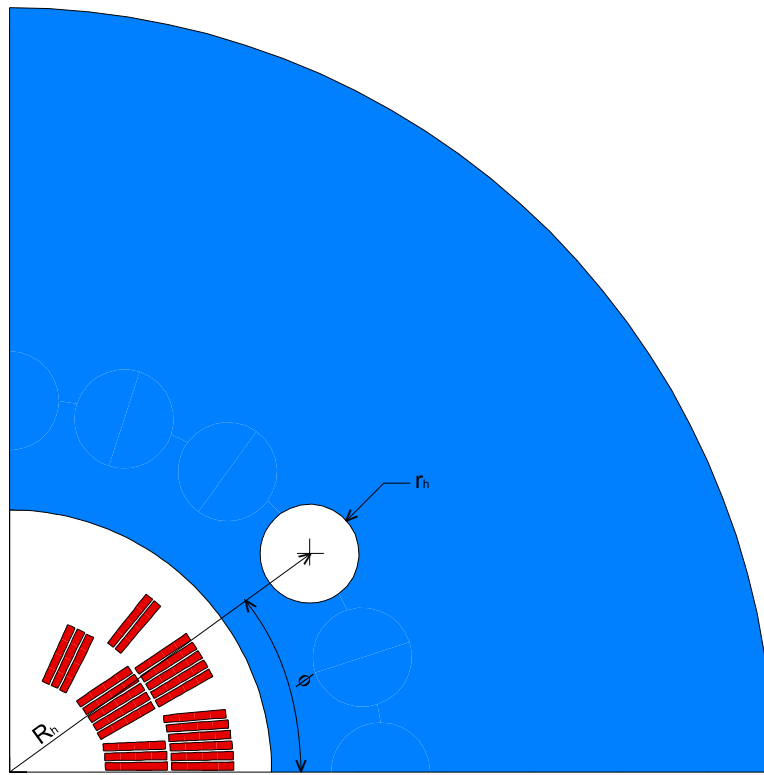

Figure 2.4.1. Model for studying of the hole effect.

Inner radius of the yoke was fixed at 60 mm (Chapter 1) and the yoke outer radius was fixed at the optimum value of 175 mm, determined early. Initially, the correcting hole with constant parameters R_h = 75 mm and r_h = 10 mm was moved azimuthally. Figures 2.4.2-2.4.3 present sextupole and decapole deviations produced by the hole (the plots show the difference between the cases with and without hole). Both hole-generated multipoles change the signs within the 0-90 degrees range of azimuthal positions. It is also illustrated in Figure 2.4.4, presenting the maximum multipole deviations in 0-12 T or longer fields range (since the multipoles have the maximum at 5-8 T field).
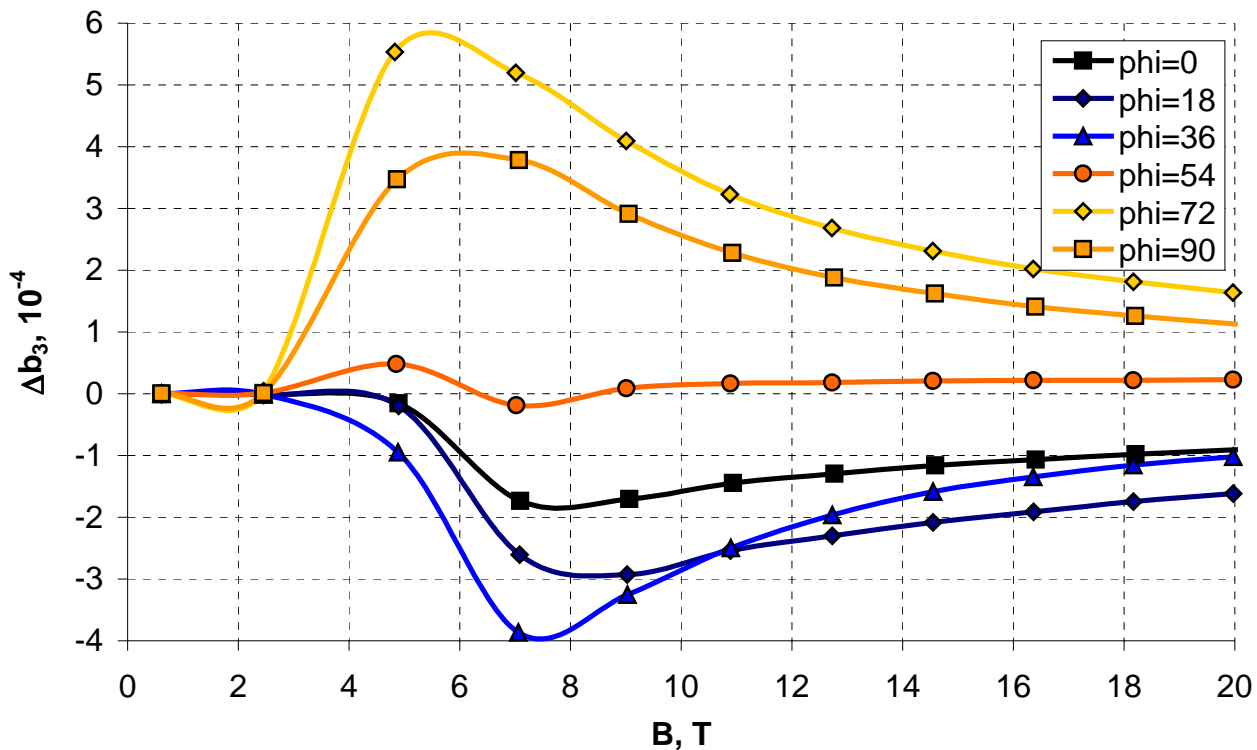
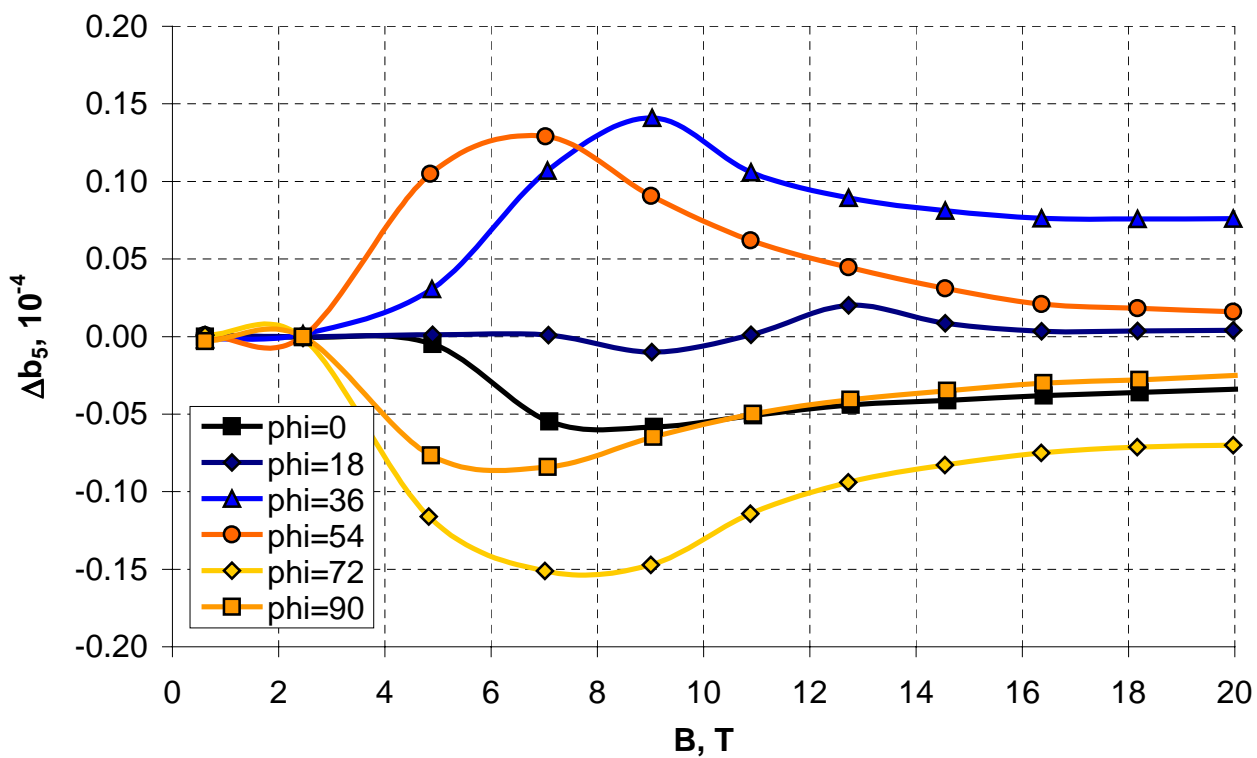Figure 2.4.2. Sextupole deviations as functions of the bore field.

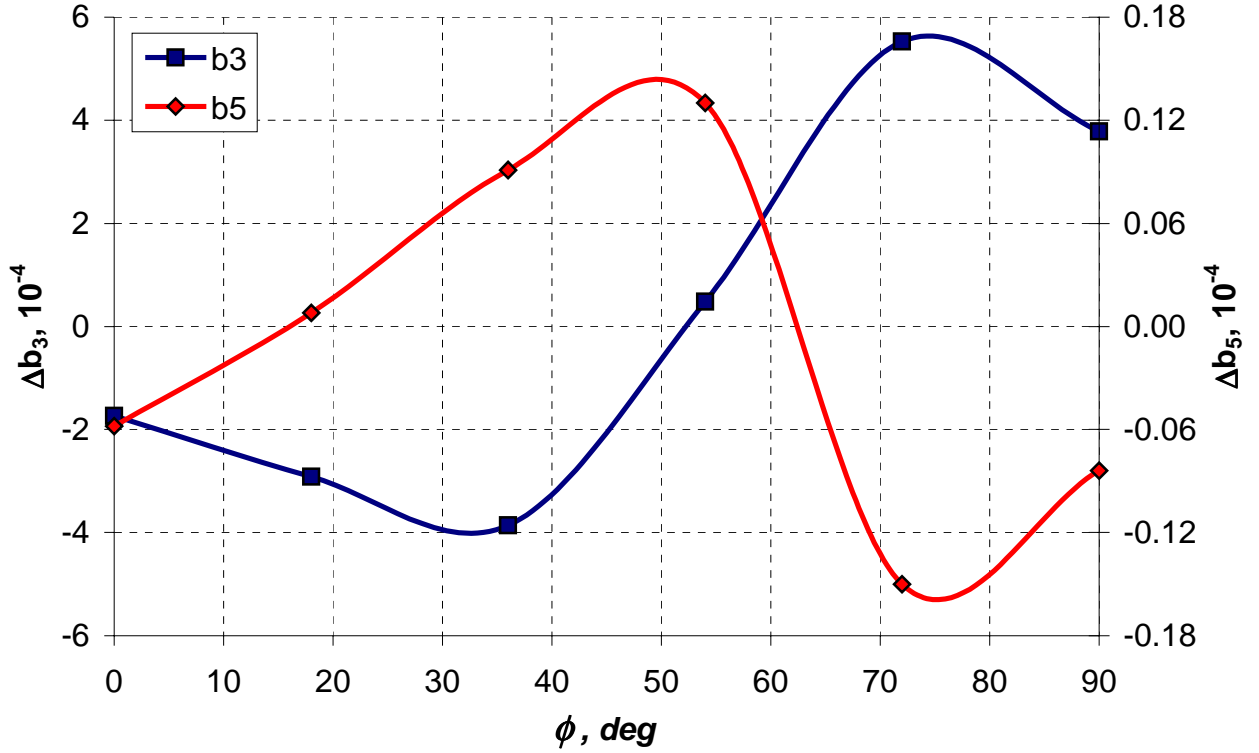Figure 2.4.3. Decapole deviations as functions of the bore field.

Figure 2.4.4. Maximum harmonic deviations as functions of the hole position.

Correction of the yoke saturation effect at intermediate fields requires the hole-induced sextupole and decapole to be negative (Figures 2.4.2-2.4.3). It occurs for the hole placed within 0-15 degrees (in the magnet midplane). However, the most effective hole position in terms of the sextupole correction is at 30-35 degrees, while in the midplane its effect is by a factor of two smaller. Due to relatively small decapole deviations, one can consider this hole position to be optimal for the correction of the yoke saturation effect in the dipole magnets. The hole with specified parameters placed at this angle virtually eliminates the saturation sextupole component at 4-8 T fields. However, at higher fields the saturation sextupole becomes negative as well as the effect of the hole, which together produces a large negative sextupole. This problem can be easily avoided by increasing the yoke outer radius (Figure 2.2.2).

Figure 2.4.5 shows the yoke saturation effect in terms of the sextupole component, corrected by the hole with $R_h = 75$ mm and $r_h = 10$ mm, placed at 36 degrees from the midplane for different yoke outer radii. One can see that combination of the correcting hole effect together with optimization of the yoke outer radius allows reduction of the saturation-induced sextupole by factor of two. Obviously, introduction of several holes can further improve the situation.

In order to understand the effect of the parameter R_h, it was varied within 75-85 mm. The hole radius r_h was proportionally increased so the hole spans the same angular width as at R_h=75 mm.
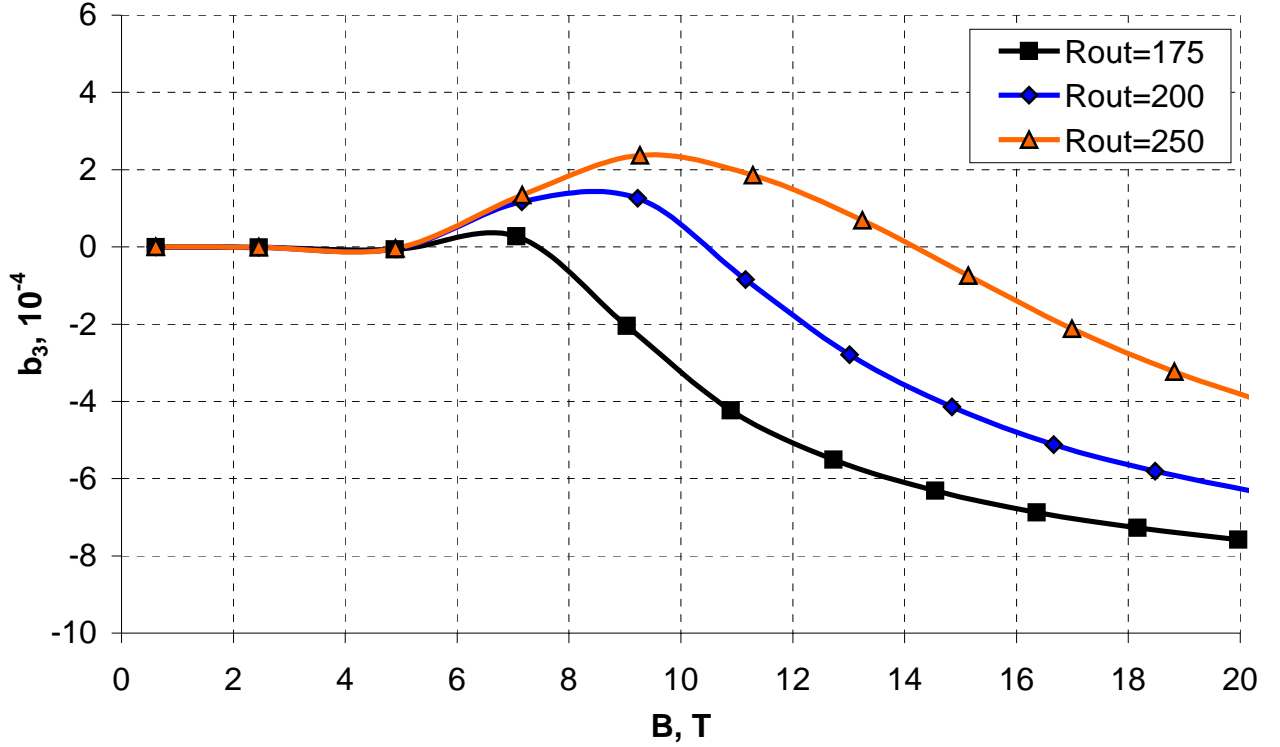
Figure 2.4.5. Corrected yoke saturation effect.

Figures 2.4.6-2.4.7 show the hole-induced sextupole and decapole components for different positioning radii. Increasing of the hole-positioning radius reduces the maximum hole effect on both multipole. Thus at $R_h = 85$ mm the hole is equally ineffective within 0-35 azimuthal range.

Finally, was determined the dependence of the hole effect on the radius r_h. For this purpose, the hole was set at $R_h = 85$ mm and $\phi = 36$ degrees, and r_h was varied within 5-19 mm. Figure 2.4.8 presents the hole-induced sextupole deviations as functions of the field and Figure 2.4.9 shows the hole-induced multipoles as functions of the hole radius.

It is notable that the sextupole and decapole dependencies on the hole radius can be well approximated by a function, proportional to r_h^2 (or the hole cross-section area) within quite a large range of the size variations. This observation is important for choosing the optimization strategy and can significantly reduce the optimization time. Thus, it is enough to find the effect of some reference size hole at several positions using a finite-element analysis. Then one can scale the dependencies for different hole sizes and find a good approximation to the optimum hole position and radius analytically.
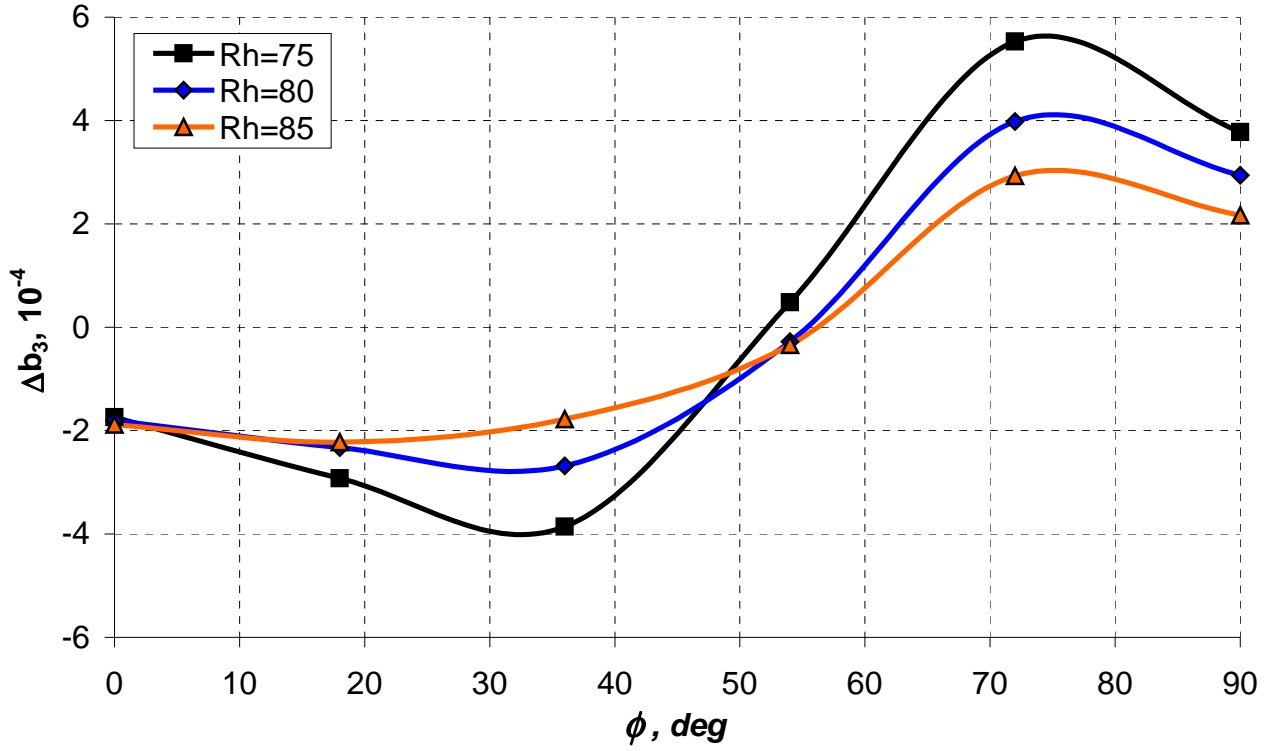
Figure 2.4.6. Maximum sextupole deviations as functions of the hole azimuthal position.
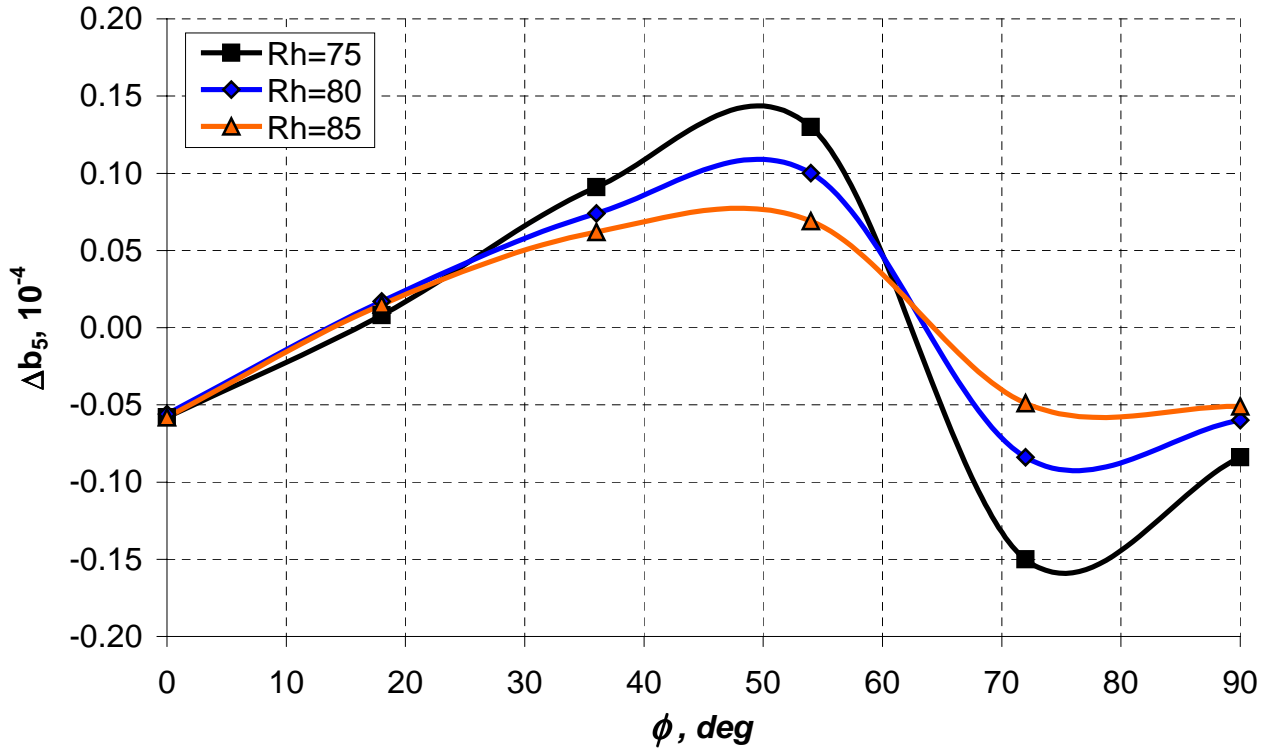

Figure 2.4.7. Maximum decapole deviations as functions of the hole azimuthal position.
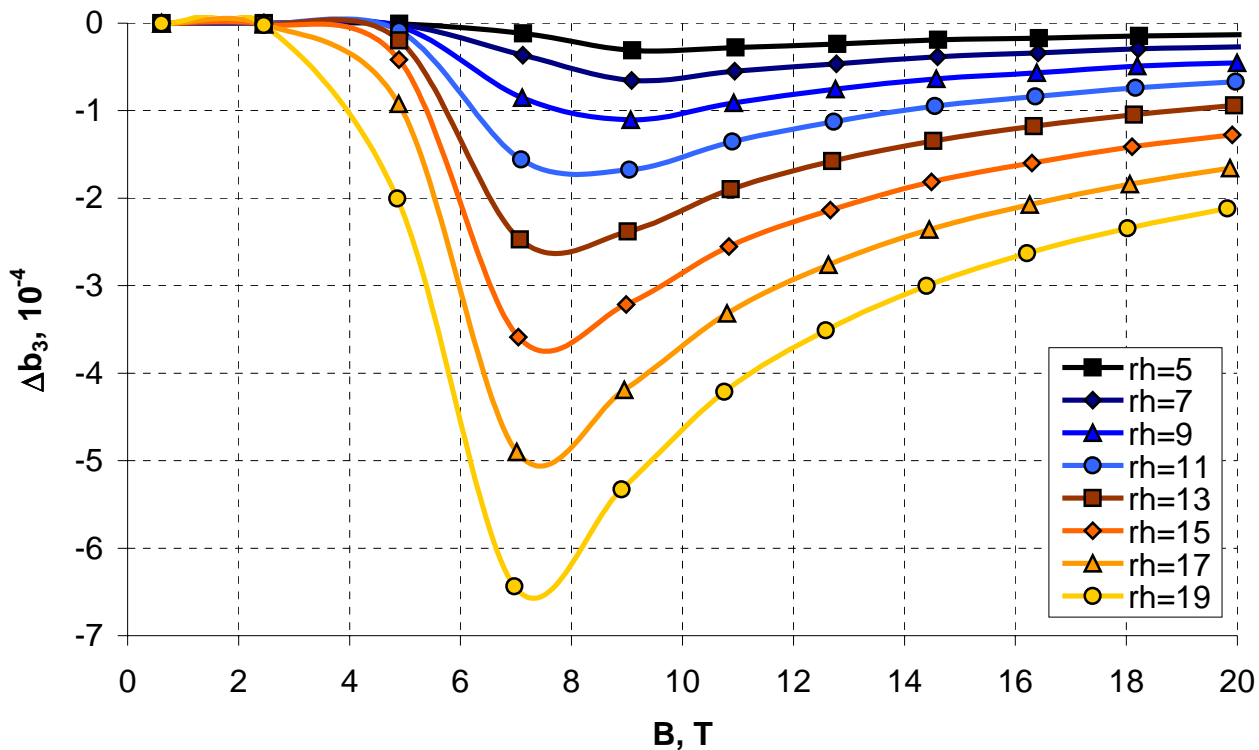
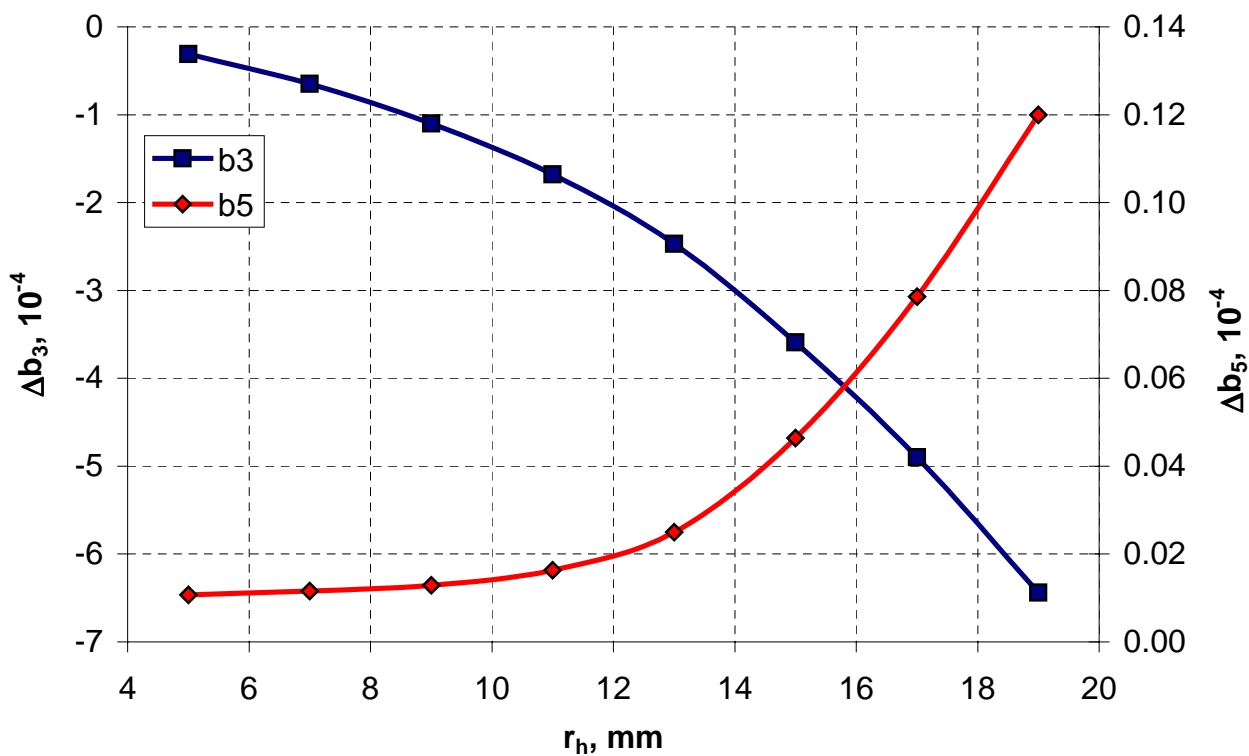Figure 2.4.8. Sextupole deviations as functions of the bore field.

Figure 2.4.9. Multipole deviations as a functions of the hole radius.

The method of passive correction using holes is in principle applicable for any low-order multipole affected by the yoke saturation effect. For example, the double aperture dipole magnets with horizontal bore separation have the left-right magnetic asymmetry resulting in the non-linear quadrupole component. This asymmetry can be eliminated or at least significantly reduced by holes placed in the vertical plane of symmetry.

There is the top-bottom magnetic asymmetry in the dipole magnets with the vertical bore separation that can be corrected by holes placed in the horizontal plane of symmetry. However, due to peculiarities of flux distributions in different magnets the final position of the holes has to be optimized separately in every particular case.

2.6 Summary

The results of study the yoke design parameters can be summarized as follows:

- The iron saturation effect in high field magnets is a source of considerable field quality distortions, which require correction.
- Optimization of the yoke inner and outer radii in a single aperture magnet may improve the field quality. These parameters however, do not provide the adequate correcting effect within the acceptable range of parameter variations, which makes it reasonable to chose them based on other than the field quality considerations (such as the minimum yoke size with an acceptable fringe field).
- Introduction of the yoke inner surface ellipticity makes a considerable change in the sextupole curve. However, the integral correcting effect is fairly small and the optimum yoke inner surface is close to the circular. Small "horizontal" ellipticity allows some field quality improvement at very high fields, however, complication of the magnet construction may not justify this small benefit.
- There are optimum yoke outer radii and bore separation distances in the double aperture dipole magnets with horizontal bore separation. It is possible to choose the optimum parameters for a desired accelerating cycle and level of the fringe field.
- The optimum bore separation distance in the dipole magnets with the vertical bore arrangement is approximately equal to the yoke outer radius. Reasonable restrictions on the fringe field define the yoke outer radius and thus the bore separation distance that is 40 % larger than for the dipole magnet with horizontal bore separation at the same fringe field.
- There are preferable pairs of the dipole and quadrupole magnets, based on the optimum bore separation distances. Thus, the FD quadrupole magnet is preferable for the dipole magnet with horizontal bore arrangement and the FF quadrupole is preferable for the dipole magnet

with vertical bore arrangements. Using of the unpreferable combinations is feasible, but reduces the overall system efficiency.

- Correction of the yoke saturation effect by holes seems to be the most effective method, providing the adequate correction at virtually no extra cost. Combination of this method with optimization of the yoke outer surface further improves the field quality.

CHAPTER 3. OPTIMIZATION OF SUPERCONDUCTING MAGNETS

3.1 Introduction

Fermilab is being developed high field magnets, based on Nb_3Sn technology for future high-energy accelerator – Very Large Hadron Collider (VLHC). Based on chosen lattice design and machine operation parameters, the Stage II arc magnets should meet the following general requirements, implying constrains on the magnetic design [10], [41]:

- Nominal field in arc dipole magnets ≥ 10 T.
- Nominal gradient in arc quadrupole magnets ≥ 400 T/m.
- Geometrical field quality satisfying the field error table. Field quality deterioration due to the iron saturation effect is $< 10^{-4}$ within operating cycle.
- Horizontal or vertical beam orientation.
- Coil aperture ≥ 40 mm, sufficient for installation of the beam screen.
- Operating temperature range 4.5-5.5 K.
- Sufficient critical current and critical temperature margin for a reliable operation under high heat load from synchrotron radiation. The non-copper critical current were assumed 2000 A/mm^2 and 3000 A/mm^2 at 12 T and 4.2 K, achieved in the short and long terms correspondingly [93].

In order to determine the optimum arc dipole and quadrupole magnet designs, several different approaches, based on either horizontal or vertical bore separations with "cold" and "warm" iron yokes were studied. The shell type dipole magnets were based on the optimized (Chapter 1) coils, with minor changes in the geometry when it was necessary. All quadrupole magnets were based on the same coil geometry described in Chapter 1.

Results of the parametric study, described in Chapter 2, allowed determining general rules of building the magnet geometry. Final optimization required a significant amount of time and computing recourses was done separately for every particular design.

3.2 Optimization of the Fermilab shell type dipole model

As the first step of the high field Nb_3Sn magnet R&D program at Fermilab, building of short (1 m long) shell type dipole models with single aperture was considered. There were performed conceptual design study [42], [44], analysis of manufacturing technology [94], [95] and final design optimization [96] for these magnets. The single aperture magnets were based on

analytically optimized coil cross-section with 43.5 mm bore diameter, containing the cable with copper to non-copper ratio of 0.85. The yoke inner radius, used during coil optimization was 60 mm.

The mechanical support structure consisted of two vertically split iron parts, locked by aluminum clamps and prestressed by the weld-shrinkage of the stainless-steel skin/helium vessel. Two 8 mm thick aluminum spacers filled the space between the coil and yoke and protected coils from damage during assembly [94]. The yoke outer radius was fixed at 200 mm in order to take advantage of available assembly equipment. It allowed speeding up the manufacturing process, while having the yoke size close to the optimum (Chapter 2).

Figure 3.2.1 shows the optimized magnetic system with the flux lines and flux density plot at 11 T bore field, containing all the technological cutouts and the "cold" block mechanical structure. One can see that the field reaches 4.8 T in the iron yoke near pole area, which is far above the iron saturation threshold. Thus the holes, places at ~ 30 degrees from the midplane were used for correction of sextupole component [96]. Figure 3.2.2 presents the sextupole deviations with and without correction as functions of the bore field. The sextupole has relatively large deviations within 0-12 T region that may be corrected by increasing of the yoke outer radius.

The magnet quench field was determined for a short sample limit of the relevant virgin strand, measured at Fermilab Short Sample Test Facility [97]. Figure 3.2.3 shows a set of the measured short sample limits and the magnet load line in units of current density and peak field. Points of intersection between the short sample limits and the magnet load line give the quench field (in the coil), reachable for the given superconductor parameters. It can be conveniently represented in terms of the magnet bore field as a function of the critical current in non-copper at the reference field and temperature (Figure 3.2.4). Thus, for the expected critical current density of 1800 A/mm^2 at 12 T and 4.2 K one obtains 11.7 T bore field. Cabling and bending degradation would reduce the critical current density by 10-15 % and consequently the bore field to 11.4 T.

Figures 3.2.5-3.2.6 illustrate the magnet transfer function, cable current and stored energy, inductance as functions of the bore field. The quench current, determined for 11.4 T bore field is 20.5 kA and the transfer function is 0.55 T/kA. The strong iron saturation effect results in non-linearity of all the magnet parameters that is especially noticeable in inductance, changing from 1.49 mH/m at low field to 1.30 mH/m at the maximum field, or by 15 %.

Component: |B|, T
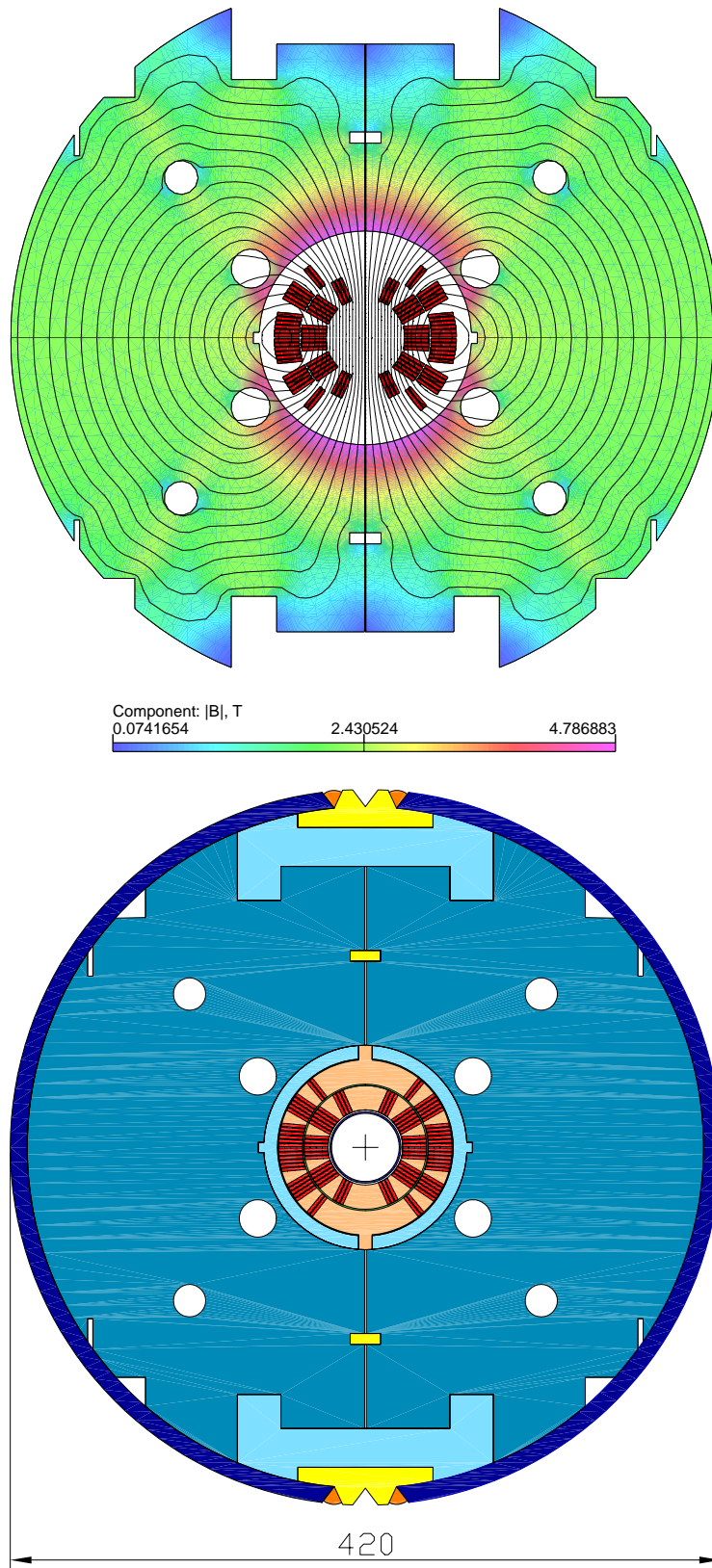0.0741654   2.430524   4.786883

420

Figure 3.2.1. Flux distribution (top) and mechanical structure (bottom) of the single aperture dipole magnet.
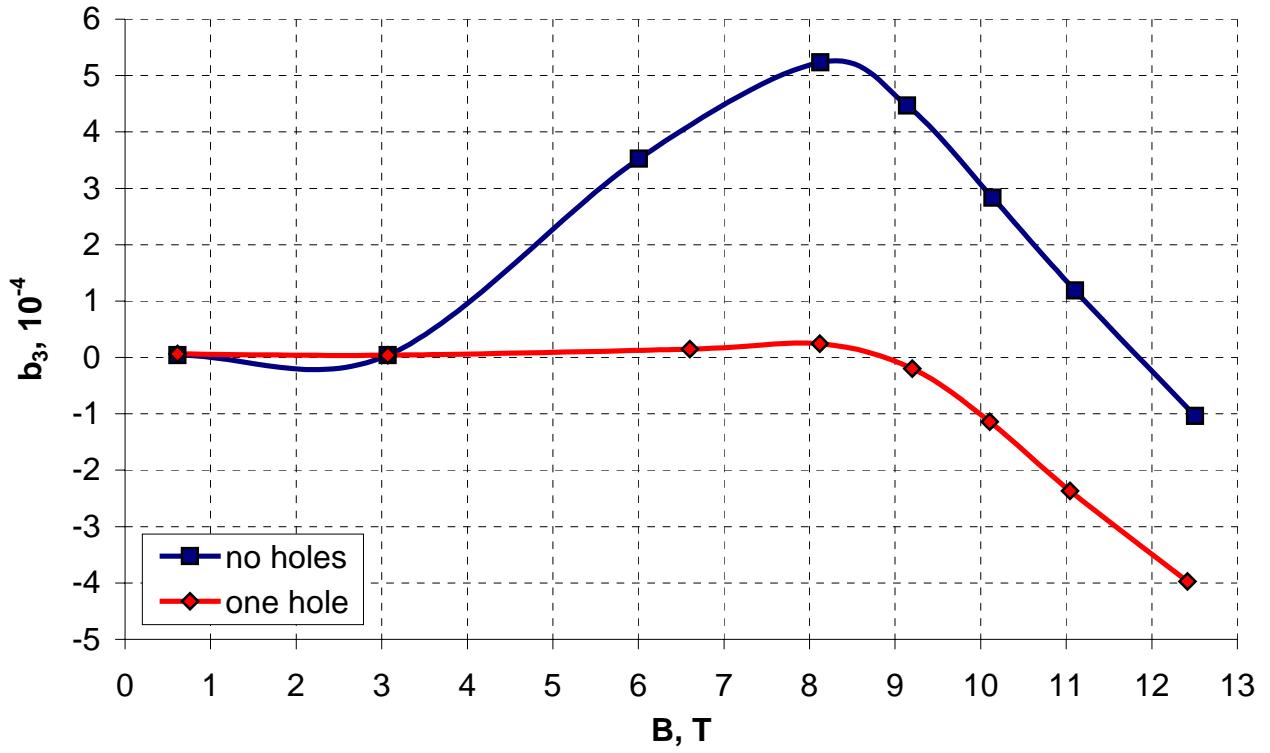
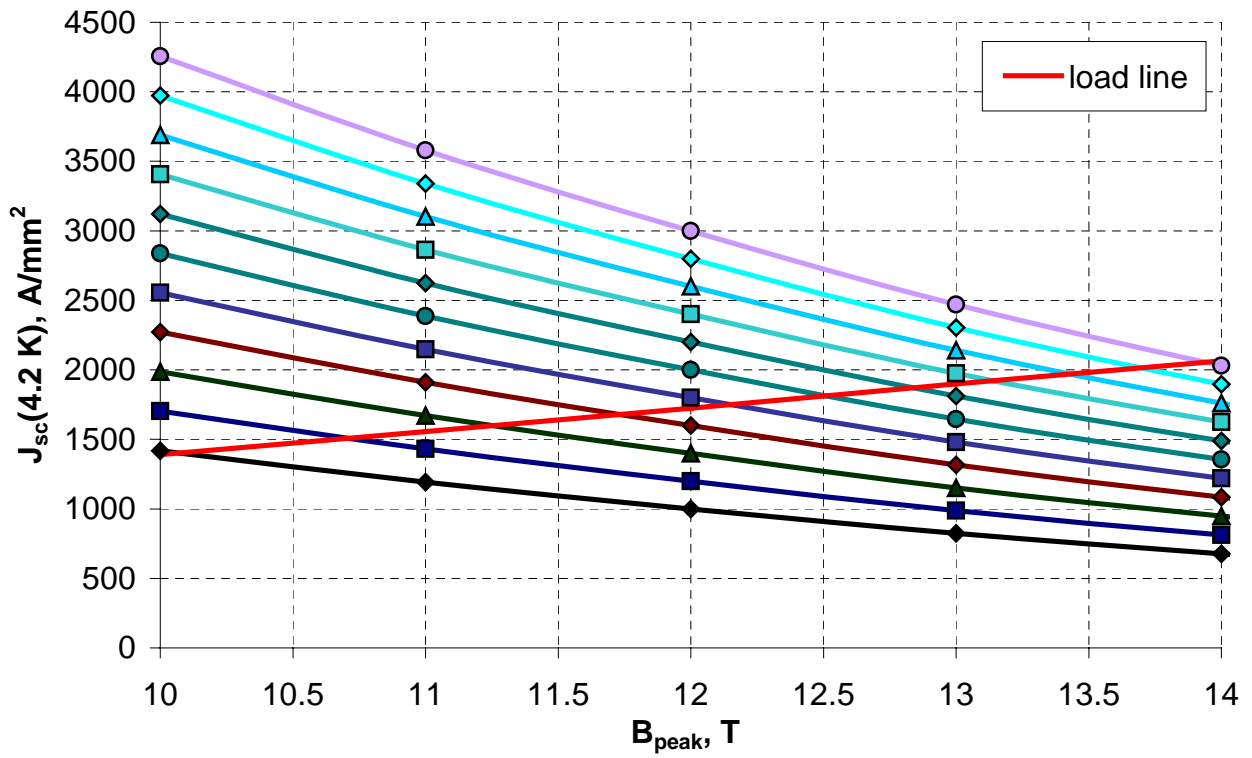Figure 3.2.2. Sextupole components as functions of the bore field.

Figure 3.2.3. Short sample limits and magnet load line as functions of the peak field.
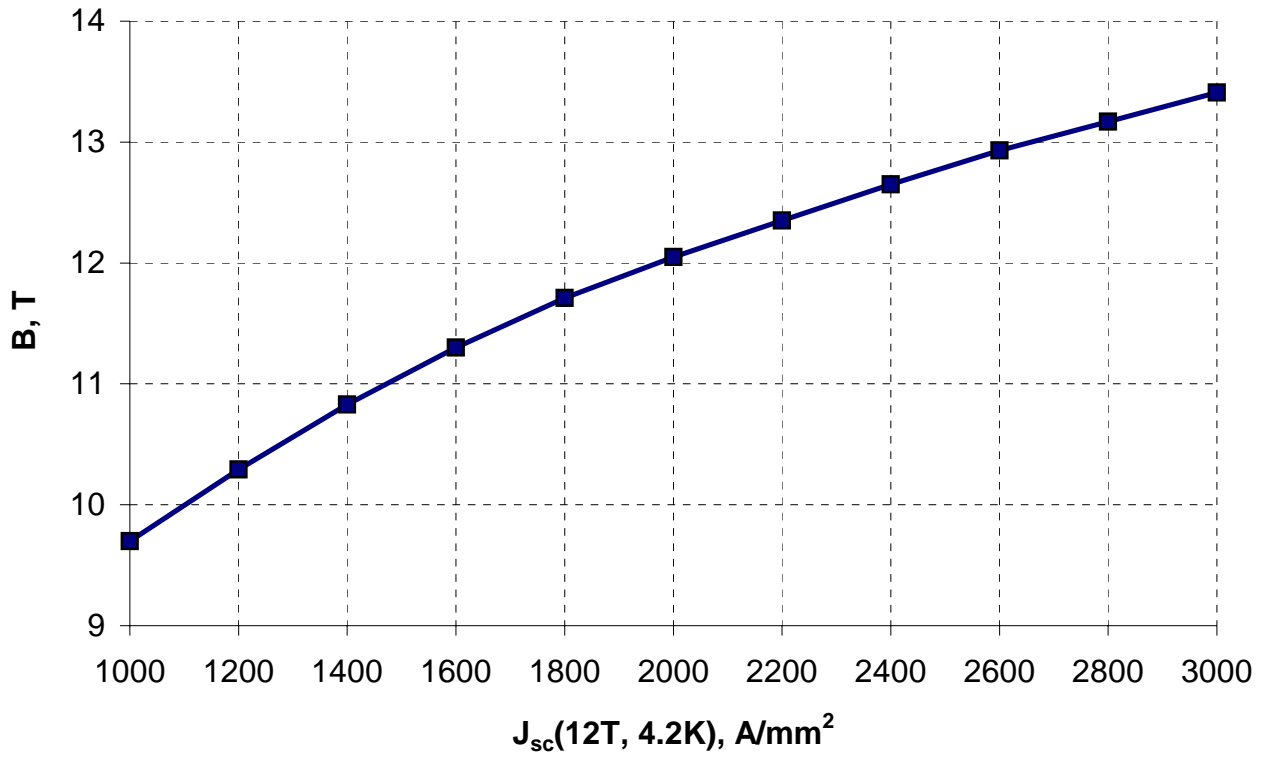
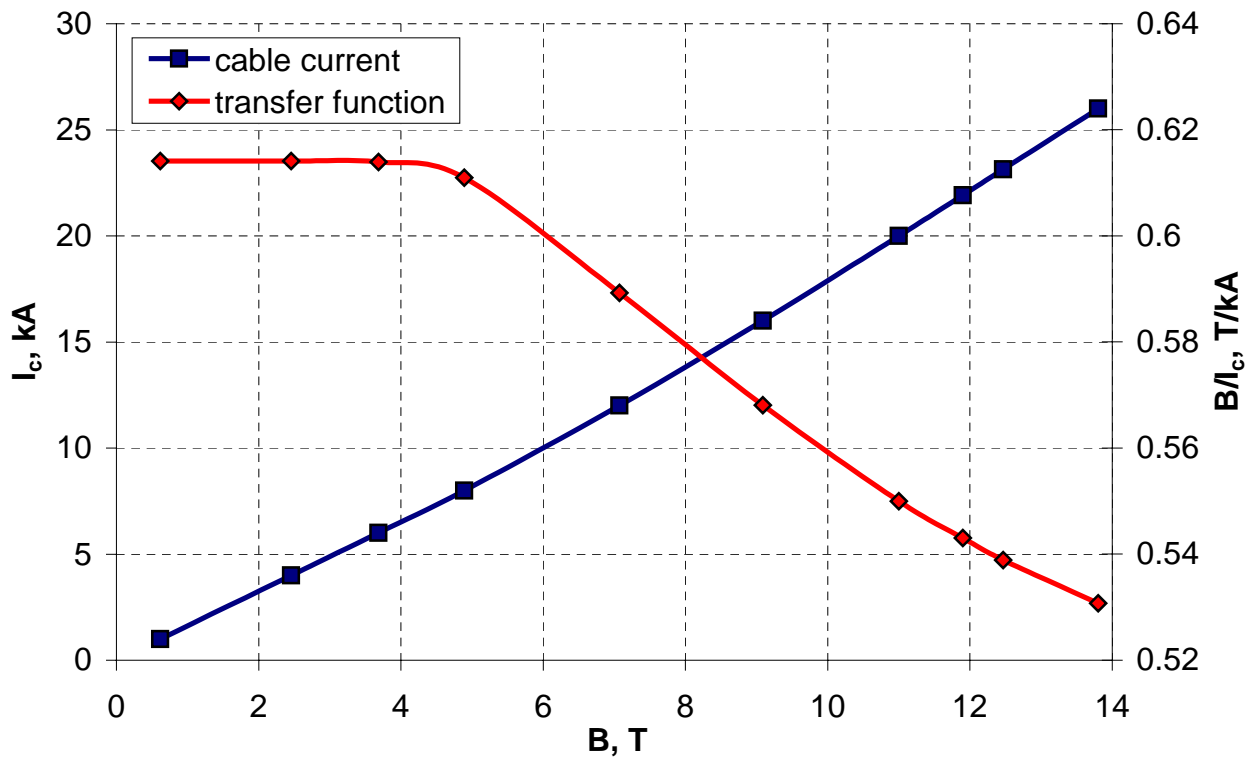Figure 3.2.4. Magnet bore field as a function of the critical current density.

Figure 3.2.5. Cable current and transfer function as functions of the bore field.
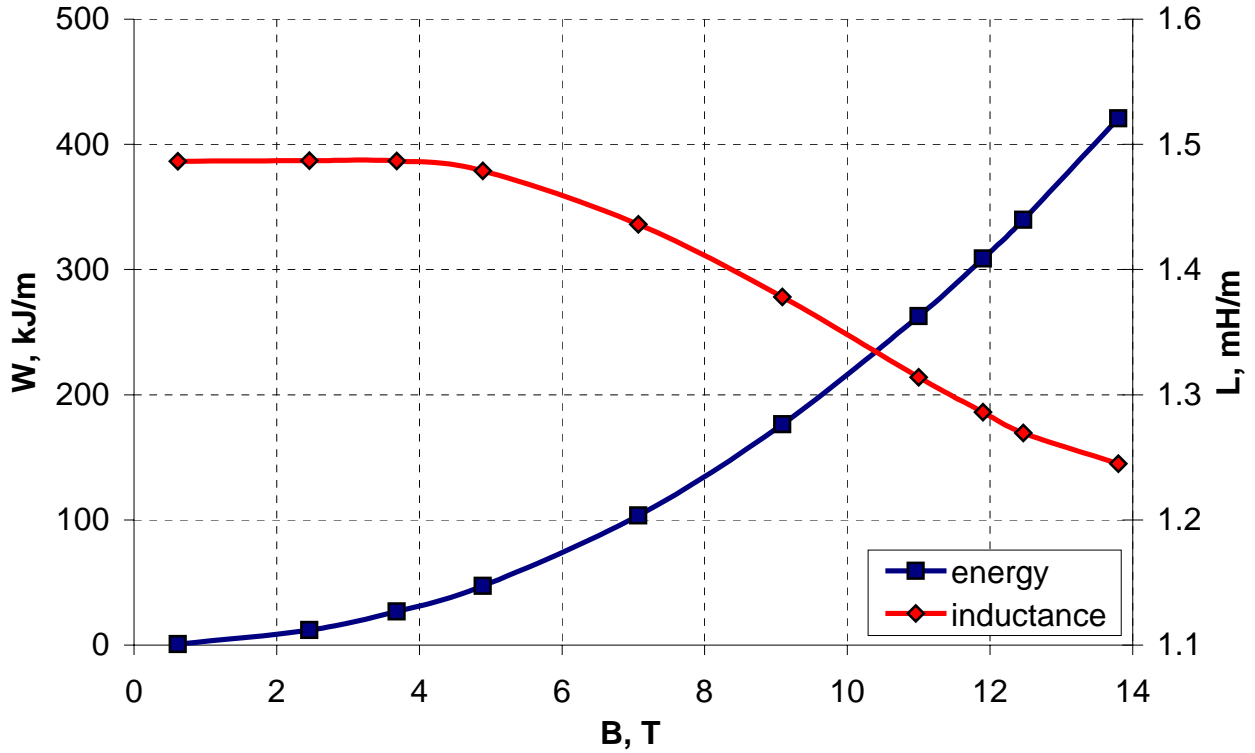
Figure 3.2.6. Stored energy and inductance as functions of the bore field.

3.3 Optimization of double aperture dipole magnets with horizontal bore arrangement

Double aperture dipole magnets are considered as the only option for VLHC [10] due to the space savings, reduction of installation and alignment procedures and the overall magnet cost. Several different designs, depending on the accelerator lattice requirements, utilizing "cold", "warm" or "split" iron yokes have been optimized in order to reach the specified parameters.

3.3.1 "Cold" yoke design

Magnets with "cold" yoke design have the iron yoke placed inside the cryostat at a small distance from the coil. The peculiarity of dipole magnet with horizontal bore separation imposes the optimum bore separation within 160-200 mm (Chapter 2). Larger distances would simplify accommodation of the beam instrumentation (such as the beam position monitors), when smaller ones are preferable for an easier beam shuffling. Thus, the bore separation distance was chosen in the middle of the optimum range at 180 mm, which is close to the bore separation distance of LHC (190 mm), proven to be reliable.

Mechanical considerations require the vertically split yoke with a permanently open gap during the magnet assembly and operation [95]. Since the gap should pass through both apertures to allow assembly of the coils within one yoke - the yoke has to be split into three parts. The gap variations under electromagnetic forces would cause redistribution of the magnetic flux and deviations in the field multipoles. However, making the split parallel to a flux line can significantly reduce this effect [98]. In this case, the small gap variations do not change the flux map and thus do not affect the field quality.

Figure 3.3.1 illustrates how the split may look like in the double aperture dipole with the horizontal bore separation. In this configuration, the gap crosses only some small number of the flux lines. Making the split parallel to the flux line, going to the infinity (which cuts the yoke at ~70 degrees from the midplane) would eliminate this problem, but complicate the magnet mechanical structure, since two gaps of complicated shape have to be controlled simultaneously.
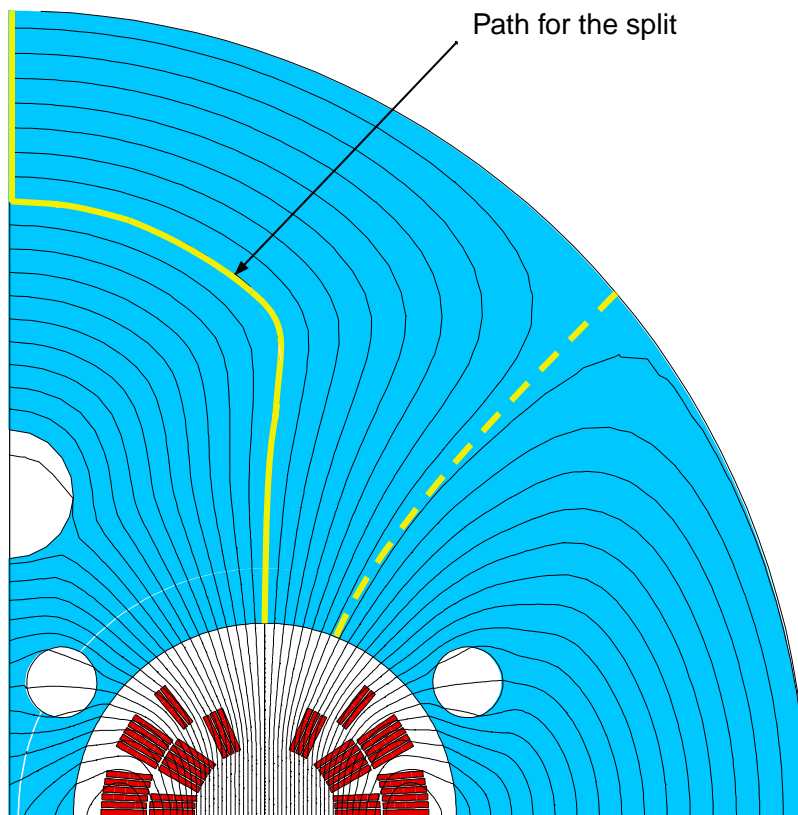

Figure 3.3.1. Iron yoke split partially parallel to a flux line.

The case shown in Figure 3.3.1 is more preferable, since it needs controlling of only one vertical gap. It can be accomplished in the way similar to the single bore dipole magnet by means of two clamps. In addition, the split geometry can be quite well approximated by three straight lines and two arcs that simplify the yoke manufacturing and quality control.

99

The iron yoke with 0.5 mm gap per aperture was optimized for the best field quality [96]. Figure 3.3.2 shows the optimum yoke with the outer radius of 260 mm and 2.5 holes per quadrant used for correction of the sextupole and quadrupole components (bore field is 11 T) and the "cold" block mechanical structure. It was possible to restrict the low order multipole deviations within +/- 0.5 units for 0-11 T field range [99], shown in Figure 3.3.3 (the curves can be shifted vertically by adjusting the coil geometry).

Figure 3.3.4 presents the quench field dependence on the critical current density for two copper to non-copper ratios: 0.85 that will be used for the short R&D model and 1.2 that is required for the long magnet quench protection [100], [101]. One can notice that quench performance of the R&D magnet is identical to the single bore magnet, when the long magnet quench performance is 0.6 T below. However, the expected long term grows of the critical current density to 3000 A/mm^2 would allow reaching the field of 12.0 T with 10 % degradation and 10 % safety margin. Figures 3.3.5-3.3.6 show the load and energy-related parameters per one aperture, which are essentially the same as for the single aperture dipole.

The effect of gap variation in the described geometry was studied by moving the outer part of the yoke with respect to the central part [98]. Figures 3.3.7 shows deviations of the quadrupole and sextupole components during the gap variation. The curves are linear that is obvious for the small gap variations, when the flux distribution virtually does not change. It is convenient to represent the field sensitivity to the gap variation in terms of constant derivatives: $\Delta b_2/\Delta gap = -0.36 \cdot 10^{-4}$ 1/mm and $\Delta b_3/\Delta gap = 0.21 \cdot 10^{-4}$ 1/mm. These values are small with respect to the yoke saturation effect. Thus the gap increase by ~0.3 mm during the field ramp from 0 to 12 T [102], estimated by the mechanical analysis, would change the quadrupole and sextupole components by only $-0.1 \cdot 10^{-4}$ and $0.06 \cdot 10^{-4}$ respectively.

Conceptual design of the mechanical support structure has been analyzed and developed [103]. According to the design, both the clamps and the skin provide the necessary prestress to the coils, while the vertical gap is open at all stages of the magnet operation. This design concept is similar to the single bore design, described in previous paragraph. The analysis demonstrated that the stress level in the coil assembly is less than 150 MPa threshold of irreversible critical current degradation and the peak equivalent stress in the support structure components is within their elastic limits.
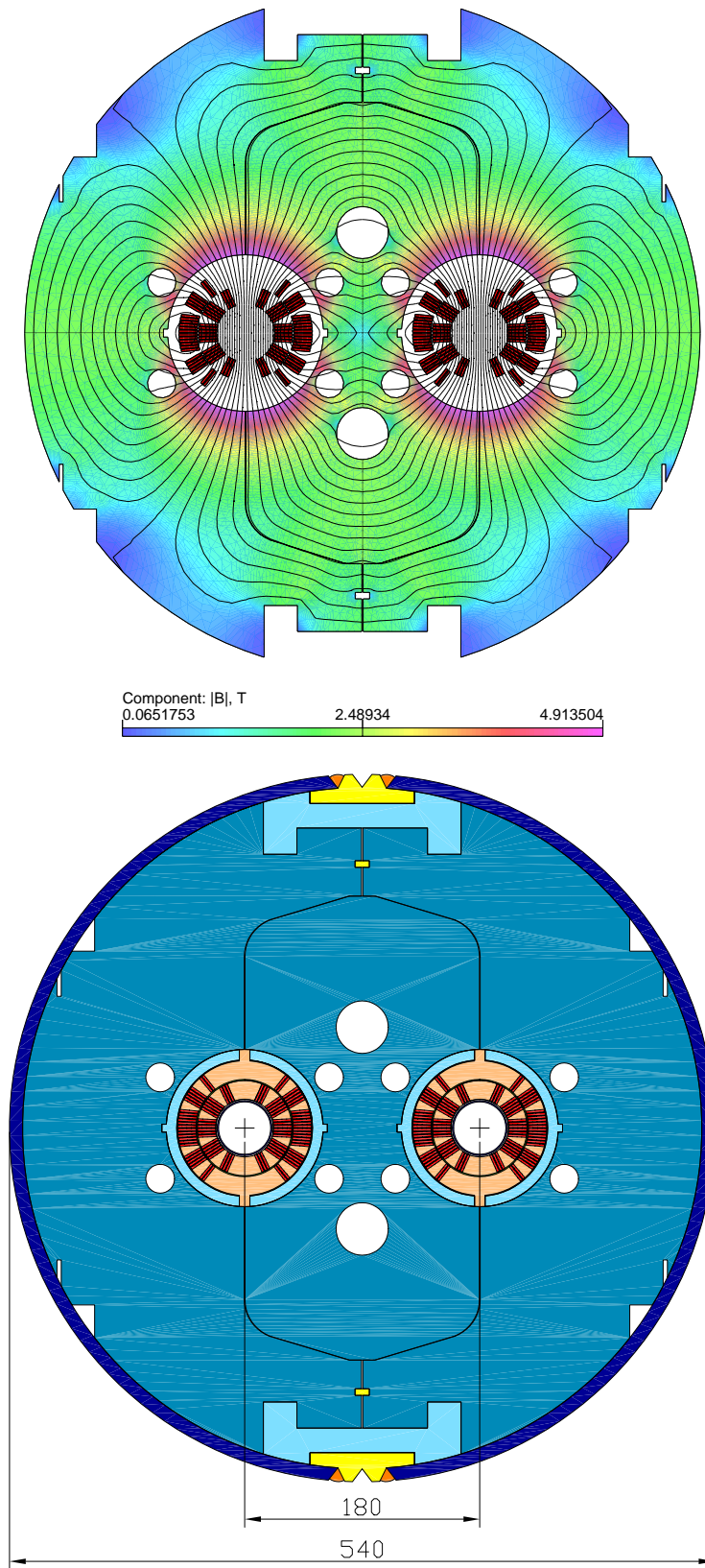
Component: |B|, T
0.0651753   2.48934   4.913504

180
540

Figure 3.3.2. Flux distribution (top) and mechanical structure (bottom) of the double aperture dipole magnet with "cold" iron yoke.
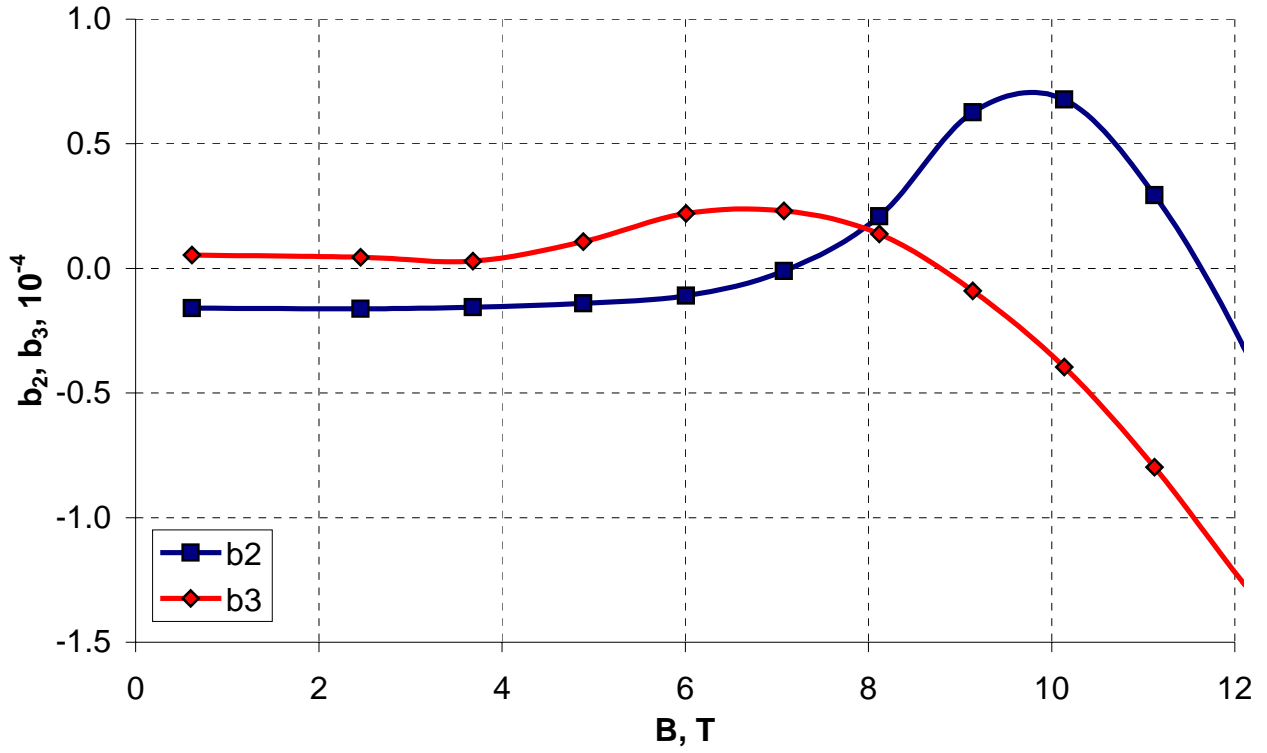
Figure 3.3.3. Quadrupole and sextupole deviations as functions of the bore field.
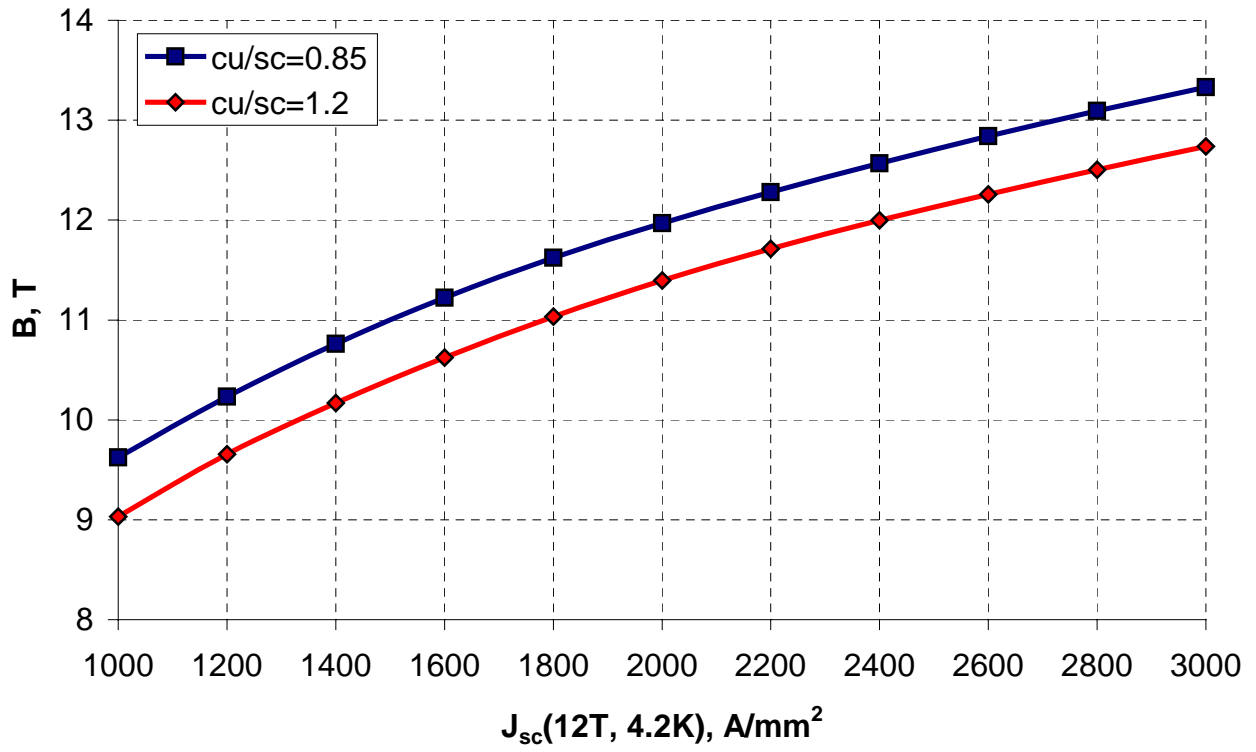

Figure 3.3.4. Quench field as a function of the critical current density.
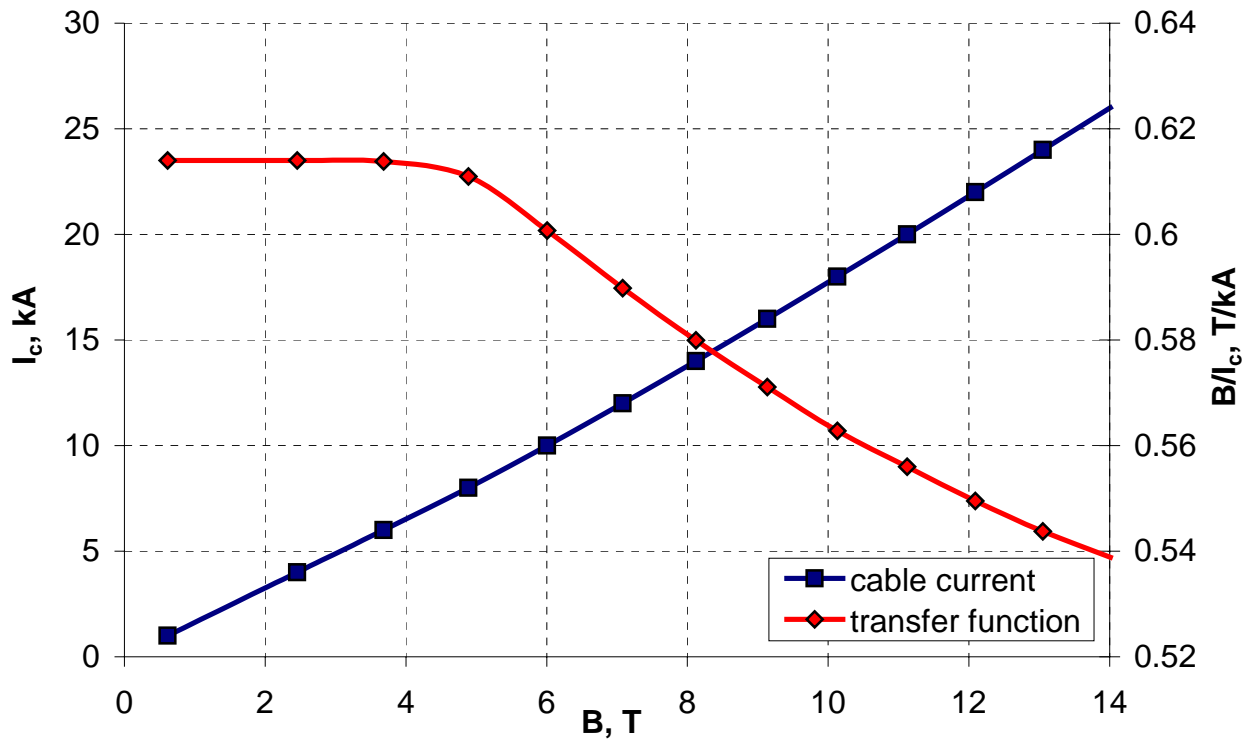
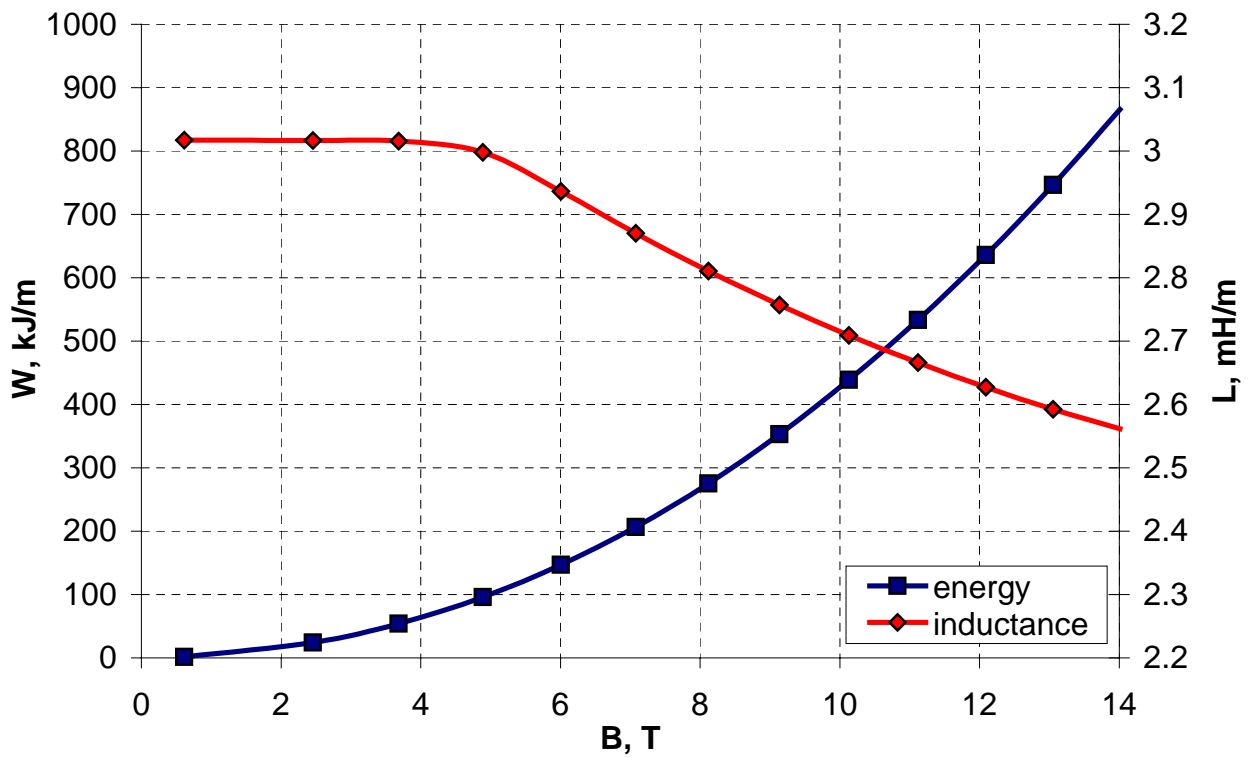Figure 3.3.5. Magnet current and transfer function as functions of the bore field.

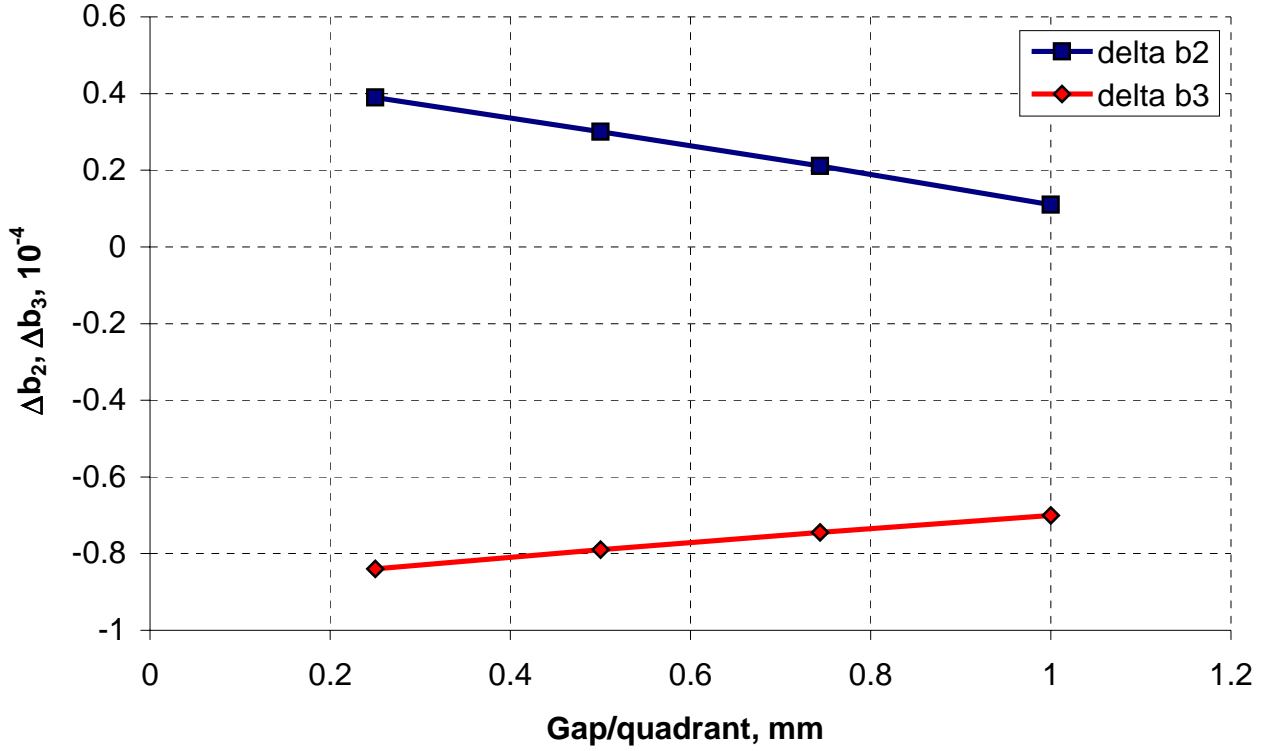Figure 3.3.6. Stored energy and inductance as functions of the bore field.

Figure 3.3.7. Quadrupole and sextupole components as functions of the gap thickness.

3.3.2 "Warm" yoke design

The first superconducting accelerator magnets built for the large-scale application (Tevatron) utilized the "warm" yoke design concept. According to this concept, the coil is prestressed at a room temperature and constrained against electromagnetic forces by means of non-magnetic collars of necessary thickness. The iron yoke is removed from the coil assembly by the thermal insulation width and is in direct contact with outside air. Advantage of this concept is in relatively small iron saturation effect due to a significant coil to yoke distance and small cold mass dimensions that reduces the refrigeration power, necessary to cool the magnet and keep it at low temperature. However, the coil block must be well centered within the yoke to avoid large eccentricity forces and field distortions, which was accomplished in Tevatron by means of "smart" bolts [5].

The double aperture magnet concept with the "warm" iron yoke can be of direct interest for VLHC, due to the mentioned advantages. Thus, it was analytically and numerically analyzed and optimized in order to meet the specifications.

First, the study of the yoke saturation effect versus the yoke design parameters was performed [104]. Figure 3.3.8 shows the finite-element model used in this study. The bore separation

distance was fixed at the same 180 mm value as for the double bore magnet considered in previous paragraph. The yoke inner and outer radii were varied within reasonable limits.

Figures 3.3.9 presents quadrupole and sextupole deviations coming from the iron saturation effect (a constant geometrical component due to the mutual influence of the coils was subtracted) for different yoke inner radii within 0-11 T field range. The yoke outer radius was fixed at the high enough value (~1m) so it would not have any effect on the field quality. Large distance from the yoke to the coil bore does not give the opportunity of correction the yoke saturation effect by the hole technique, as the holes would have an enormous size. Therefore, this problem must be entirely solved by optimizing the yoke inner and outer radii. The maximum multipole deviations of 10^{-4} correspond to the yoke inner radius of about 182 mm. The distance between coil and yoke surfaces in the horizontal plane in this case is about 40 mm that seems hardly enough to accommodate the coil support structure and the cryostat.

Thus the inner yoke radius was fixed at 250 mm that lefts the minimum free space of 110 mm, in the assumption that 30-40 mm of the space is used for the coils support structure and remaining for the cryostat. Figures 3.3.10-3.3.11 show the multipole deviations within 0-11 T field cycle, coming from the yoke saturation effect, maximum fringe field at 1 cm from the outer yoke surface (at 11 T) and the yoke cross-section area. The maximum multipole deviations of 10^{-4} correspond to the yoke outer radius of 288 mm. The maximum fringe field outside such yoke is about 50 mT that is generally acceptable without further reduction. Thus, the inner and outer yoke radii of this magnet were fixed at 250 mm and 290 mm for the following optimization.
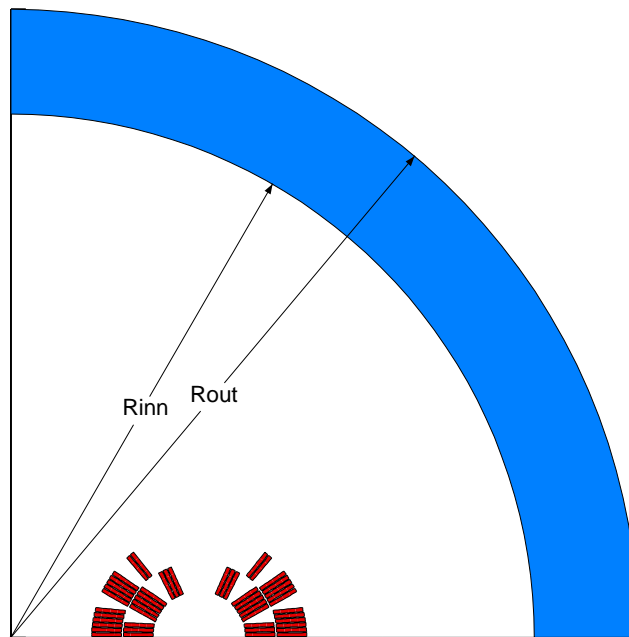

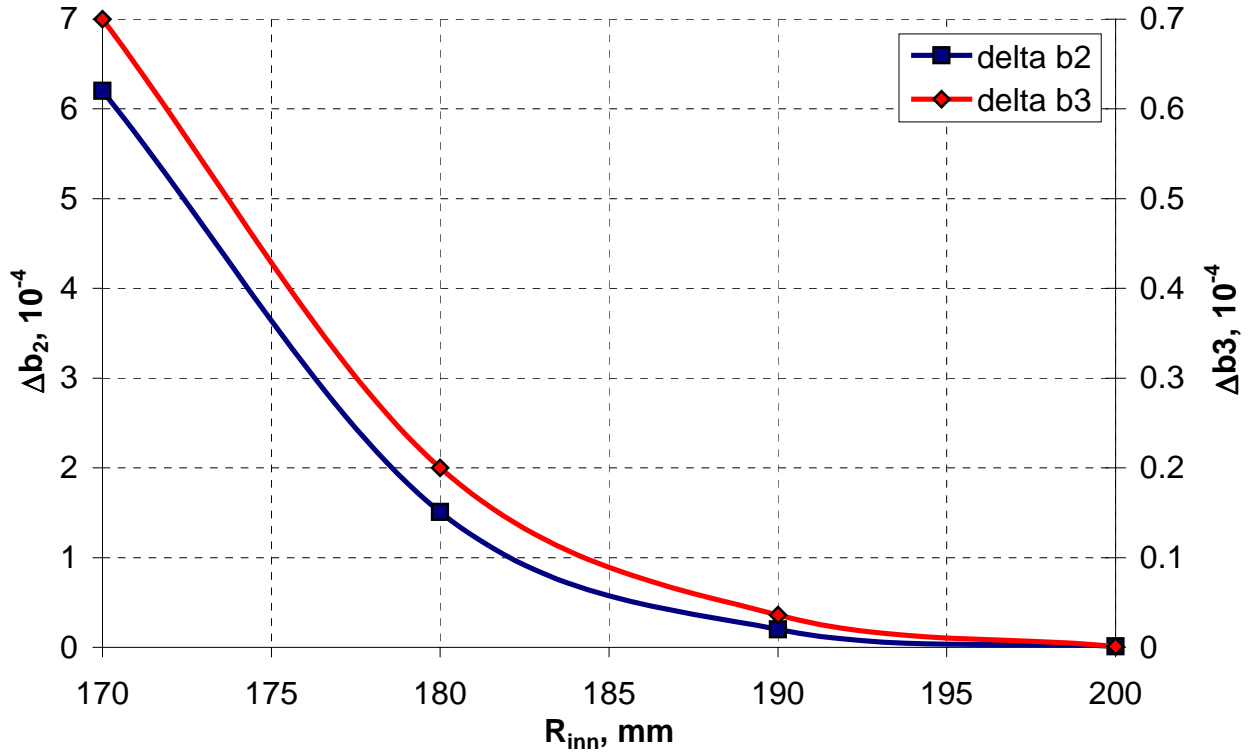Figure 3.3.8. The model for study of the yoke design parameters.

Figure 3.3.9. Multipole deviations as functions of the yoke inner radius.

Left-right asymmetry in the considered magnet leads to unallowed by the dipole symmetry geometrical multipole errors (iron does not screen coils from each other as in the "cold" yoke design). These errors are quite large – about $30 \cdot 10^{-4}$ for the quadrupole component that must be eliminated by optimization of the coil geometry. Obviously, such coils must have the corresponding left-right asymmetry in order to correct the field. Figure 3.3.12 presents the coil with the bore diameter of 43.5 mm being optimized for the minimum geometrical field errors by ROXIE code in the double aperture configuration with the bore separation distance of 180 mm and the yoke inner radius of 250 mm. Table 3.3.1 summarizes the geometrical multipoles.

Breaking of the left-right symmetry allows all the normal in the field distribution. However, it was possible to significantly reduce even harmonics by introduction a small (within +/-1 mm) asymmetry into three blocks per quadrant, keeping the number of blocks and turns per block equal to the symmetric coil design [105]. Such coils were used for the final finite-element simulation to obtain all the essential magnet parameters.

Figure 3.3.13 presents the magnet cross-section with the flux distribution at 11 T bore field and the magnet mechanical structure. Maximum field in the yoke is around 2 T that does not create the saturation problems. Figure 3.3.14 confirms it numerically for the quadrupole and sextupole deviations. The quadrupole deviation is within $0.8 \cdot 10^{-4}$ and the sextupole is close to zero.
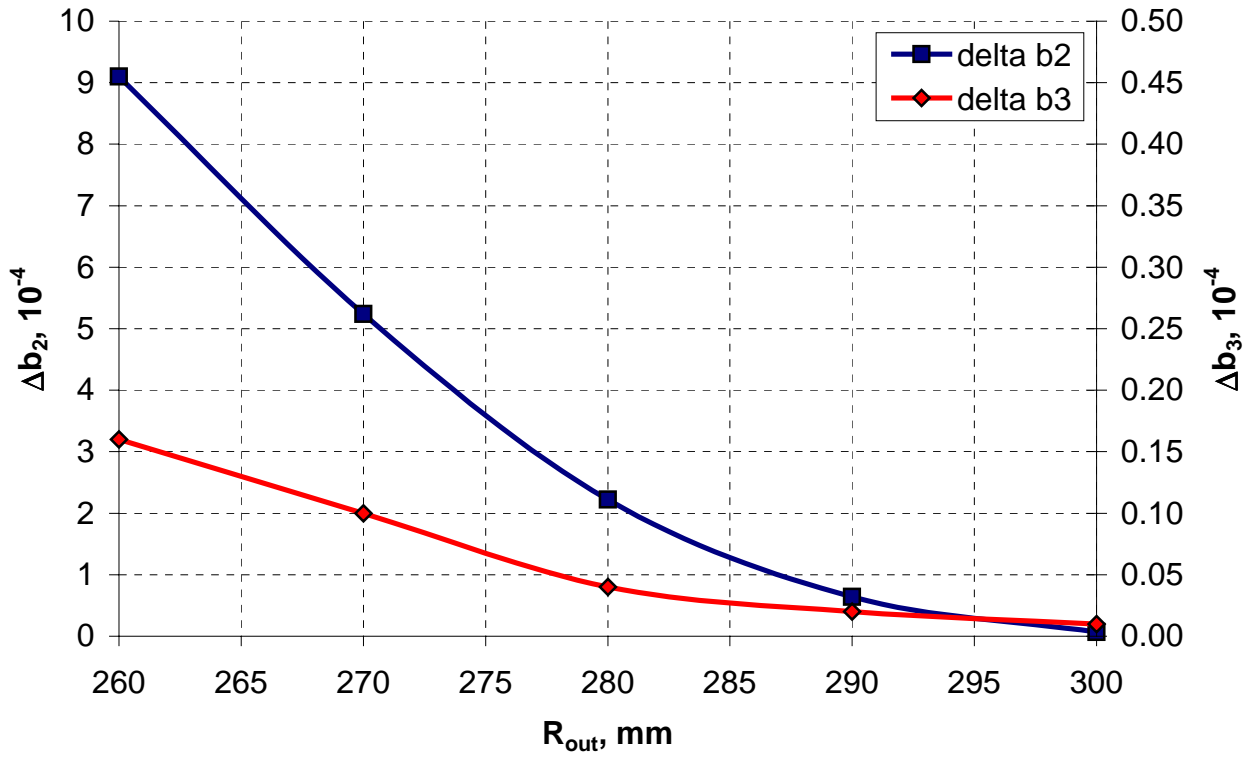
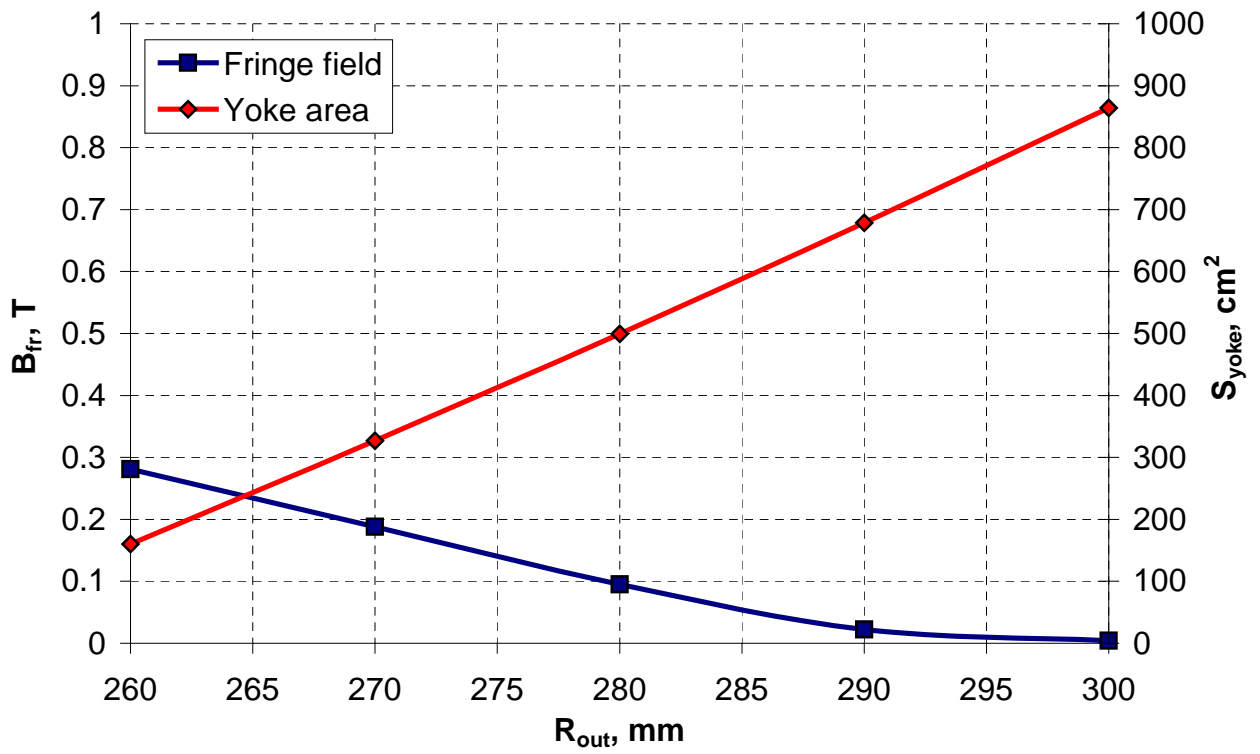Figure 3.3.10. Multipole deviations as functions of the yoke outer radius.

Figure 3.3.11. Fringe field and yoke area as functions of the yoke outer radius.
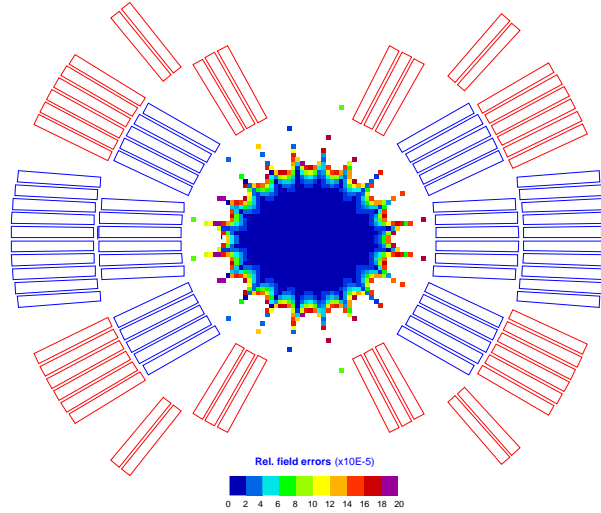
Figure 3.3.12. Asymmetric shell type coil (magnet center is at the left).

Table 3.3.1. Geometrical harmonics in 10^{-4} for the asymmetric coil design.

b_2	b_3	b_4	b_5	b_6	b_7	b_8	b_9	b_{10}	b_{11}
0.000	0.000	0.000	0.001	-0.012	-0.011	0.031	-0.130	-0.011	0.129

Figure 3.3.15 shows the quench field as a function of the critical current density for two copper to non-copper ratios. It is by 6 % smaller than in the magnet with "cold" iron yoke, which is the price of the "warm" yoke. However, this is not a big price for a factor of two smaller magnet size and at least factor of 3 smaller weight of the "warm" yoke magnet.

The magnet load line and transfer function are shown in Figure 3.3.16. One can see that virtual absence of the yoke saturation effect makes them close to linear. The current in this magnet must be 17 % higher with respect to the "cold" yoke design to reach 12 T field, nevertheless it is not a limiting factor for the magnet design. The stored energy is close to one in the "cold" yoke magnet and inductance is by 23 % smaller at 12 T field, which is beneficial for the voltage reduction during quench (Figure 3.3.17).

Analysis of the mechanical structure was performed for the optimized coil and yoke configurations [103]. It suggested that both coils were assembled within common aluminum or stainless steel structure, constraining the electromagnetic forces during energizing. In order to compensate for the differential thermal contraction, Nitronic 40 inserts used in the center [106]. Coil prestress at a room temperature is provided by means of the pressure bladders [107] and keys between the Nitronic 40 inserts. The stainless steel skin, simultaneously serving as a helium vessel, is covered by several layers of Mylar thermal insulation. The "cold" block was suspended within the "warm" yoke by the G10 "spiders".

Component: |B|, T
0.106199   1.079035   2.051872
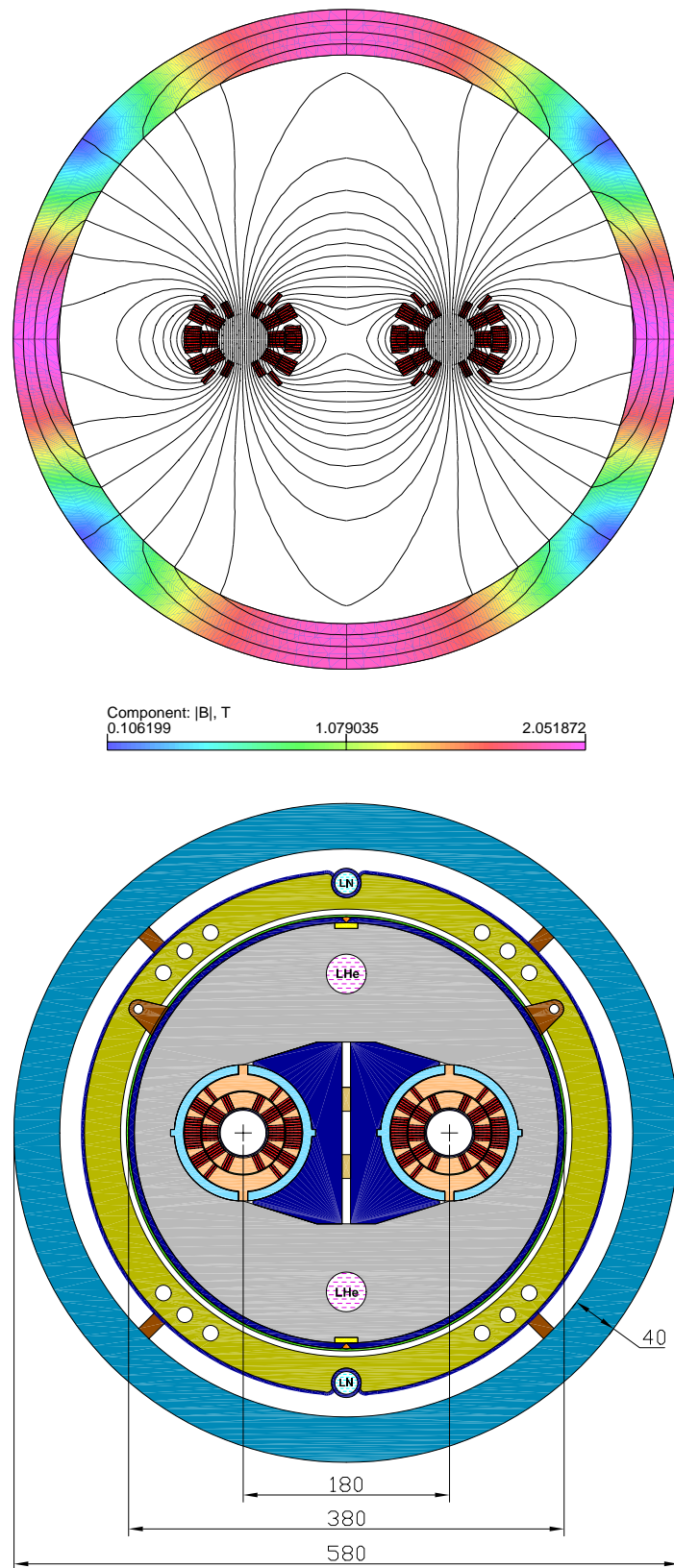
Figure 3.3.13. Flux distribution (top) and mechanical structure (bottom) of the double aperture dipole magnet with "warm" iron yoke.
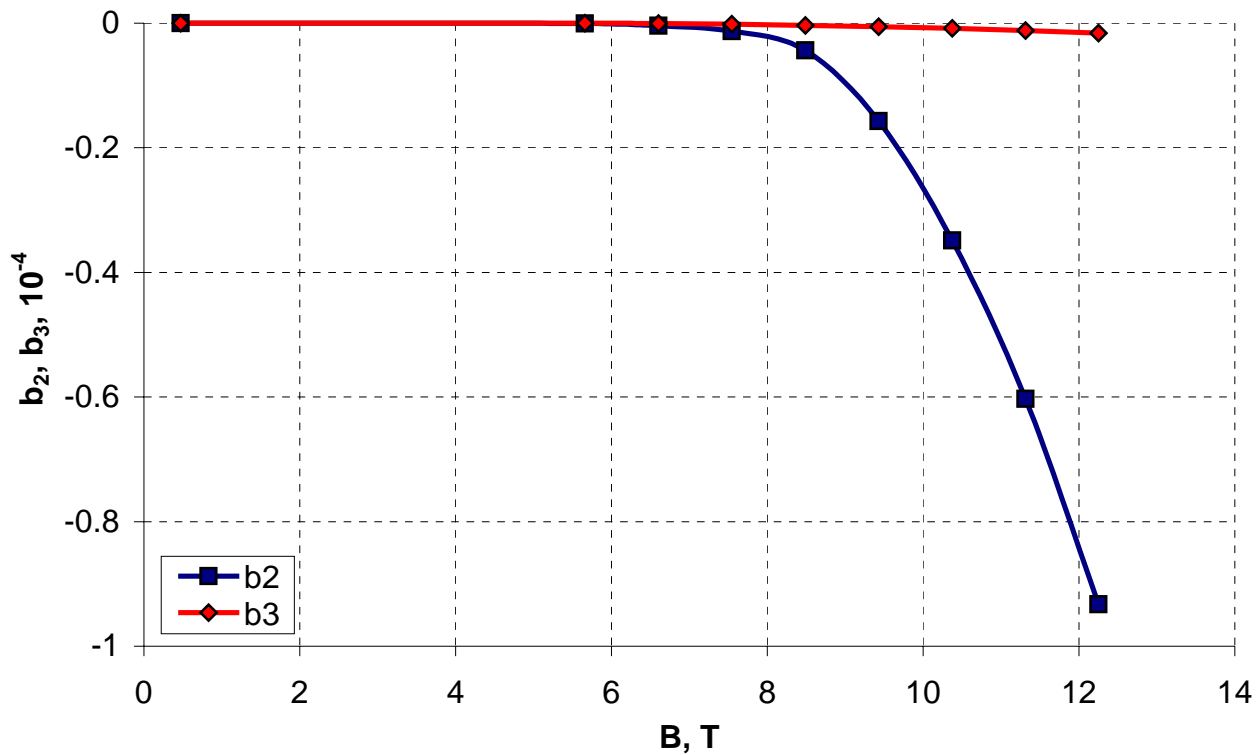
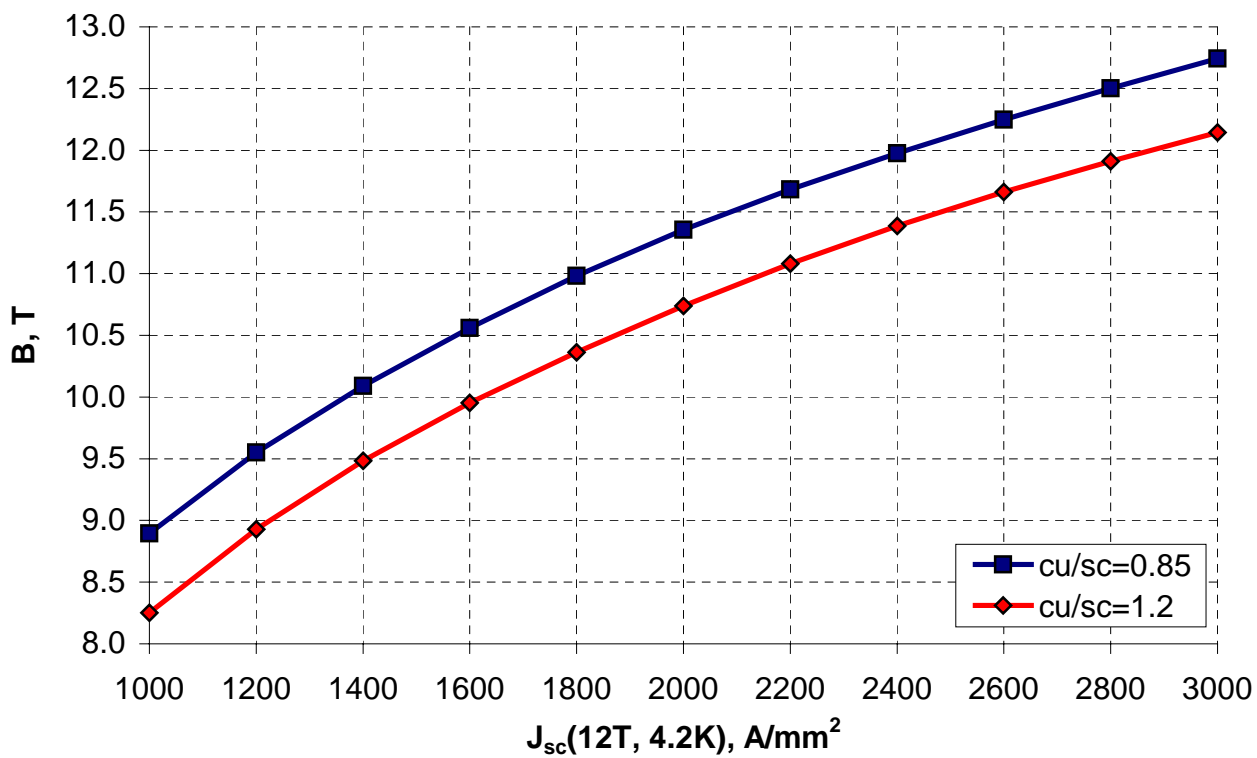Figure 3.3.14. Quadrupole and sextupole components as functions of bore field.

Figure 3.3.15. Quench field as a function of SC critical current density.
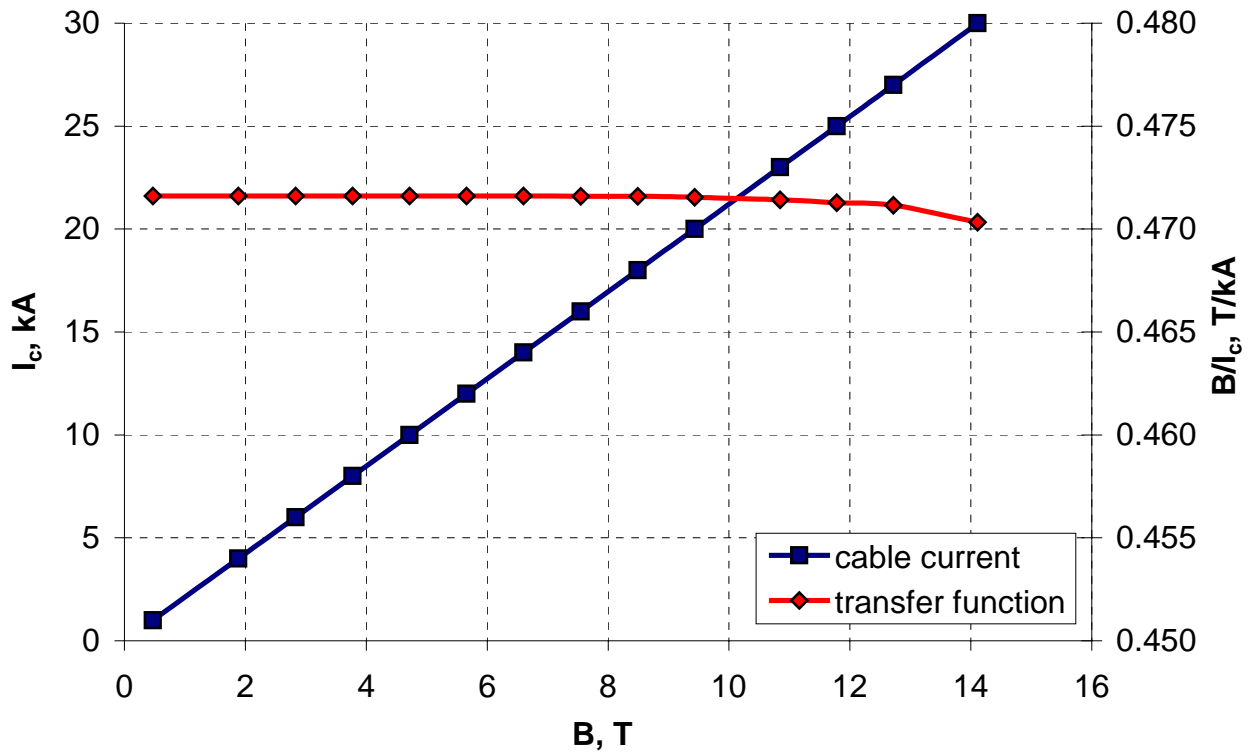
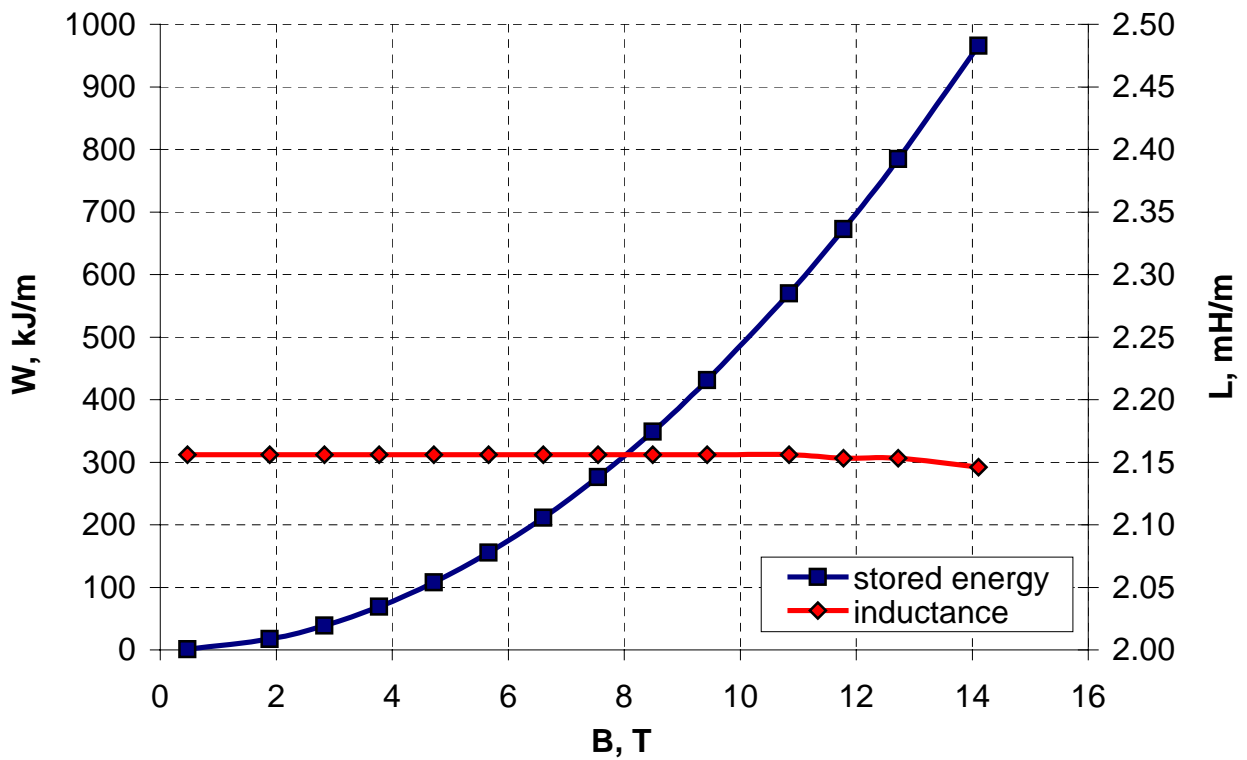Figure 3.3.16. Cable current and transfer function as functions of bore field.

Figure 3.3.17. Stored energy and inductance as functions of bore field.

A sensitivity analysis was performed in order to determine tolerances acceptable for centering the "cold" mass within the "warm" iron yoke. Both coils were simultaneously moved from the nominal position in the horizontal and vertical directions. The consequences of these displacements in terms of the field multipoles and force imbalance (vector sum of all electromagnetic forces, acting in the "cold" block) are summarized in Table 3.3.2. The horizontal displacement by 5 mm causes a large horizontal force imbalance, comparable with the "cold" block weight, which required at least 100% safety margin in the support stricture. For the similar vertical displacement the force is by factor of two smaller and acts in the direction of gravitational force that makes it less dangerous. However, the highest multipole deviations occur during the vertical displacements, when the skew dipole reaches $3 \cdot 10^{-4}$. The first allowed multipole for horizontal displacement - quadrupole does not exceed 10^{-4} for 5 mm displacement. The acceptable tolerance on the "cold" block position must presumably be around +/- 1.5 mm, which keeps the force imbalance within ~30 % of the "cold" block weight and the multipole deviations within 10^{-4}.

Table 3.3.2. Forces and multipoles due to eccentricity displacements.

Shifts, mm		Forces, kN/m		Multipole deviations, 10^{-4}				
Δx	Δy	ΣF_x	ΣF_y	Δb_2	Δb_3	Δa_1	Δa_2	Δa_3
5.0	0.0	10.3	0.0	0.7	0.1	-	-	-
0.0	5.0	0.0	5.8	0.0	0.0	3.0	-0.4	0.0

3.4 Optimization of double aperture dipole magnets with vertical bore arrangement

Using of the "flat" beam optics is considered as a possible implementation for VLHC [10]. In terms of the magnet design, it requires the vertical bore arrangement. As shown in Chapter 2, the vertical bore arrangement implies larger optimum bore separation distances in dipole magnets than in case of the horizontal bore arrangement. In addition, the field quality errors induced by the iron saturation are noticeably larger than in a case of the horizontal bore arrangement that forces implementation of larger correcting holes.

3.4.1 Common coil design

The block type coil presented in Chapter 1 was considered in the common-coil geometry. A plane racetrack shape of the coil and an inherently large bore separation distance of the magnet with the vertical bore arrangement makes it attractive to use the "react and wind" technology for the coil production. In order to reduce the bending degradation of the reacted cable made of

strands 0.7 mm in diameter, the minimum bending radius should be 90 mm [47] that automatically determined the bore separation distance of 290 mm [49].

The coils are constrained by the Nitronic 40 collar, serving also as the coil winding structure, allowing simultaneous winding of both single-layer coils. This technology would significantly accelerate the winding process with respect to the traditional techniques. However, such common collar structure requires a mechanical link between collars of two apertures. Therefore, a special cutout in the iron yoke is necessary in order to accommodate the link that generates the top-bottom field asymmetry within each aperture, which must be corrected by the coil geometry. In addition, the mechanical analysis demonstrated the preference of a relatively slim collar structure with a flat collar-iron interface [47] that demanded further coil optimization. It was done by the finite-element code OPERA2D.

Figure 3.4.1 shows the optimized coil cross-section and the yoke geometry and Table 3.4.1 summarizes the geometrical field harmonics. All the harmonics were kept within specification in spite of both normal and skew harmonics are allowed. It was accomplished by introduction of a small top-bottom asymmetry into the coil geometry [49].
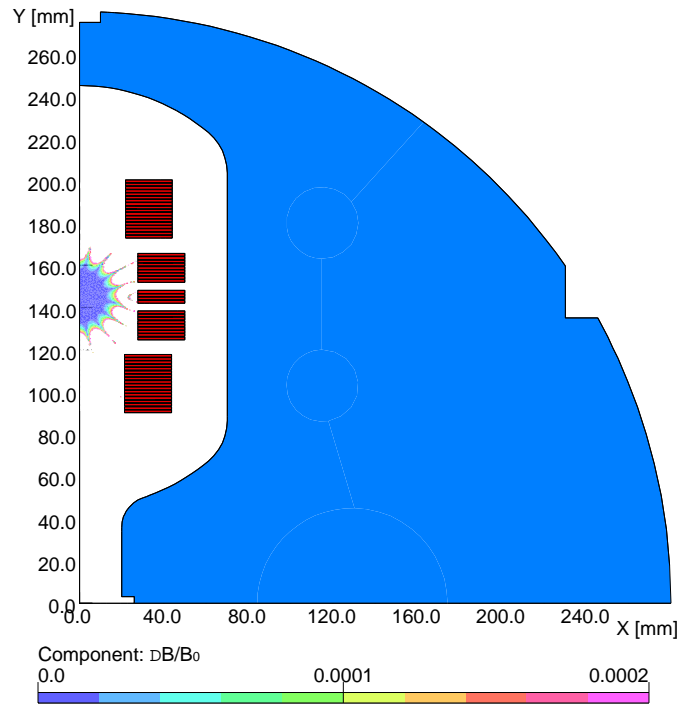

Figure 3.4.1. Asymmetric common coil with the field quality plot.

Table 3.4.1. Geometrical harmonics in 10^{-4} for the asymmetric common coil.

a_2	b_3	a_4	b_5	a_6	b_7	a_8	b_9	a_{10}	b_{11}
-0.006	-0.001	-0.003	0.001	0.000	0.003	0.012	-0.028	0.000	-0.000

In order to correct the iron saturation effect, 2.5 holes per quadrant were introduced into the yoke. Figure 3.4.2 presents the optimized yoke cross-section with the flux distribution and the magnet mechanical structure. The holes next to the coil are primarily used for the sextupole component correction. The flat iron boundary resulted in a more uniform field distribution on the yoke inner surface and smaller yoke saturation effect with respect to the circular yoke case. It allowed moving the sextupole correction holes further away from the yoke surface that reduced mechanical stresses during operation.

However a large top-bottom yoke asymmetry especially enhanced by the central cutout resulted in a big skew quadrupole component caused by the iron saturation, which required using big (90 mm in diameter) correcting holes in the magnet midplane. These holes are aside from the high stresses region and should not create mechanical problems, while providing space for cooling channels and power supply buses. The harmonic deviations due to the yoke saturation presented in Figure 3.4.3 were suppressed to $0.8 \cdot 10^{-4}$.

Figure 3.4.4 presents the quench field as a function of the critical current density at two copper to non-copper ratios, necessary for the quench protection of the short and long magnets [108], [109]. One can see that the field is 14 % smaller than in the shell type magnet with the "cold" iron yoke and 7 % smaller than in the magnet with the "warm" yoke. It is a result of lower efficiency of the block type magnet with respect to the shell type, which was illustrated in Chapter 1 and the negative coupling between two vertically arranged coils.

The large cable cross-section causes the high current and low transfer function, presented in Figure 3.4.5. Thus, the bore field of 11 T corresponds to 26 kA current and the transfer function of 0.423 T/kA.

The large effective coil aperture and vertical coil size lead to a large stored energy (Figure 3.4.6). The stored energy is almost by factor of two larger than in a shell type magnet with "cold" iron yoke. The difference in inductances is not that large (9 %) due to the current higher than in the shell type magnet.

Similarly to the shell type dipole, a "warm" iron yoke can be implemented for the common-coil design. Obviously, it would allow reducing the magnet mass and dimensions. The nominal field however, in such a magnet would be below 10 T due to a lack of the iron contribution and shielding of the second aperture plus the large cable bending degradation inherent to the "react and wind" approach, which would make it of no interest for the VLHC.

Development of the short common coil models at Fermilab, based on the optimized coil and yoke geometry is described in [110]-[112].

Component: |B|, T
0.136151   1.981772   3.827393

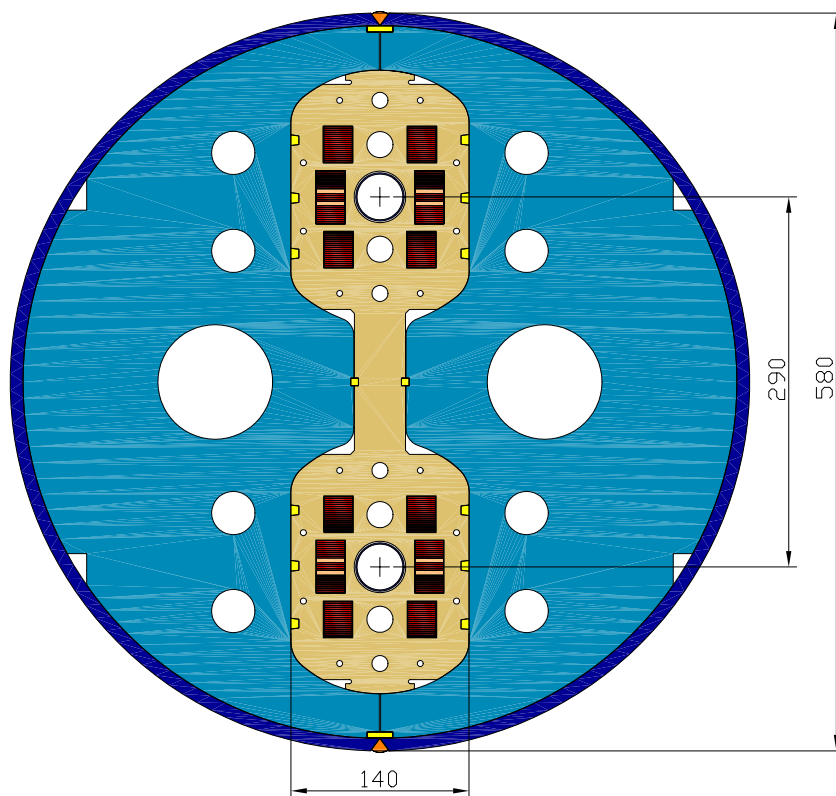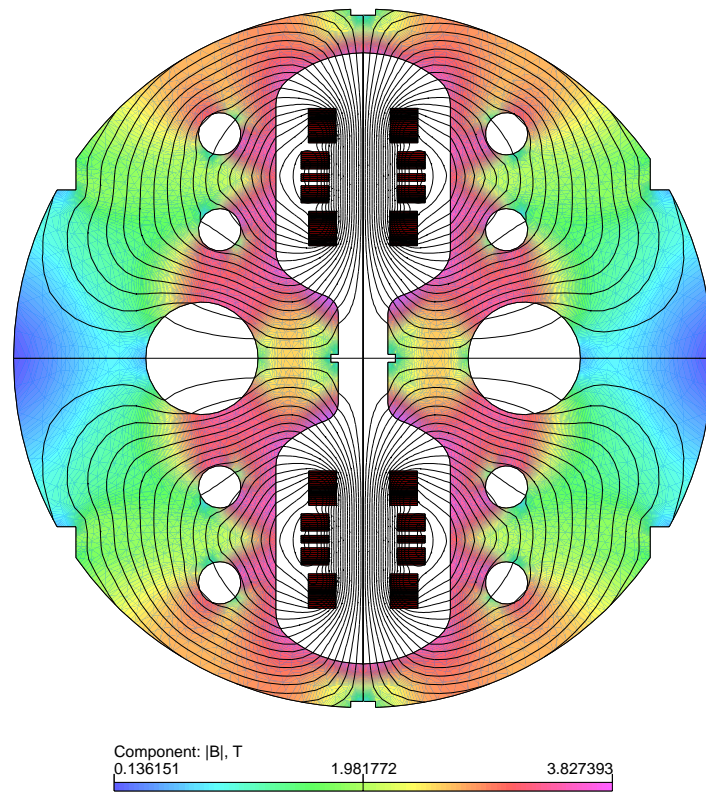Figure 3.4.2. Flux distribution (top) and mechanical structure (bottom) of the common coil magnet.
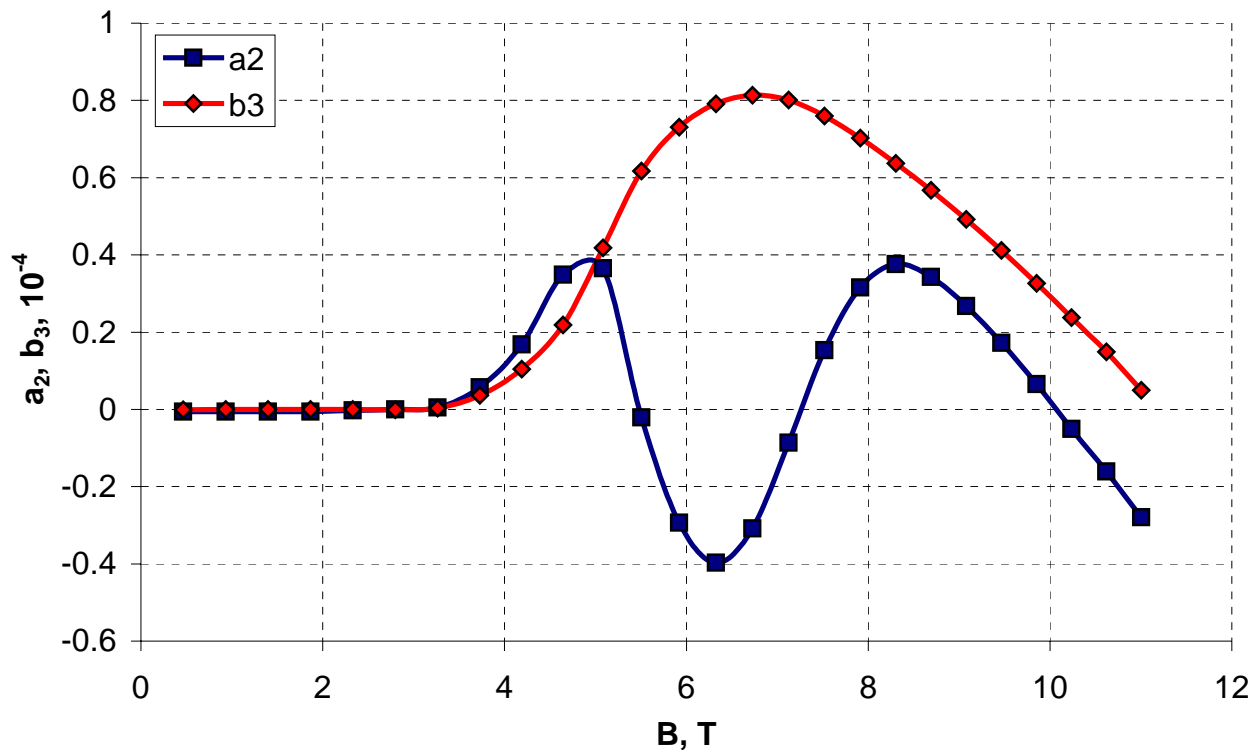
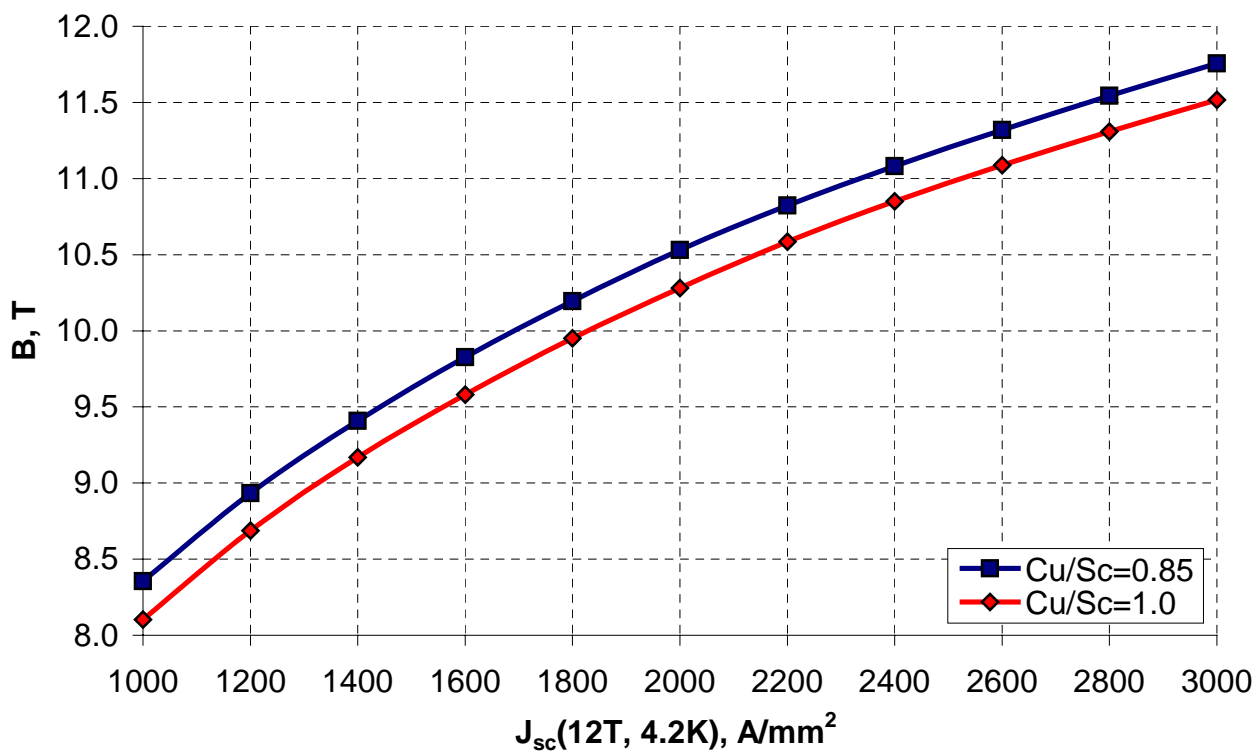Figure 3.4.3. Harmonic deviations as functions of the bore field.

Figure 3.4.4. Quench field as a function of the critical current density.
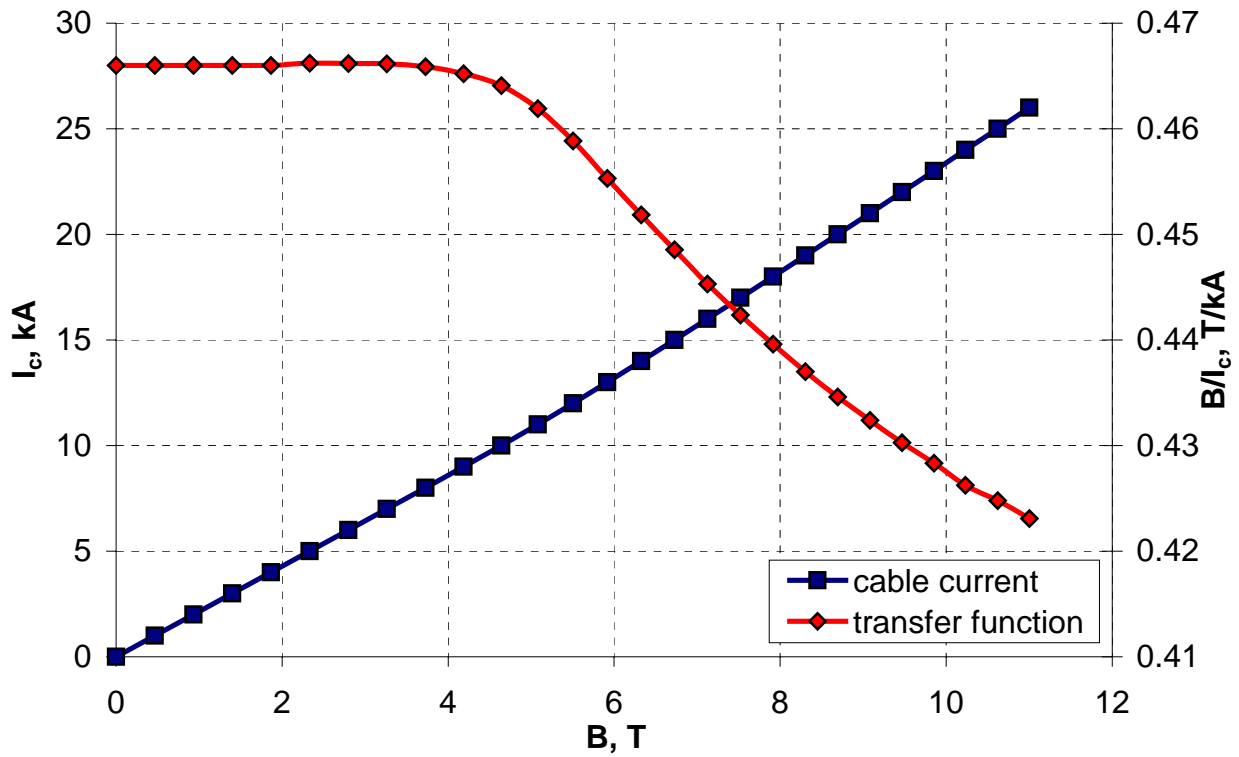
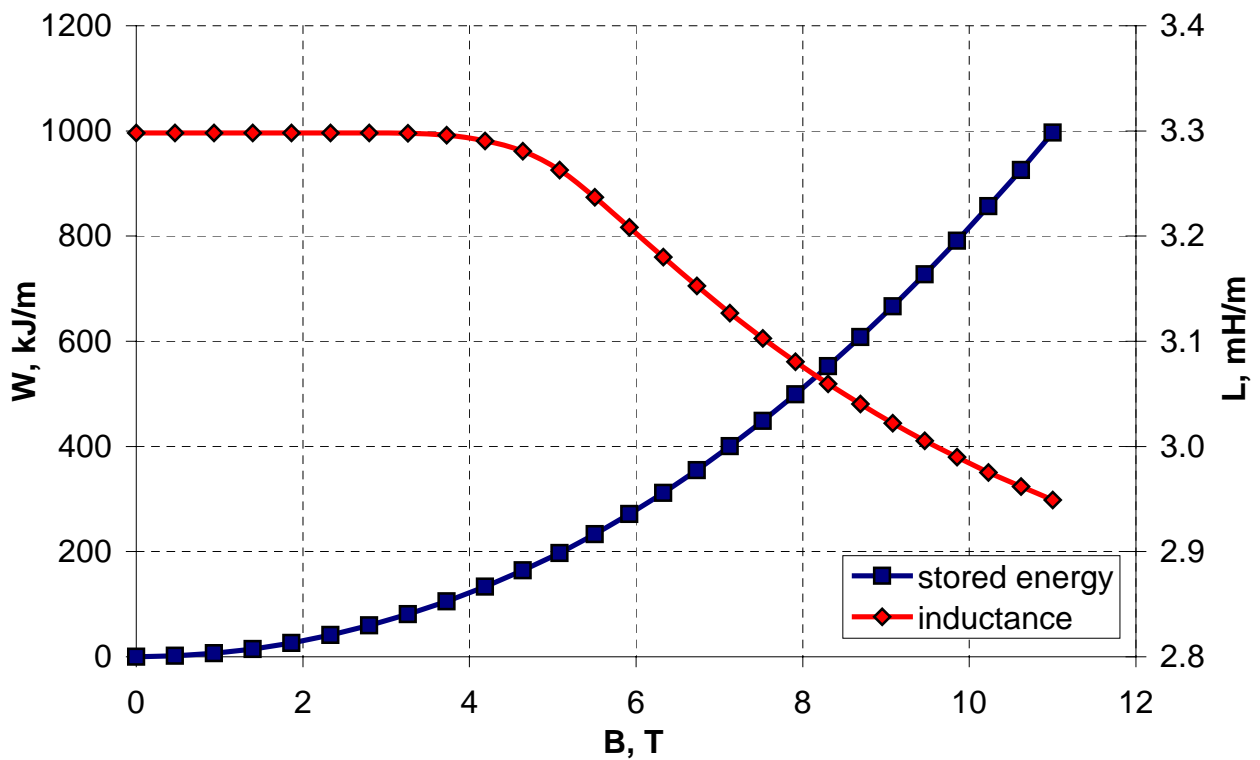Figure 3.4.5. Cable current and transfer function as functions of the bore field.

Figure 3.4.6. Stored energy and inductance as functions of the bore field.

3.4.2 "Cold/Warm" yoke design

Magnet of this type utilizes the shell-type coils arranged vertically within the common yoke. The negative coupling between two apertures decreases the transfer function and maximum field. In addition, the boundary conditions imposed by the vertical coil arrangement require the bore separation distance to be approximately equal to the yoke outer radius. Restrictions of the fringe field and multipole deviations at a reasonable level in this case would lead to noticeably larger yoke size, in comparison to the magnet with horizontal bore arrangement, making such design less economically attractive. The common coil magnet considered in the previous paragraph serves as a good example of larger yoke size in a magnet with vertical bore arrangement.

The "cold" mass size can be partially reduced by subdivision the iron yoke into two parts – "cold" and "warm", when both serve as the flux returns and are the elements of the magnetic design. Optimization strategy for such a magnet can be following: minimization of the "cold" yoke part by decreasing its outer radius while keeping the bore field quality and fringe field outside the "warm" yoke at the necessary level by optimizing geometry of the holes within the "cold" yoke and thickness of the "warm" yoke. The distance between "cold" and "warm" parts is determined by the cryostat needs. For example, in the LHC dipoles the minimum distance is about 100 mm.

Optimization according to the defined strategy was done by OPERA2D code, for the shell type coil described in Chapter 1 and the yoke inner radius of 60 mm. It was found that deviations of the sextuple component exceeded 10^{-4} even after correction by the holes for reasonable yoke and hole sizes due to inherently larger yoke saturation effect in the magnet with vertical bore arrangement [113]. Therefore, the yoke inner radius was increased by 5 mm that in turn required further optimization of the coil geometry.

Figure 3.4.7 presents the coil geometry after optimization. It consists of the same number of turns and blocks as the initial coil design. The only noticeable difference is in closer to the midplane position of the pole and middle blocks of the outer layer. Table 3.4.2 summarizes the geometrical multipoles for the new coil, which are within the specification.

The yoke optimization was repeated with the new coil cross-section. Figure 3.4.8 shows the flux distribution within the optimized yoke cross-section at 11 T bore field and the "cold" block mechanical structure. One can see the large holes in the magnet midplane similar to those in the common coil magnet that primarily serve for correction of the skew quadrupole component. The rest of the holes are intended for the sextupole correction. Figure 3.4.9 shows that it was possible to restrict the skew quadrupole and sextupole component deviations within $0.5 \cdot 10^{-4}$ and $1 \cdot 10^{-4}$ in the 0-11 T field range.
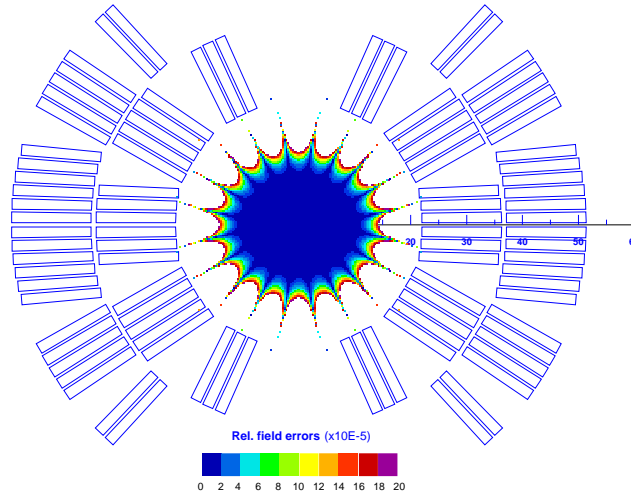
Figure 3.4.7. Optimized shell-type coil geometry.

Table 3.4.2. Geometrical multipoles in 10^{-4} for the shell-type coil.

b_3	b_5	b_7	b_9	b_{11}
0.000	0.000	-0.006	-0.067	0.104

The optimum "cold" block radius of 240 mm was smaller than the bore the separation distance of 266 mm due to contribution of the "warm" part. The distance between the "cold" and "warm" parts was kept constant and equal to 100 mm throughout the optimization. Due to a small amount of iron in the "cold" part there was a significant fringe flux that could be suppressed to ~ 40 mT at 11 T bore field by 15 mm "warm" iron screen. The field in the "warm" screen reaches 2 T.

Figure 3.4.10 presents the quench bore field for two copper to non-copper ratios. The quench field is by only 3.5 % smaller than in the double aperture shell type magnet with horizontal bore separation, while in the common coil dipole the field is by 14 % smaller. Thus, the expected critical current density of 3000 A/mm^2 would allow reaching the 11.6 T field with 10 % degradation and 10 % safety margin.

Figures 3.4.11-3.4.12 show the cable current, transfer function, stored energy and inductance as functions of the bore field. There is no essential difference in these parameters with respect to the shell type magnet with horizontal bore separation.

The coils can be accommodated within the vertically split iron yoke, similarly to the common coil magnet. However, the mechanical structure is similar to the shell type magnet with horizontal bore arrangement, as there was no special collars intended for constraining the electromagnetic forces. The full prestress is provided by means of the stainless steel skin, which has to be twice thicker than in the magnet with horizontal bore arrangement, where electromagnetic forces acting in two coils partially cancel each other [114].

Component: |B|, T

0.0200332   2.094961   4.169889
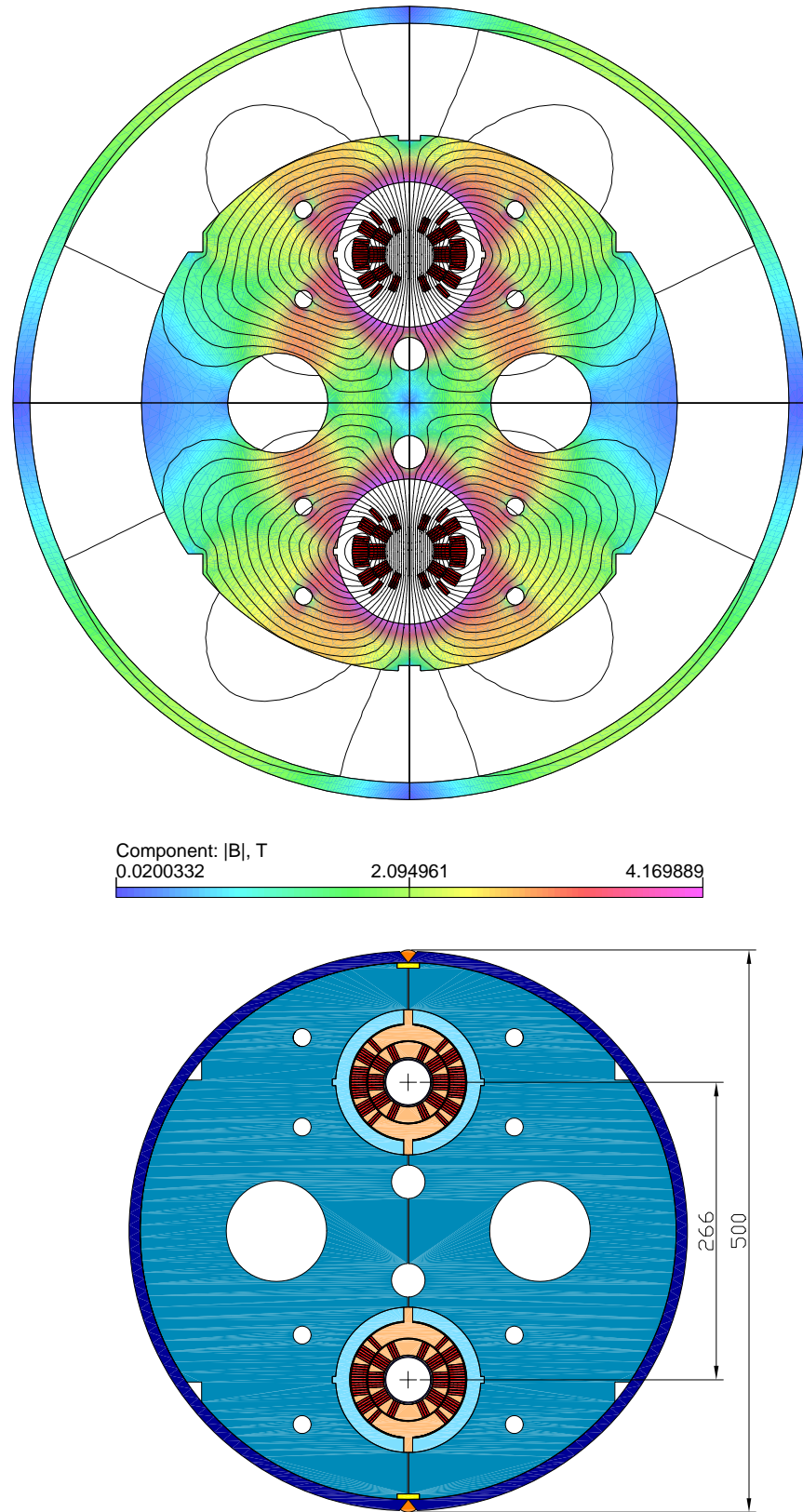
Figure 3.4.8. Flux distribution (top) and mechanical structure (bottom) of the shell type magnet with vertical bore arrangement.
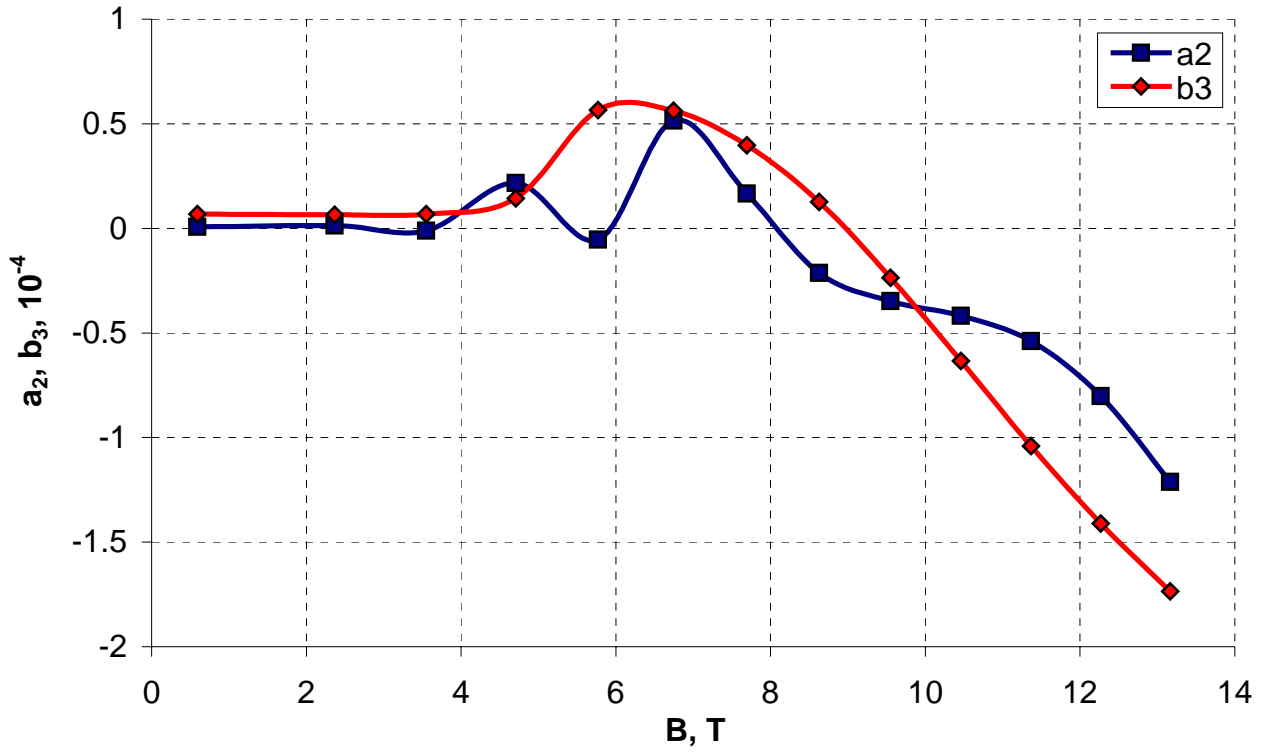
Figure 3.4.9. Skew quadrupole and sextupole deviations as functions of the bore field.
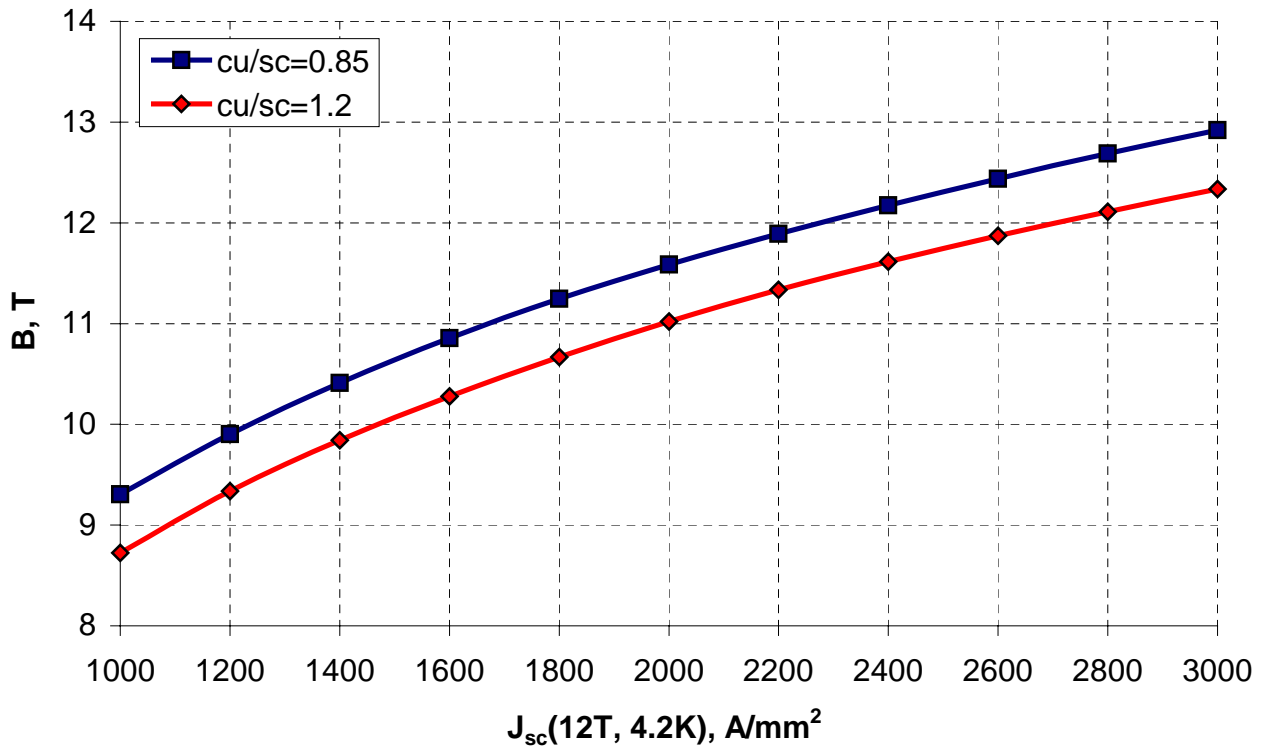
Figure 3.4.10. Bore quench field as a function of the critical current density.
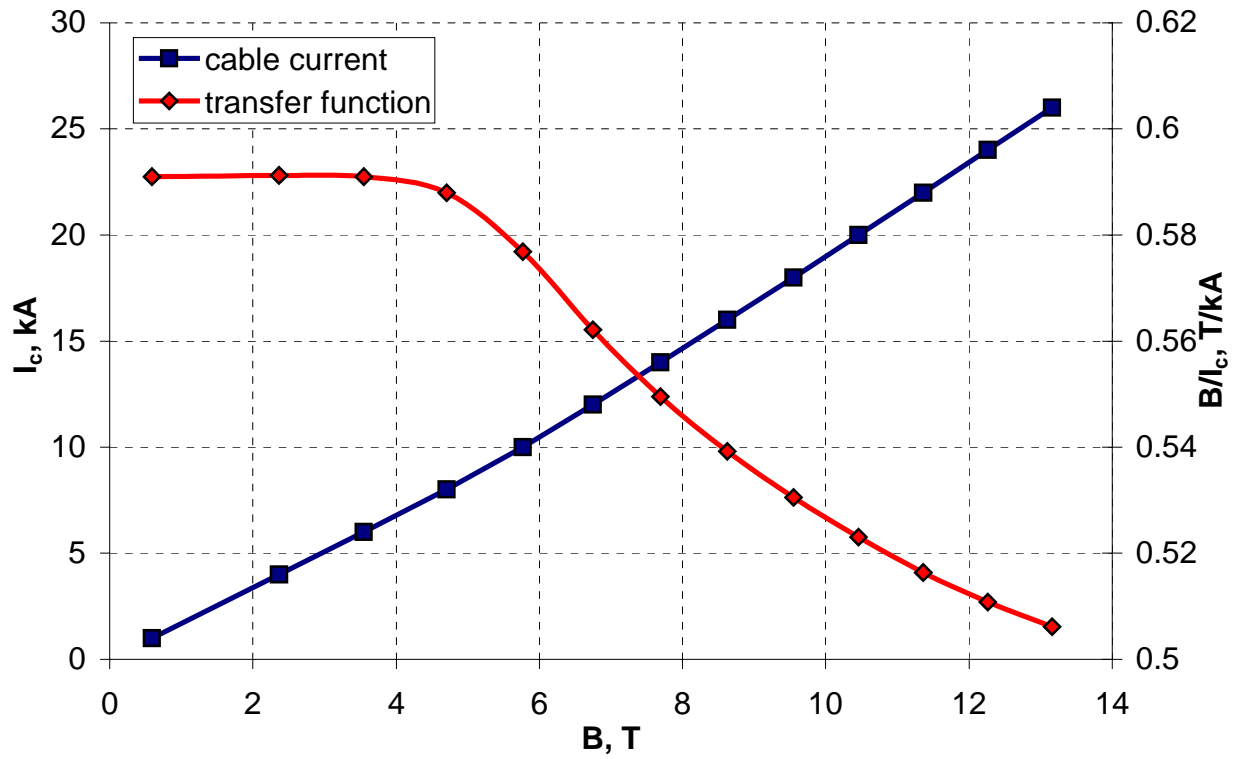
Figure 3.4.11. Cable current and transfer function as functions of the bore field.
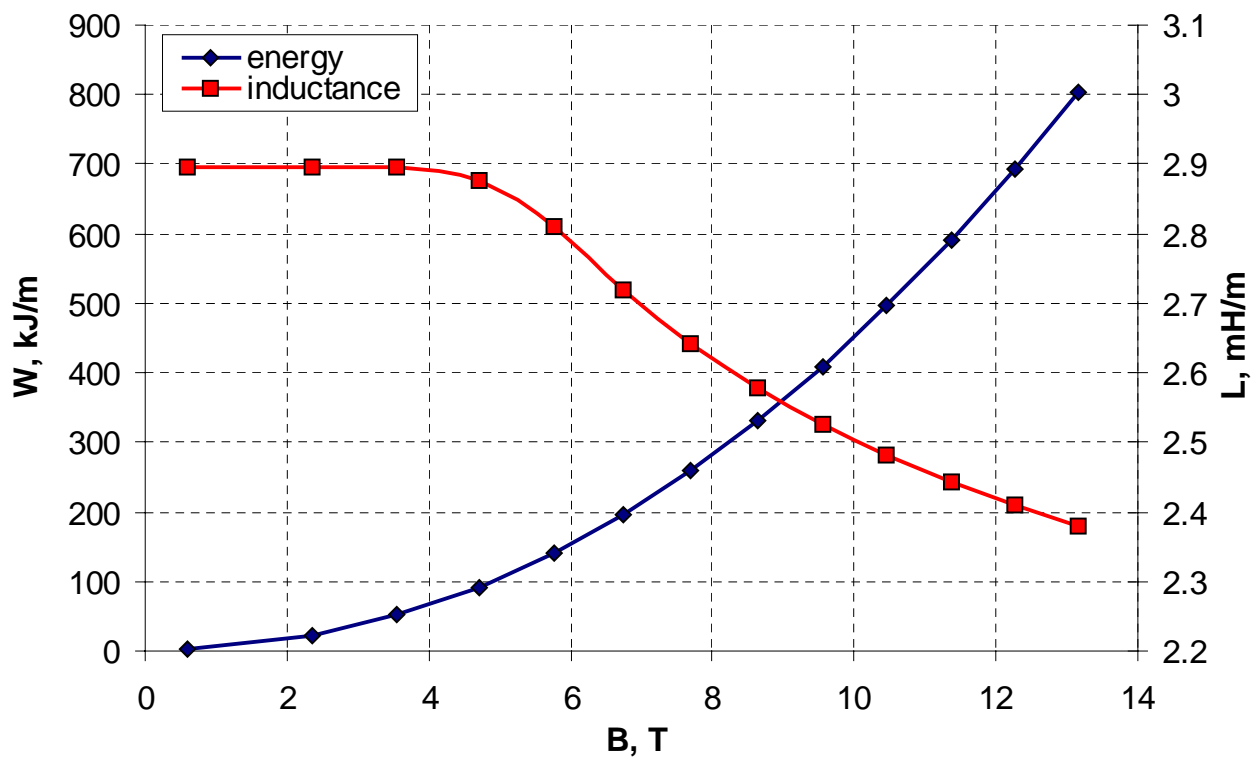
Figure 3.4.12. Stored energy and inductance as functions of the bore field.

3.5 Optimization of quadrupole magnets

Optimization of arc quadrupole magnets was based on the similar to the dipole magnet general criteria – meeting the requested magnet parameters at the minimum cost. The quadrupole magnets are intended to work in a FODO structure with separate functions. Therefore the bore separation distance has to be equal to the one in the main dipole magnets.

The quadrupole magnet designs were optimized by OPERA2D code in order to match with different dipole magnets and meet VLHC specifications. All of them were based on the same collared coils with 43.5 mm bore diameter [55], descried in Chapter 1. The coils were prestressed and mechanically supported by means of Nitronic 40 stainless steel collar laminations. The collar thickness of 20 mm was scaled from the design of the LHC IR quadrupoles developed at Fermilab [115]. The coil support structure is capable of keeping the coils under compression with the maximum stress in the coil less than 150 MPa in the operation gradient range of   0-400 T/m [116]. Thick aluminum end cans provided prestress and mechanical support of the magnet ends. No additional radial support from the iron yoke was required.

An alternative collar design with two pares of laminations and the adequate support capability was also proposed [117].

3.5.1 FD quadrupole for dipole magnets with horizontal bore arrangement

Quadrupole magnet of this type is intended to work together with the shell type dipole magnet with the horizontal bore arrangement. Thus, the bore separation distance has to be equal to 180 mm. The iron yoke is split horizontally into two pieces to allow assembly of two coils in one yoke. The gap between the two iron pieces is always closed in order to reduce the effect of gap variation on the field quality.

The baseline design of the arc quadrupoles with horizontal bore arrangement is FD configuration suitable for the round beam optics, which imposes a boundary condition of zero normal derivative of vector potential in the vertical plane of symmetry and therefore positive coupling between the coils. Correcting holes were optimized along with the yoke outer radius in order to reduce the yoke saturation effect [56].

Figure 3.5.1 shows the optimized yoke cross-section with the flux distribution at 400 T/m bore gradient and the "cold" mass mechanical structure. The maximum field in the yoke reaches 3.5 T that is by 40 % smaller than in the relevant dipole, yet high enough to generate the field quality deviations due to the yoke saturation effect. It was corrected by the holes in the magnet vertical plane of symmetry.

Component: |B|, T
0.057667   1.694105   3.330544
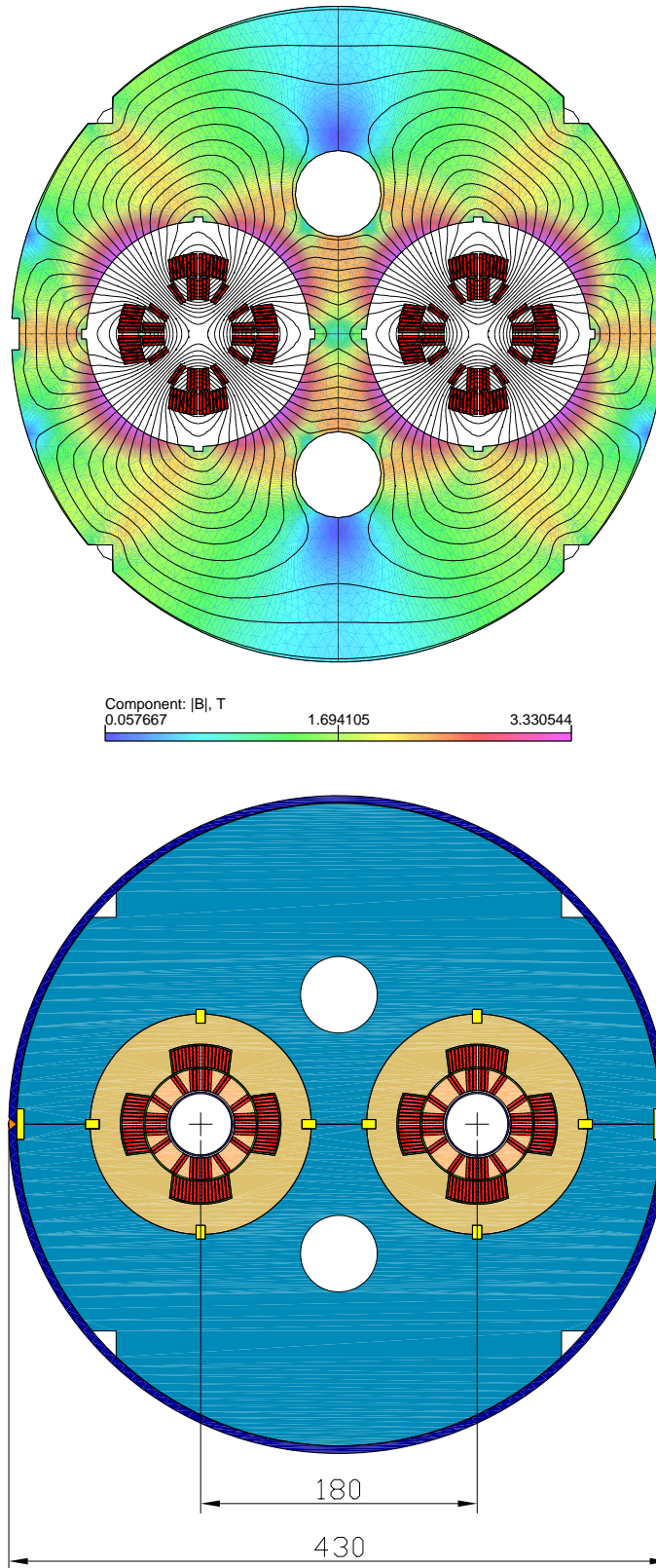
Figure 3.5.1. Flux distribution (top) and mechanical structure (bottom) of the FD quadrupole magnet with horizontal bore arrangement.

There were only normal harmonics allowed in this type of symmetry. Figure 3.5.2 presents harmonic deviations due to the yoke saturation effect. The biggest harmonic is the dipole that is not zero at low field due to a large coupling between two apertures. However, it was possible to restrict the dipole deviations within 10^{-4} in 0-400 T/m gradient range. The next allowed harmonic is sextupole that varies within $0.2 \cdot 10^{-4}$.

Figure 3.5.3 shows the maximum gradient as a function of the critical current density for two copper to non-copper ratios, required for a short and long magnet quench protection [100], [109]. Thus, the expected critical current density of 3000 A/mm^2 with 10 % degradation and 10 % margin allows reaching the nominal gradient of 425 T/m.

The quadrupole magnet has larger current than in the relevant dipole, but the stored energies are nearly the same (Figures 3.5.4-3.5.5). It explains by the negative coupling between half of the turns within one each coil, resulting in negative mutual inductances and lower total inductance. Reaching of 400 T/m gradient leads to the current around 28 kA that is by 30 % larger than in the dipole magnet at 11 T bore field. Obviously, the quadrupole magnet should be powered separately in order to work at peak efficiency. This option is considered for the VLHC magnets [10]. If the quadrupole magnet has to be powered in series with the dipole, its cable cross-section can be reduced in order to achieve the same nominal current as in the dipole magnet.
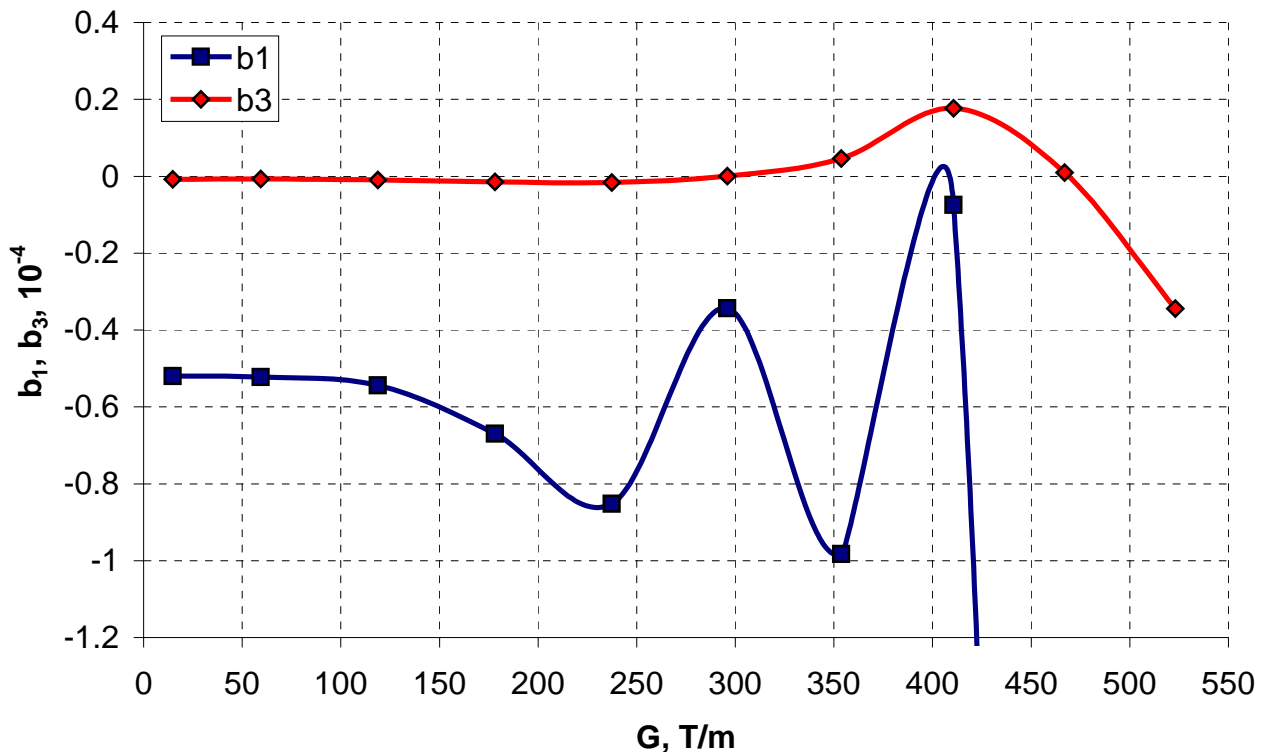
Figure 3.5.2. Multipole deviations as functions of the bore gradient.
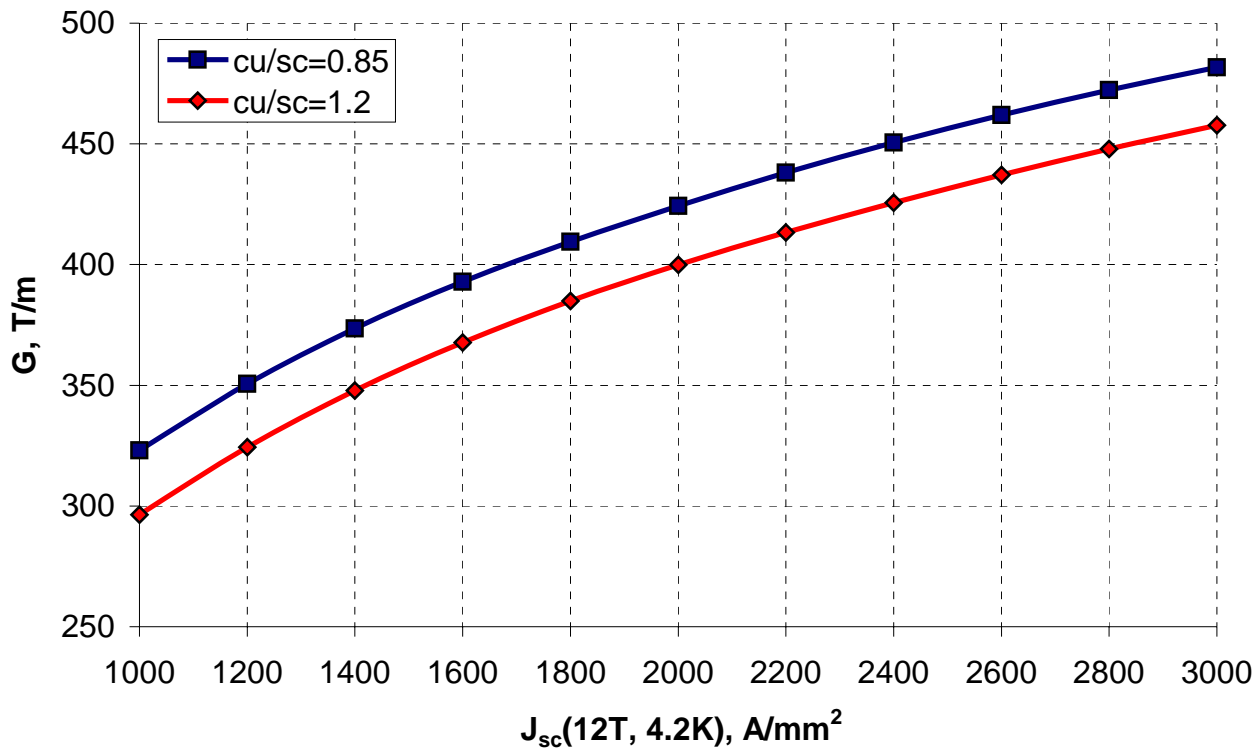
Figure 3.5.3. Magnet quench field as a function of the critical current density.
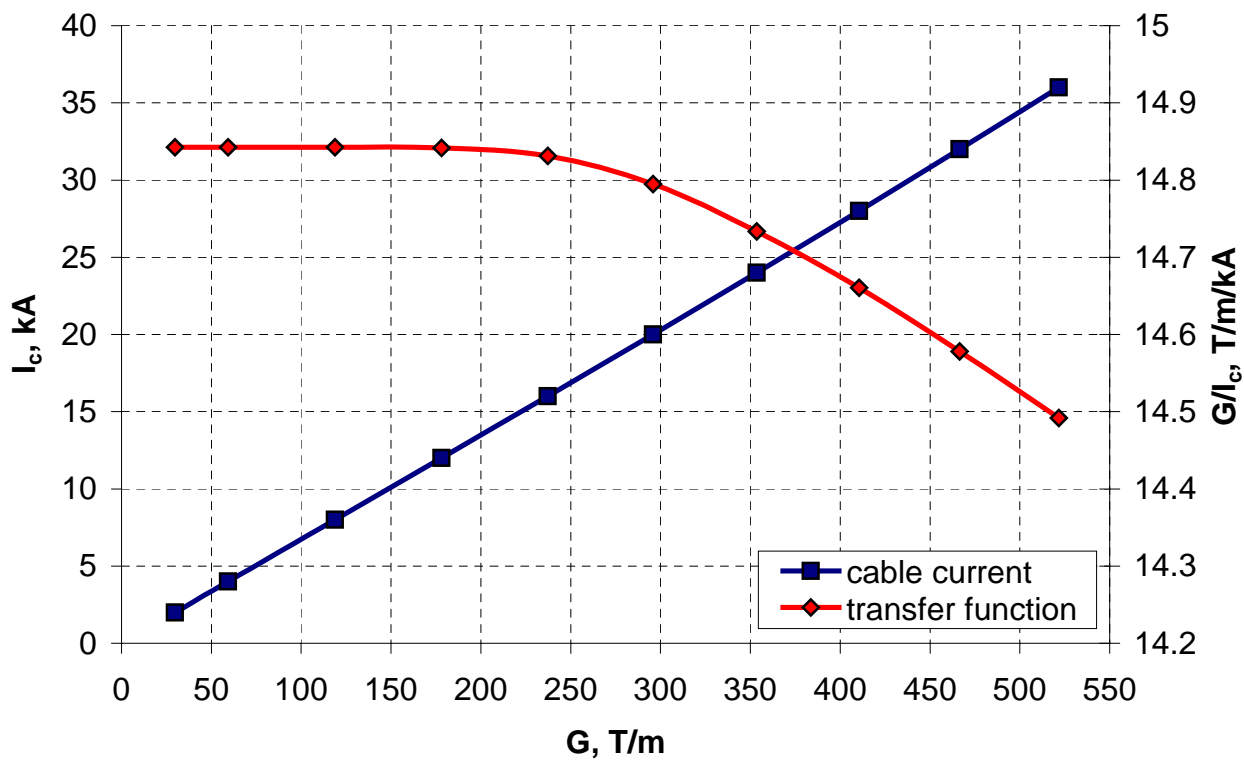
Figure 3.5.4. Cable current and transfer function as functions of the bore gradient.
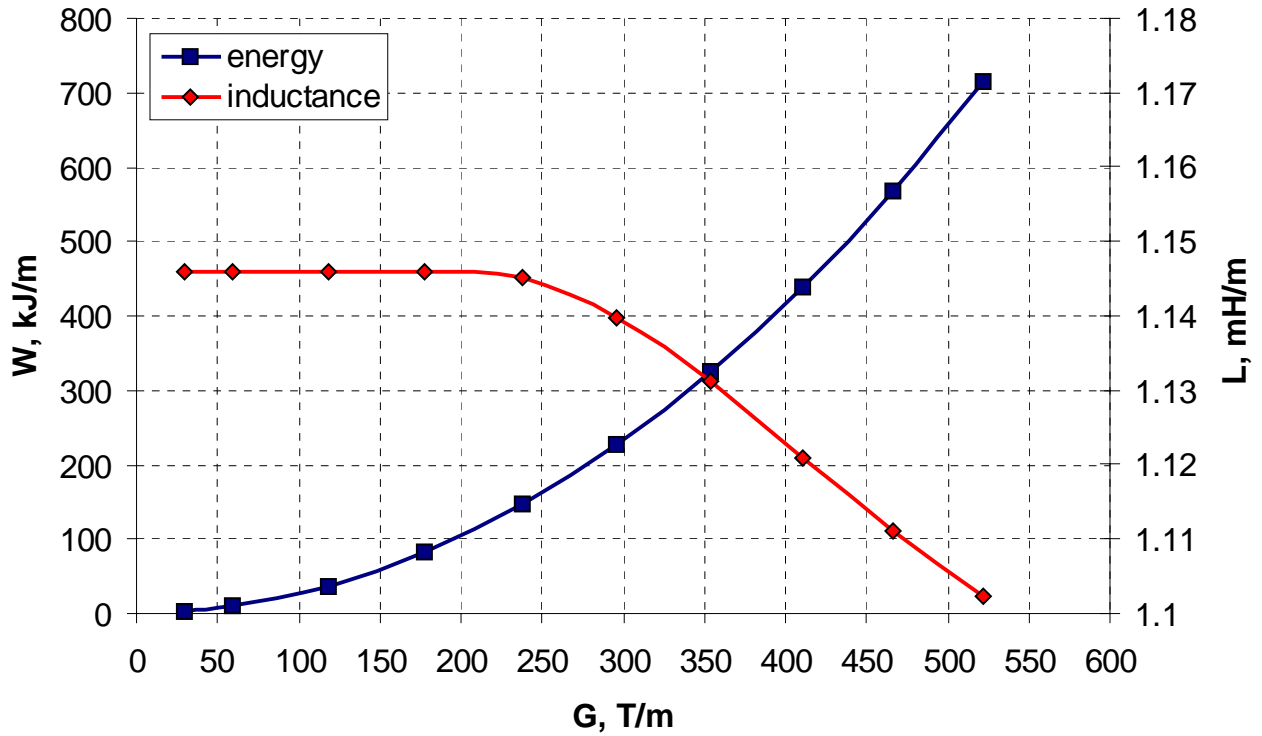
Figure 3.5.5. Stored energy and inductance as functions of the bore gradient.

The magnet inductance becomes a function of the field starting at the gradient of 200 T/m due to the yoke saturation. It is by factor of two smaller than in the dipole magnet due to the negative mutual inductance between half of the turns of one coil. However, it does not simplify the quench protection due to the larger magnet current [100]. If necessary, the bore separation distance in this magnet can be easily reduced by ~50 %, as required for VLHC-I magnets [118].

3.5.2 FF quadrupole for the common coil dipole

Quadrupole magnets of this type are intended to work together with the common coil dipole magnets. Thus, the bore separation distance should be 290 mm. The "flat" beam optics inherent to the vertical bore arrangement requires FF quadrupole magnets. It imposes a constant vector potential in the magnet midplane and, therefore, negative coupling between two coils. The coils were accommodated within the common, vertically split yoke with permanently closed gap. Figure 3.5.6 presents the optimized magnet cross-section with the flux distribution at 400 T/m bore gradient and the "cold" block mechanical structure. The main correcting holes were of the same size and position as in the relevant dipole magnet. Since minimization of the yoke outer radius at the fixed bore separation distance produced a large top-bottom flux imbalance, an additional hole in the magnet center was required for the field quality improvement [56].

Figure 3.5.6. Flux distribution (top) and mechanical structure (bottom) of the FF quadrupole magnet with vertical bore arrangement.

It was possible to restrict the skew dipole and skew sextupole deviations, shown in Figure 3.5.7 within $0.4 \cdot 10^{-4}$ and $0.1 \cdot 10^{-4}$ respectively in the 0-400 T/m gradient range. Similar coils and iron contribution as in the previous quadrupole magnet design resulted in essentially the same quench field, current, transfer function, inductance and stored energy (Figures 3.5.3-3.5.5).
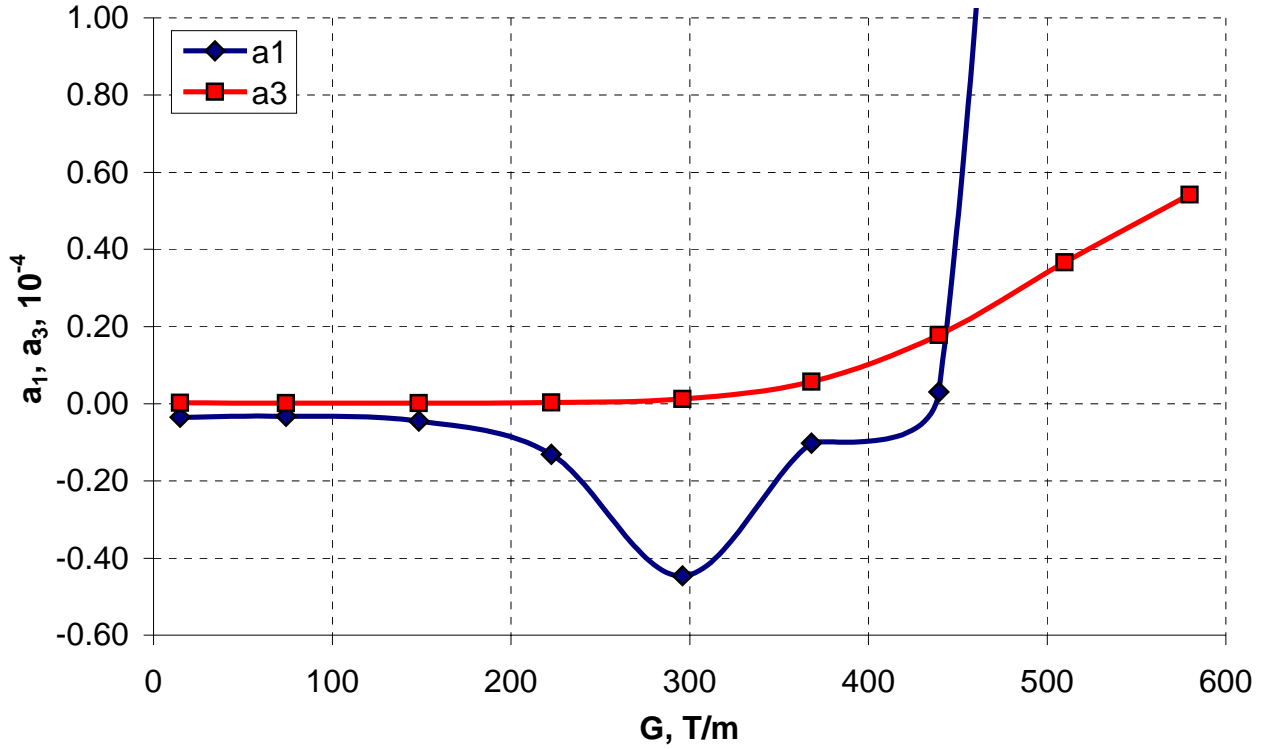
Figure 3.5.7. Multipole deviations as functions of the bore field.

3.5.3 FF quadrupole for the shell type dipole with vertical bore arrangement

Quadrupole magnets of this type are intended to work together with the shell type dipoles with the vertical bore arrangement. The bore separation distance in this case should be 266 mm. Also, utilizing the cryostat similar to the dipole magnet ("warm" yoke) would be preferable by economical reasons. Therefore, the quadrupole magnet should be based on the subdivided "cold/warm" yoke concept as well.

The "flat" beam optics suitable for the vertical bore arrangement requires FF quadrupole magnets. In terms of the boundary condition, it imposes a constant vector potential in the magnet midplane and, therefore, negative coupling between the coils, similarly to the previous case. The coils are accommodated within the vertically split common yoke with permanently closed gap. Figure 3.5.8 presents the optimized magnet cross-section with flux distribution at 400 T/m bore gradient and the "cold" mass mechanical structure.
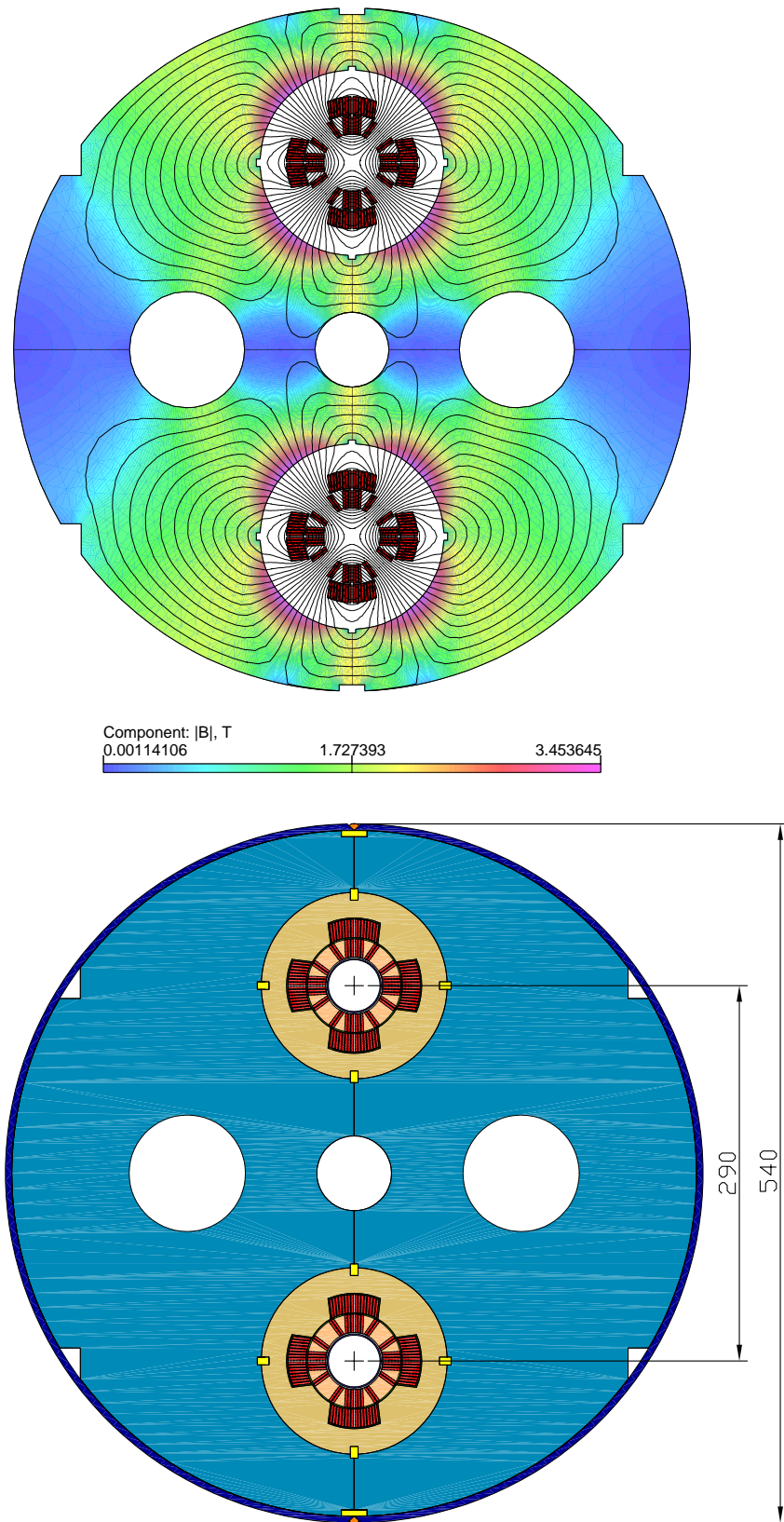
Component: |B|, T
0.00406589   1.656194   3.308323
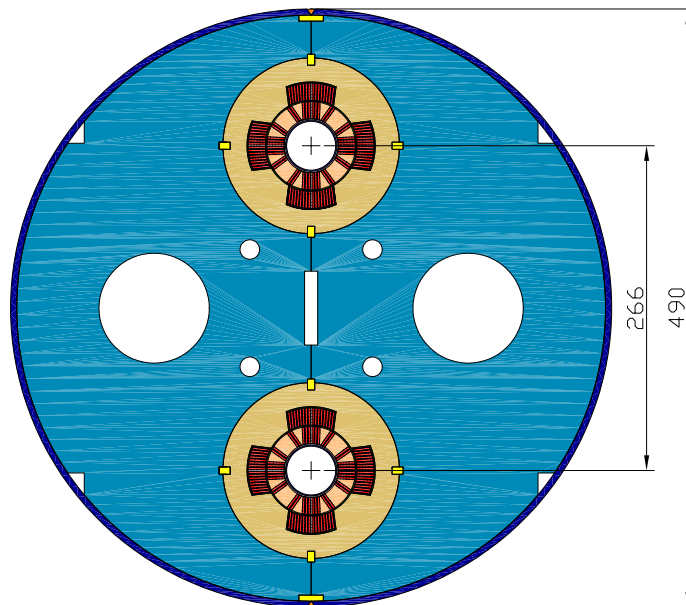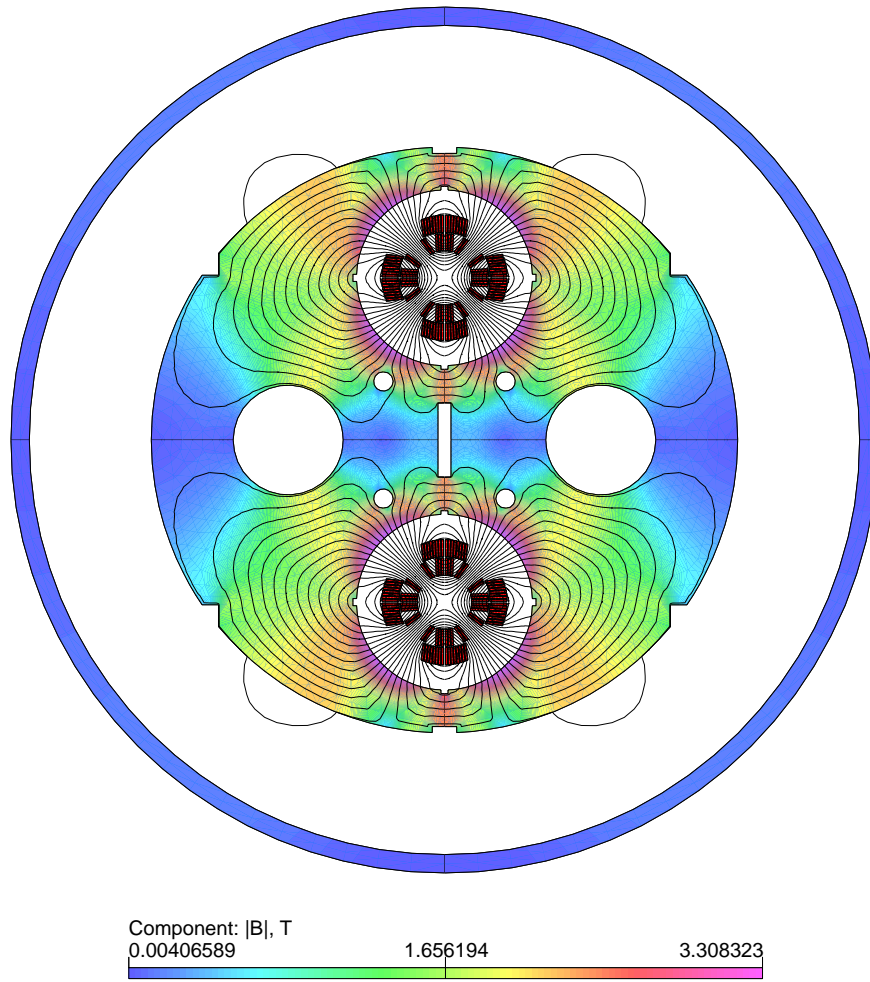
Figure 3.5.8. Flux distribution (top) and mechanical structure (bottom) of the FF quadrupole
magnet with vertical bore arrangement.

The "warm" screen is not saturated, unlikely to the dipole magnet. However, its close proximity to the "cold" part affects the flux distribution that had to be taken into account during optimization. The main cooling channels are of the same size and position as in the relevant dipole magnet. It was necessary to introduce the rectangular hole in the magnet center to minimize the skew dipole component, and other holes used for correction of the skew sextupole component [56].

Figure 3.5.9 shows the multipole deviations, which were possible to keep within $0.8 \cdot 10^{-4}$ and $0.4 \cdot 10^{-4}$ correspondingly for the skew dipole and skew sextupole in the 0-400 T/m gradient range. The rest of parameters is the same as for the previous two magnets (Figures 3.5.3-3.5.5) due to the same coil and iron contribution.
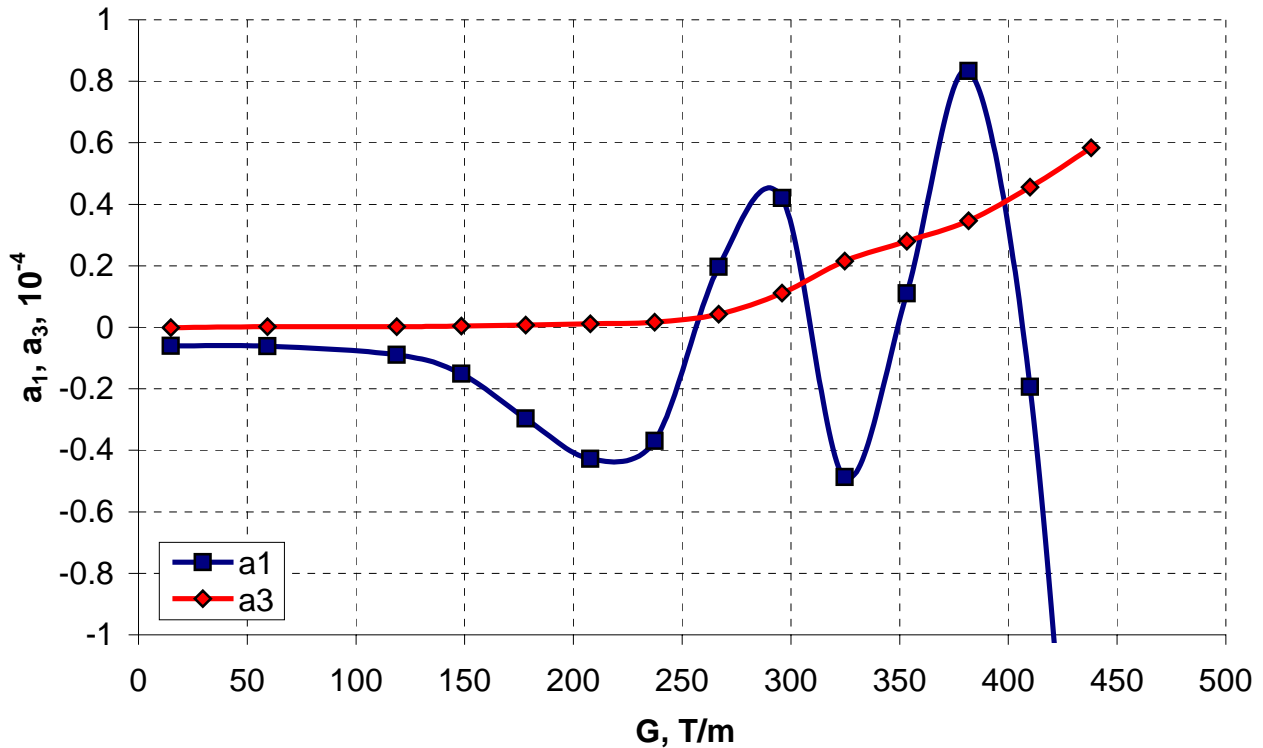
Figure 3.5.9. Multipole distributions as functions of the bore gradient.

3.6 Summary

Results of study and optimization magnetic systems of superconducting accelerator magnets can be summarized as follows:

- Developed design of the single aperture shell type Nb_3Sn dipole magnet with the nominal field of 11-12 T. Short magnet models based on the developed geometry are in production and test.

- Developed designs of the shell and block type magnets with the horizontal and vertical bore separation. All of them satisfy the second stage VLHC requirements, giving possibility of the optimum design choice depending on additional constrains. Table 3.6.1. summarizes the main dipole magnet parameters.

Table 3.6.1 Dipole magnet parameters

| Parameter	Unit	Aperture arrangement			
		horizontal	horizontal	vertical	vertical
Coil type		shell	shell	racetrack	shell
Yoke type		cold	warm	cold	cold+warm
Aperture	mm	43.5	43.5	40.0 (51.6)[I]	43.5
Bore separation	mm	180	180	290	266
Quench[II] field	T	12.4	11.8	10.8	12.0
Quench current	kA	22.6	25.0	25.5	23.4
Transfer function at 11 T	T/kA	0.56	0.47	0.42	0.52
Inductance at 11 T	mH/m	2.68	2.15	2.95	2.46
Stored energy at 11 T	kJ/m	521	587	997	554
Strands cross-section area	cm^2	2x21.6	2x21.6	2x26.8	2x21.6
"Cold" yoke cross-section	cm^2	1722	-	1709	1378
"Warm" yoke cross-section	cm^2	-	679	-	327
"Cold" block diameter	mm	540	380	580	500
"Cold" block weight	kg/m	1516	495/904[III]	1755	1248
Cryostat outer diameter[IV]	mm	750	580	790	710

- Performed optimization of the shell type magnet with the "cold" iron yoke and horizontal bore separation. The approach of making gaps in the yoke parallel to the flux lines was proposed and numerically verified. It minimizes the field quality deviations due to the gap variations under electromagnetic forces.

- Proposed perspective design of the shell type dipole magnet with the "warm" iron yoke and horizontal bore separation. The magnet outer size has been reduced by factor of 2 and the magnet weight has been reduced by factor of 3-4 with respect to existing (LHC dipole) shell type magnets. It was shown that compensation of the coil magnetic coupling can be easily accomplished by introduction a small (less than +/-1 mm) left-right asymmetry in the three

---

[I] The number in brackets shows available space for the beam tube in the magnet straight section.
[II] Quench parameters are calculated in following assumptions:
  - The short sample limit is 3000 A/mm^2 at 12 T and 4.2 K for the shell type dipoles. Cabling and other types of degradation reduce this value by 10%. Copper to non-copper ratio is 1.2.
  - The short sample limit is 3000 A/mm^2 at 12 T and 4.2 K for the common coil dipole. Cabling and other types of degradation reduce this value by 20%. Copper to non-copper ratio is 1.1.
[III] First number is for the coil support made of aluminum, second is for stainless steel.
[IV] A reference parameter obtained in assumption of 100 mm distance between the "cold" and "warm" parts.

coil blocks per quadrant. The magnet inductance is 23 % smaller than in the shell type dipole with "cold" iron yoke that reduces the voltages, generated during quench and allow the magnet length increasing. It was demonstrated that in case of a reasonable restriction of the "cold" block misalignment within +/-1.5 mm, the eccentricity forces do not exceed 30 % of the "cold" block weight and the harmonic deviations are within +/-10^{-4}.

- Proposed and numerically verified design of the single-layer common coil dipole magnet. The simple, flat geometry gives possibility of winding the coil inside of the common mechanical structure that reduces manufacturing time and cost. Large bending radius allows using of the "react and wind" technique. It reduces the furnace size and allows control of the cable dimensions during all stages of coil fabrication that reduces the random field errors spread.

- Studied design of the shell type dipole magnet with the vertical bore separation and the subdivided iron yoke. Performed optimization has demonstrated that separation of the yoke into the "cold" and "warm" parts allows reduction of the magnet dimensions by 30 % with respect to the "cold" design.

- Developed effective designs of the shell type quadrupole magnets, with different functions and bore orientations, coordinated with the dipole magnet parameters.

CHAPTER 4. STUDY AND CORRECTION OF THE COIL MAGNETIZATION EFFECT

4.1 Introduction

Accelerator magnets must meet quite strong field quality requirements. It was demonstrated in the previous chapters that the multipole deviations due to conductor misalignment and the yoke saturation effect could be suppressed to 10^{-4} within operating field range in most of the high field magnets.

However, results of magnetic measurements in superconducting accelerator magnets show that the field quality significantly deteriorates at low fields. For example, the sextupole component in NbTi dipole magnets of Tevatron, HERA, SSC, LHC distorts by $\sim 10\text{-}20 \cdot 10^{-4}$ at injection field [120]-[125]. This effect known as the coil magnetization or the persistent current effect in superconducting magnets caused by persistent currents induced in the superconducting filaments. It is large at low fields but rapidly reduces when the main field increases. The negative consequences of this effect are: decreasing of the dynamic aperture, reduction of the operation field range, complication and cost growth of the correction system.

The situation becomes noticeably worse for high field accelerator magnets based on the Nb_3Sn superconductor. Commercially available Nb_3Sn strands provide the critical current density sufficient to increase the magnetic field in accelerator magnets up to $14 \div 15$ T. However, their large effective filament diameter, inherent to the manufacturing technology along with high critical current density increases the coil magnetization effect by an order of magnitude with respect to NbTi magnets.

Correction of the coil magnetization effect in case of Tevatron and LHC is accomplished by the active correcting system, containing variety of different multipole corrector magnets. Precision of the HERA active correcting system was enhanced using the feedback signal form magnetic measurements in reference magnets [123]. Methods of the passive correction were considered by different authors.

M.A. Green from LBNL studied correction in the NbTi magnets arranging the passive superconducting strands with a large effective filament diameter inside of the coil aperture [121]-[122]. Disadvantage of this method is relatively large volume of the passive superconductor (~ 7 % of the coil volume at twice larger effective filament size), necessary to cancel the coil magnetization effect that reduces useful space in the coil aperture. It is unacceptable for the field correction in the Nb_3Sn magnets as commercial Nb_3Sn strands have already too large effective

filament diameter. The passive superconductor would have to have the effective filament size on the order of 200 μm that would make it unstable.

E. W. Collings from Ohio State University studied possibility of correction the coil magnetization effect by addition of low-magnetic materials (Mn, Ni) into the NbTi strand structure [126]. However, in case of Nb_3Sn superconductor, amount of the correcting material has to be comparable with the coil volume. It practically eliminates advantage of high critical current density achievable in this material.

H. Gurol, G.W. Albert, R. Simon and M. Marietta from San Diego considered installation of nickel tapes inside of the NbTi magnet aperture [127]. They have experimentally demonstrated positive effect of the corrector on the sextupole and decapole field components, however the measures corrector efficiency was only 55 % from numerically estimated. Presumably, the reason of the difference was in uncertainty of magnetic properties of the corrector material during numerical simulation.

A. Asner from CERN considered implementation of permanent magnets for correction of the coil magnetization effect in NbTi magnets [128]. It was shown that the length of external samarium-cobalt sextupole corrector should be about 1 % of the magnet length. In the case of Nb_3Sn magnet, the external corrector length has to be several times higher that would correspondingly reduce the magnets filling factor of the tunnel.

A passive field correction could be a very attractive implementation for high field superconducting accelerator magnets, based on Nb_3Sn superconductor. However, none of the considered methods provides a reliable correction without impact on the magnet performance, which makes their implementation unreasonably complex and expensive. Therefore, development of alternative methods of passive correction is essential for a future high-energy collider.

4.2 Simulation of the coil magnetization effect

The most widely used method of calculation the coil magnetization effect is analytical simulation of contribution made by magnetization of every particular strand into the field at a reference radius. Several practical implementations of this method, based on different approaches are described in [120], [121], [125]. However, most of them do not allow accurate simulation of the non-linear iron magnetization effects as well as complicated yoke surfaces, affecting the coil magnetization field, that limit their capabilities.

Another method, proposed by S. Caspi, W.S. Gilbert, M. Helm and L.J. Laslett from LBNL is based on the finite-element code POISSON, which allows accurate consideration of all the magnetic elements [129]. This approach will be used for simulations of the coil magnetization effect in this chapter.

4.2.1 Method description and verification

The finite element code OPERA2D was used for simulation of the coil magnetization. It allows taking into account complicated geometry and real magnetic properties of all the magnetic elements. The coil magnetic properties were characterized by the magnetization of a reference Nb_3Sn strand, 1 mm in diameter with the critical current density of 1600 A/mm^2 at 12 T and 4.2 K and copper to non-copper ratio of 0.85, measured at Fermilab [130].

Figure 4.2.1 presents the averaged magnetization curves per strand volume (copper + non-copper) for the first (virgin) and consequent field cycles. The effective filament diameter, derived from the curve was about 120 μm.
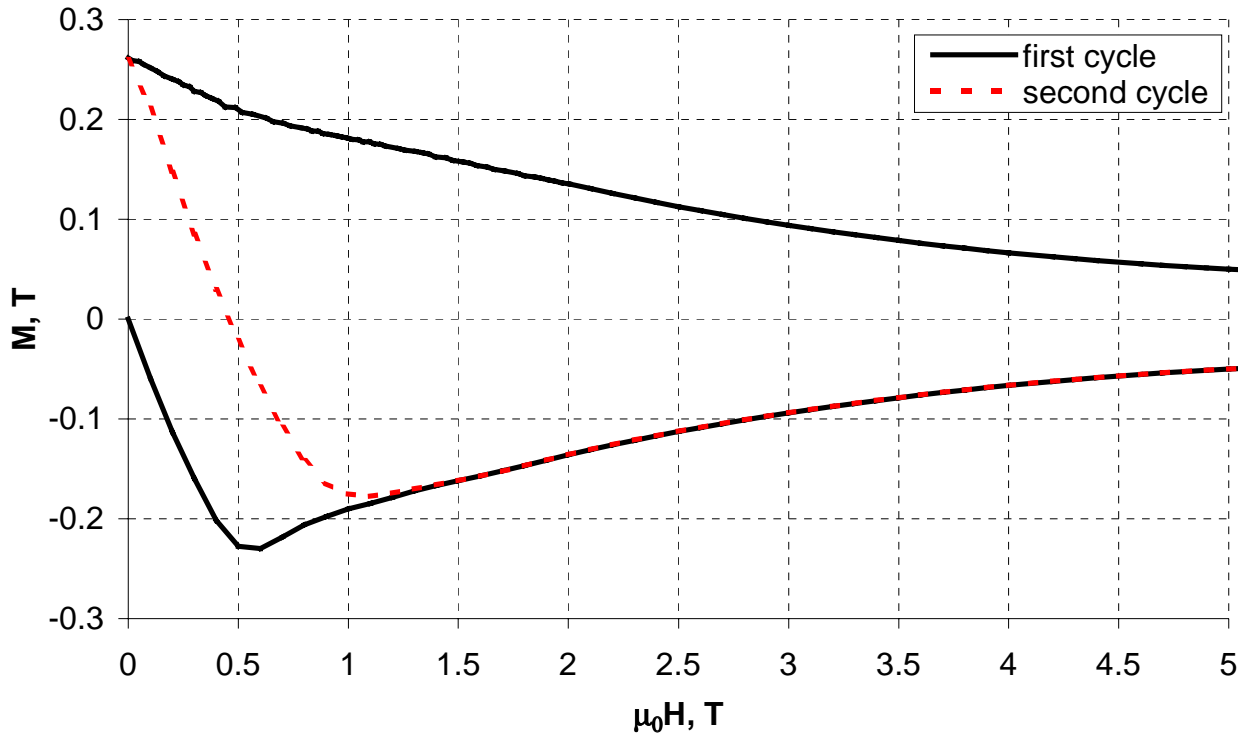

Figure 4.2.1. Superconductor magnetization as a function of applied field.

In order to assign the integral cable magnetic properties for the OPERA 2D model, the magnetization curve of the reference strand was transformed into a $B(H)$ curve according to the expression:

$$B(H) = \mu_0 H + M_{ref}\, \lambda_{str} \left(\mu_0\, \frac{H}{\lambda_{str}} \right), \qquad (4.1.1)$$

where λ_{str} is an average packing factor of strands in the cable.

Before performing extensive simulations of the coil magnetization effect, the method based on the finite-element code was verified by comparison with the analytical solution for a simple model. Geometry of the single bore dipole magnet, presented in Chapter 3 was used in the verification process. The strand packing factor was $\lambda_{str} = 0.88$. The analytical simulation of the coil magnetization effect was done according to the Bean model [131] in assumption of constant iron yoke permeability of 1000 [132].

Figure 4.2.2 shows the finite-element model with distribution of the magnetization within the coil and Figures 4.2.3-4.2.4 present sextupole and decapole curves for the first and second field cycles. One can notice that the maximum difference between analytical and numerical solutions is about 5 % at 1 T field. It was considered as tolerant enough verification of the method based on the finite-element code as the flux motion in superconductor leads to comparable uncertainty in the magnetization [97]. A higher accuracy can be achieved by introduction in (4.2.1) the packing factor, variable across the cable. One also should notice that reduction of the critical current density and therefore magnetization due to the transport current in the cable is not taken into account. This effect is negligibly small at low fields, where the coil magnetization causes maximum problems but starts playing a role at intermediate fields [133].
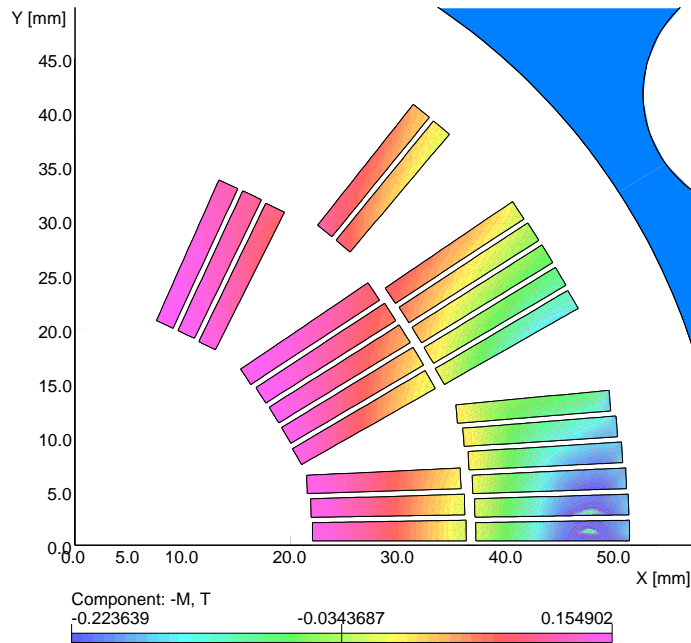

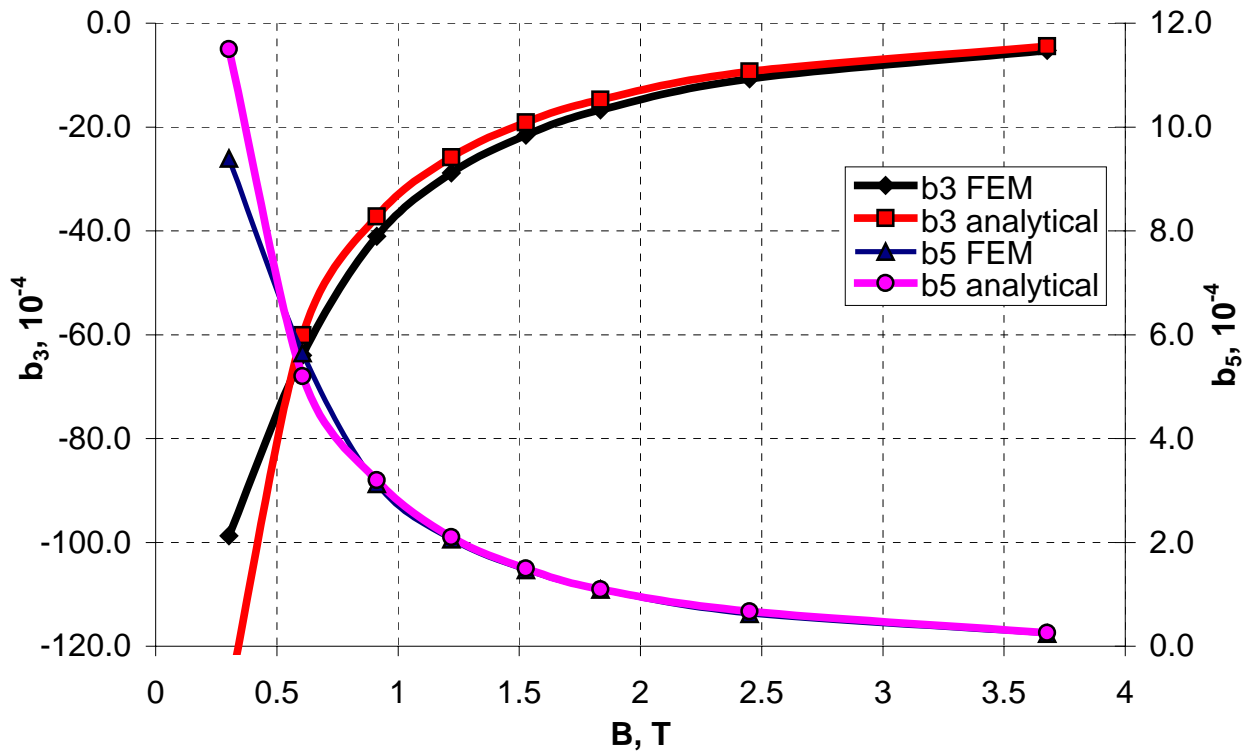Figure 4.2.2. Model for simulation of the coil magnetization effect.

Figure 4.2.3. Multipole deviations in the first cycle as functions of the bore field.
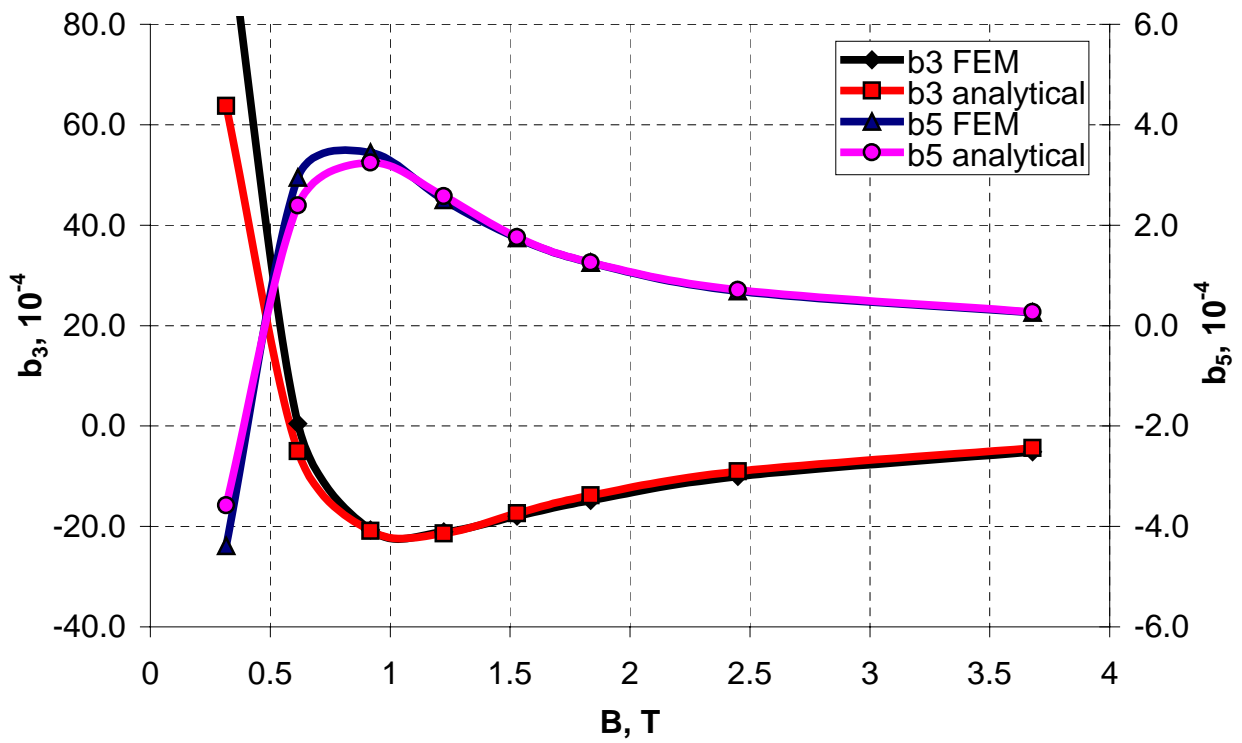

Figure 4.2.4. Multipole deviations in the second cycle as functions of the bore field.

4.2.2 Coil magnetization effect in different types of dipole magnets

In order to estimate impact of the magnet design on the coil magnetization effect, it was computed in different types of Nb_3Sn dipole magnets [134]. Since the collider magnets operate in a cycling mode, magnetization curve for the second cycle was used. All the magnets were assigned the same magnetization of the superconductor, equal to the reference. Thus, the $B(H)$ curves were calculated from the reference magnetization curve shown in Figure 4.2.1, taking into account the copper to non-copper ratios and packing factors, relevant to every particular design:

$$B(H) = \mu_0 H + \lambda_{str} M_{ref} \left(\mu_0 \frac{H}{\lambda_{str}} \right) \cdot \frac{1 + K_{cusc}^{ref}}{1 + K_{cusc}}. \qquad (4.1.2)$$

The coil magnetization effect was computed first for the shell type and common coil magnets described in Chapter 3 and [96], [49]. Figure 4.2.5 (designs A and B) presents the coil cross-sections of these magnets with the flux lines produced by the coil magnetization only (other effects were subtracted) at 1 T bore field. The copper to non-copper ratio in the strands is shown as well. The flux increment between adjacent lines was kept constant and equal to $5 \cdot 10^{-5}$ Wb/m in all the similar plots of this chapter for easier illustrative comparison.

One can notice that the magnetization flux, flowing through the coil aperture in the shell type magnet is significantly larger than in the common coil magnet. Thus, one can expect similar difference in multipole distributions. It is quantitatively confirmed in Figures 4.2.6-4.2.7, presenting incremental values of the sextupole and decapole components due to the coil magnetization effect in the second cycle. Geometrical field errors and non-linear iron saturation effect were taken into account during simulation in order to obtain the correct field map but subtracted from the presented curves. The plots indicate that the shell type magnet has a strong persistent current effect resulting in the sextupole and decapole deviations of $-20 \cdot 10^{-4}$ and $+3.5 \cdot 10^{-4}$ respectively at 1 T field. The harmonic deviations in the common coil magnet are by factor of 15 smaller and comparable with the yoke saturation effect. This observation might lead to the conclusion that the block type magnets are preserved from the persistent current effect.

In order to check this assumption, two other magnet designs with the block type coils developed at Texas A&M University [135] and BNL [136], [137] were considered. Coil cross-sections of these magnets with the flux lines produced by the coil magnetization at 1 T bore field are shown in Figure 4.2.5 (designs C and D). One can see a significant magnetization flux passing through the coil apertures of both magnets that comparable with the one in the shell type magnet. It produces the sextupole deviations of $-30 \cdot 10^{-4}$ at 1 T field. The decapole deviations are especially large in the design C, reaching $+9 \cdot 10^{-4}$ at 1 T field.
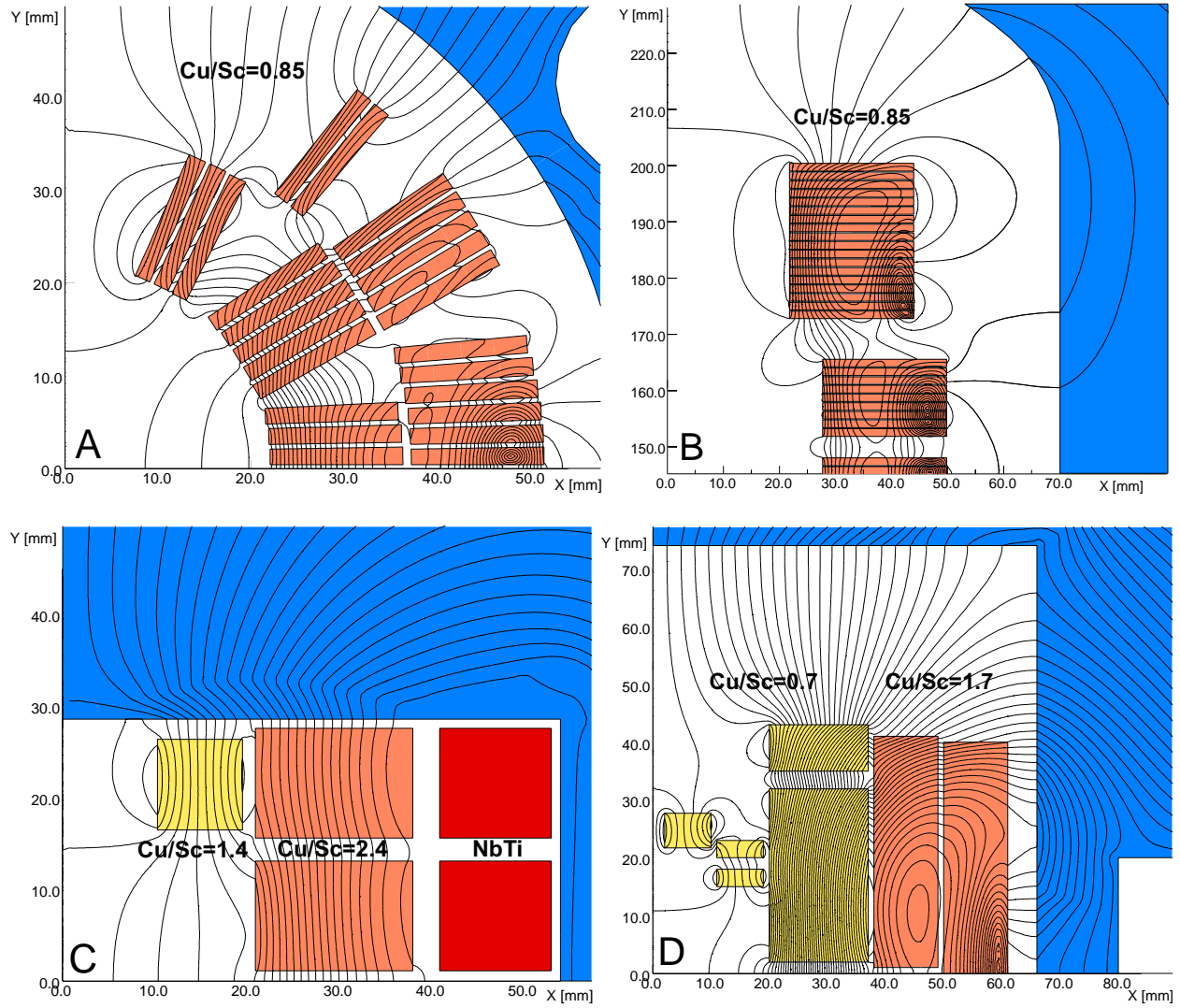
Figure 4.2.5. Cross-sections of different magnets with magnetization flux distribution.

A cause of the large persistent current effect in these magnets is in presence of the field-forming auxiliary coils, adjacent to the aperture. Such coils have no close boundary conditions from below (the nearest one is their midplane) that allow spreading of magnetization flux in horizontal direction on its way through the coil bore.

The single-layer common coil magnet does not have the auxiliary coils. The field-forming shift of the outer coil blocks occurs at a significant distance from the coil midplane and does not produce the multipole deviations in the good field region. In fact, the largest part of the magnetization flux is contained within the coil package due to its simple, flat inner boundary.

The coil magnetization effect was analyzed in the quadrupole magnet as well. Since the first allowed multipole is dodecapole, one can expect its deviations to be much smaller than for the sextupole in the dipole magnets.

140
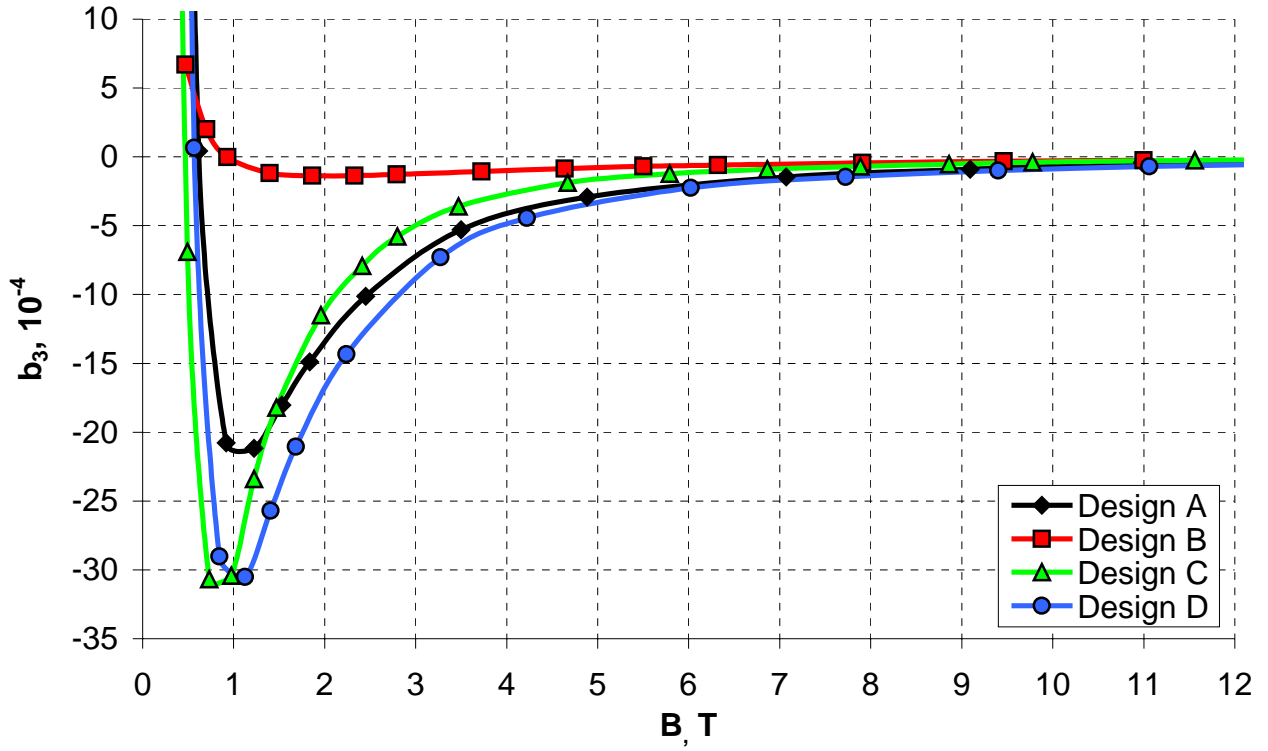
Figure 4.2.6. Deviations of the sextupole components as functions of the bore field.

Figure 4.2.7. Deviations of the decapole components as functions of the bore field.

Figure 4.2.8 shows one octant of the quadrupole magnet used in the simulation with the magnetization flux distribution at 44 T/m ($I_c = 3$ kA) bore gradient. The coil geometry and inner yoke surface were assumed the same as for quadrupole magnets considered earlier. It is notable that some part of magnetization flux, not coinciding with the quadrupole field, passes through the coil bore and causes the multipole deviations (Figure 4.2.9). Thus, b_6 and b_{10} components reach $-6.3 \c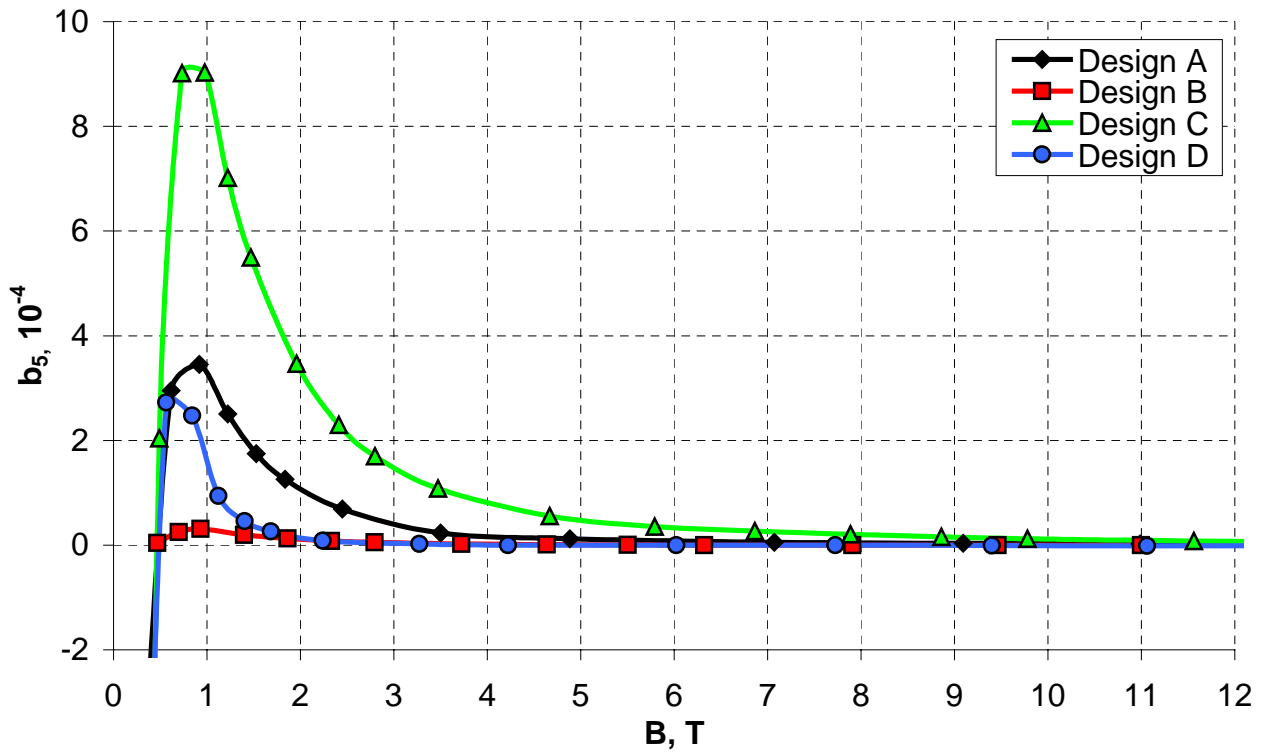dot 10^{-4}$ and $+0.2 \cdot 10^{-4}$ correspondingly at the bore gradient of 40 T/m, which are smaller than deviations of the sextupole and decapole components in the dipole magnets, yet by an order of magnitude larger than the yoke saturation effect.

The data indicate that all the considered magnets, except the single-layer common coil design, have a large persistent current effect. For the commercially available Nb_3Sn strands, the maximum value of sextupole ranges from $-20 \cdot 10^{-4}$ to $-30 \cdot 10^{-4}$ and the maximum value of decapole ranges from $+3 \cdot 10^{-4}$ to $+9 \cdot 10^{-4}$, depending on the dipole magnet geometry. Since the superconductor magnetization is proportional to $J_c \cdot D_{eff}$, the effect increases for the Nb_3Sn strands with higher J_c unless D_{eff} is proportionally reduced. In order to decrease the sextupole deviations to at least 10^{-3}, D_{eff} must be reduced from 120 μm to 30 μm.

The coil magnetization effect rapidly decreases with the ramp of the magnetic field. However, the sextupole is larger than 10^{-3} even at $B = 2$ T, therefore using a pre-injector based on iron-dominated magnets as suggested in [137] cannot solve the problem. It leads to the conclusion that in general, the coil magnetization effect in Nb_3Sn dipole and quadrupole magnets is the largest distortion of the field quality, which requires a strong correction.
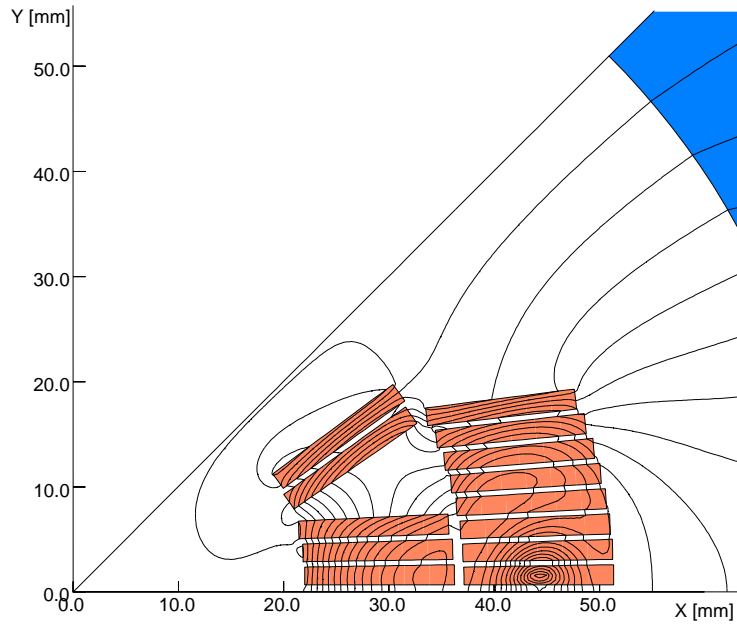
Figure 4.2.8. Cross-section of the quadrupole coil with the magnetization flux.
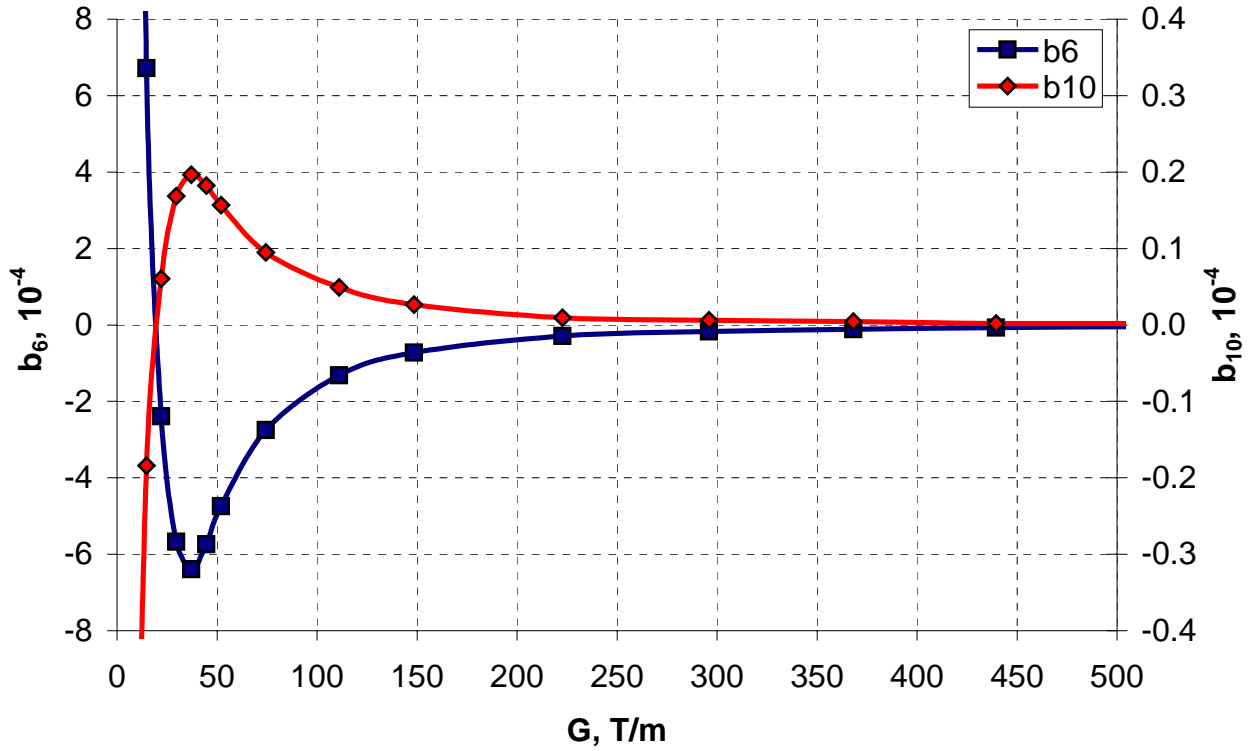
Figure 4.2.9. Deviations of the multipole components as functions of the bore gradient.

4.3 Passive correction of the coil magnetization effect

A study of passive correction based on ferromagnetic material was performed using the method of numerical simulation described. The idea was in arranging the iron strips (shims) in appropriate places in the magnet in order to correct the field deviations, generated by the coil magnetization effect. It was assumed that the strips material has magnetic properties identical to the iron yoke material.

4.3.1 Dipole magnets

Since the coil magnetization effect results in deviations of the allowed multipoles only – the correcting strips must be placed according to the main field symmetry as well. There are two places, which can be relatively easy accessed after manufacturing of the coil for installation of the correcting strips – the inner and outer coil surfaces. Figure 4.3.1 shows the coil and strip arrangement scheme used for simulation of these possibilities.
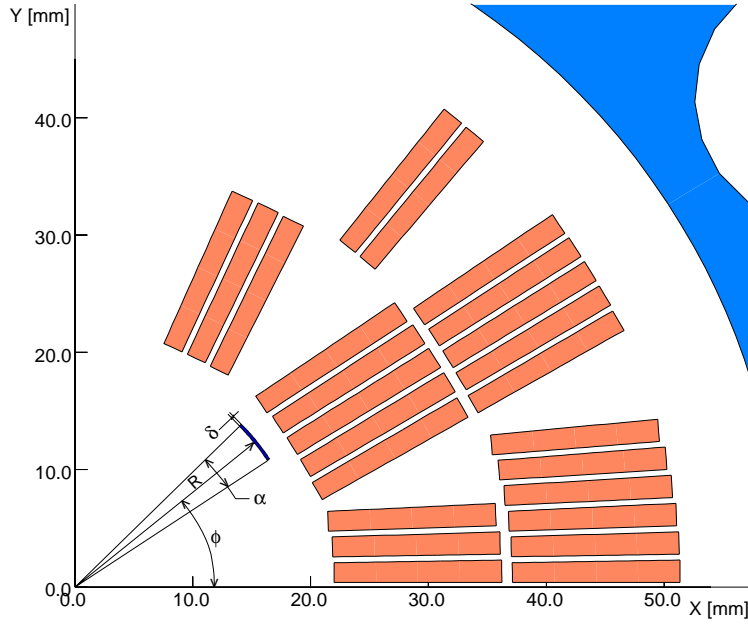
Figure 4.3.1. Correcting strip arrangement.

Initially, a strip with the angular dimension $\alpha = 7.5$ degrees was installed at the outer coil surface with $R = 52$ mm. Its thickness $\delta = 2$ mm was chosen small enough in order to avoid noticeable field map distortions. The strip azimuthal position ϕ was varied within $0 – 90$ degrees with the increment α to obtain continuous harmonic distributions. Figure 4.3.2 presents the sextupole and decapole deviations as functions of the strip position at 1.2 T bore field ($I_c = 2$ kA). The curves change signs within the specified region making it possible to choose a position for their simultaneous cancellation. An optimum strip position would be between 30 and 60 degrees, where the sextupole is positive and the decapole is negative [138]. However, due to a large distance from the region of interest, such strip should be about 7 mm thick if it spans the whole 30-60 degrees region in order to have a correcting effect adequate to the coil magnetization. Such thick strip (shell) would affect the field quality at high fields due to its saturation effect, as well as complicated the mechanical design making its implementation unreasonably difficult.

This idea was further developed in the LHC dipole magnet [139], where the coil protective sheet can be made from iron. Due to relatively small coil magnetization effect in the LHC NbTi magnet, 0.5 mm thick coil protective sheet provides the adequate correcting effect for the sextupole. However, the tuning capability of such sheet is practically limited by variation of its thickness only since the sheet should obviously have the same radial and angular dimensions as its stainless steel predecessor. Therefore, it does not allow simultaneous eliminating of the sextupole and decapole components. Moreover, the thermal contraction coefficient of pure iron is by 60 % smaller than that of the coil, when for the stainless steel it is smaller by only 10 %. Thus, during cooling down there would be large shear stresses generated between the coil, iron

sheet and the stainless steel collar, which could accidentally release enough energy to quench the magnet.

On the other hand, installation of the correcting strips on the inner coil surface or on the beam pipe would allow a significant reduction of their thickness and eliminated the thermal contraction problem. To study this possibility, the strip of angular dimension $\alpha = 7.5$ degrees was installed at the outer surface of the beam pipe with $R = 19.75$ mm. In this case, the strip of the thickness $\delta = 0.2$ mm provided the desired effect. Figure 4.3.3 shows the multipole distributions as functions of the strip azimuthal position. One can notice that simultaneous sextupole and decapole cancellation can be achieved within $50 - 75$ degrees region, where a strip with $\alpha = 7.5$ degrees provides adequate effect on both harmonics.

Cancellation of higher order multipoles can be done by optimization of several strips. It was found that two 0.14 mm thick correcting strips with azimuthal positions of $\phi_1 = 39$ degrees and $\phi_2 = 65$ degrees and azimuthal widths $\alpha_1 = 11$ degrees and $\alpha_2 = 15$ degrees provided simultaneous correction of $b_3 - b_7$. Figure 4.3.4 illustrates the strip arrangement with respect to the coil and Figure 4.3.5 presents the sextupole and decapole distributions before and after correction.
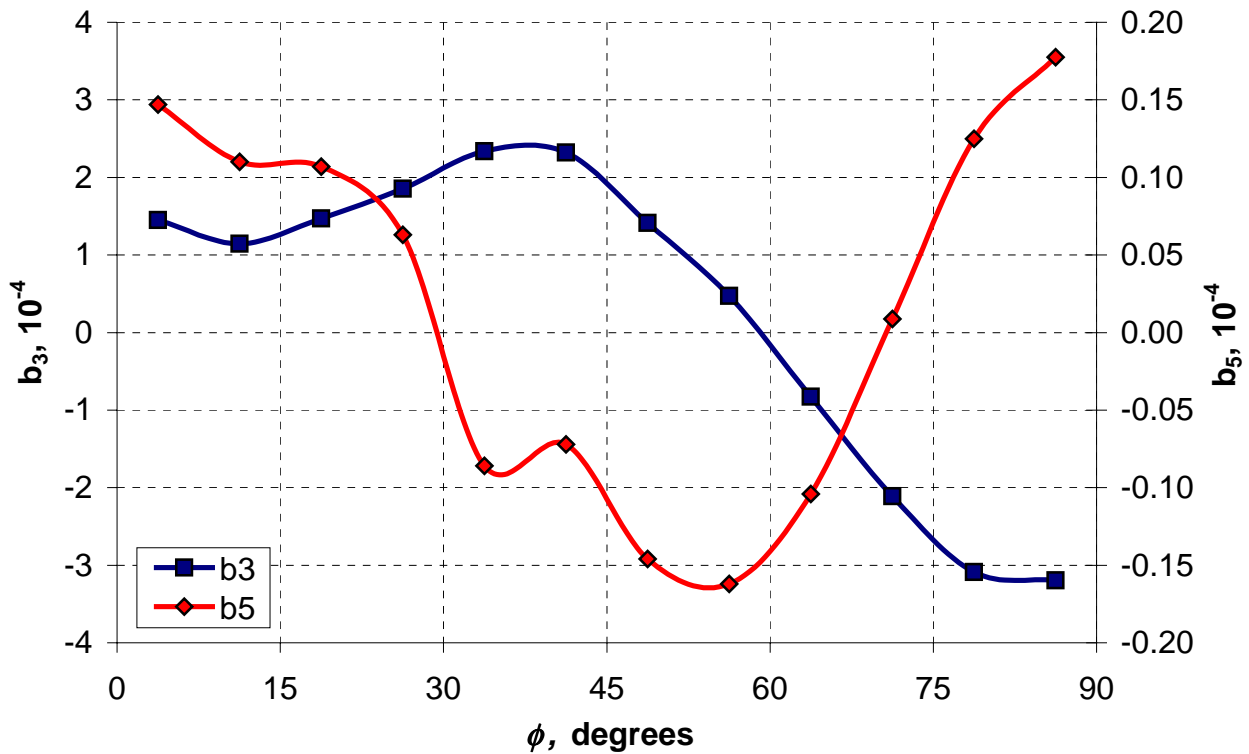
Figure 4.3.2. Multipole deviations as functions of the strip position.
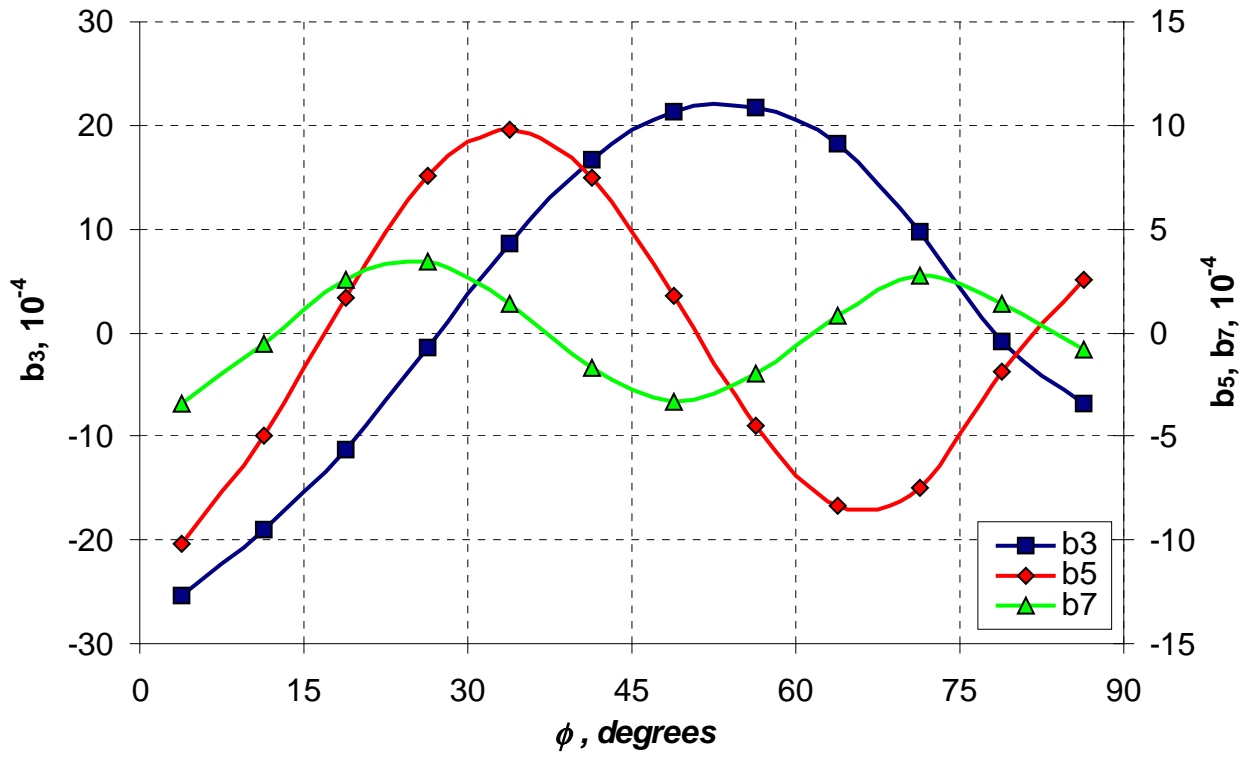
Figure 4.3.3. Multipole distributions as functions of the strip position.
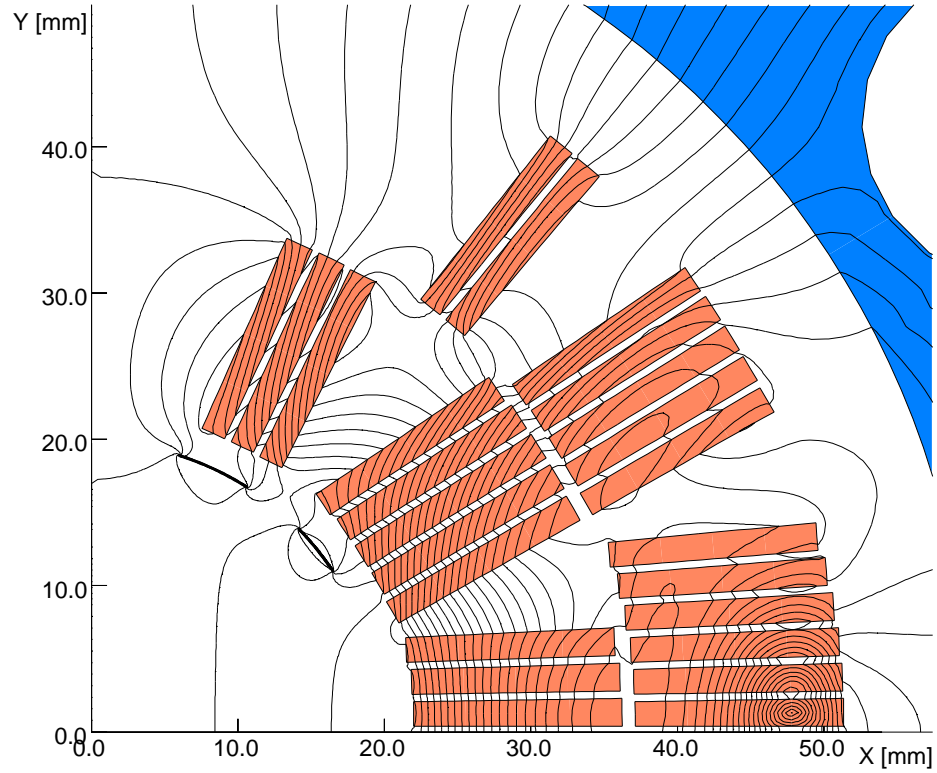
Figure 4.3.4. Strips arrangement with respect to the coil.

146
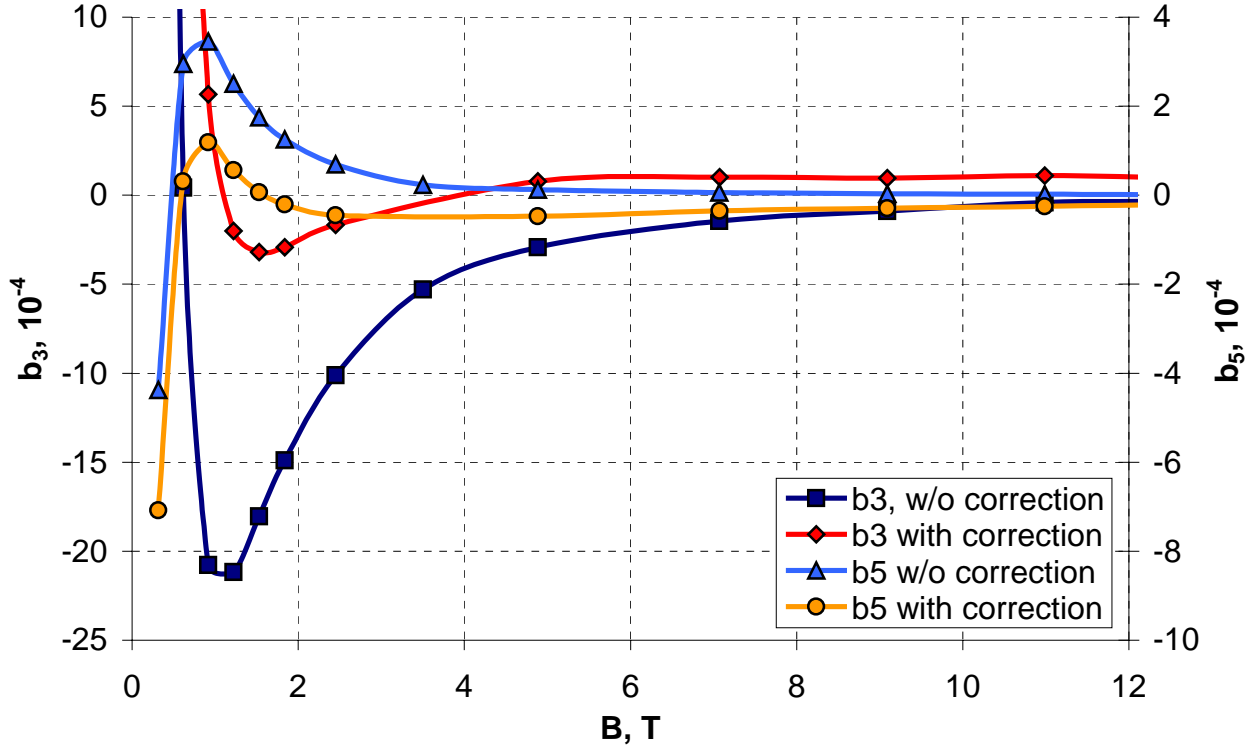
Figure 4.3.5. Multipole deviations as functions of the bore field.

It is notable that the correcting strips do not significantly reduce the magnetization flux passing through the aperture. Instead, they force the flux lines to be parallel to the vertical axis, decreasing the dipole component only, without affecting higher order harmonics. Thus, the strips allow reduction of the sextupole and decapole components by factors of 7 and 3 respectively at low fields, which makes them an attractive implementation for the Nb_3Sn dipole magnets.

The inner and outer coil surfaces are not the only places, acceptable for installation of the correcting strips. The strips can also be installed on the wedges, separating the coil blocks. In this case, however, number of the design parameters is reduced to one per strip, which is the strip thickness. Therefore, in order to eliminate several low-order harmonics and not to create additional distortions in others, one may need to use larger number of the correcting strips than in that of strips installed inside the coil aperture.

This possibility was evaluated using a semi-analytical approach. Initially, the iron strip with fixed 0.1 mm thickness was consequently aligned at every wedge surface of the inner coil layer and its effect to the harmonics was computed using the finite-element code along with effect of the coil magnetization (Figure 4.3.6). Table 4.3.1 presents the analyzed data with subtracted coil magnetization effect for every strip position at 1.2 T bore field (I_c = 2 kA), which comprised matrix of influence M used for analytical optimization.

Table 4.3.1. Influence of the strips installed on the wedges.

Strip number	Relative multipoles, 10^{-4}				
	b_3	b_5	b_7	b_9	b_{11}
1	5.0738	1.9507	0.4566	0.0686	0.0025
2	5.1564	2.0228	0.4327	0.0498	-0.0047
3	6.5934	-1.5439	-0.3183	0.0828	0.0140
4	4.2915	-2.0716	0.0382	0.0930	-0.0092
5	-4.0632	-0.4280	0.3731	-0.1036	0.0187

The solution corresponding to the optimum corrector geometry was found using the Levenberg-Marquardt method implemented in MathCad package solving the following system of equations:

$$\begin{cases} M_{i,j} \cdot K_i + P_j = H_j \\ K_i \geq 0 \\ K_i \to 0 \end{cases} , \; i \in 1...5 \; \text{for every} \; j \in 1...5,$$

where i is the number of strip, j is the number of harmonic, K_i is the scaling factor for i-th strip thickness, P_j is j-th multipole deviation due to the coil magnetization effect and H_j is the desired value of j-th multipole after correction. The last condition in the system minimized the thickness and number of the strips. After several iterative steps on refining values of K_i, solution with three strips per coil quadrant (numbers 2,3,5) was found. As the optimum thickness of strip 2 matched the thickness of strip 5 with 3 % accuracy, they were set to the same value for simplification. The strip arrangement within the coil is shown in Figure 4.3.7 and their thickness was 0.15, 0.27 and 0.15 mm from the midplane respectively. The field multipoles are presented in Figure 4.3.8. One can see that the correcting strips installed on the coil wedges have nearly the same effect as for the strips placed within the coil bore. Similarly to the previous case, the strips do not noticeably reduce magnetization flux passing through the coil bore, but reshape it appropriately.

The method based on the strips installed within the coil aperture has a good flexibility. It allows manufacturing several correctors with a different magnetic strength and geometry and testing them with available dipole magnets, which is beneficial at the stage of magnet R&D. However in terms of the magnet mass production, the second approach with the strips installed on the coil wedges is preferable as it assures automatic strip alignment during the coil winding and requires minimum changes in coil production technology. The different thermal contraction issue can be resolved by making cuts across the strip length as its integrity does not required. There was also proposed a correcting method based on ferromagnetic pipe in coil aperture [140]. However, the analysis and comparison [141] shown that such method had rather low correcting capability with respect to the separate iron strips and allowed effective reduction of only one harmonic.
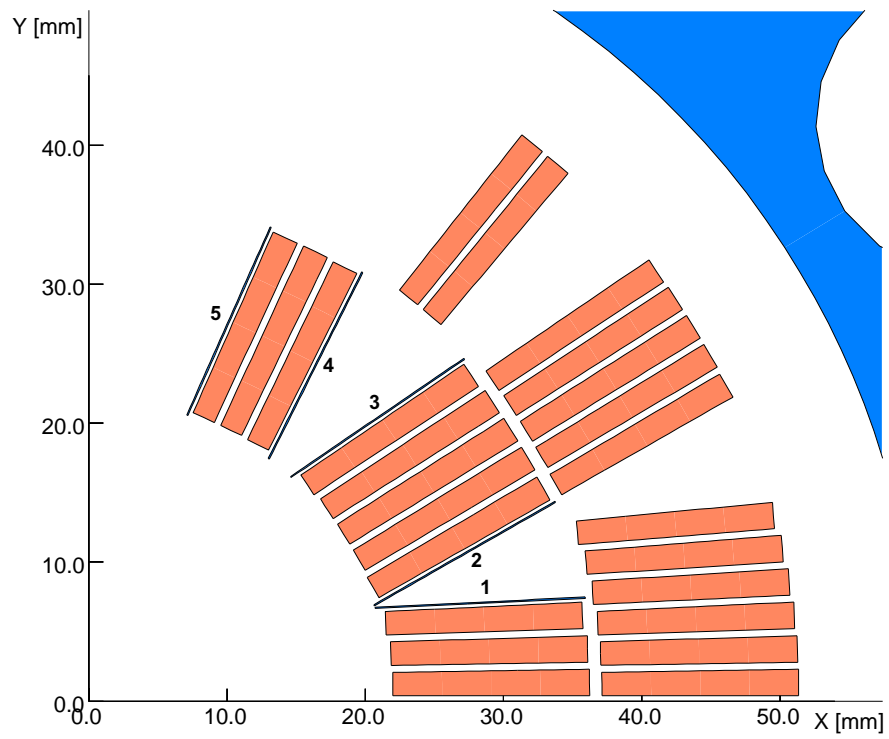
Figure 4.3.6. Correcting strips arrangement within the coil.
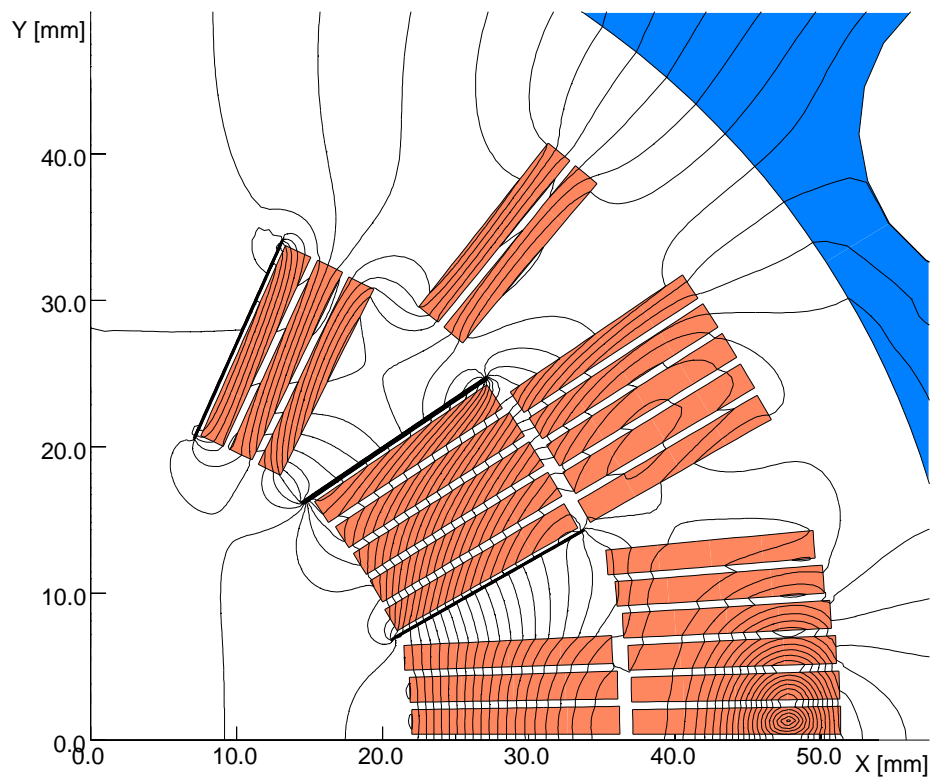
Figure 4.3.7. Optimized strips geometry.

149
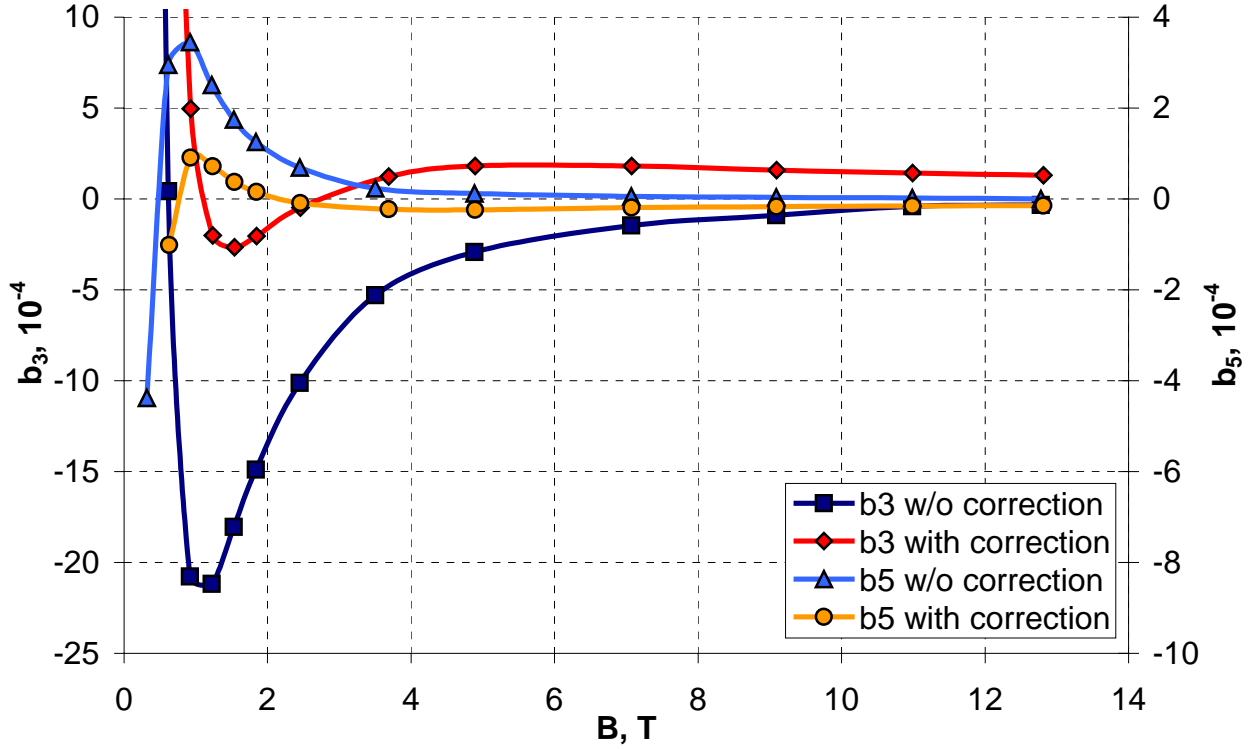
Figure 4.3.8. Multipole deviations as functions of the bore field.

4.3.2 Quadrupole magnets

A study of passive correction was performed for the quadrupole magnets as well. The correction by strips installed on the beam pipe surface was considered first. One correcting strip with the angular width $\alpha = 3$ degrees and thickness $\delta = 0.1$ mm was aligned on the circular surface with the radius $R = 19.75$ mm. The azimuthal strip position ϕ was varied within 0-45 degrees with α increment.

Figure 4.3.9 presents effect of the strip on the first two allowed by the quadrupole symmetry multipoles at the bore gradient of 44 T/m ($I_c = 3$ kA). Similarly to the dipole magnet there is a region where b_6 is positive and b_{10} is negative, which makes it possible to use one strip for correction of both harmonics. The optimum strip parameters in this case are: $\phi = 26.65$ degrees, $\alpha = 4.7$ degrees and $\delta = 0.1$ mm. Arrangement of the strip within the coil bore is shown in Figure 4.3.10 and its correcting effect is presented in Figure 4.3.11.

It was possible to reduce the coil magnetization effect on b_6 and b_{10} by factors of 7 and 3 respectively at low gradients that proves high efficiency of the passive correction for the quadrupole magnets as well.
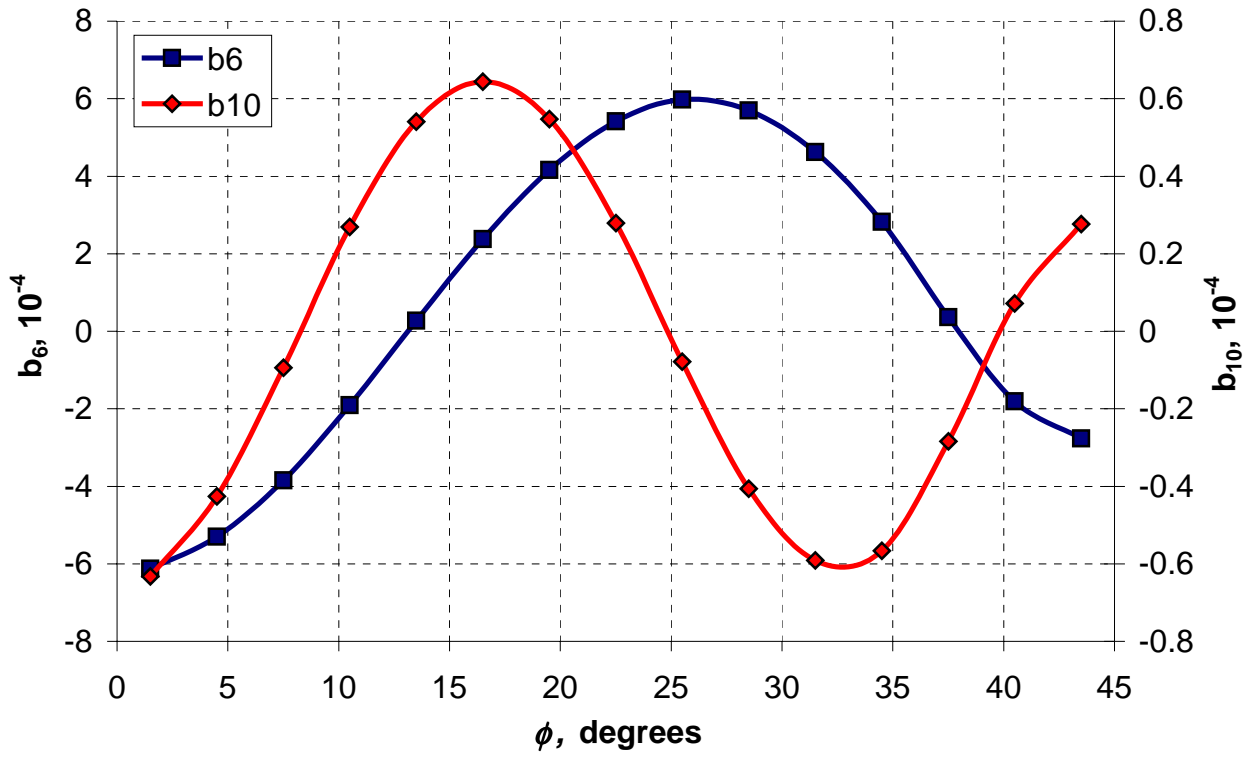
Figure 4.3.9. Multipole deviations as functions of the strip position.
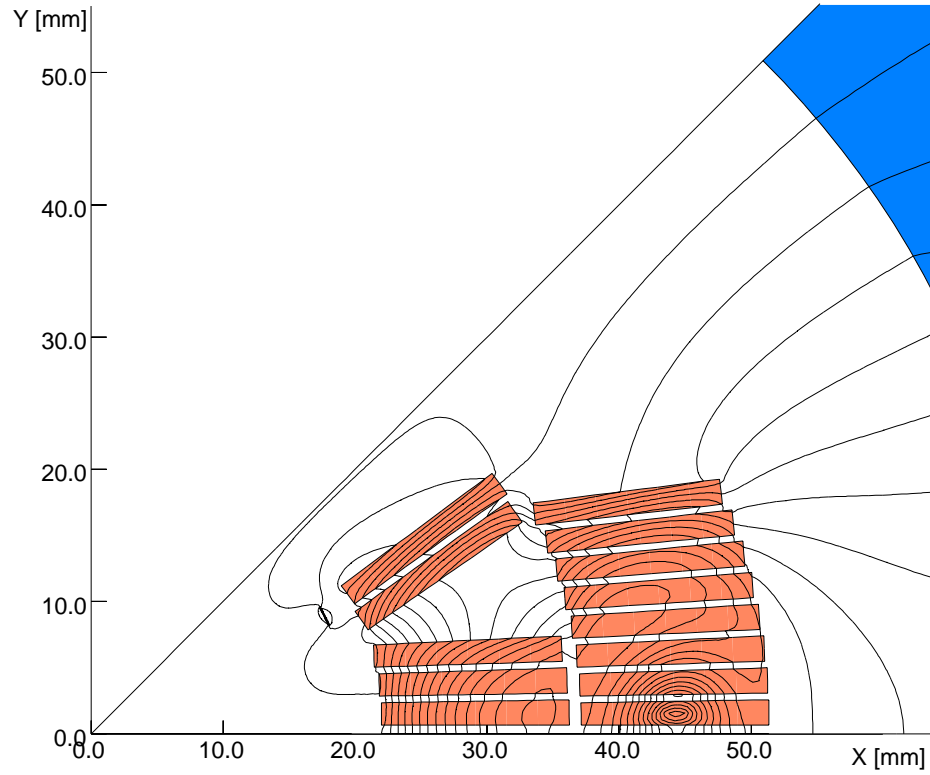
Figure 4.2.10. Optimized strip position.
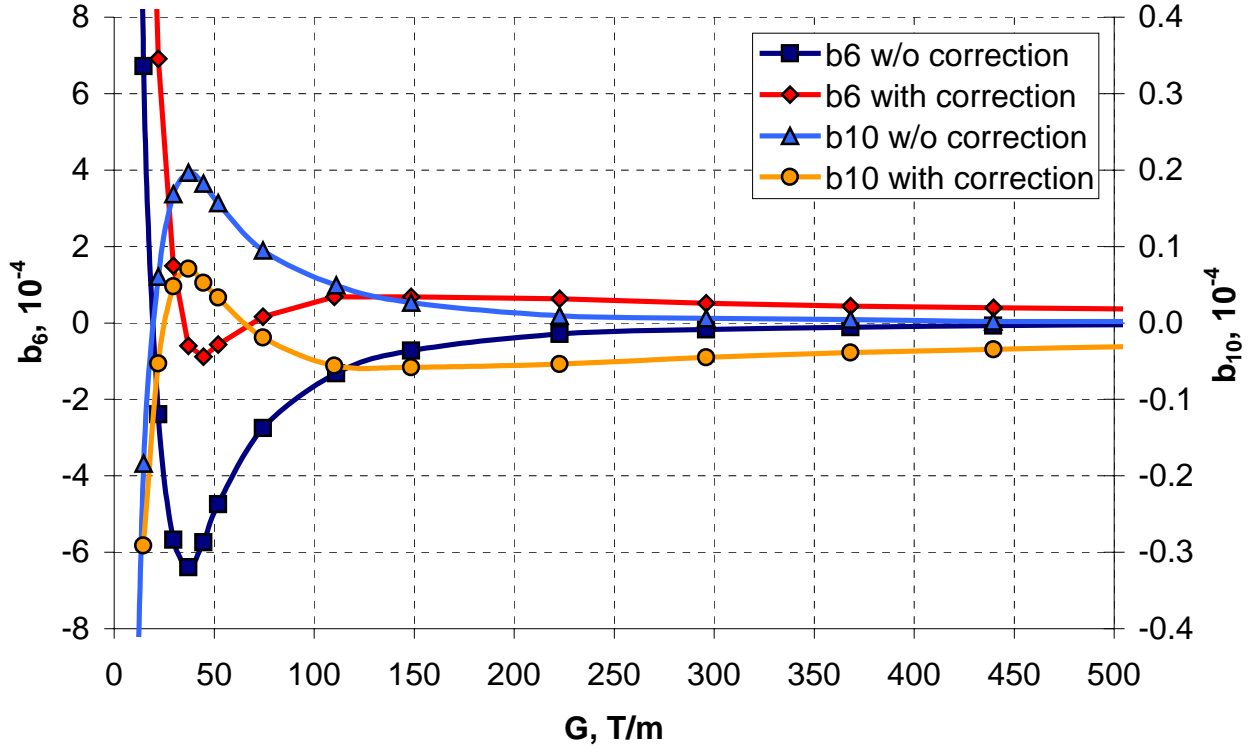
Figure 4.2.11. Multipole deviations as functions of the bore gradient.

A possibility to install the correcting strips on the coil wedges was studied in a way similar to the dipole magnet. Due to smaller number of harmonics needed correction in the quadrupole magnet and relatively small effect of the coil magnetization – only one strip per coil octant was considered.

It was found that an optimum location of the strip is on the upper surface of the wedge in the inner layer. The strip thickness was optimized so that its effect on b_6 is nearly equal to the previously considered case. The optimum strip thickness was 0.09 mm. Arrangement of the correcting strip inside of the coil and its effect on the field multipoles are shown in Figures 4.3.12-4.3.13.

It is notable that the correcting strip forces the magnetization flux to coincide with the quadrupole symmetry, when it affects only the main field component. The strip does not significantly reduce the b_{10} field component, which is relatively small and presumably acceptable without correction. Should one need to reduce it as well – two strips per coil octant can be optimized for simultaneous b_6 and b_{10} compensation.
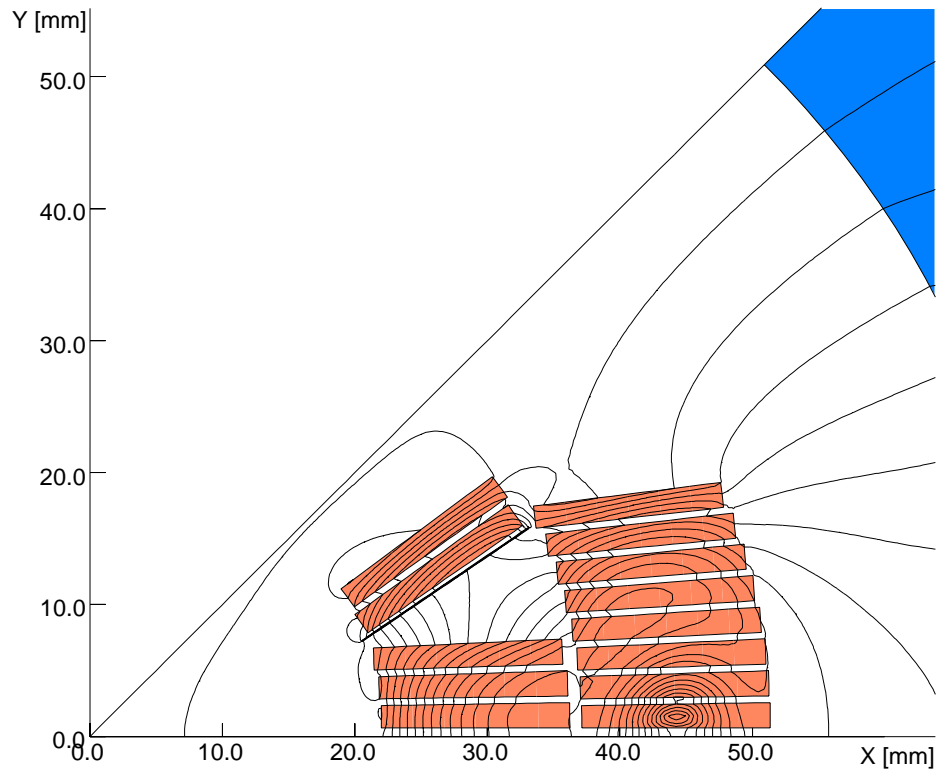
Figure 4.3.12. Optimized strip position within the coil.
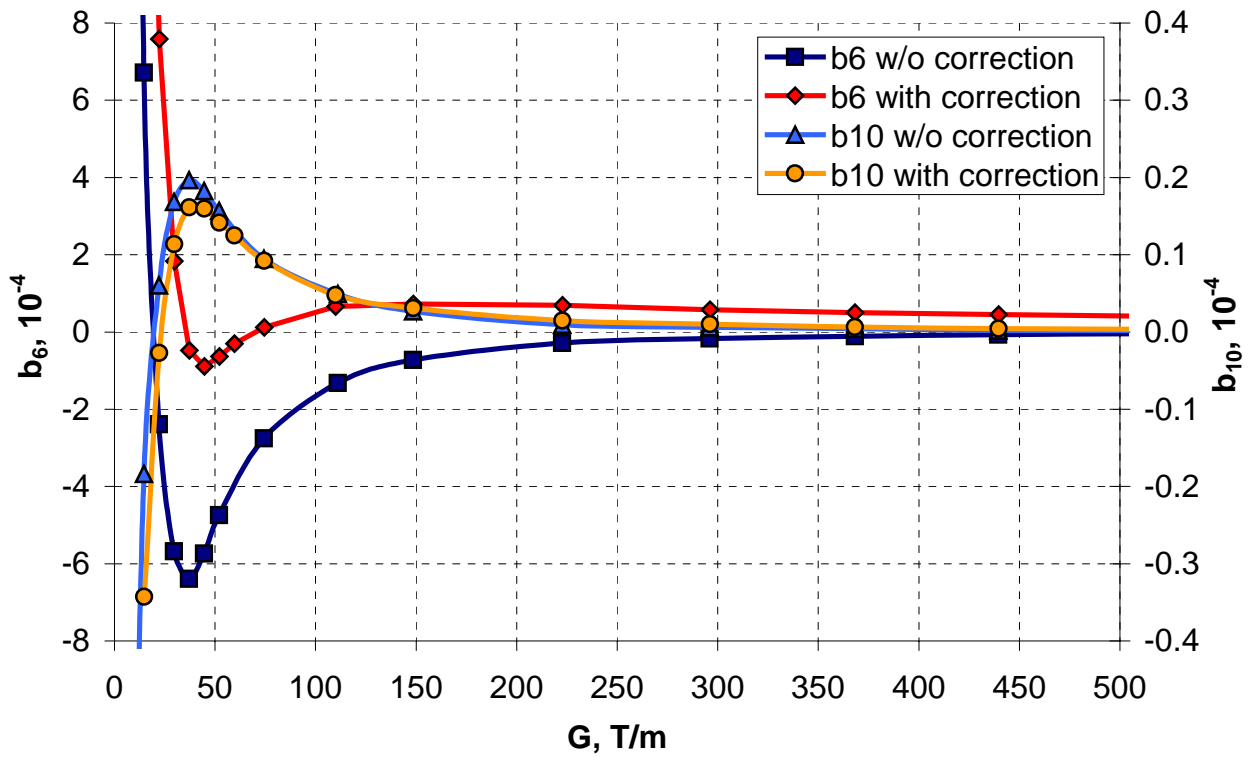
Figure 4.3.13. Multipole deviations as functions of the bore gradient.

4.4 Internal compensation of the cable magnetization

The method of passive correction of the coil magnetization effect using iron strips, placed within the coil bore or to the coil wedges has rather good correcting capability. In this approach, a significant distance separates the source of correcting effect from the source of unwanted magnetization. In case of misalignment between the sources, the correcting strips can produce additional allowed and unallowed by the coil symmetry harmonics. In addition, the number of correcting strips growth proportionally to the number of multipoles to be corrected, making it reasonable to correct only few low-order harmonics.

Another possibility of the passive correction is based on mixing the sources of magnetization and opposite to it correcting effect. It can be achieved by equal distribution of the correcting material within the coil, cable or strand, depending on required and technically achievable powers of discretization. For instance, the correcting material can be applied on strand surfaces as a thin film using electroplating or sputtering techniques. Alternatively, it can be implemented inside the Rutherford type cable as a core between two layers of strands during the cable manufacturing or between the cables during the coil winding [142].

In any of these cases one can talk about the internal <u>compensation</u> of the coil magnetization effect, not affected by misalignment between the two sources, when the compensation simultaneously occurs for all the field multipoles (for high enough discretization). Magnetic properties of the compensating material obviously must be opposite to the properties of the superconductor. Ideally it should be positive for the up ramp and negative for the down ramp, or switch from paramagnetic to diamagnetic behavior depending on the ramp sign. Since there are no magnetic materials with similar or at least close properties, one has to stick with compensating at up ramp only that imposes using of the ferromagnetic materials.

Amount of ferromagnetic material that would compensate magnetization effect of superconducting cable with bare area S_{cable} can be determined analytically. Flux density in any material can be expressed in terms of the field strength and magnetization:

$$\vec{B} = \mu_0 \cdot \vec{H} + \vec{M}.$$
(4.4.1)

Assuming that the cable is made of strands with magnetization per strand $M_{sc}(H)$ and packing factor of the strands in the cable λ_{str}, one can consider ferromagnetic material with magnetization $M_{fe}(H)$ and packing factor λ_{fe}, which is equally distributed within the cable by some technological process. The cable area and strands packing factor are assumed unchanged after addition of the correcting material that is correct for relatively small amount of the added

material. In case when vectors $\vec{M}$ and $\vec{H}$ are collinear (field pattern in the coil does not change from cycle to cycle), the total flux density inside the cable is:

$$B(H) = \mu_0 \cdot H + \lambda_{sc} \cdot M_{sc}\left(\frac{H}{\lambda_{sc}}\right) + \lambda_{fe} \cdot M_{fe}\left(\frac{H}{\lambda_{fe}}\right). \tag{4.4.2}$$

Since $M_{sc}(H)$ and $M_{fe}(H)$ are not exactly inverse functions, the full compensation can be provided only at some reference field H_{ref}. It means the flux density at H_{ref} in the superconducting cable with ferromagnetic material inside should be equal to the flux density of non-magnetic material:

$$B(H_{ref}) = \mu_0 \cdot H_{ref}. \tag{4.4.3}$$

Subtracting (4.4.3) from (4.4.2) at $H = H_{ref}$ one can find the packing factor of ferromagnetic material inside of the cable:

$$\lambda_{fe} = -\lambda_{sc} \cdot \frac{M_{sc}(H_{ref} / \lambda_{sc})}{M_{fe}(H_{ref} / \lambda_{fe})}. \tag{4.4.4}$$

The amount of ferromagnetic material was calculated using the reference magnetization curve of the Nb$_3$Sn strand in the second cycle (Figure 4.1.1). As a reference field was taken $\mu_0 H_{ref} =$ 3.7 T, when $M_{sc} = $ -0.073 T. Ferromagnetic coating had magnetic properties of steel used for the magnet iron yokes, with saturation magnetization $M_{fe} = 2.12$ T (Figure 2.2.1). Packing factor of the strands within the Rutherford type cable, used in the shell type magnets is $\lambda_{sc} = 0.88$. Then the packing factor of ferromagnetic material within the cable is $\lambda_{fe} = 0.030$ or just 3.0 %.

Figure 4.4.1 illustrates the magnetization curves after applying of the relevant packing factors. It is notable that the iron can be treated as a material with constant magnetization for fields higher than ~ 0.2 T. Thus, it shifts the superconductor magnetization curve by a constant value $\lambda_{fe}M_{fe}$ that is truly beneficial for correction of the coil magnetization effect at low fields. However, the coil magnetization virtually vanishes at high fields, while ferromagnetic still generates the same $\lambda_{fe}M_{fe}$, leading to overcompensation. A way to avoid this problem is discussed in next paragraph.

If the cable consists of N strands with the diameter D_{str}, and the ferromagnetic material is introduced using the strands coating, the thickness of such coating would be:

$$\Delta_{fe} = \frac{\sqrt{\dfrac{4 \cdot \lambda_{fe} \cdot S_{cable}}{N \cdot \pi} + D_{str}^2} - D_{str}}{2}. \tag{4.4.5}$$
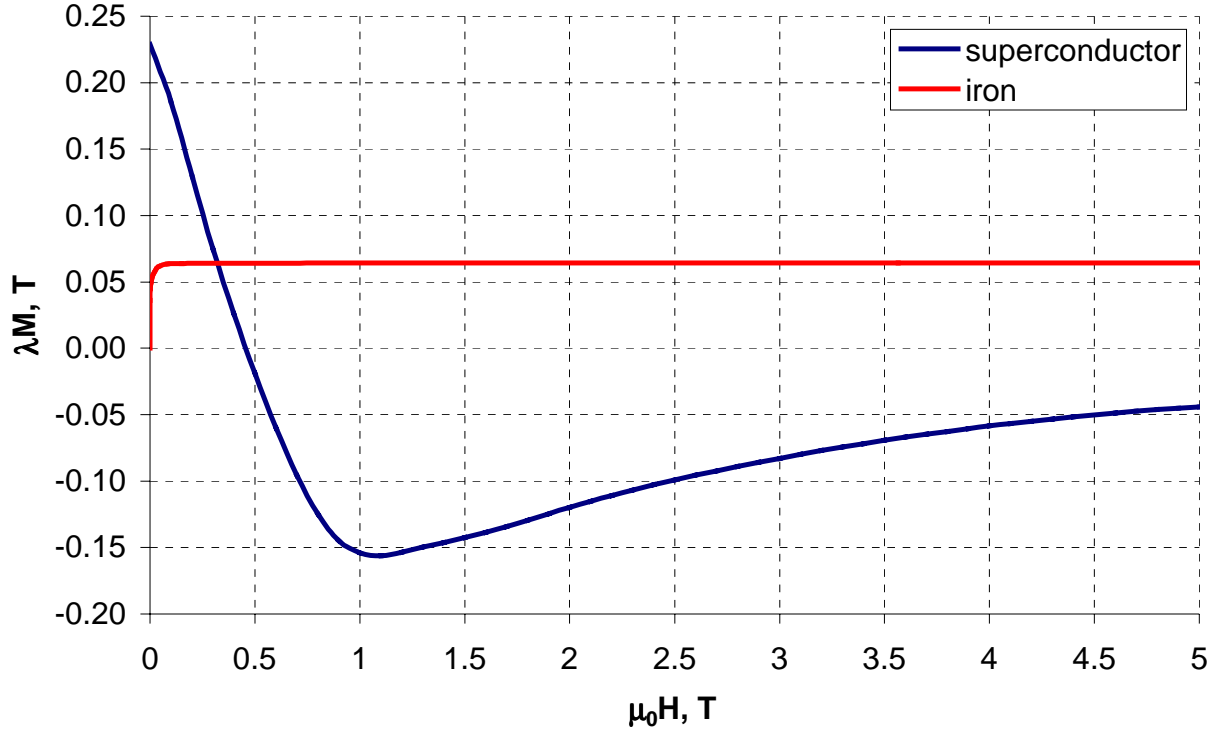
Figure 4.4.1. Superconductor and iron magnetization as function of the applied field.

For the Rutherford cable used in the shell type magnets, the cable area is $S_{cable} = 25.6$ mm^2 and the thickness of the strand coating is 8.6 microns for compensation of the superconductor magnetization at $\mu_0 H_{ref} = 3.7$ T.

If the ferromagnetic material is introduced as a foil core inside the cable – cross-section area of the core must be:

$$S_{fe} = \lambda_{fe} \cdot S_{cable},$$

giving is 0.77 mm^2 for the specified cable area. Thus if the core width, for example, equals to the cable width its thickness must be 54 μm.

One should notice that the above estimations are based on the assumption that the field distribution within the cable and coil is uniform. In reality, the field varies from the peak value in the pole turn to almost zero in the midplane block of the outer layer. Therefore, ideally every turn in the coil requires different amounts of the ferromagnetic material to eliminate its magnetization, otherwise leading to non-uniform compensation of the magnetization and harmonics.   Practically it would be difficult to accomplish, especially in the case with ferromagnetic core inside the cable, when two layers of the coil are wound from one piece of the cable without the interlayer splice.

To confirm a possibility of compensation the coil magnetization effect by iron core of uniform thickness inside the cable, a finite element OPERA2D model based on the optimized shell-type dipole magnet was analyzed. Width of the cable core in this model was assumed equal to the cable width and its thickness was optimized in order to have zero integral effect on the sextupole component at $\mu_0 H_{ref} = 3.7$ T. The optimum thickness was 57 μm. This number is by 5 % larger than the one determined analytically, obviously due to the non-uniform coil magnetization. However, the difference is not too large that allows using the analytical approach for a fast estimation of the compensating effect.

Figure 4.4.2 shows the model geometry with the magnetization flux lines and Figure 4.4.3 presents distribution of the field multipoles. The correction capability for the sextupole component is essentially the same as with the strips inside the aperture, when there is virtually no effect on the decapole. This is due to the uniform distribution of ferromagnetic materials in the cables, when there is only one power of freedom during optimization (strip thickness), making it possible to effectively eliminate only one harmonic. However, taking into account relatively small deviations of the decapole component, one can consider this method as effective for reduction of the coil magnetization effect as the strips installed on beam pipe or on the coil wedges. There is also a possibility of introduction ferromagnetic material inside of the coil during winding in form of the iron strips between the cables with equal efficiency [142].
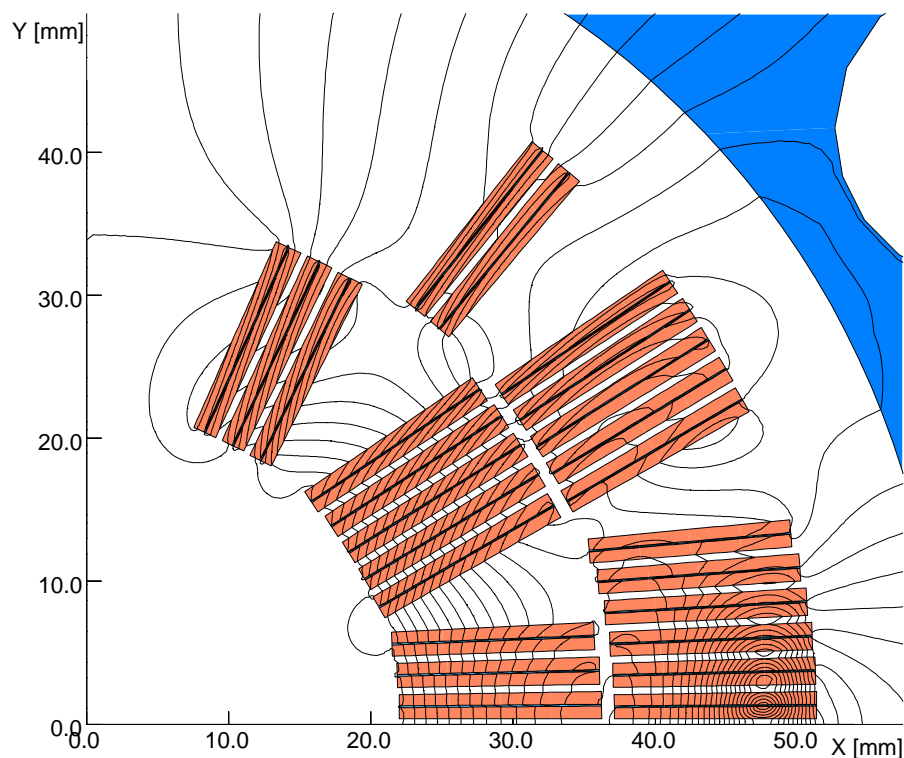
Figure 4.4.2. Compensation of the coil magnetization by iron core inside the cable.
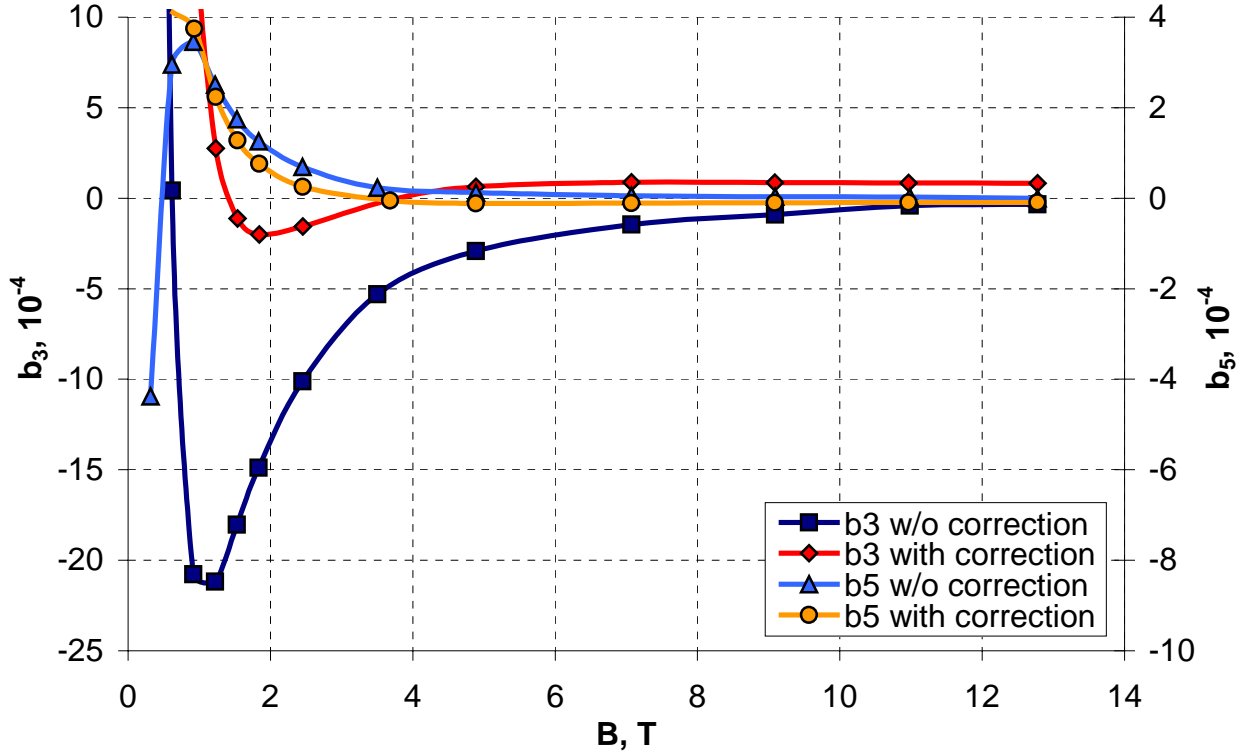
Figure 4.4.3. Multipole deviations as functions of the bore field.

4.5 Combination of the passive correction with the coil geometry optimization

The data presented in previous paragraphs show that the passive correction of the coil magnetization effect is effective at low fields. However, it makes a positive overcompensation at high fields that may need a correction itself. To understand efficiency of the passive correction within the operating field range, it is convenient to represent multipoles in absolute units, where the active corrector strength is a straight line, parallel to the horizontal axis.

Figure 4.5.1 illustrates the sextupole curves with and without the passive correction (by strips inside the cable) as well as the active corrector contribution. The active sextupole corrector should have the maximum strength of $B_3 = \pm 1$ mT/cm^2 in order to eliminate the sextupole component, remaining after the passive correction within 1 - 11 T field region. The active corrector has to work in the bipolar mode, which is not well-suited regime for the superconducting magnet. In addition, the maximum active corrector strength is driven by the passive overcompensation at high fields. Nonetheless, just the passive correction itself allows reduction of the active corrector strength by factor of 2.8 with respect to the non-corrected case that proves its efficiency. Furthermore, as follows from Figure 4.5.1, the positive part of the corrected sextupole curve can be quite well approximated by a straight line. Since geometrical

multipoles (defined by the coil geometry) in absolute units are the straight lines, proportional to the field - a cancellation of the linear sextupole part at high fields can be accomplished by introducing an appropriate geometrical harmonic.

Figure 4.5.2 shows the result of introduction the geometrical sextupole ($b_3 = -0.86 \cdot 10^{-4}$), which virtually eliminates the magnetization sextupole for fields above 6 T. Then the required maximum of the active sextupole corrector strength is reduced to $B_3 = 0.6$ mT/cm^2. In this case the active corrector does not reverse polarity and can be switched off after the field reaches 6 T.

The geometrical correction was also considered for the case without the passive correction. Figure 4.5.3 shows result of introduction the geometrical sextupole ($b_3 = 0.66 \cdot 10^{-4}$) that cancels the non-corrected sextupole at 11 T field. The minimum on the sextupole curve at low fields virtually does not change due to a small effect of the geometrical component at low field.

Finally, Figure 4.5.4 presents the sextupole deviations corrected geometrically in one case and using combination of geometrical and passive corrections in another. One can see that in the case with passive and geometrical correction the maximum strength of the active sextupole corrector is by factor of 4.5 smaller than in the case with the geometrical only correction. In addition, the active corrector has to operate in 1-6 T region in the case with passive correction and in 1-11 T region in the case without passive correction.
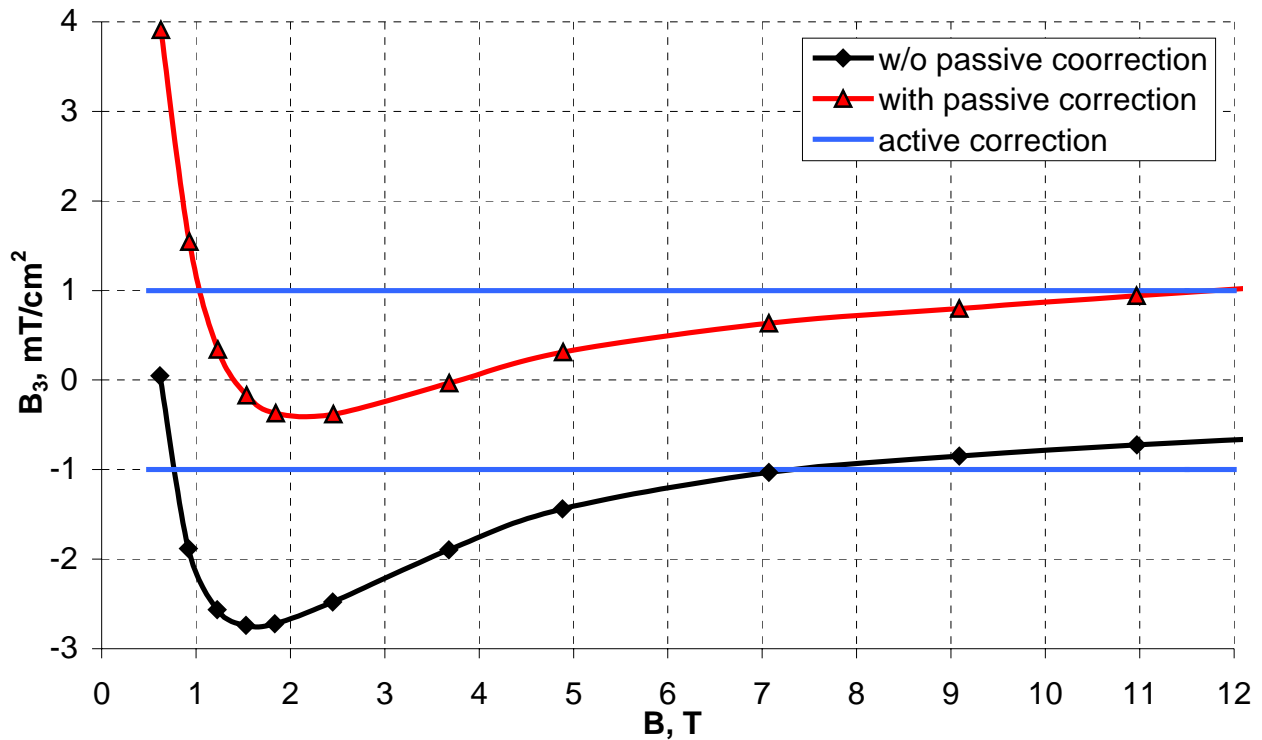
Figure 4.5.1. Absolute sextupole components as functions of the bore field.
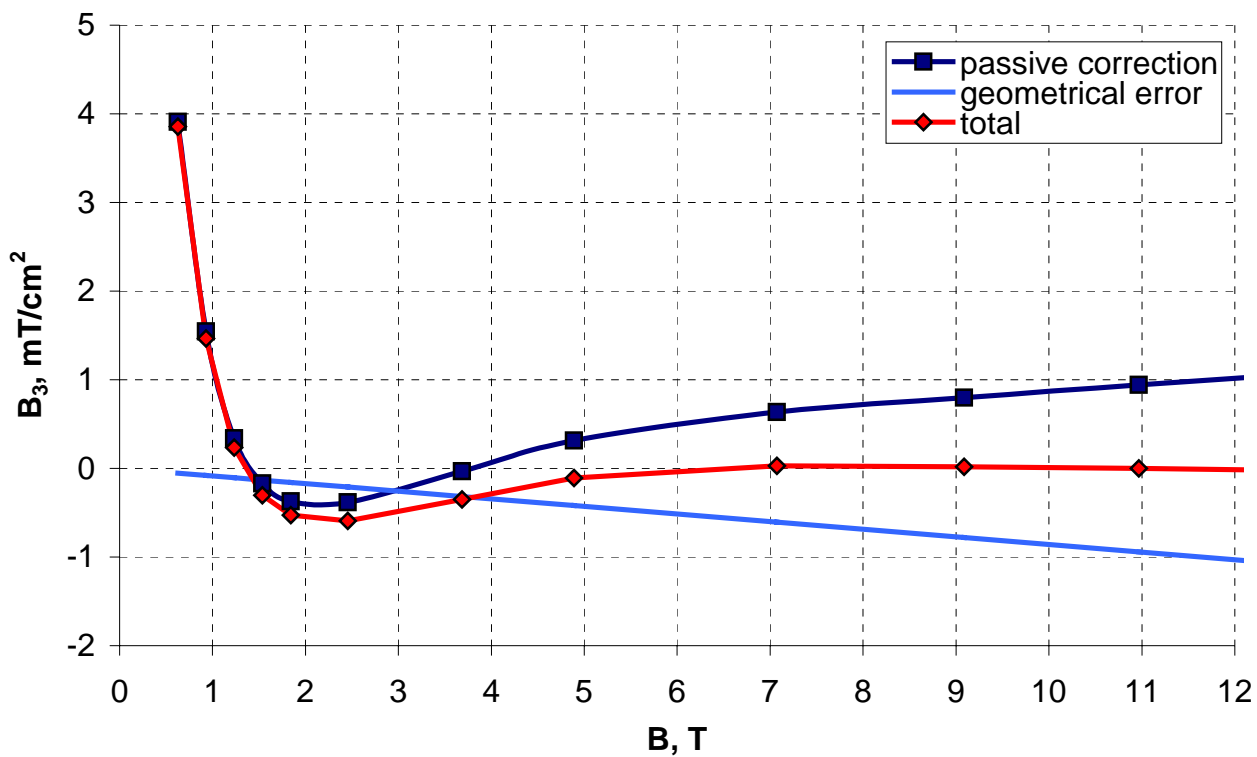
Figure 4.5.2. Absolute sextupole components as functions of the bore field.
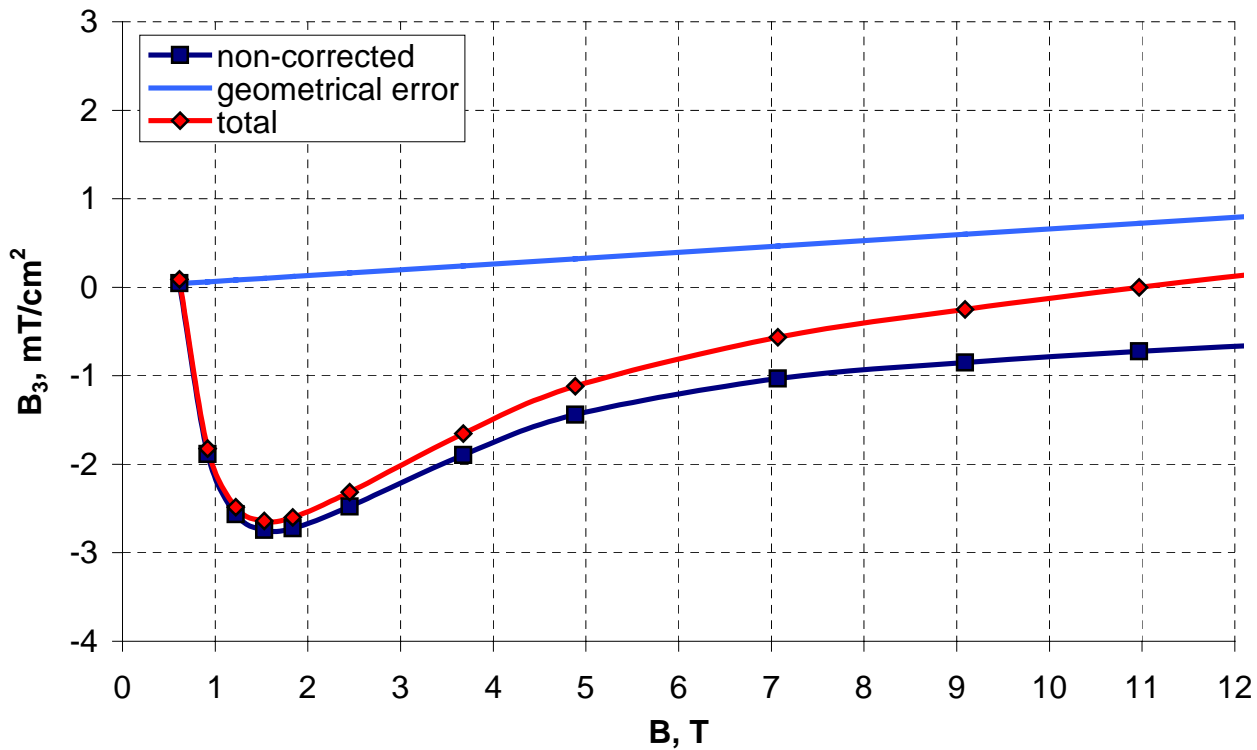
Figure 4.5.3. Absolute sextupole components as functions of the bore field.
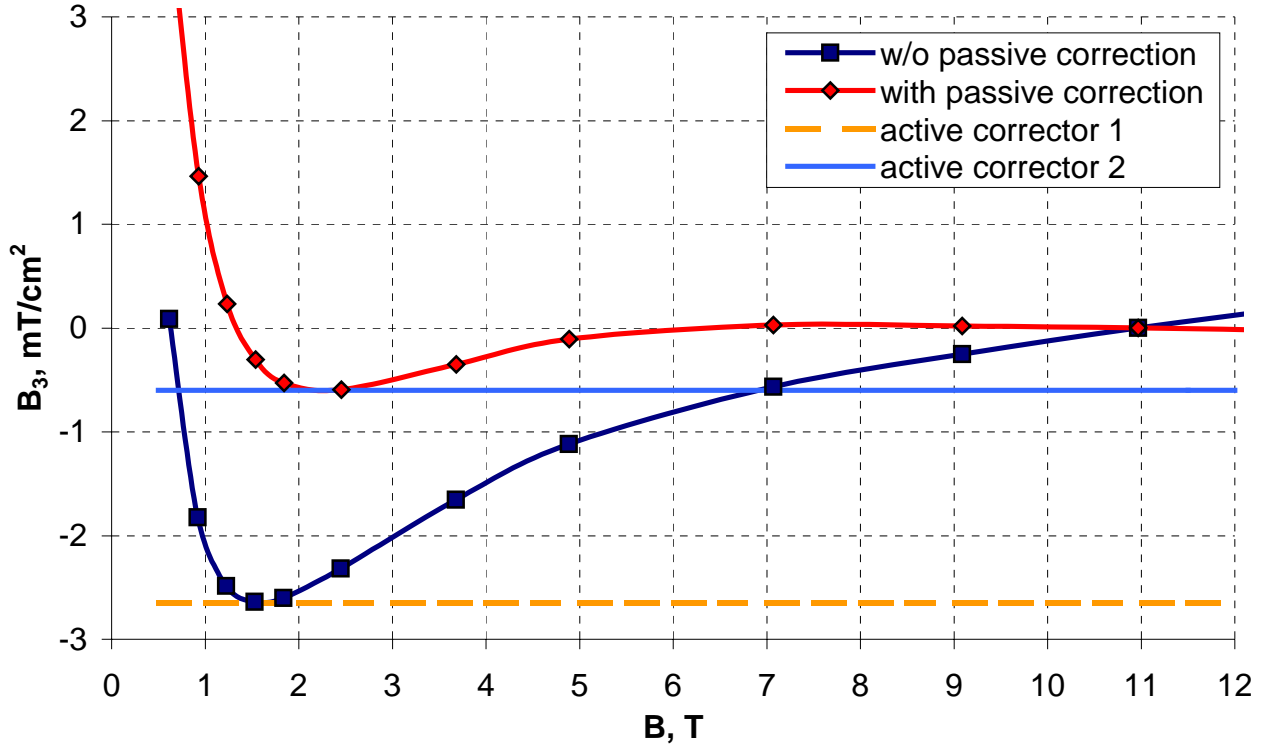
Figure 4.5.4. Absolute sextupole components as functions of the bore field.

These observations prove high efficiency of the proposed passive correction method of the coil magnetization effect that along with the coil geometry optimization offers considerable improvement of the field quality.

4.6 Sensitivity analysis of the passive correctors

Small distance between the passive corrector and the good field region makes proper alignment of the corrector an important issue. In order to evaluate acceptable tolerances on alignment, depending on the corrector configuration, a sensitivity analysis using OPERA2D code was performed [143]. The bore field was chosen close to the minimum on sextupole curve (1.2 T), where the corrector is most required.

The passive corrector installed within the coil aperture with the nominal configuration described in paragraph 4.3.1 was considered first. Tables 4.6.1-4.6.2 show the multipole sensitivity to the major symmetrical (one-quadrant symmetry) and asymmetrical misalignments between the corrector and the coil. The field is most sensitive to the thickness of the strips, which should be controlled with better than 7 μm (or 3 % of strip thickness) accuracy in order to keep the sextupole deviations within 10^{-4}.

Table 4.6.1. Multipole increments due to the corrector symmetric misalignment.

Errors in position	Increment in multipoles, 10^{-4}/mm	
	Δb_3	Δa_5
Azimuthal	3.4	0.2
Radial	2.5	4.4
Strip width	7.2	2.4
Strip thickness	179.0	74.2

Table 4.6.2. Multipole increments due to the corrector asymmetric misalignment.

Errors in position	Increment in multipoles, 10^{-4}/mm								
	Δb_2	Δb_3	Δb_4	Δb_5	Δa_1	Δa_2	Δa_3	Δa_4	Δa_5
Pipe horizontal	7.4	0.24	1.32	0.24	0	0	0	0	0
Pipe vertical	0	0	0	0	0	7.4	0	1.08	0
Pipe azimuthal	0	0.32	0	0.1	0.90	0	6.24	0	0.78
One strip angular	0.5	0.72	1.00	0.20	0.08	1.04	0.96	0.18	0.74

It does not look like a serious restriction since there are foils available on the market from different manufacturers rolled down with better than 1 μm precision. The strip width should be controlled with better than 0.1 mm accuracy that also looks easy to accomplish. Azimuthal and radial strip alignment should be set with better than 0.2 mm and 0.1 mm accuracy for the symmetric displacements and better than 0.1 mm for the asymmetric. Meeting these requirements can be a problem for a long magnet, where the corrector position is controlled only at the magnet ends. However, this problem can be overcome by attaching the strips to the inner coil surface, which is to be controlled with better than 50 μm accuracy due to the geometrical field quality requirements.

In case of the strips installed on the coil wedges or inside (outside) the cables, the proper alignment is automatically achieved by controlling the coil geometry. Moreover, deviations of unallowed magnetization multipoles in case of the coil block misplacements would be cancelled by the proportional misplacements of the correcting strips, since sources of magnetizing and correcting effects are mechanically linked together. Thus, possible errors in these cases are reduced to variations of the strip thickness only. Sensitivity of the sextupole component to the strip thickness variation inside of the cable is $\Delta b_3 = 414 \cdot 10^{-4}$ 1/mm that is a factor of two larger than for the strips installed in the aperture. The tolerance on the strip thickness in this case is 2.5 μm (or 4 % of the strip thickness), which is acceptable.

Field sensitivity to variation of the strip magnetic properties was estimated by introducing the anisotropy (different magnetization along and across the strip cross-section) for the strip material. In many cases, the magnetization along the sheet of the foil is close to the one for a

bulk material, when the magnetization across depends on the amount of applied "cold" work. For the rolled down foils it can be by factor of 3÷5 smaller than magnetization along the strip.

The case when passive corrector is made of material with a ratio of magnetization along over across the strip of 1/0.2 was considered for the corrector inside the coil aperture. Deviations of the sextupole and decapole components with respect to the case with the isotropic material were $\Delta b_3 = 0.81 \cdot 10^{-4}$ and $\Delta b_5 = 1.40 \cdot 10^{-4}$. The decapole deviations exceed 10^{-4} threshold. Nevertheless, the known material anisotropy can be easily taken into account during corrector optimization leaving only a question about variations of magnetic properties from one roll of foil to another. A relatively small amount of corrector material required for 233 km VLHC ring (~25 tons in case of corrector inside the coil aperture and ~250 tons when it is inside the cable) makes it possible to produce from a single or low number of casts that would ensure equal magnetic properties in all the strips.

4.7 Summary

Results of analysis the coil magnetization effect and methods of its passive correction can be summarized as follows:

- Considered and numerically verified the method of simulation the coil magnetization effect, based on the finite-element code, which allows precise simulation of all the magnetic elements. Using this method, there was performed analysis of the coil magnetization effect in different magnet designs.

- Analysis of the coil magnetization effect in the dipole and quadrupole magnets has demonstrated that for commercially available Nb_3Sn strands, the coil magnetization effect exceeds other distortions (such as the iron saturation effect) by factor of 10-30. Expected reduction of the effective filament diameter to an order of 30-40 μm will not lead to an essential reduction of the magnetization due to the current density increase. It proves a necessity of development methods for the correction of the coil magnetization effect.

- It was found that the reason of large coil magnetization effect in the dipole magnets of TAMU and BNL is in presence of the auxiliary coils, adjacent to the aperture. Flat boundary of the iron yoke, parallel to the horizontal axis does not eliminate the coil magnetization flux, flowing through the aperture and therefore does not improve the field quality.

- Proposed simple, effective and cheap methods of passive correction the coil magnetization effect, base on thin iron strips. Considered and numerically verified possibilities of

installation the passive corrector inside of the aperture, outside of the coil and on the coil wedges. The passive correctors were parametrically studied that allows designing of the corrector geometry depending on the necessary effect. Demonstrated that the most efficient is the corrector inside the aperture, which provides the adequate effect at the minimum self volume. However, the post precise is the corrector on the coil wedges, whose proper geometry is automatically creates during coil manufacturing.

- Proposed an alternative method of the passive compensation the coil magnetization effect using ferromagnetic material. The iron strips, introduced inside of the cable or between the cables produce effect on the sextupole component, equal to the corrector inside the aperture. Compensation of the coil magnetization effect can be conveniently combined with reduction of the eddy currents, choosing the ferromagnetic core material with high specific resistance. In this case, there is automatic corrector alignment during coil fabrication as well.

- It was shown that using the proposed methods of the passive correction, strength of an additional active sextupole corrector reduces by a factor of 2.8. In this case, strength of the active corrector is driven by the passive overcompensation at high fields. Proposed the method, further enhancing the passive corrector effect by small adjustment of the coil geometry, which along with the passive correction provides reduction of the active corrector strength by factor of 4.7. In this case, participation of the active corrector is not required starting from 6 T field.

- The sensitivity analysis demonstrated that the field quality is most sensitive to the strip thickness variation, which in case of the corrector inside the aperture should be manufactured with better than 7 μm accuracy on order to keep the field quality within 10^{-4}. The strip width and corrector position variations should not exceed 0.1-0.2 mm, depending on the displacement. The ferromagnetic strip inside the cable should be made with better than 2.5 μm accuracy. Magnetic properties of the material can be controlled well due to its relatively small amount.

CHAPTER 5. DEVELOPMENT AND TEST OF SHORT NB$_3$SN DIPOLE MODELS

5.1 Introduction

A series of short dipole models have been built and tested at Fermilab in order to optimize the manufacturing technology, determine reproducibility of the magnet performance and verify the calculation results. All the magnets were based on the two-layer shell type coils with 43.5 mm bore diameter described in Chapter 1 and the single bore yoke geometry described in Chapter 3.

The coil ends were optimized by the code BEND [144] in order to minimize internal stresses in cables at the coil ends [145]. Optimization of the coil ends for minimum integral field harmonics have not been done for these models, but foreseen in the future.

5.2 Magnet 3D simulation and optimization

Due to the cost saving reasons, the short models should have the smallest possible length without affecting the field quality in the magnet straight section. In addition, the coil peak field, which determines the magnet quench performance should be within the straight section and not in the coil ends in order for the magnet to work at its maximum efficiency. It forced using of finite-element code OPERA3D for simulation and optimization of the coil and yoke geometry.

A preliminary coil length of 1 m (shoe to shoe) was chosen. The coil 3D geometry used in the simulation is presented in Figure 5.2.1 along with the right Cartesian coordinate system for the field representation (origin is at the coil geometrical center). A particular attention was paid on precise simulation of the coil ends and transition from the inner to outer layer.

At the first step, the field distribution was calculated at 18 kA current for different yoke lengths. Figure 5.2.2 shows the peak field distributions along the inner pole turn in the coil return end (field in the lead end is smaller) as functions of the longitudinal coordinate for different half-yoke lengths. The maximum field in the coil end occurs at zero yoke length due to a lack of the iron contribution in the magnet straight section and also prevails for long yoke lengths due to larger contribution of the yoke in coil ends. Obviously, it is preferable to have longest possible yoke length, while the peak field occurs within the straight section.

Figure 5.2.3 shows the peak field distribution as a function of the half-yoke length. One can see that for the iron yoke longer than 690 mm, the peak field in return end becomes larger than in the straight section. Thus, it was considered as an upper boundary for the iron yoke length, which should not be exceeded. The yoke length fixed set at 600 mm, providing 8 % peak field margin.
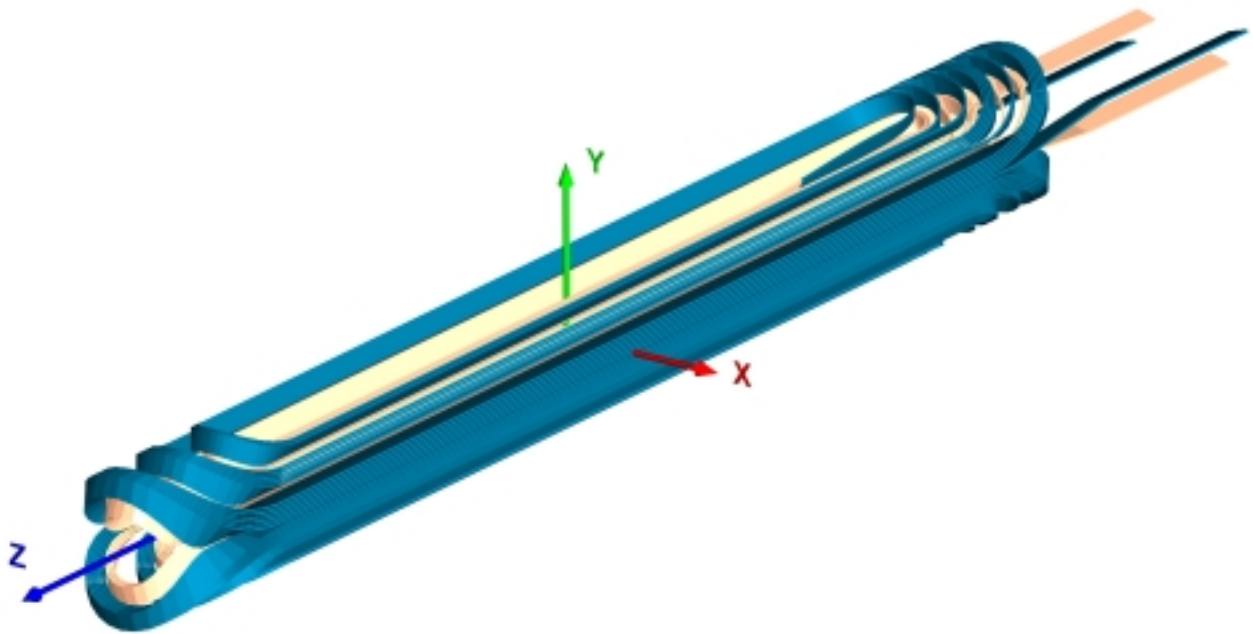
Figure 5.2.1. Coil 3D geometry.
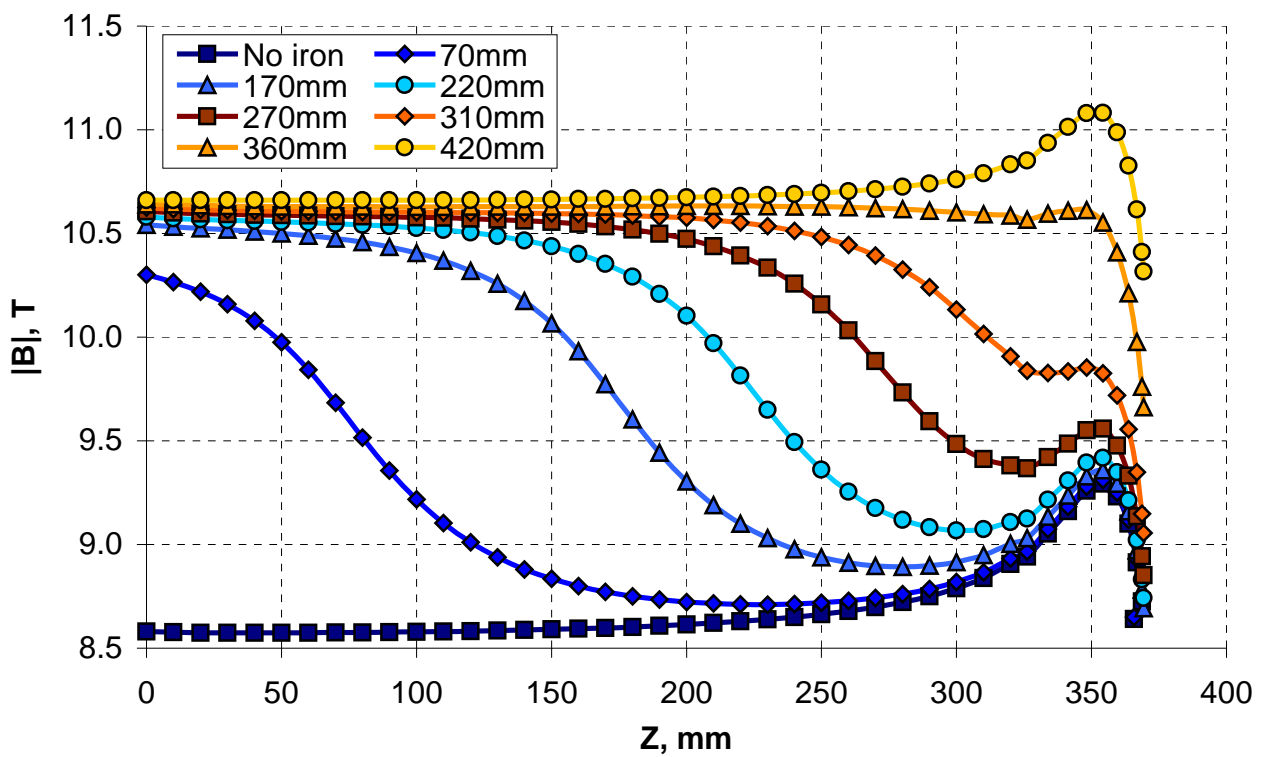
Figure 5.2.2 Peak fields as functions of the longitudinal coordinate.
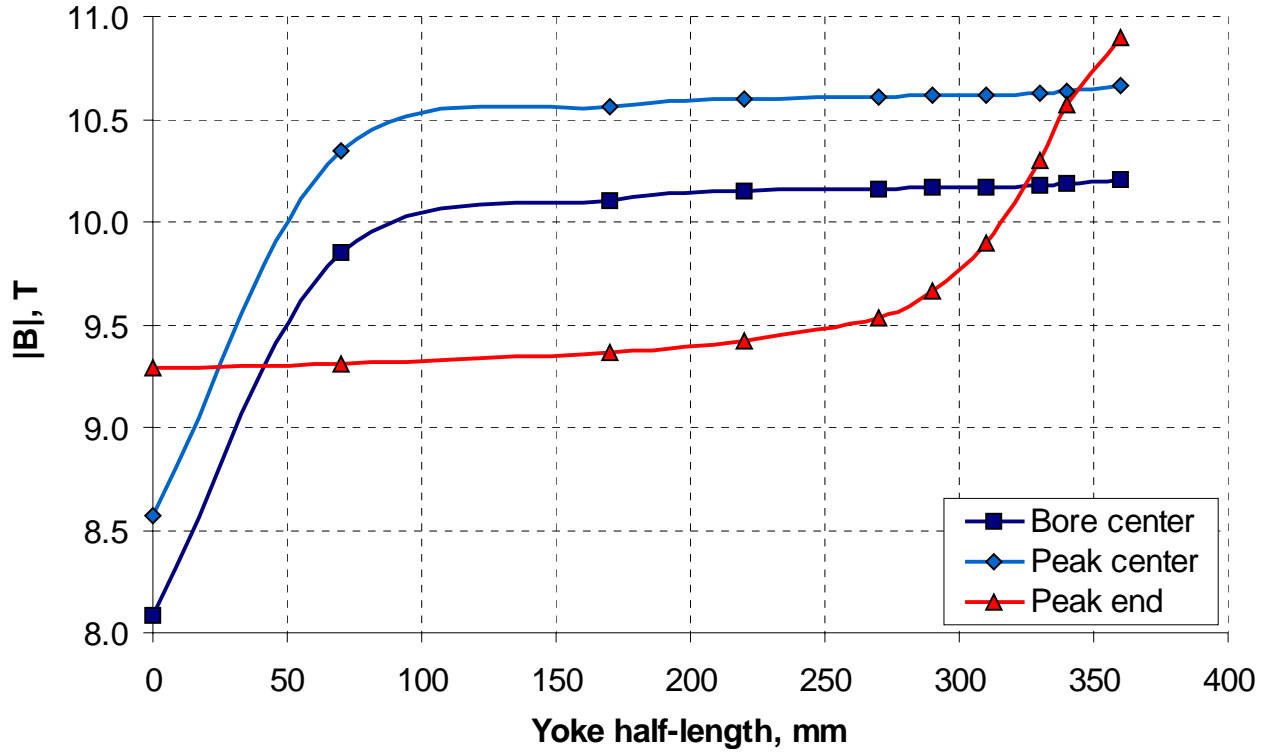
Figure 5.2.3. Peak fields as a function of the yoke half-length.

Figure 5.2.4 shows the magnet 3D geometry with the chosen yoke length (one yoke quadrant is removed for clarity) and the flux density distribution in the iron at 18 kA current. Although 3D field quality optimization was not a goal at this stage of R&D, it was necessary to determine the field quality for comparison with results of magnetic measurements. The 3D finite-element model with optimized iron yoke length was used for this purpose. Since the field quality simulation required higher accuracy than for the peak field simulations, several iterations on verifying accuracy of the field calculations and refinement the model were performed. The first iterations established the element subdivisions in the central part by comparison of harmonics between 2D and 3D simulations in the XY plane (Z=0). Then the subdivisions in the coil end regions were found by comparison of longitudinal harmonics in 3D cases without iron yoke, calculated by integration of the conductor field (analytically) and from the finite-element mesh. A general accuracy of better than 10^{-5} was achieved along the coil bore, which was considered precise enough for this type of simulation.

Figure 5.2.5 presents distribution of the dipole field component in longitudinal direction and Figures 5.2.6-5.2.7 show the low order geometrical harmonics, related to the dipole field component at Z=0 and 1 kA current. Table 5.2.1 summarizes the integrated longitudinal harmonics, normalized by the model magnetic length of 809.38 mm.

Component: |B|, T
0.2286   2.8079   5.3873
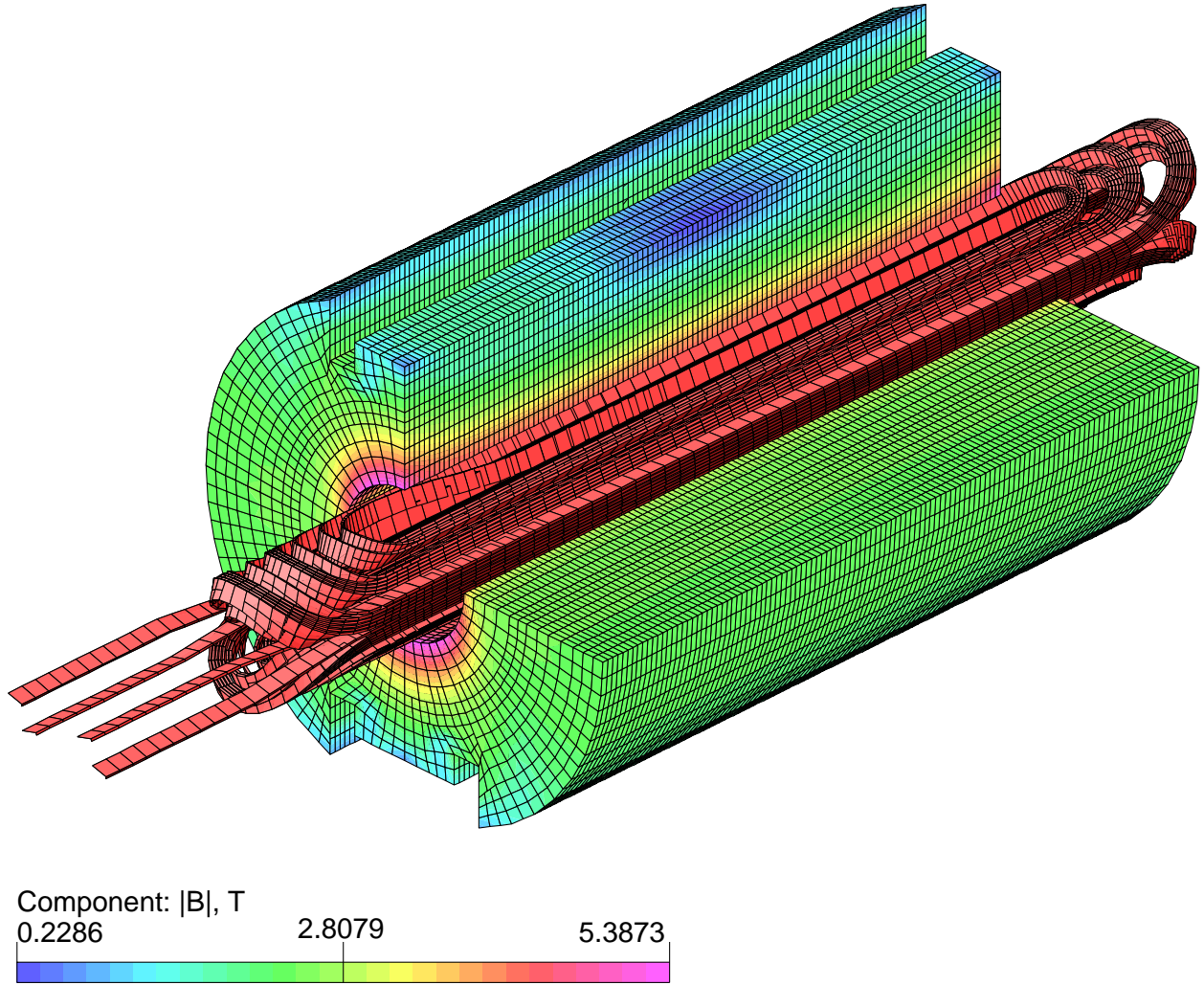
Figure 5.2.4. The magnet 3D finite-element model.

One can see that the top-bottom asymmetry in the coil lead end causes unallowed in 2D case skew multipoles. In addition, the cable bending at both coil ends produced deviations in normal harmonics. Thus, integrated skew dipole and normal sextuple components reach $22 \cdot 10^{-4}$ and $17 \cdot 10^{-4}$ respectively for 1 m long model. In case of a longer model they would be proportionally smaller, still reaching $\sim 10^{-4}$ for the magnet length of 15-20 m. Therefore, optimization of 3D coil geometry will be necessary to improve the integral field quality.
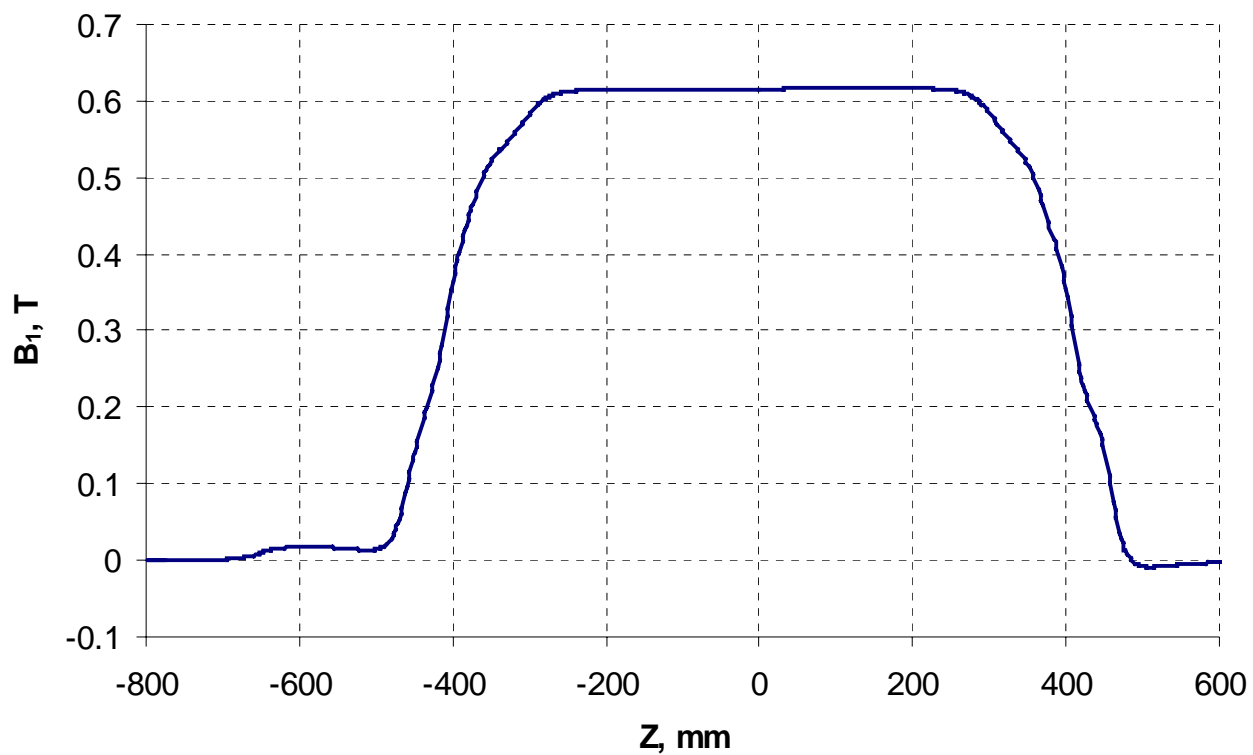
Figure 5.2.5 Dipole component deviations in longitudinal direction.
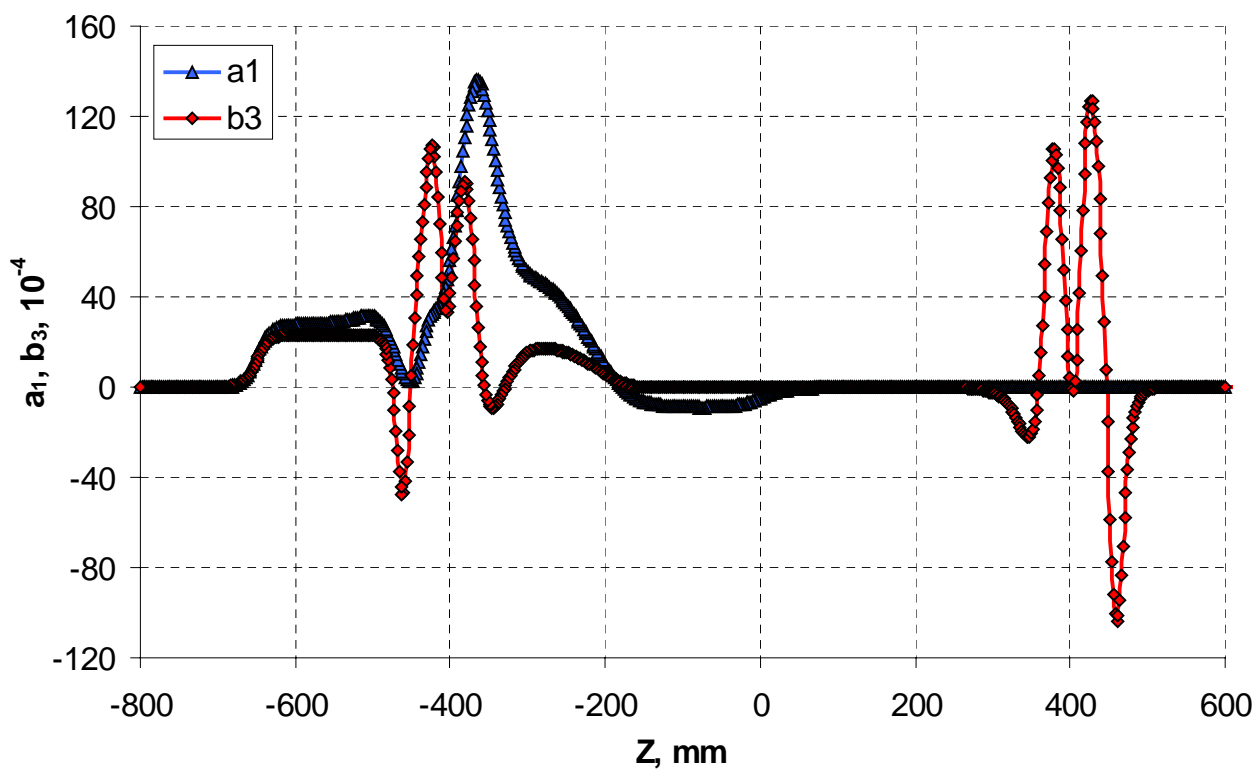
Figure 5.2.6 Skew dipole and sextupole deviations in longitudinal direction.
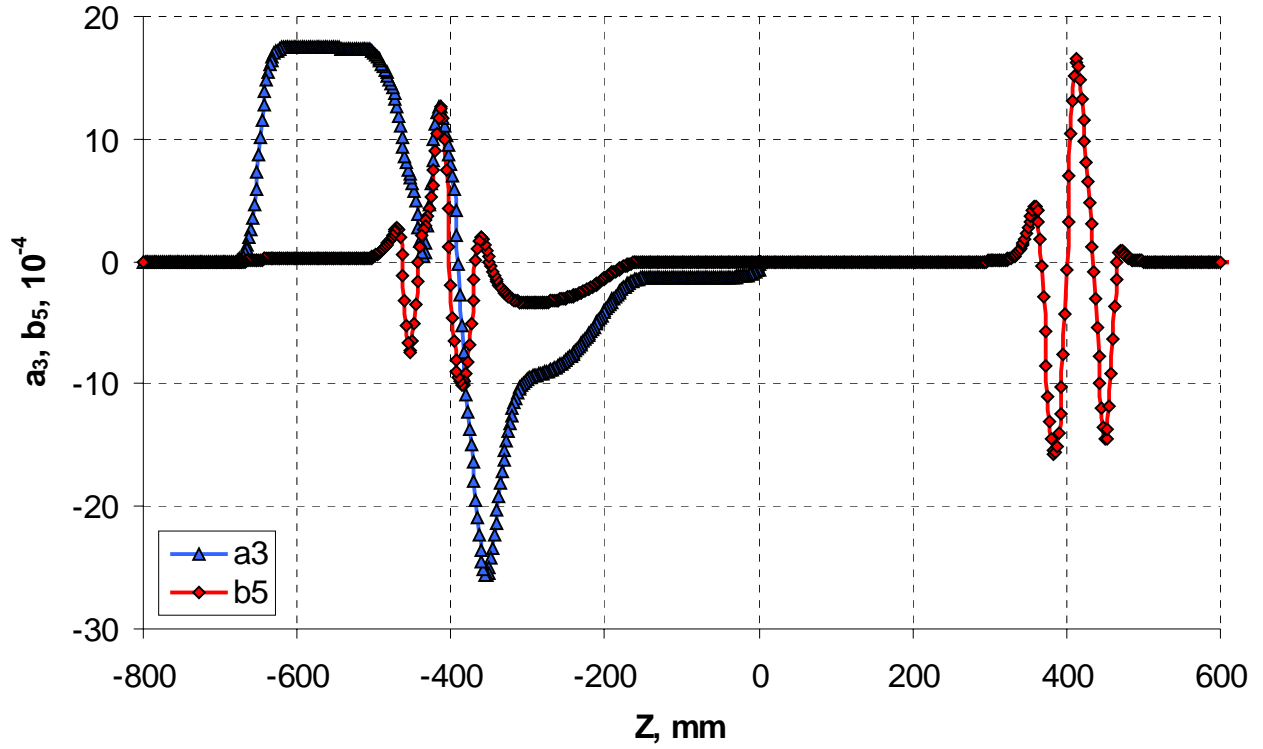
Figure 5.2.7 Skew sextupole and decapole deviations in longitudinal direction.

Table 5.2.1 Integral field harmonics.

Harmonic #	a_n, 10^{-4}	b_n, 10^{-4}
1	22.18	10000.000
2	-	-
3	1.43	17.08
4	-	-
5	0.68	-0.65
6	-	-
7	0.26	-0.11
8	-	-
9	-0.01	-0.07
10	-	-
11	0.00	0.04

5.3 Magnet fabrication

Two 1-m long Nb_3Sn dipole models (HFDA02 and HFDA03) based on the optimized shell type coil with 43.5 mm bore and 600 mm long iron yoke have been fabricated at Fermilab. All major steps of fabrication process are described in [146], [147], [148].

The reacted and impregnated coils were mechanically supported by a vertically split iron yoke, locked by two aluminum clamps and surrounded by 8 mm thick stainless steel skin. The clamps provided the initial preload to the coils and aided in the yoke assembly. Both the clamps and the skin provide the final coil prestress at a room temperature. The space between the coils and the yoke was spanned by 8 mm aluminum spacers. Thick (50 mm) end plates were used to restrict the longitudinal coil motion under the electromagnetic forces.

Nb_3Sn strand and cable parameters used in the model are listed in Chapter 1. The conductor was manufactured by OST using the Modified Jelly Roll (MJR) process. Keystoned Rutherford type cable with stainless steel core was manufactured at LBNL. The cable was wrapped with a ceramic tape from CTD using 50 % overlap. The nominal thickness of the cable insulation was 250 μm. An inorganic ceramic matrix was then applied to the insulated cable by rollers and cured at 80 °C during 20 min. This step resulted in the cable with a strong insulation [149].

The coil end parts and pole pieces were made out of aluminum-silicon bronze. This material was chosen because its melting temperature is high enough to withstand the reaction cycle and its thermal contraction coefficient is similar to that of the coil in the azimuthal direction. The end parts were designed using the code BEND. Those were fabricated at LBNL by 6-axis EDM machine [145] for the first magnet and at an outside company using the water jet machine with the jet nozzle diameter 1.07 mm and the water pressure 378 MPa for the following magnets. Figure 5.3.1 shows the end parts of the inner coil layer produced by the water jet.

Each half-coil, consisting of 24 turns was wound from a single piece of cable without the interlayer splice. Fig. 5.3.2 shows the complete half-coil after winding. After winding, each layer was painted with liquid ceramic matrix and cured for 30 minutes at 150 °C. The coil ground insulation consisted of two 0.25 mm layers of the ceramic cloth. There were two 25 μm stainless steel strip heaters per coil quadrant, installed between the layers of ground insulation.

Two manufactured half-coils were assembled around a stainless steel mandrel along with the ground insulation and placed into the reaction fixture, shown in Figure 5.3.3. The lead cable ends were welded to prevent tin from leaking during the reaction. The leads were also supported during reaction to avoid any motion. The reaction fixture was assembled with the retort and then placed in the furnace. The retort was pumped out for several hours and later purged with Argon.

The reaction process followed three steps, summarized in Table 5.3.1. The Nb_3Sn to NbTi splicing between the half-coils was performed when the coil assembly was inside the reaction fixture. In order to increase the splice quality, it was placed inside 0.125 mm copper cage. The splice length was equal to 125 mm. The Nb_3Sn leads and the splice cables were supported to prevent any possible damage. Figure 5.3.4 shows the reacted coil spliced to the NbTi cables.
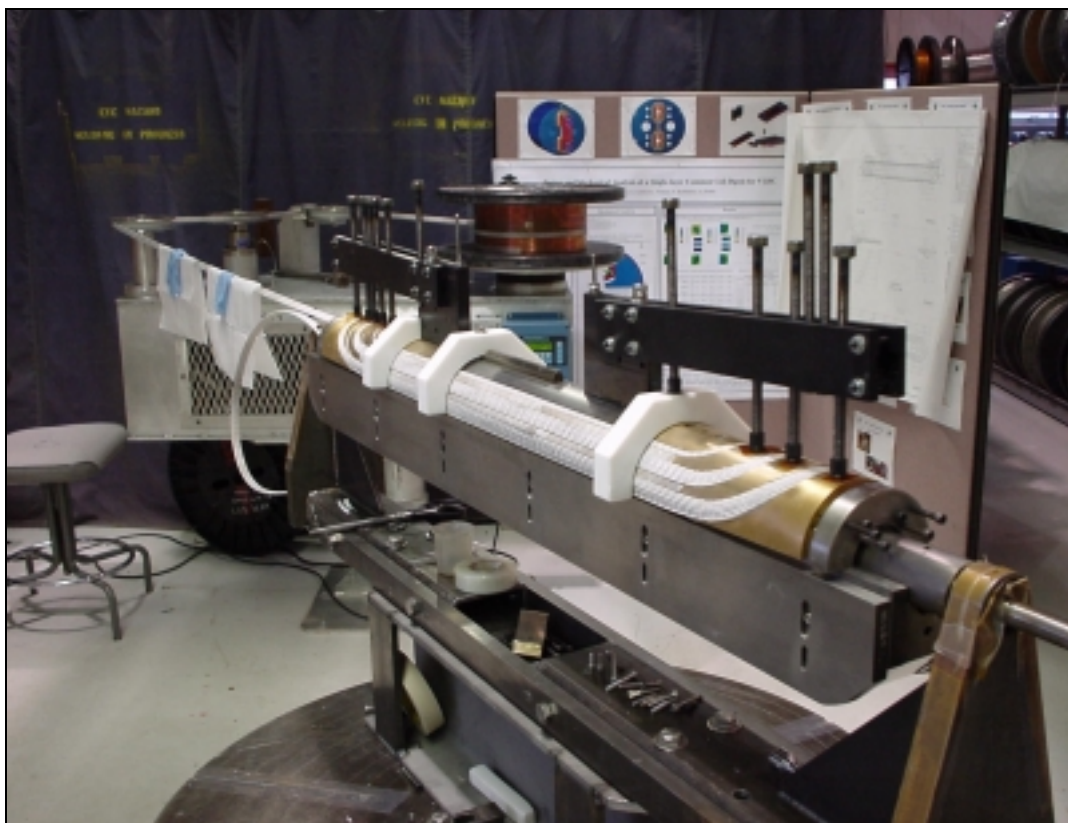
Figure 5.3.1. Coil end parts.

Figure 5.3.2. Half-coil after winding.

Figure 5.3.3. Coil in the reaction fixture.

Figure 5.3.4. Coil after splicing.

Table 5.3.1 Coil reaction steps.

Step #	Ramp Rate, °C/hr	Temperature, °C	Dwell Time, hr
1	25	210	100
2	50	340	48
3	75	650	180

After the splice joints were made, the coil assembly was transferred from the reaction to the impregnation fixture. The rollover tooling was used to facilitate this process. The stainless steel mandrel used during the reaction was removed and the Teflon mandrel was installed in its place. Since the thermal expansion coefficient of the Teflon is more than that of the coil, the mandrel diameter was chosen such that during curing it would expand to fill the whole aperture. The coil was impregnated by CTD-101K epoxy during 5 hours at the temperature 60 °C. The epoxy volume, residing in the coil after impregnation was 1.2 liters. Figure 5.3.5 shows the impregnation fixture with the coil inside and Figure 5.3.6 shows the impregnated coil.

The impregnated coil and various magnet elements were instrumented with gauges to measure stresses during the magnet assembly and operation. One outer pole piece on each half-coil was mold released before epoxy impregnation so that it could be removed. Modified outer pole pieces instrumented with capacitance gauges were placed at these locations. Aluminum spacers between the coil and yoke, clamps and skin were instrumented with the resistive gauges.

The coil and yoke were assembled in the contact tooling. The yoke halves were then compressed vertically in a press and the aluminum clamps were inserted from the sides. After that the pump pressure was released, the assembly sprang back to an equilibrium position. Figure 5.3.7 illustrates yoked magnet with the clamps installed in place.

At the next step, two skin halves assembled around the yoke were compressed by a vertical press for automatic welding. The necessary stress in the coil was reached after several welding passes. The mean azimuthal stress in the skin was about 180 MPa. The ends of the skins were cut to the right dimensions after welding. The end plates were then welded at both lead and return ends to provide axial support to the coils.

The bullet gauges were installed on the end plates of the lead and return ends. Five resistive gauges were also installed along the magnet skin to measure the longitudinal stresses. The last mechanical assembly involved the half-coil splicing. The outer layer leads from both half-coils were spliced together and captured in a G-10 box. The inner layer leads were used for the magnet powering. Figure 5.3.8 presents completed magnet assembly, ready for shipment to the test facility.
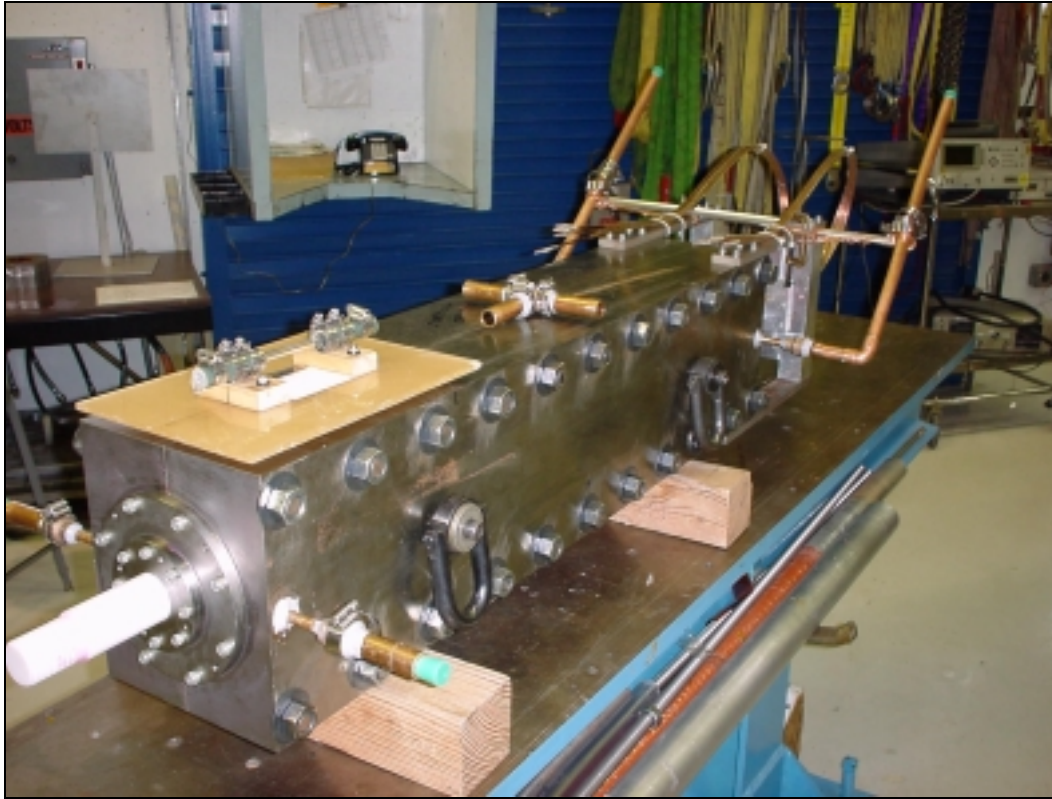
Figure 5.3.5. Coil in impregnation fixture.
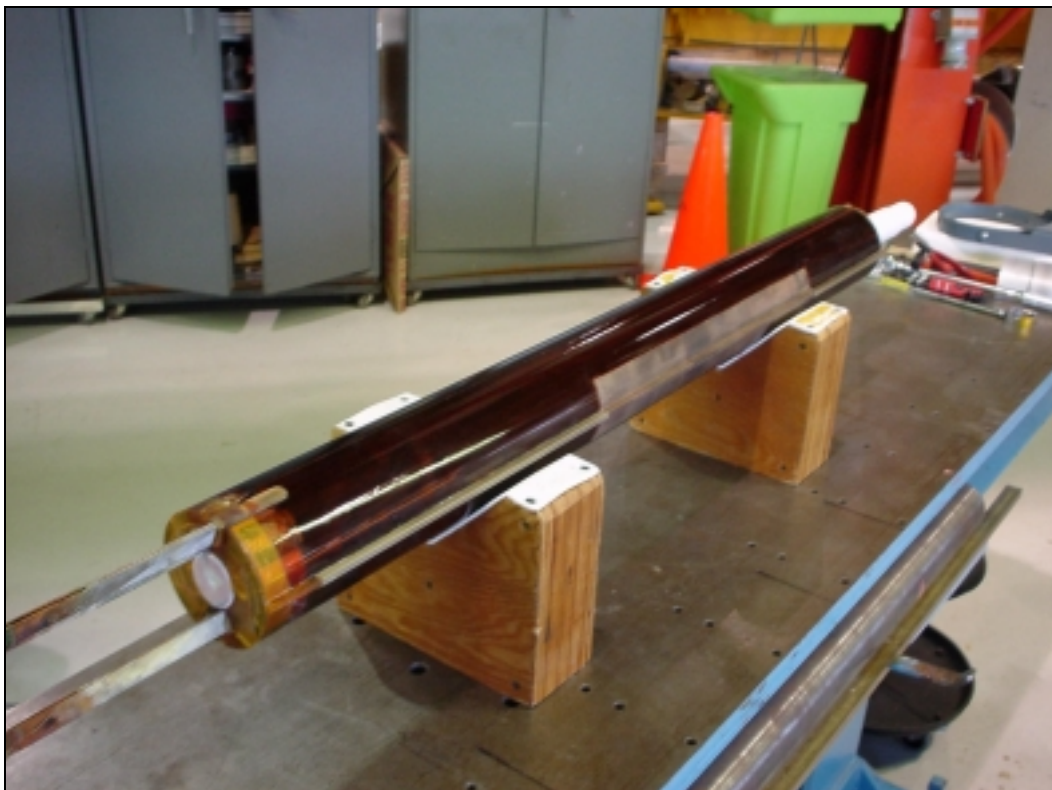
Figure 5.3.6. Coil after impregnation.

Figure 5.3.7. Yoke assembly.

Figure 5.3.8. Completed magnet assembly.

5.4 Testing and comparison with calculations

The magnets were tested at the Fermilab Vertical Magnet Test Facility (VMTF). Figure 5.4.1 shows the magnet in assembly with suspension, current leads, cryostat top head and instrumentation tree.

Figure 5.4.1 Magnet prepared for testing.

The magnets were tested in a boiling liquid helium at 4.5 K. HFDA02 had voltage taps installed on each half-coil and across all the $Nb_3Sn/NbTi$ splices [150]. There were two taps added in HFDA03 in order to detect quenches in the inner and outer layer of each half-coil [151].

Coil azimuthal stresses and longitudinal end forces in both models were measured during fabrication and cold tests at each excitation cycle using the resistive and capacitance gauges. Azimuthal coil prestress and longitudinal end prestress remained after cooling to 4.5 K. The strain gauge data did not indicate unloading of the coils up to the maximum reached currents. The coil deformation due to the electromagnetic force was elastic throughout the tested range.

Quench performances at 4.5 K for HFDA02 and HFDA03 are presented in Figure 5.4.2. The quench performance of both magnets was very similar. The maximum achieved current was less than 10 kA, which is a factor of two smaller than the expected magnet critical current. The magnets were excited with different current ramp rates within 20 A/s to 500 A/s range. No noticeable effect of the ramp rate on the magnet quench performance was found.

Figure 5.4.2. Magnets quench behavior.

All the quenches in both magnets occurred in the Nb_3Sn coil leads near the splices with NbTi cables, which was confirmed by the voltage tap signals [151]. The quenches never occurred in the magnet coils. The most probable reason of the observed quench behavior was in mechanical damage of the Nb_3Sn cable during splicing procedure.

5.4.1 "Warm" geometrical harmonics

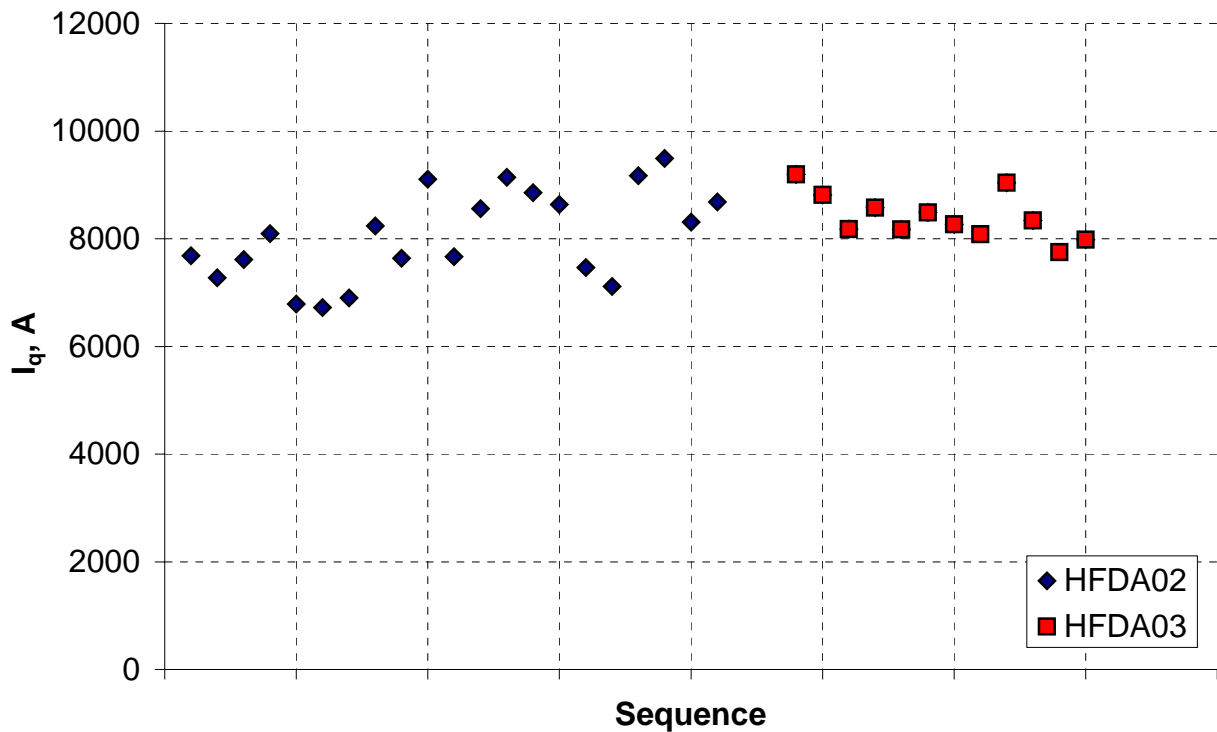The warm magnetic measurements were performed at a room temperature in order to obtain the field quality of the "as build" magnet. Two measurement systems were used. The first one was used before final splicing of the coil leads at the assembly bench. It was based on a rotating coil probe (mole), 1 m long and 25 mm in diameter. The probe had 5 windings on its G10 mandrel: two orthogonal dipole, two orthogonal quadrupole and one tangential. It was driven with a speed of 0.3 rotations per second by the electrical motor implemented in the mole body. The second, vertical drive rotating coil system was set up above VMTF cryostat and utilized 250 mm long probe coil with 25 mm diameter. It had a tangential winding for measurement of higher order harmonics as well as dedicated dipole and quadrupole windings for measurements of low order harmonics, similar to the mole probe. Those windings also allowed bucking of the large dipole component in the main coil signal.

Generated coil voltages were sampled and read 128 times per rotation using HP3458 digital voltmeters (DVM). An additional DVM was used to monitor the magnet current. DVMs were triggered simultaneously by an angular encoder on the probe shaft, synchronizing measurements of the field and current. A centering correction was performed in assumption that the unallowed by dipole symmetry a_8 and b_8 harmonics are zero and there was no skew dipole component (twist). The magnets were energized by a small (10 A) current that changed the polarity once at every probe position in order to cancel possible weak fields (Earth field, remanent yoke magnetization, etc.), not related to the magnet current.

Figures 5.4.3-5.4.7 show the transfer function and low order harmonic distributions along the magnet. For an easiest comparison, all the measured data were transformed into coordinate system used in the calculations (Figure 5.1.1) and normalized by the measured dipole field component at the magnet center. Since the acquisition system had longitudinal "resolution" equal to the probe length and (in fact) integrated harmonics along this length, the calculated data were integrated between corresponding points as well. The measured transfer function matches well with calculations. There is a small (25 mm) longitudinal shift between the calculated and measured distributions of the transfer function in HFDA02 due to uncertainty in establishing the VMTF coordinate system. It was corrected during HFDA03 measurements. The transfer function value, measured in magnet body by the mole is ~20% smaller than the value measured by the vertical probe that is a result of large difference in probe lengths used in the two systems.

There are large deviations in the measured allowed and unallowed harmonics. The harmonics noticeably change within the magnet body (Z = (-25; 175)), where they should be constant. Thus, the quadrupole and sextupole vary by $\sim12{\cdot}10^{-4}$ and $\sim9{\cdot}10^{-4}$ respectively in both magnets.

Figure 5.4.3. Longitudinal deviations of the transfer function.

Figure 5.4.4. Longitudinal deviations of the normal quadrupole.

180

Figure 5.4.5. Longitudinal deviations of the normal sextupole.

Figure 5.4.6. Longitudinal deviations of the skew quadrupole.

Figure 5.4.7. Longitudinal deviations of the skew sextupole.

Such big changes in harmonics over the straight section could not be explained by the errors in the conductor position, as it would not comply with the used production technology. The reason of large harmonics was understood after the "cold" measurements, described in the next paragraph.

5.4.2 "Cold" geometrical harmonics

The "cold" magnetic measurements were performed after cooling the magnets to 4.5 K. Measurements at the magnet body were done in both magnets and longitudinal Z-scan was done in HFDA03 at the same points as during the warm magnetic measurements. The procedure of measurements and following analysis was different from the warm magnetic measurements due to a large coil magnetization effect.

In order to obtain the correct values of geometrical harmonics it was necessary to make measurements at every current and Z-position twice: during the current up-ramp and down-ramp. Mean values between the two measurements would provide the correct harmonics, relevant to the coil geometry. The maximum current was limited by the magnet quench performance at 8000 A.

In order to avoid a non complete superconductor re-magnetization, the following current change sequence was used: 0→5000→0→3000→5000→7000→5000→3000→0 A, where the magnetic measurements were performed at 3000 A and 5000 A on the up-ramp and down-ramp. Figures 5.4.8-5.4.12 show the transfer function and multipole distributions in longitudinal direction and Table 5.4.1 summarizes the geometrical harmonics in the magnet body at 3000 A current.

There are deviations of the measured harmonics from the calculated values in the magnet body. However, the harmonic distributions are essentially better with respect to the warm measurements. Thus, the low order harmonics were improved by a factor of 3-5. This observation allows concluding that there was some <u>undefined magnetic object</u> (UMO) in the system, which affected the field quality at low currents, but disappeared at higher currents. Such object could presumably be the anti-cryostat stainless steel pipe or the stainless steel core inside of the cable, which could attain some magnetic properties during manufacturing.

In addition, shapes of the measured curves have a clear correlation with the calculated ones. It proves an essential correctness of the coil geometry, while the harmonic offset in the magnet center can be satisfactory well explained by the coil production technology [150]. Obviously, the technology has to be improved in order to achieve the necessary field quality.
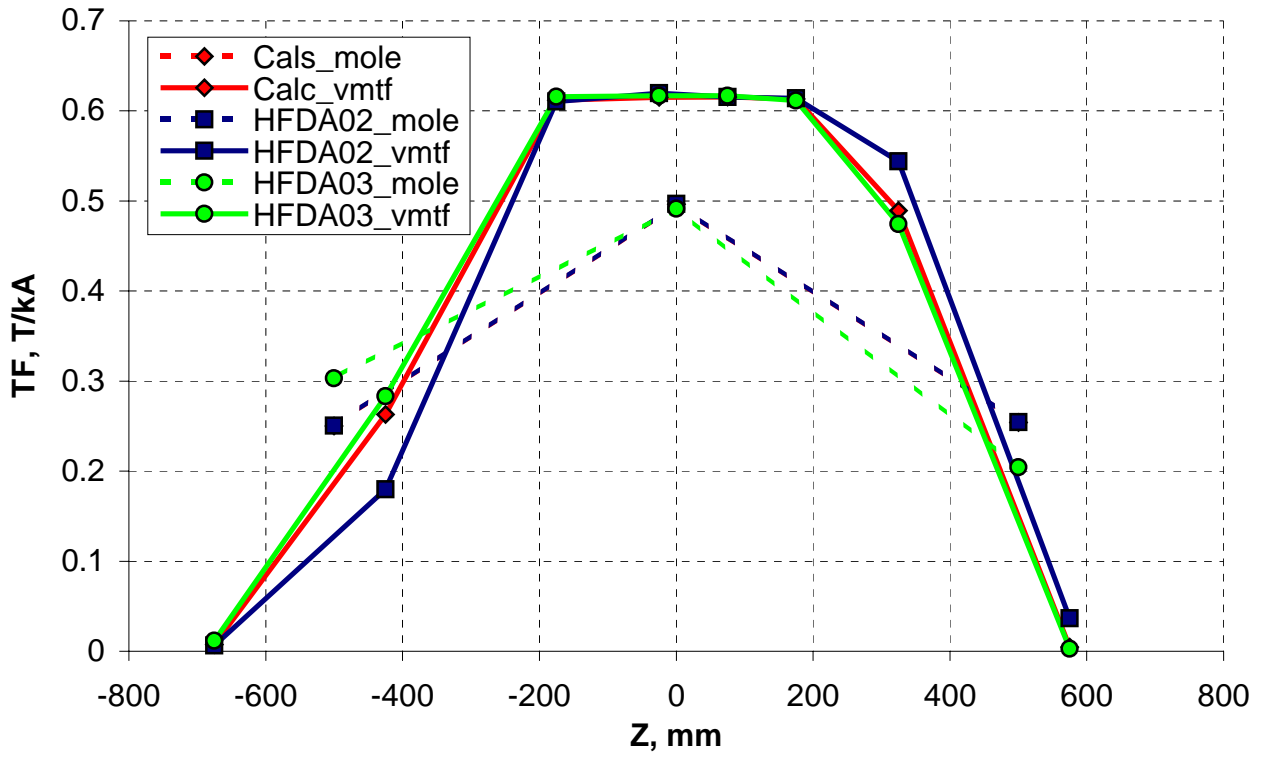

Figure 5.4.8. Longitudinal deviations of the transfer function.
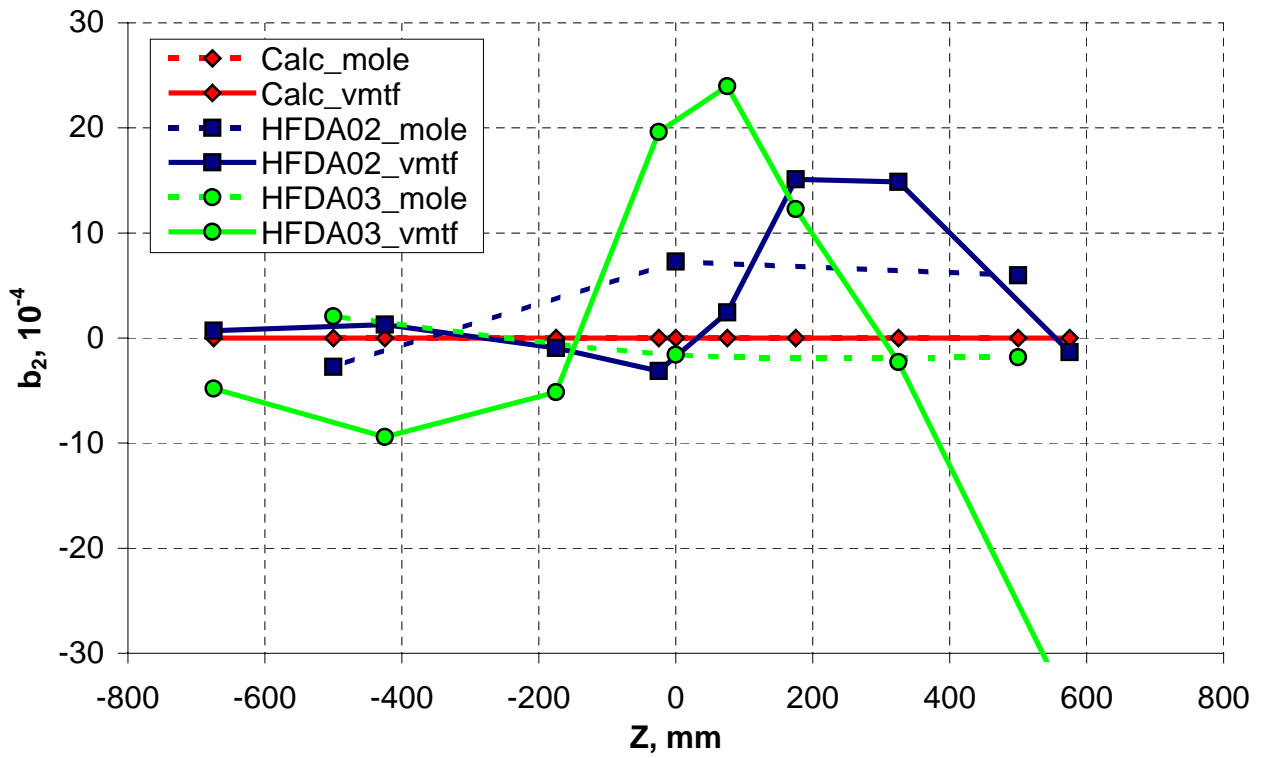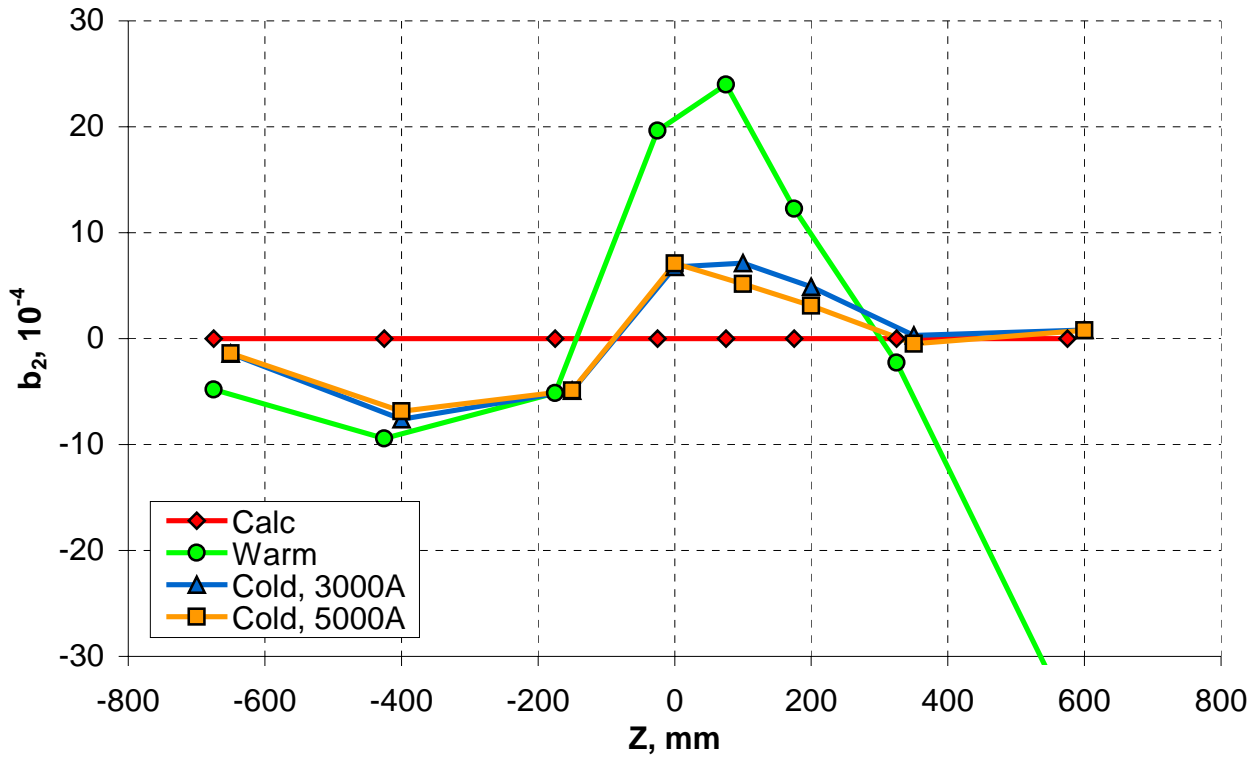
Figure 5.4.9. Longitudinal deviations of the normal quadrupole.
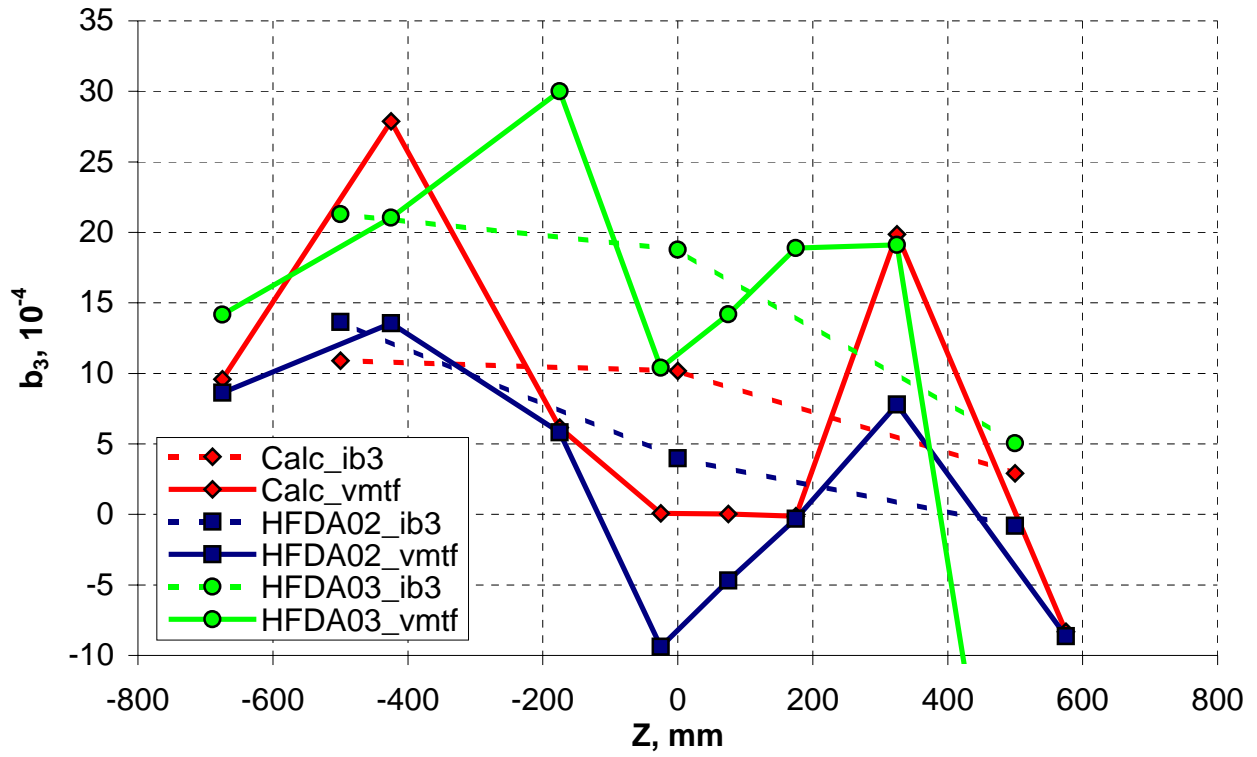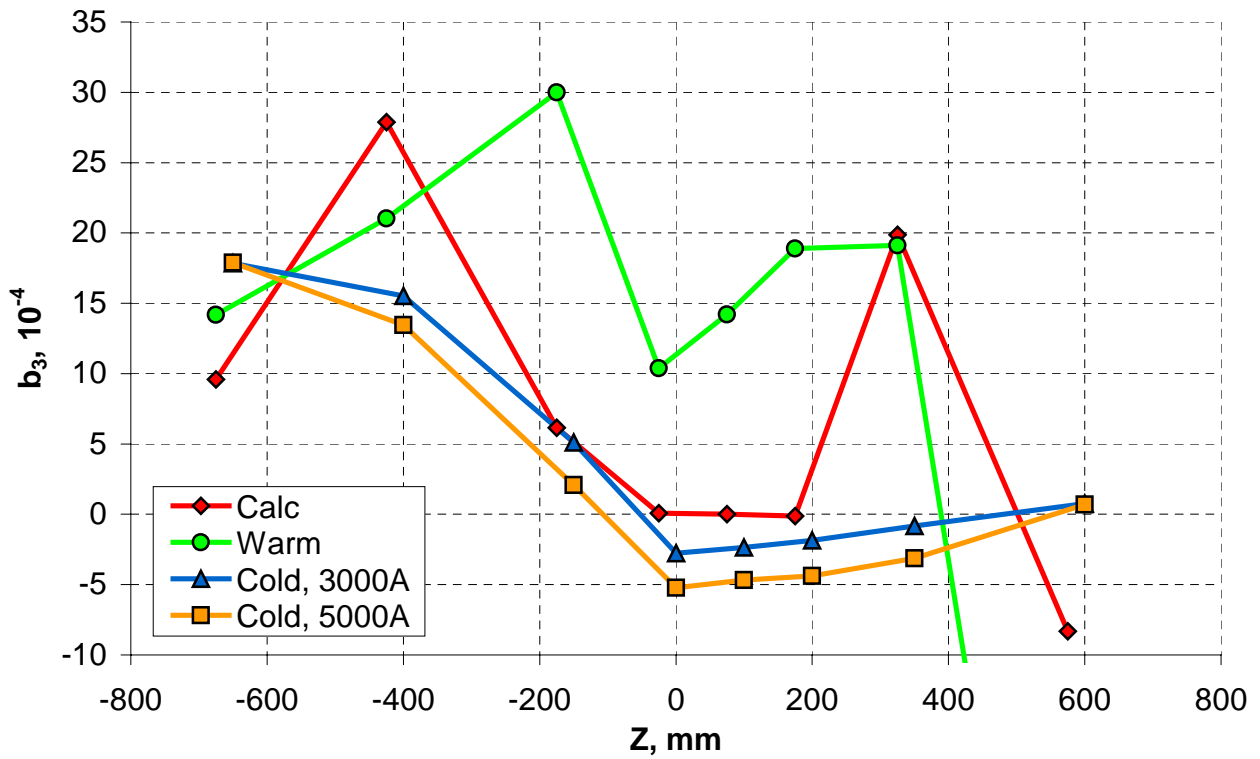

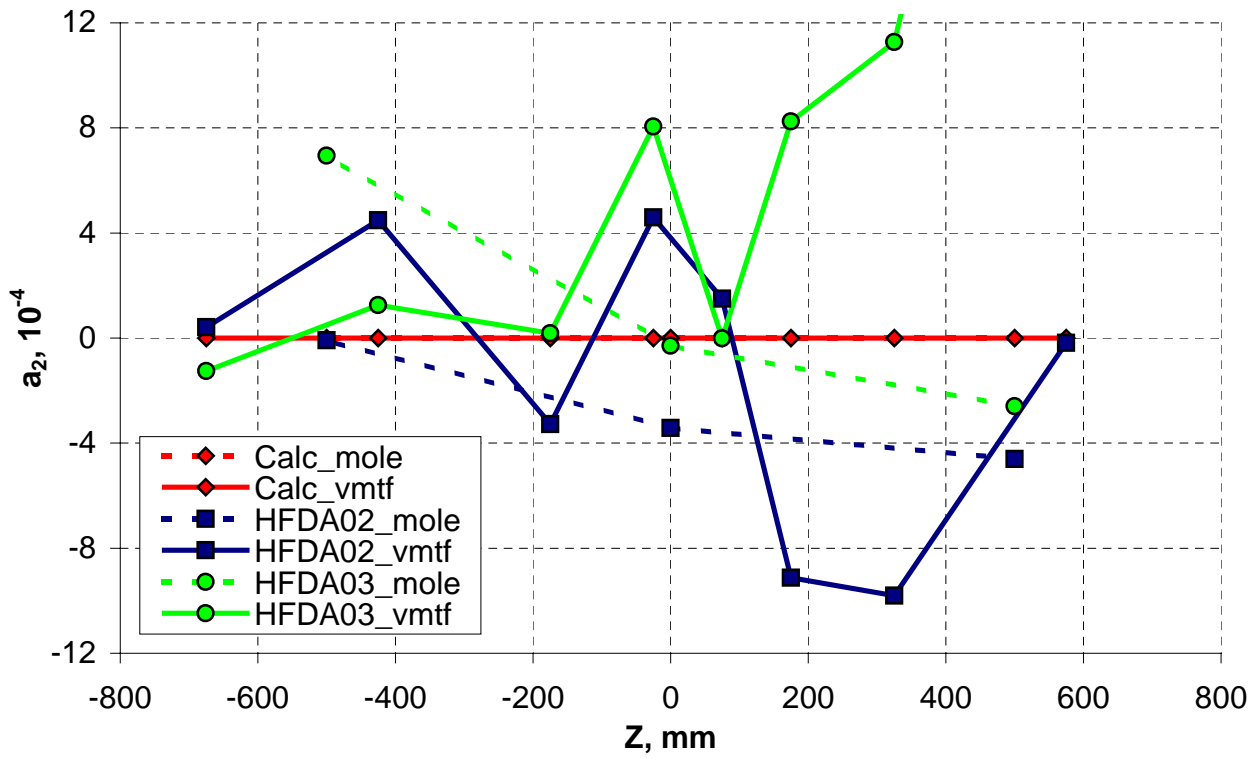Figure 5.4.10. Longitudinal deviations of the normal sextupole.

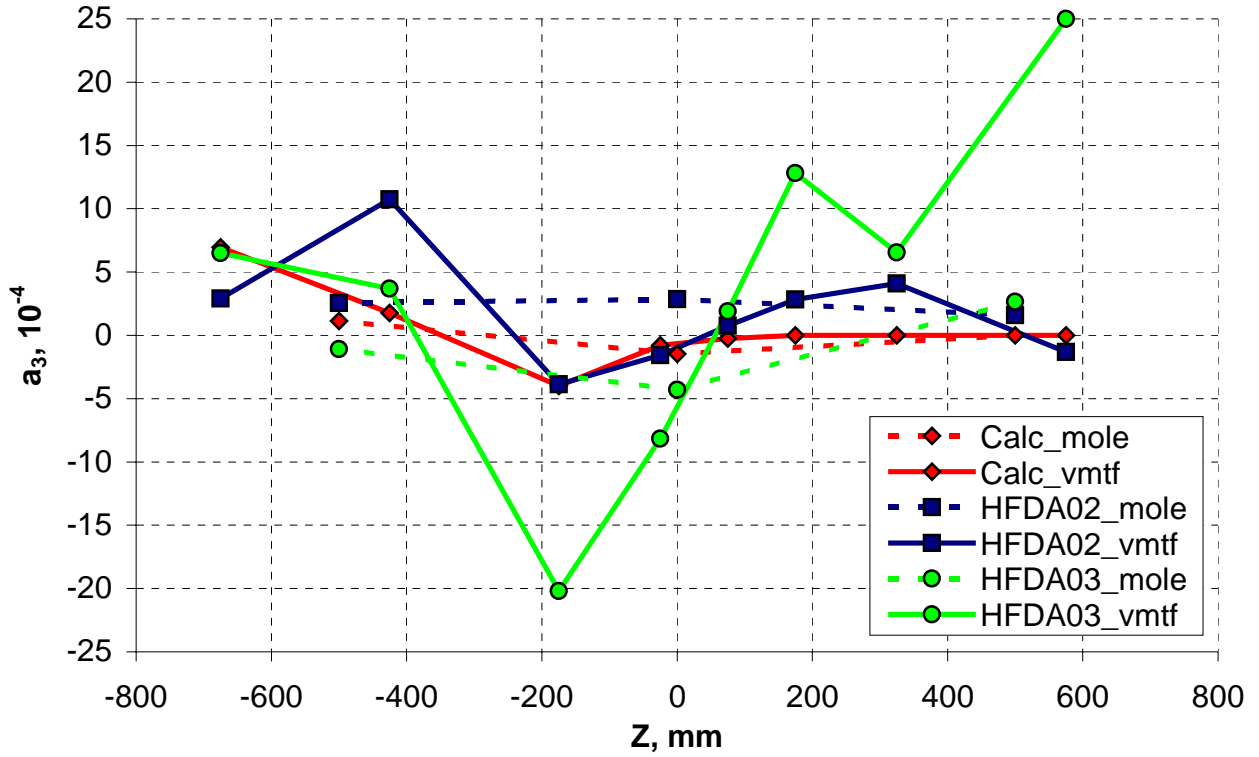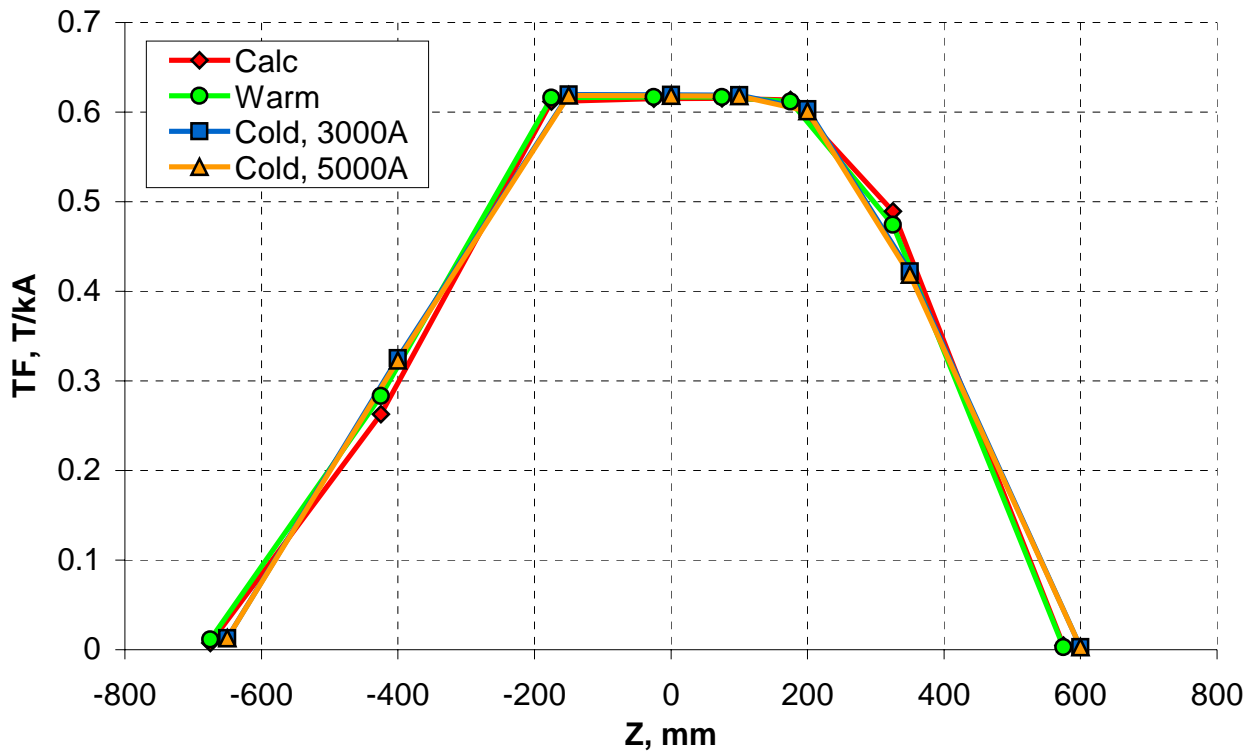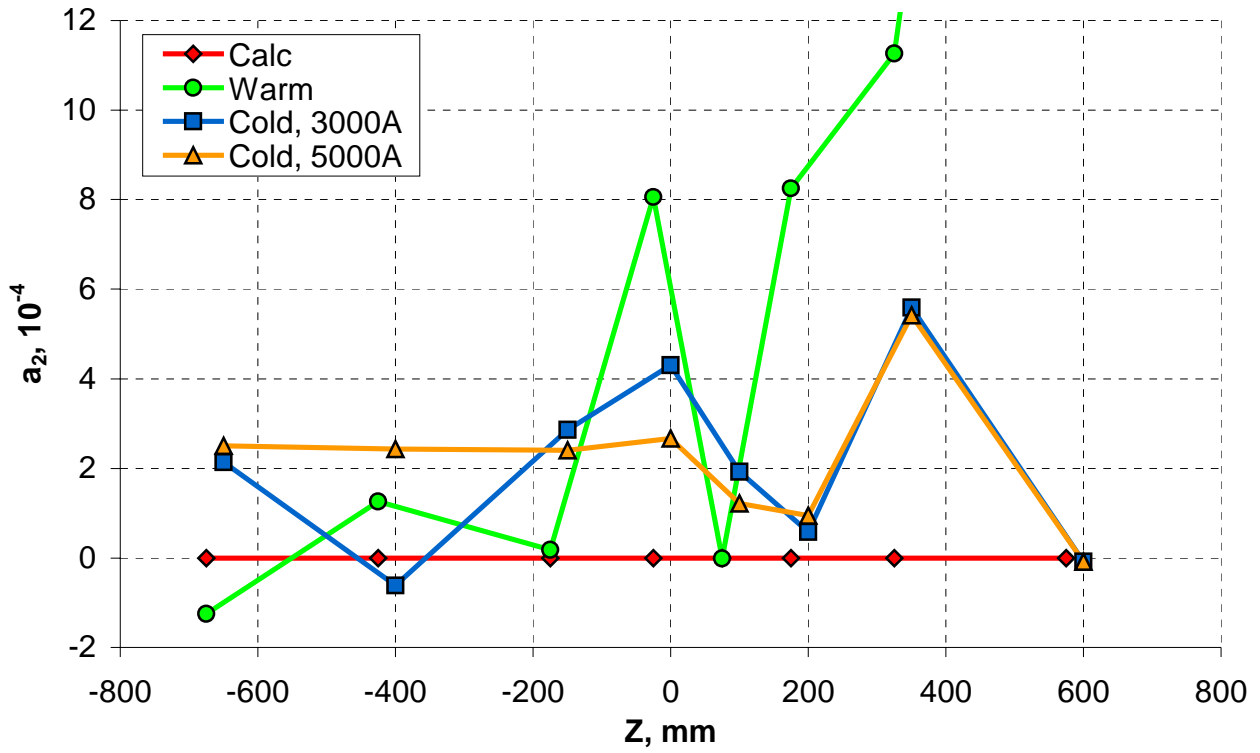Figure 5.4.11. Longitudinal deviations of the skew quadrupole.
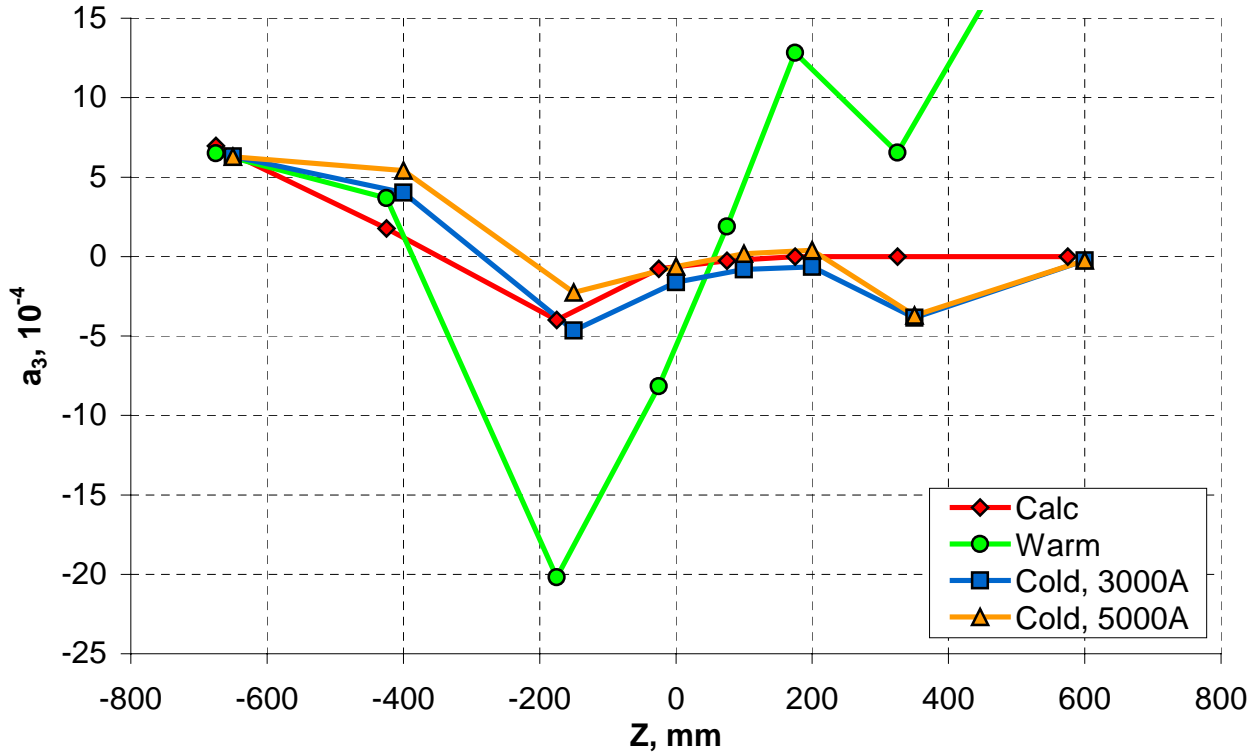
Figure 5.4.12. Longitudinal deviations of the skew sextupole.

Table 5.4.1. Geometrical harmonics in the magnet body at 3000 A.

n	Calculated		HFDA02		HFDA03	
	b_n	$\sigma_{an,bn}$	a_n	b_n	a_n	b_n
2	-	1.20	-9.6	-4.1	1.93	7.13
3	0.00	0.56	0.2	-4.0	-0.81	-2.36
4	-	0.28	-1.1	-0.4	-0.75	0.19
5	0.00	0.10	-0.3	0.0	-0.04	-0.53
6	-	0.05	0.3	0.0	0.03	-0.12
7	0.00	0.02	0.1	0.1	-0.03	0.04
8	-	0.01	-	-	-	-
9	-0.09	0.00	0.2	-0.2	-0.04	-0.01

5.4.3 Persistent current effect

The magnet models were tested in a cycling mode at the current ramp rate of 20 A/s in order to determine the persistent current effect. The current was changed from zero to 8000 A and back to zero three times and measurements were made in center of the magnet straight section (Z = 75 mm) by the vertical rotating probe. In order to make a correct comparison between the measured and calculated hysteresis loops, all the other effects, affecting the field quality had to be subtracted.

Figures 5.4.13-5.4.14 show averaged between the three cycles and calculated hysteresis loops of the sextupole and decapole components, their mean values and the difference between the mean values that represents effect of UMO (that for simplicity also included constant geometrical harmonics) in the system. Extrapolated (by a 5th power polynom) to zero values of sextupole and decapole components match well with results of the warm magnetic measurements, which proves consistency of such model.

There is unpredicted by UMO model linear drop in the sextupole starting from ~3 T field that can be explained by a non-complete coil re-magnetization after switching from the up-ramp to down-ramp. The superconductor magnetization used in simulation of the persistent current effect was measured for the relevant virgin strands at the Fermilab Short Sample Test Facility [97]. In order to represent the real cable magnetization it was adjusted with assumption of the critical current degradation $K_{deg} = 10$ % and the strand packing factor $\lambda_{str} = 0.88$ according to:

$$M(H) = M_{measured}\left(\mu_0 \frac{H}{\lambda_{str}K_{\deg}}\right) \cdot \lambda_{str}K_{\deg}.$$
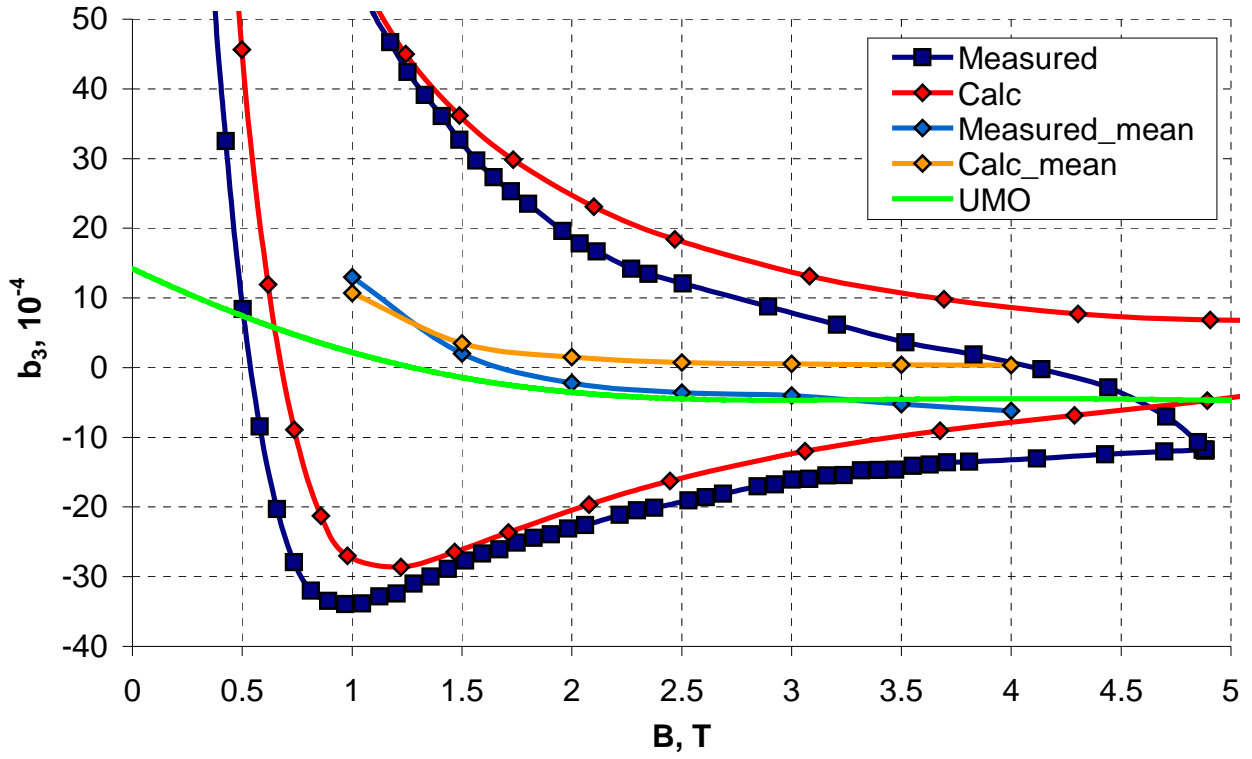
Figure 5.4.13. Different factors in the sextupole hysteresis.
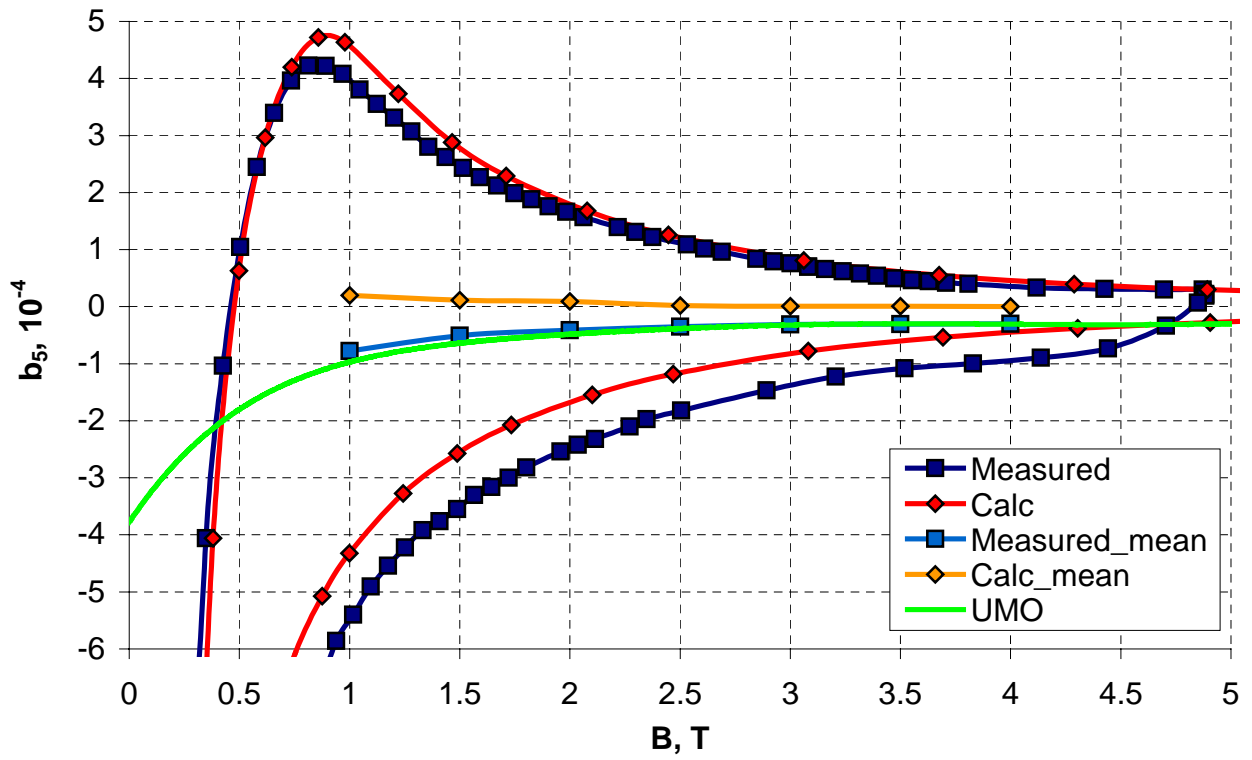
Figure 5.4.14. Different factors in the decapole hysteresis.

5.4.4 Corrector of the persistent current effect

The proposed persistent current corrector with the "strips on the pipe" geometry was produced and installed inside the HFDA02 coil bore between two thermal cycles. For simplicity of construction, the corrector was optimized with only one 15.85x0.1 mm iron strip per coil quadrant, providing a positive effect on the sextupole and decapole components.

The strips were installed between several layers of epoxy-impregnated fiberglass tape at 21.4 mm radius and 55.2 degrees azimuthal positions from the coil midplane to the strip center. Afterwards, the corrector was cured at ~120 °C that formed a rigid G10 pipe with implemented iron strips inside.

Figure 5.4.15 shows the corrector after curing. Figures 5.4.16-5.4.17 show normalized sextupole and decapole loops (with subtracted UMO effect) measured in the second cycle and calculated.
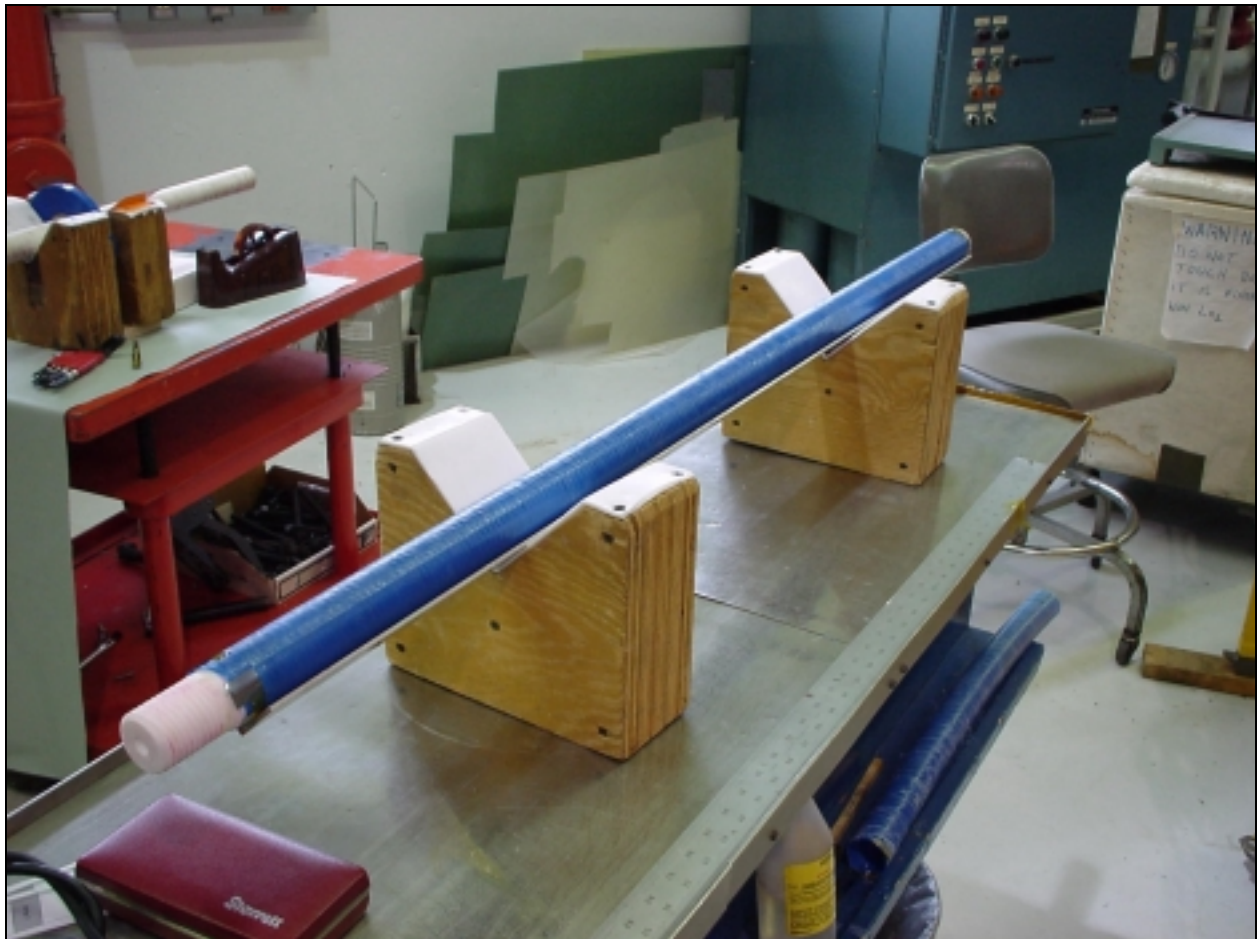
Figure 5.4.15. Passive corrector of the persistent current effect.

There is a large persistent current effect, which produces significant field quality deterioration at small fields. The measured and calculated curves match with 5 % accuracy at the fields above 1.5 T for the sextupole and 1 T for the decapole at the up-ramp and down-ramp. The difference at fields below 1.5 T can be explained by a non-complete field penetration inside the superconductor due to a short measurement cycle. Thus there was a significant fraction of the coil working on magnetization curve of the first (virgin) or intermediate cycle that has lower magnetization minimum than the second cycle curve. It results in lower sextupole and higher decapole values than was calculated in assumption of the whole coil working on the second cycle curve. The difference at low fields would be smaller for the nominal (0÷11 T) cycle.

Table 5.4.2 summarizes the correcting effect of the persistent current corrector on the sextupole and decapole components. It was defined as the ratios between incremental values of the non-corrected and corrected harmonics within $B_{peak}÷4$ T field range, where B_{peak} is the field at the harmonic peaks.

There is clear positive correcting effect on both harmonics, which considerably improves the magnet field quality. The differences between calculated and measured correcting effects for the sextupole and decapole can be explained by deviations from the designed geometry in the hand-made corrector and smaller than was expected saturation magnetization of the strip material (it was not purposely measured for the relevant strips).
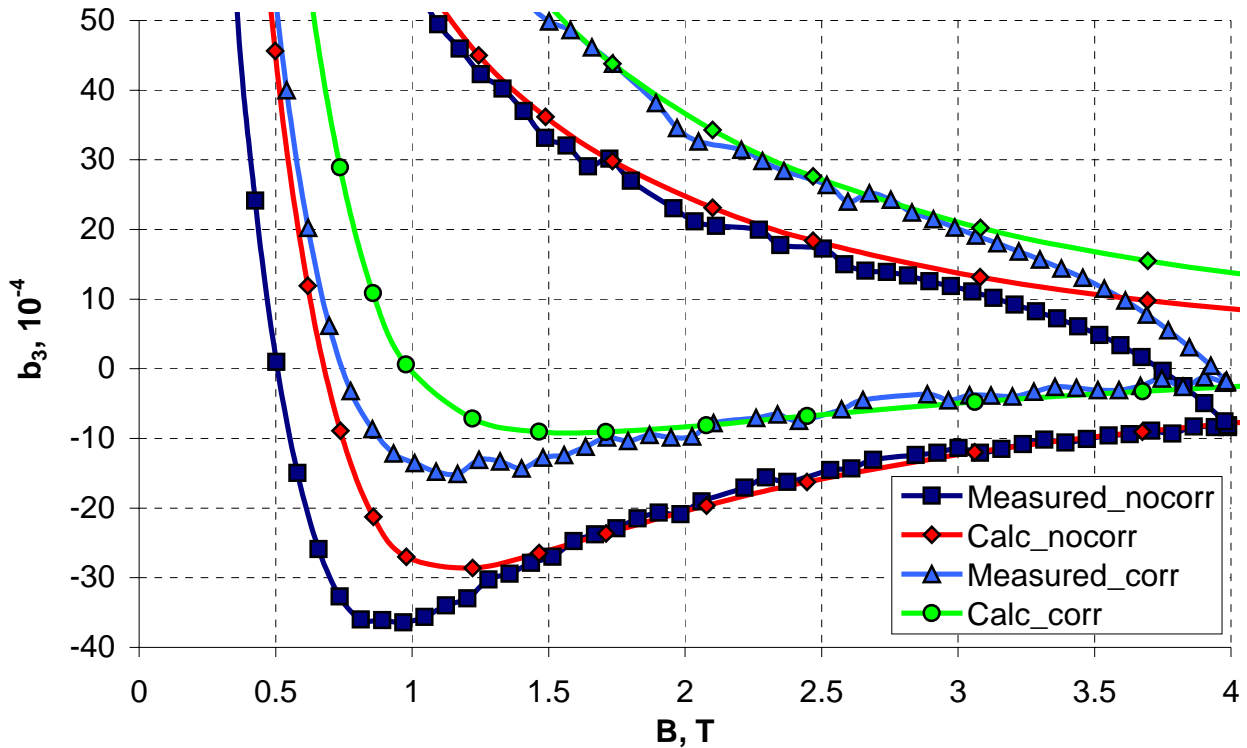
Figure 5.4.16. Normalized sextupole hysteresis as functions of the bore field.
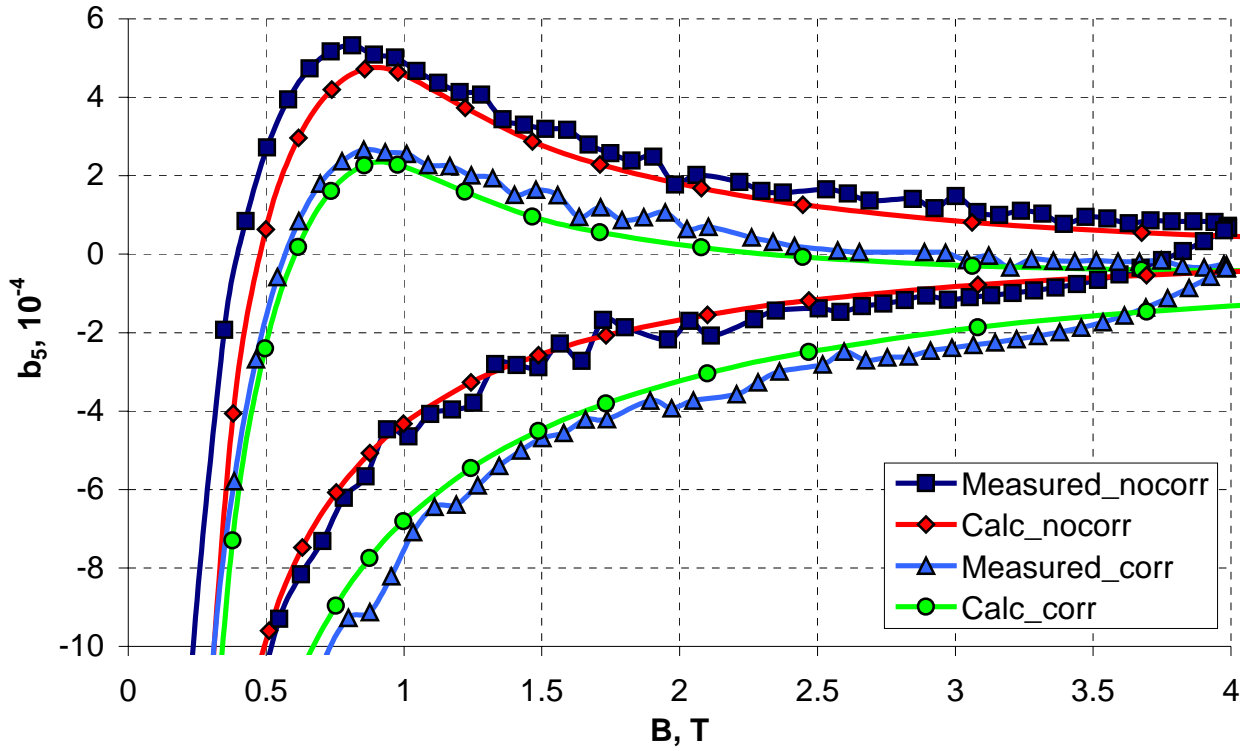
Figure 5.4.17. Normalized decapole hysteresis as functions of the bore field.

Table 5.4.2. Correcting effect of the passive corrector.

Harmonic	Before correction		After correction		Correcting factor	
	calculated	measured	calculated	measured	calculated	measured
Δb_3	20.2	28.5	6.6	11.4	3.1	2.5
Δb_5	4.2	4.4	2.7	2.9	1.6	1.5

5.4.5 Eddy current effect

Nb_3Sn magnets fabricated by the "wind and react" technique usually show a large eddy current effects due to a small strand crossover resistance, created during coil reaction [152]. To increase the crossover resistance, the cable in both magnets had a 25 µm stainless steel core inside. The magnets were tested at different ramp rates in order to determine influence of the eddy currents on the field quality. Figures 5.4.18-5.4.19 show sextupole and decapole components (with subtracted UMO contribution) measured at current ramp rates of 20 A/s and 80 A/s in the magnet center. There is no visible ramp rate dependence in harmonics within 20-80 A/s range that proves high efficiency of the stainless steel core for increase of the strand crossover resistance. However, there was observed large, unexpected ramp rate dependence in the magnet transfer function (or the main field component), shown in Figure 5.4.20. The eddy currents in the coil could not explain it, as they would necessarily produce deviations in all other allowed harmonics.
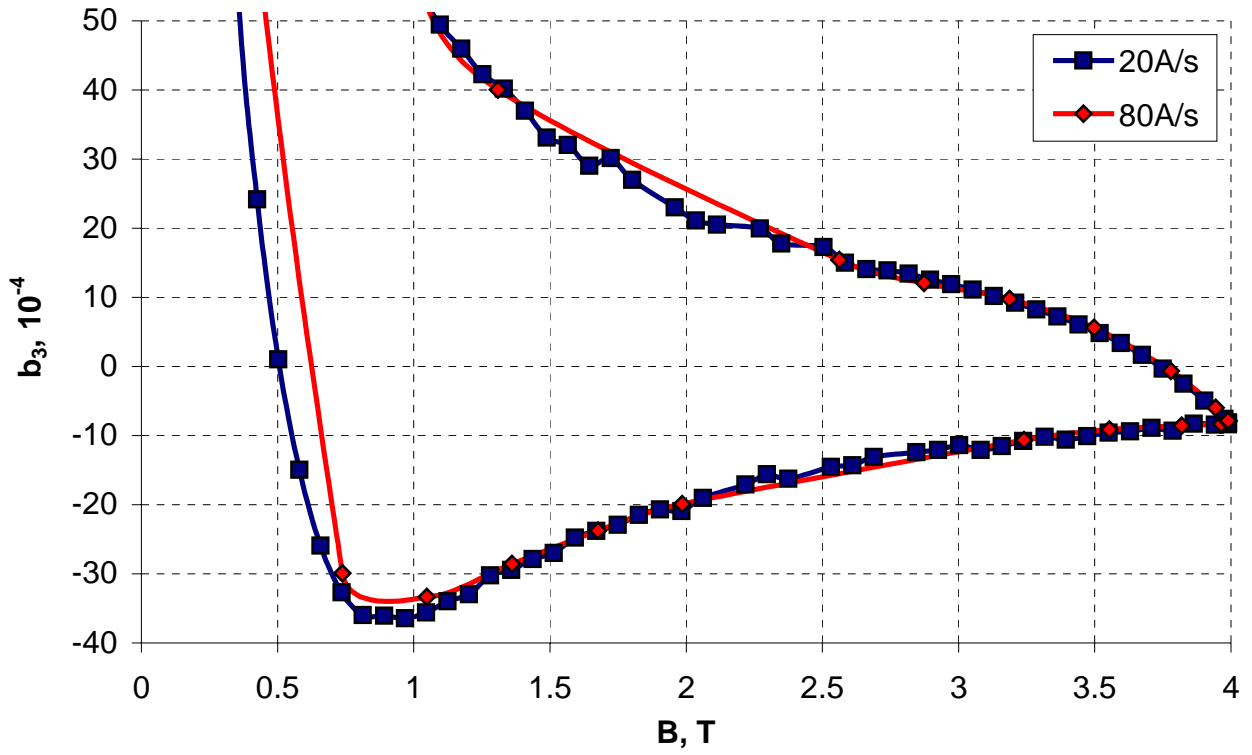
Figure 5.4.18. The sextupole component at different ramp rates.
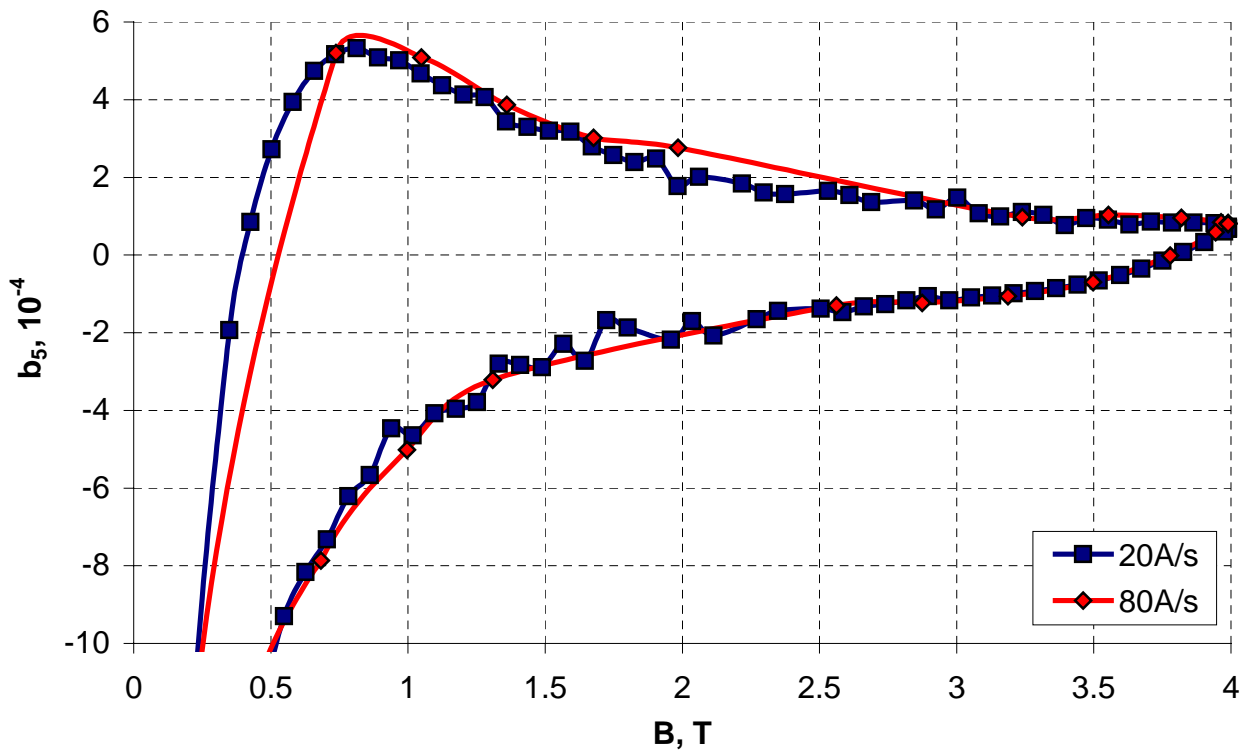
Figure 5.4.19. The decapole component at different ramp rates.
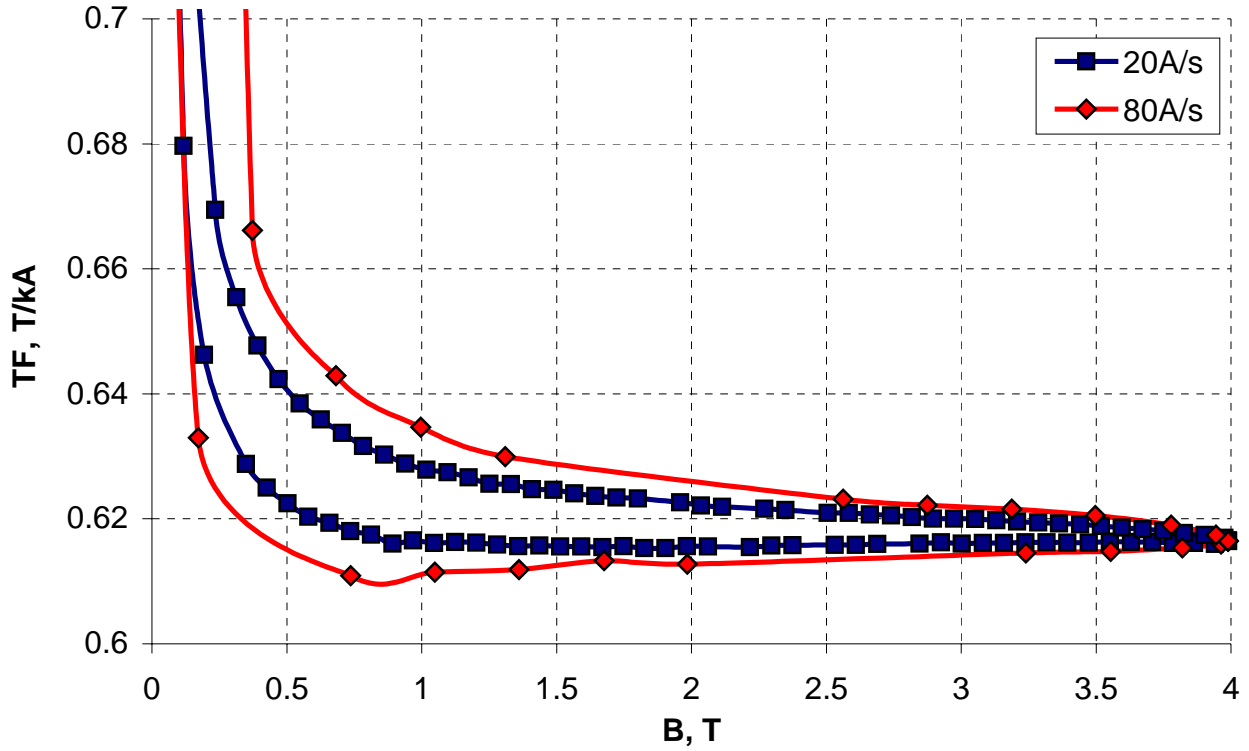
Figure 5.4.20. The transfer function at different ramp rates.

In order to determine source of the eddy current effect, the ramp process was simulated in a finite element model using the transient analysis module of OPERA2D. All the elements with essentially low specific resistance were assigned corresponding properties and current sharing laws. Thus, the specific resistance was assumed to be $8 \cdot 10^{-10}$ Ohm·m for aluminum and $3.5 \cdot 10^{-9}$ Ohm·m for aluminum bronze at 4.2 K temperature.

The coil current was changed with the constant ramp rate of 80 A/s during simulation. In one case two aluminum shells were electrically connected in the pole region, in another case they were disconnected. Such models were expected to estimate the upper and lower boundary of the eddy current effect, since simulation of a precisely "as built" model would be complicated due to unknown value of the contact resistance between the two shells.

Figure 5.4.21 shows the eddy current density within aluminum bronze wedges and aluminum shells for the considered cases of electrical connection between the shells. The eddy currents in both cases have maximum density in the aluminum shells, which are the primary reason for the ramp rate dependence in the transfer function. There was no ramp rate dependence in harmonics found during simulations nor the measurements that explains by the fact that the dipole field ramp generates close to the cosine-theta current distribution in the solid cylindrical aluminum shell. The induced current produces the dipole-only component of the opposite to the main field

sign. In case of the split spacer, the changing dipole field generates two dipole-like current distributions of the opposite sign that partially cancel effect of each other, having smaller effect on the transfer function than in the solid case. Figure 5.4.22 illustrates difference in the transfer function during the up-ramps at 20 A/s and 80 A/s measured and calculated in two models.
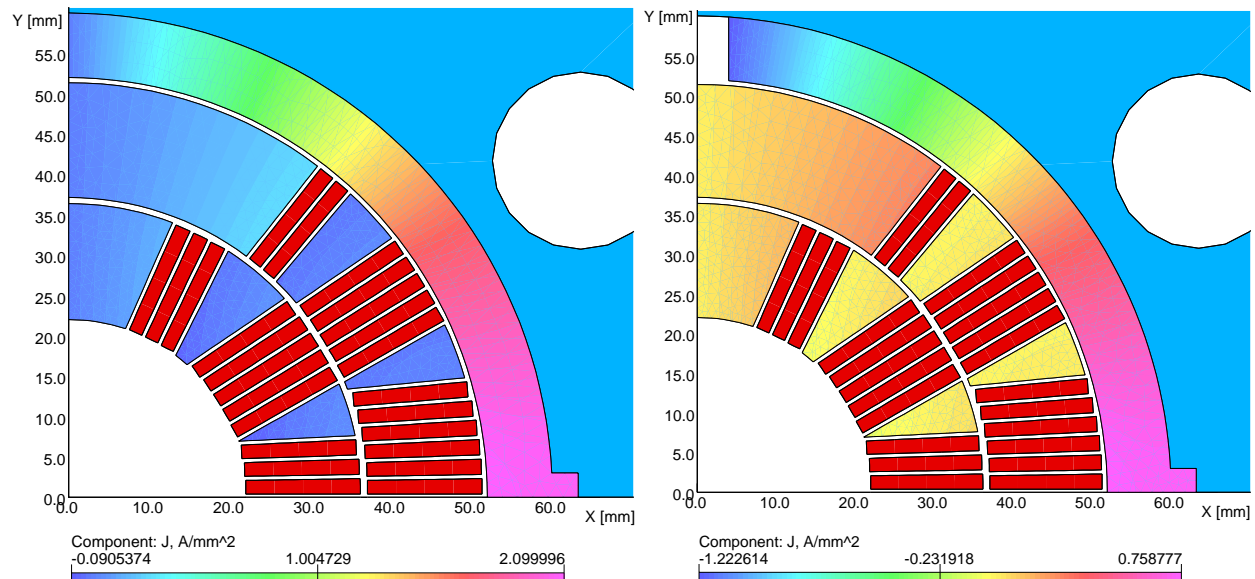
Figure 5.4.21. Eddy current density in cases of solid (left) and split (right) spacers.
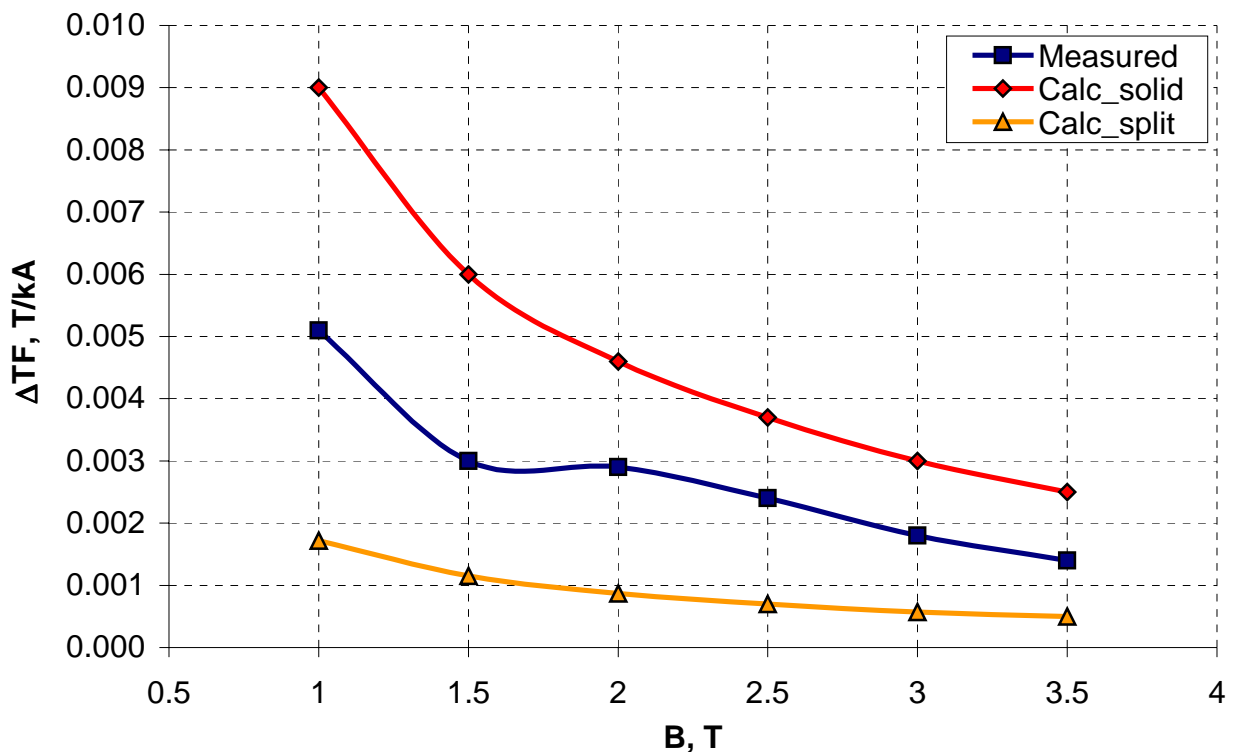
Figure 5.4.22. Differences in transfer functions between ramps with 20 A/s and 80 A/s.

The measured dependence lays between the calculated for two models curves. It proves validity of the assumption that the aluminum spacer outside of the coil is the major cause of the ramp-rate dependence in the transfer function. There is a contact resistance between two aluminum shells, larger than the resistance of pure aluminum. Calculations show that a good electrical insulation between the shells could reduce the effect in transfer function by factor of two.

5.4.6 Field decay and the "snap back" effect

It is known that most of the NbTi magnets apart from the persistent current effect, possessed to another unwanted field quality deterioration at injection, called the "snap back" effect. This effect, first discovered in Tevatron [153], is related to decay of allowed harmonics during a long stay at the injection plateau. A reason of the decay seems to be in a slow flux creep in the superconductor and current redistribution between strands of superconducting cable [21], [154].

After resuming of acceleration, harmonics snap back to the initial hysteresis curves within a short time, causing the beam stability problems. For example, the sextupole component decays by $5 \cdot 10^{-4}$ (or 17 %) during injection in HERA dipole magnets, complicating the field correction system [123].

The magnetic measurements were performed for 30 minutes at the constant current of 1750 A in order to determine decay effects in the built magnets. The plateau was preceded by $0 \rightarrow 6500 \rightarrow 0 \rightarrow 1750$ A pre-cycle with the ramp rate of 40 A/s, resumed after 30 minutes with the ramp rate of 20 A/s. The magnet transfer function and main field component are presented in Figure 5.4.23, and the low order harmonics (not normalized) are shown in Figure 5.4.24. There is a clear snap in the transfer function after resuming of the ramp, extended over 1 minute range due to a slow acceleration of the current. This effect is related to the eddy currents in aluminum spacers, as shown in previous paragraph and can be reduced by increasing of the contact resistance.

Deviations of the low order harmonics at 30 minutes plateau are less than $0.5 \cdot 10^{-4}$. This number is by factor of 2-3 smaller than the natural "noise" in harmonic curves (due to the flux jumps) during ramp that allows concluding that there was no "snap back" effect observed in these magnets.
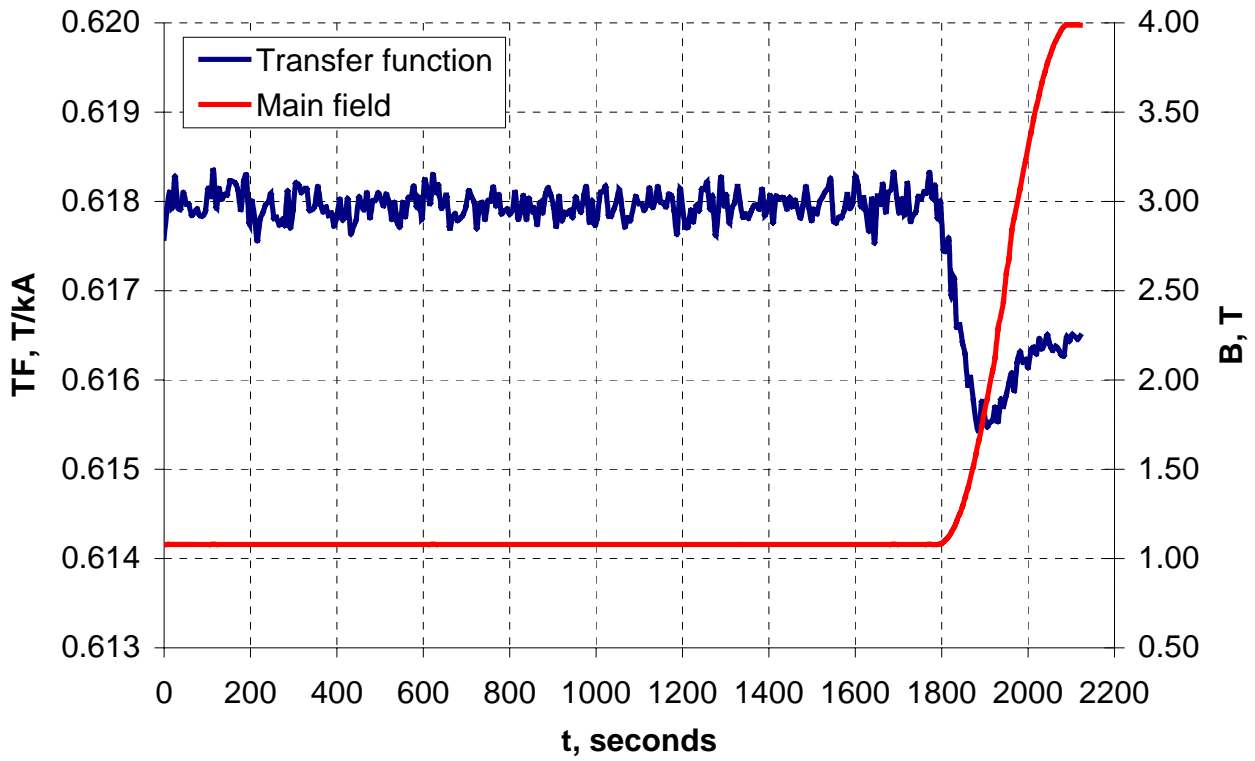
Figure 5.4.23. The transfer function and main field component at 1.75 kA plateau.
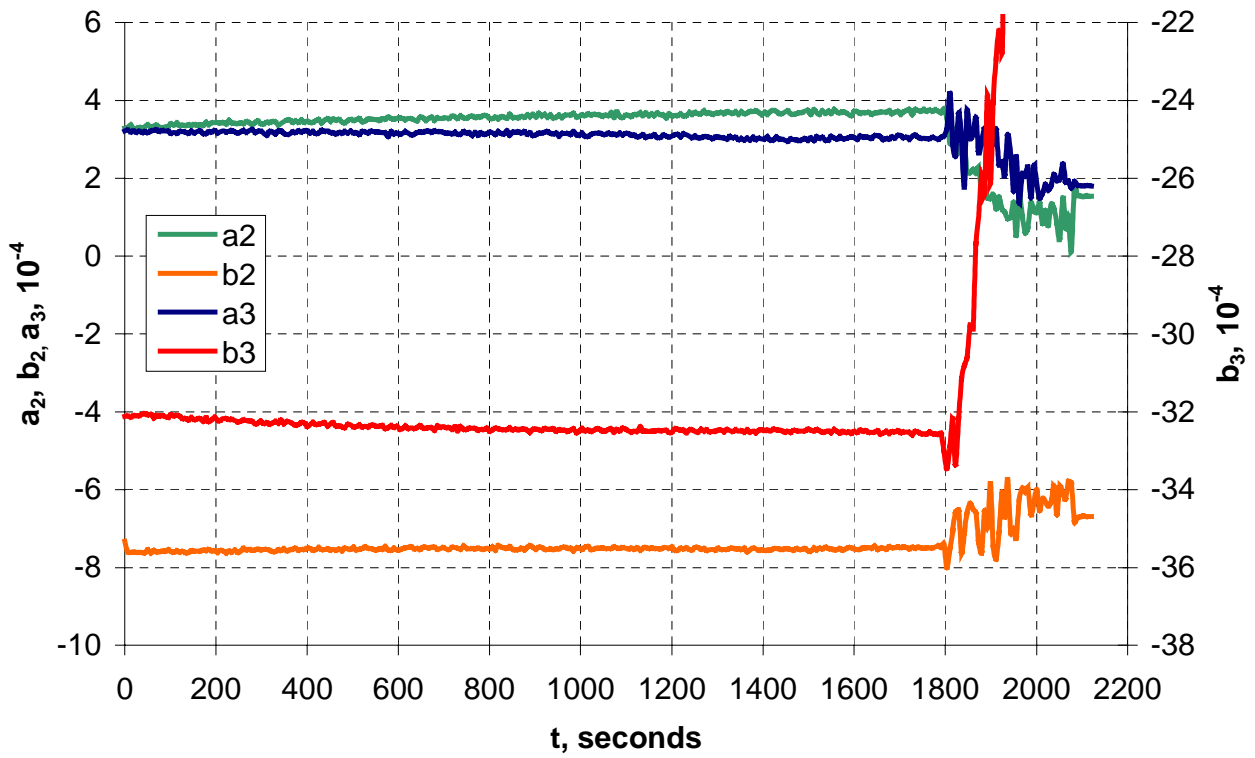
Figure 5.4.24. The low order harmonics at 1.75 kA plateau.

5.5 Summary

Two short Nb$_3$Sn dipole models were fabricated and tested at Fermilab. Low quench performance did not allow evaluation of the yoke saturation effect. However, other factors, affecting the field quality were quantitatively evaluated and compared with the numerical or theoretical predictions. The obtained results can be summarized as follows:

- Performed the 3D simulation of magnetic field in the single bore dipole magnet that allowed choosing of the coil and yoke lengths. Demonstrated that for the coil and yoke length of 1 m and 0.6 m respectively, the maximum field in the coil end is 8 % smaller than in the straight section. Calculated the longitudinal harmonics along the coil bore.

- Measured distribution of the longitudinal harmonics at medium currents matches the calculated values satisfactory well. It experimentally confirms validity of the numerical models and methods used during simulation.

- Analysis of the magnetic measurement results demonstrated presence of some undefined magnetic object, affecting the field quality at low currents. Such object could presumably be the stainless steel anti-cryostat pipe or the core inside the cable.

- Measured effect of the coil magnetization matches the calculations with 5 % accuracy. It experimentally verifies the numerical method used for simulation of the coil magnetization effect based on the finite-element code.

- Passive corrector of the coil magnetization effect, manufactured according to the proposed geometry demonstrated close to the calculated performance. It confirms correctness of the numerical simulation as well as the high corrector efficiency.

- It was found that the stainless steel core inside of the cable eliminates the ramp-rate dependence in the harmonics. Numerical simulation shown that the ramp-rate dependence in the transfer function explains by the eddy currents, flowing in the aluminum shells outside the coil. This effect can be reduced by factor of two by insulation of the shells from each other and more by choosing of the shell material with higher specific resistance.

- Apart from the most of NbTi magnets, there was no significant harmonics decay found within 30 minutes at injection plateau and no distinguishable "snap back" effect after resuming of the ramp. This encouraging result of the magnet performance may simplify the field correcting system of a future collider.

CONCLUSION

The dissertation work is devoted to study, optimization and justification of the major elements of the high field magnet design for a future proton collider. Main attention is paid to investigation of different factors, affecting magnetic field in the aperture and methods improving its quality. Addressed questions and the obtained results can be summarized as follows:

1. Developed design of magnetic system for the single bore Nb_3Sn dipole magnet with the maximum field of 12 T. Two short magnet models based on the developed design were manufactured and tested. Obtained experimental results are most comprehensively describe the field quality and corresponding effects in the Nb_3Sn magnets. Performed magnetic measurements enabled the quantitative evaluation of the geometrical harmonics in the aperture, influence of the superconductor magnetization on the field quality, dynamic effects, related to the eddy currents in the elements of construction and the harmonics drift at injection. Experimentally verified the numerical models and developed recommendations on improvement of the magnet parameters. Demonstrated that the source of a considerable dynamic effect in the transfer function is the aluminum shell outside the coil. Found absence of the "snap back" effect and harmonics drift at injection plateau that was unexpected but positive result.

2. Proposed and numerically confirmed new and perspective magnet designs, meeting requirements of the future collider VLHC:

   - Single-layer dipole magnet with common coils has various advantages with respect to other block type magnets. The auxiliary coils were eliminated that essentially simplifies the design without sacrificing the field quality. The number of the coil block was reduced to three per quadrant. Simple, flat coil geometry allows winding inside of the mechanical structure that reduces the labor expenses. Large cable bending radius makes it possible to implement the "react and wind" technique that reduces the furnace size and improves control of the cable dimensions. Demonstrated that the flat coil surface and absence of the auxiliary turns reduce the coil magnetization effect by a factor of ~20 with respect to other (dipoles TAMU and BNL) block type magnets.

   - There was proposed and numerically confirmed advantages of the iron yoke splits parallel to the flux lines, in the dipole magnet with the horizontal bore separation. Demonstrated that it reduces deviations of the field quality due to the gap variations under electromagnetic forces.

- Outer size of the shell type magnet with the "warm" iron yoke and horizontal bore separation was reduced by factor of 2 and the magnet weight was reduced by factor of 3-4 with respect to existing (dipole LHC) shell type magnets. Compensation of the coil magnetic coupling can be easily accomplished by introduction of small (less than +/- 1 mm) left-right asymmetry in the coil geometry. Demonstrated that restriction of the "cold" block alignment errors within 1.5 mm, limits the eccentricity force within 30 % of the "cold" block weight and the harmonic deviations within 10^{-4}.

- Separation of the iron yoke by the "cold" and "warm" parts allows 30 % size reduction of the dipole magnet with the vertical bore separation. The field quality satisfies the requirements.

- Developed effective designs of the quadrupole magnets with different functions and bore separation, coordinated with the relevant dipole parameters.

3. Proposed designs of the minimum inductance dipole coils based on the Rutherford type cable. Demonstrated that 12 turns in the shell type coil and 10 turns in the block type coil are necessary and enough for generation of the field with the strength and quality required for VLHC. It leads to the minimum inductance that by factor of 20-30 smaller than in existing shell and block type magnets with the same aperture size and nominal field. It allows a cardinal improvement of the mechanical structure concept and the magnet length choice. A collar with slots similar to the stator of an electrical motor can be used for support of the shell type coil, when the cable is wound inside rigid mechanical structure. It reduces errors in the cable positions and therefore the random field harmonics by an order of magnitude with respect to the usual shell type design using "floating" wedges. The block type coil can be wound inside the common collar structure similar to the one implemented in the common coil magnet. It increases tolerances on the cable positions as well. Minimum number of turns and blocks significantly reduces the coil manufacturing time and cost. Exceptionally low inductance gives possibility to increase the magnet length up to the limit driven by manufacturing and transportation issues, which is by factor of 2-3 larger that the typical length of the high field magnets. Large cable size allows implementation of the multistage strands. Demonstrated that combination of Nb_3Sn and copper sub-strands reduces the complete strand cost by 15-20 % with respect to the solid strand at the same load parameters.

4. Numerically and experimentally confirmed method of simulation the coil magnetization effect based on the finite-element code. Performed numerical simulation of the coil magnetization effect in various dipole and quadrupole magnets. Shown that all the considered designs possessed to a large coil magnetization effect, except the single layer common coil

magnet. Demonstrated that presence of the flat yoke boundary, parallel to the horizontal axis is not necessary or sufficient condition of elimination the coil magnetization effect.

5. Proposed simple, effective and cheap method of passive correction the coil magnetization effect, based on the ferromagnetic strips. Considered installation of the passive corrector inside the aperture, outside the coil and on the coil wedges. Studied influence of the corrector geometrical parameters on the low order harmonics, which allows optimization of the corrector geometry, depending on the necessary effect. Demonstrated that corrector inside the aperture has the maximum efficiency. However, the corrector on the coil wedges provides the most precise effect.

6. Proposed alternative method of compensation the coil magnetization effect, based on ferromagnetic strips, installed inside or between the cables. In case of the strip inside the cable there is a possibility of simultaneous reduction the eddy currents in the cable by choosing the strip material with high specific resistance. A small adjustment of the coil geometry allows enhancement of the corrector performance by factor of two.

7. Performed experimental study of the passive corrector installed inside the aperture of Nb_3Sn dipole magnet. The measurements confirmed high efficiency of the proposed passive corrector and verified numerical simulations of the corrector parameters.

ACKNOWLEDGMENTS

doctoral work.

I am grateful to the Fermilab Technical Division head Dr. Peter Limon for the opportunity to work as a member of the Fermilab High Field Magnet Group and participate in different aspects of the magnet design, manufacturing and testing.

APPENDIX A. COST OPTIMIZATION OF A HADRON COLLIDER

This appendix describes the cost scaling laws and optimization of hadron colliders based on the high field magnets. Using few simplifying assumptions that should give a reasonable approximation, cost of the collider magnet is divided among several major components. Scaling law for every component is determined along with the weight factors that allow cost comparison between different magnet designs. Cost of hadron collider as a function of the field, aperture size and critical current density in superconductor was described analytically that allows cost optimization by changing the magnet parameters. The optimum magnetic field was determined for machines based on NbTi superconductor, operating at 4.2 K or 1.9 K and Nb$_3$Sn superconductor operating at 4.2 K. Analyzed influence of the magnet design parameters on a machine cost provided information on ways leading to the magnet cost reduction. Economical justification of a Nb$_3$Sn collider was performed, which lets to determine the maximum price ratio between Nb$_3$Sn and NbTi superconductors that makes Nb$_3$Sn collider economically effective.

A.1 Magnet cost scaling laws

In order to perform cost analysis and optimization of a collider one has to determine the major cost drivers and their scaling laws. The magnet cost can be virtually divided among three major contributors: coil, cold mass and cryostat. Since lengths of high field magnets are usually much bigger than their transverse size, magnet cost per unit of length can be assumed proportional to the sum of cross-section areas of these three components with the relevant cost factors:

$$C'_{mag} = S_{coil}K_{coil} + S_{cm}K_{cm} + S_{cr}K_{cr} \qquad (A.1.1)$$

Scaling law for the coil area has been determined in the paragraph 1.2.1. The yoke and skin drive the cross-section area and cost of the cold mass. Assuming equal yoke saturation and fringe field as the scaling criteria for yoke size, one can require that the ratio of magnetic flux, generated by the coil to the yoke outer radius remain constant:

$$R_{yoke} \sim R_{bore}B$$

or

$$S_{yoke} \sim R_{bore}{}^2B^2 \qquad (A.1.2)$$

It leads to approximately constant flux density, yoke saturation and fringe field for yokes with relatively big radii ("cold" yoke magnets).

Scaling criteria for the skin thickness is the equal tensile stress created in skin by electromagnetic forces. Horizontal force per unit of coil shell length is proportional to:

$$F'_x \sim B_y I_z$$

or

$$F' \sim B^2$$

for a fixed bore radius. Variations in the bore radius would require proportional adjustment of the current in the coil in order to maintain a constant field. Therefore, in general, the force depends on the field and bore radius as:

$$F' \sim R_{bore} B^2 .$$

Now one can find scaling law for the skin area. Equality of tensile stresses imposes keeping a constant ratio between the force F' and the skin thickness d_{skin} that means:

$$d_{skin} \sim F' \sim R_{bore} B^2$$

Since the skin area is proportional to the skin (yoke) radius R_{yoke} times the skin thickness d_{skin} one can write the final dependence:

$$S_{skin} \sim R_{bore} d_{skin} \sim R_{bore}^2 B^3 . \tag{A.1.3}$$

Comparing (A.1.2) and (A.1.3) one can see that the skin area grows faster than the yoke area by a power of B. For simplicity, it can be assumed that the extra force is taken by some slim collar around the coil and the cold mass area scales as:

$$S_{cm} \sim S_{skin} + S_{yoke} \sim R_{bore}^2 B^2 .$$

The cryostat area is proportional to its radius times the thickness. Since the cryostat thickness virtually does not depend on parameters of the magnet it houses, one can write:

$$S_{cr} \sim R_{yoke} + \Delta R ,$$

where ΔR is the radial space between cryostat and iron yoke. For simplicity, this space can be assumed proportional to the yoke radius, then:

$$S_{cr} \sim R_{bore} B .$$

There has been determined all the laws necessary to scale magnet cost for any field and bore radius:

$$C'_{mag}(R_{bore}, B) \sim S_{coil}(R_{bore}, B)K_{coil} + R_{bore}^2 B^2 K_{cm} + R_{bore}BK_{cr}. \qquad (A.1.4)$$

In order to find the cost factors one should use some reference magnet with known contribution of magnet components into the total magnet cost. RHIC dipole magnet was picked for this purpose as is had a typical among the high field magnets design and parameters. Table A.1.1 presents cost distribution between the main magnet components [119].

Table A.1.1. Cost distribution of RHIC dipole magnet.

Component	Materials, %	Labor, %	Total, %
Coil	18	11	29
Cold mass	21	13	34
Cryostat	23	14	37
Total	62	38	100

It is clear that the labor part makes a considerable contribution into the magnet cost. However, it is difficult to establish a direct scaling laws for the labor part, as it is not obviously related to the magnet parameters, like the field and aperture size, but rather to types of materials and technological procedures used during magnet fabrication. For simplicity, it was assumed that the labor part scales directly proportional to the materials part (which should presumably be true for relatively large orders).

Taking cost of the RHIC dipole magnet for 1 unit of a relative magnet cost one can determine the cost factors. Solving system (1.2.6) for the specific RHIC parameters: $B = 3.46$ T, $R_{bore} = 4$ cm, NbTi superconductor with $C_1 = 6000$ A/mm^2, $C_2 = 600$ A/mm^2/T and $K_{cusc} = 2.2$ one finds the coil area $S_{coil} = 7.47$ cm^2. This value is smaller than the actual area of the RHIC coil since it assumes the ideal coil configuration without spacers between coil blocks and no margin in the bore field. Keeping it the same way for any other magnet with different field and bore radius would assure that the magnet has the same packing factor of cables in the coil and bore field margin (15 %) as the RHIC dipole. Table A.1.2 presents cost factors that satisfy (A.1.4) for the RHIC dipole parameters.

Note that the scale factors represent relative cost of the material and irrelevant to the magnet design or parameters, which allows cost estimating of any other high field magnet using the determined scale laws in units of the RHIC magnet cost per unit of length. Figure A.1.1 shows the relative cost of high field magnet based on the NbTi coils, operating at 4.2 K (RHIC

parameters) or 1.9 K temperature (with $C_1 = 7800$ A/mm^2, $C_2 = 600$ A/mm^2/T) and Nb$_3$Sn coil operating at 4.2 K (B$_{c2}$ = 24.88 T, J$_c$(12 T) = 3000 A/mm^2).

Table A.1.2. Cost factors.

Component	Cost factor	Scaling law
Coil	$3.88 \cdot 10^{-2}$ 1/cm^2	S_{coil}
Cold mass	$1.77 \cdot 10^{-3}$ 1/T^2/cm^2	$R_{bore}{}^2 B^2$
Cryostat	$2.67 \cdot 10^{-2}$ 1/T/cm	$R_{bore} B$

The copper to non-copper ratio in the coils was 0.85, which is a safe minimum required for the micro-quench stabilization. Necessary for the quench protection amount of copper can be introduced using the sub-strand approach [53], which does increase coil area but virtually does not contribute to the coil cost and generally leads to 15-20 % cost reduction of superconducting cable. Coil bore diameter was set to 40 mm, proven to be reliable by the VLHC Design Study [10]. The plot also shows the relative magnet cost curves for SSC and LHC machines, calculated by the same procedure.
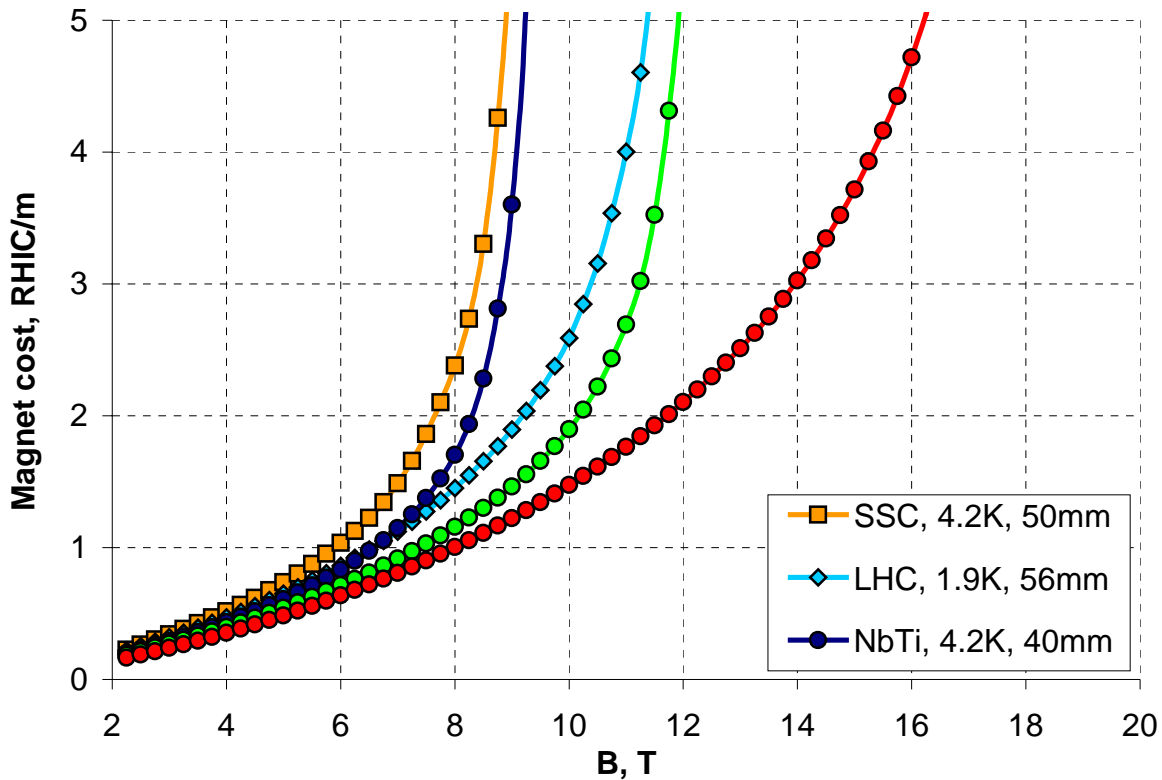
Figure A.1.1. Magnet costs as functions of the field.

A.2 Collider cost

Similarly to the scaling expression for the magnet cost, one can define a collider cost function as:

$$C_{col} = C'_{mag} \cdot L + C'_{tun} \cdot L + C_{const},$$

where L is the collider circumference, C_{mag}' is the magnets cost per unit of length, C_{tun}' is the tunnel, instrumentation and cryogenics cost per unit of length and C_{const} are some constant expenses, irrelevant to the machine parameters. It was convenient to compare costs of fully equipped tunnels in units per T·m or TeV with subtracted constant expenses:

$$C'_{eqtun} \sim \frac{1}{B}\left(C'_{mag}K_{mag} + C'_{tun}K_{tun}\right).$$

In order to determine the cost the factors one can use the cost distribution for some reference machine, similarly to the magnet case. Table A.2.1 presents cost distribution for the SSC project, escalated to financial year 2001 dollars [155].

Table A.2.1. Cost distribution of SSC project.

Component	FY2001, K$	Ratio, %
Civil Underground	558,160	15.29
Civil Above Ground	170,133	4.66
Arc Magnets	2,043,811	55.98
Correctors & Special Magnets	168,622	4.62
Vacuum	17,341	0.47
Installation	121,487	3.33
Cryogenics	266,828	7.31
Interaction Regions	87,133	2.39
Other Accelerator Systems	217,672	5.96
Total	3,651,187	100.00

The ratio between magnet and non-magnet part in this table is 56 % over 44 %. Since the cost ratio is given for the double bore magnets – the scaling will be correct for double bore magnets only. It is necessary to find the coil area for the specific SSC magnet parameters: $B = 6.8$ T, $R_{bore} = 2.5$ cm, NbTi superconductor with $C_1 = 6000$ A/mm^2, $C_2 = 600$ A/mm^2/T and $K_{cusc} = 1.6$. The coil area corresponding to these parameters is $S_{coil} = 17.73$ cm^2. Taking cost of 1 m of fully equipped SSC tunnel for 1 unit one can find the cost factors: $K_{mag} = 2.76$ T and $K_{tun} = 2.99$ T. Figure A.2.1 shows cost of the fully equipped tunnel per T·m for three choices of superconductor. Dividing the total cost of fully equipped SSC tunnel by the operating field of 6.8 T and the machine circumference of 87 km one finds the SSC cost of 6172 $/T/m, which makes it possible to plot the cost distribution in the absolute units (Figure A.2.2).
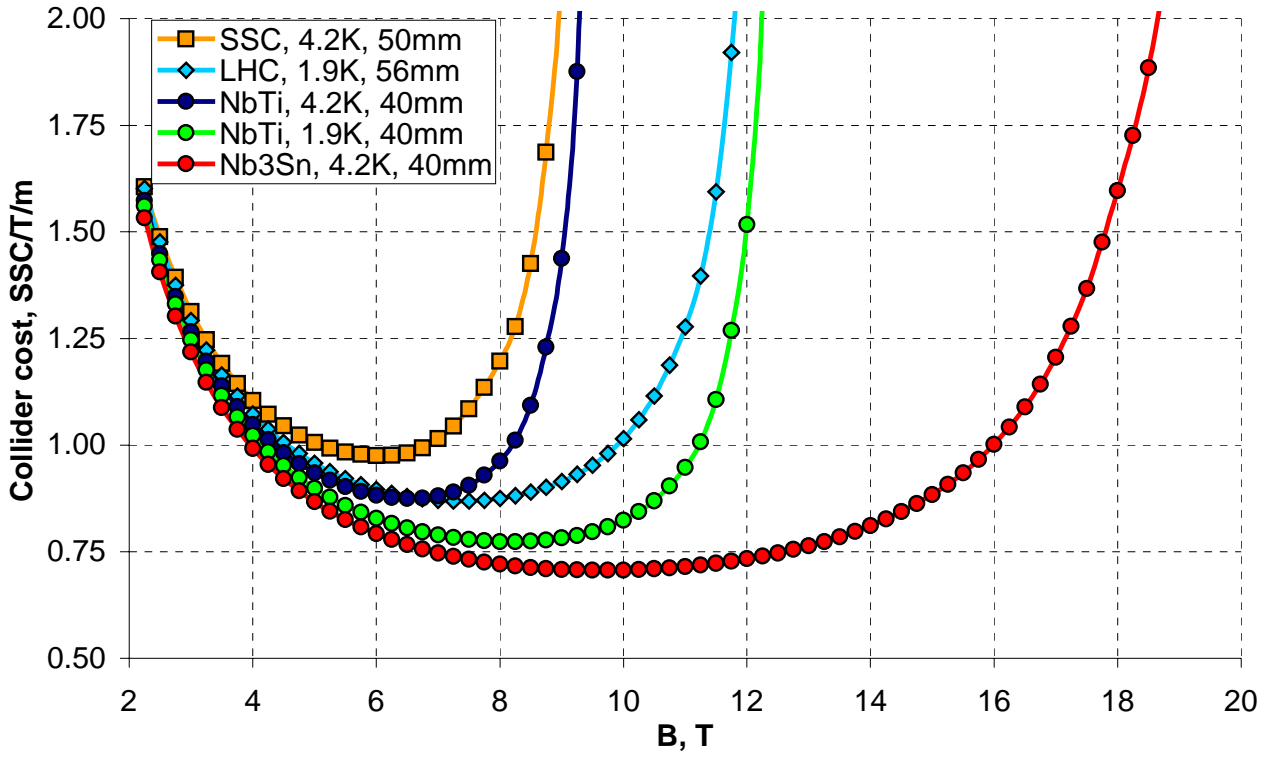
Figure A.2.1. Collider costs as functions of the field in SSC units.
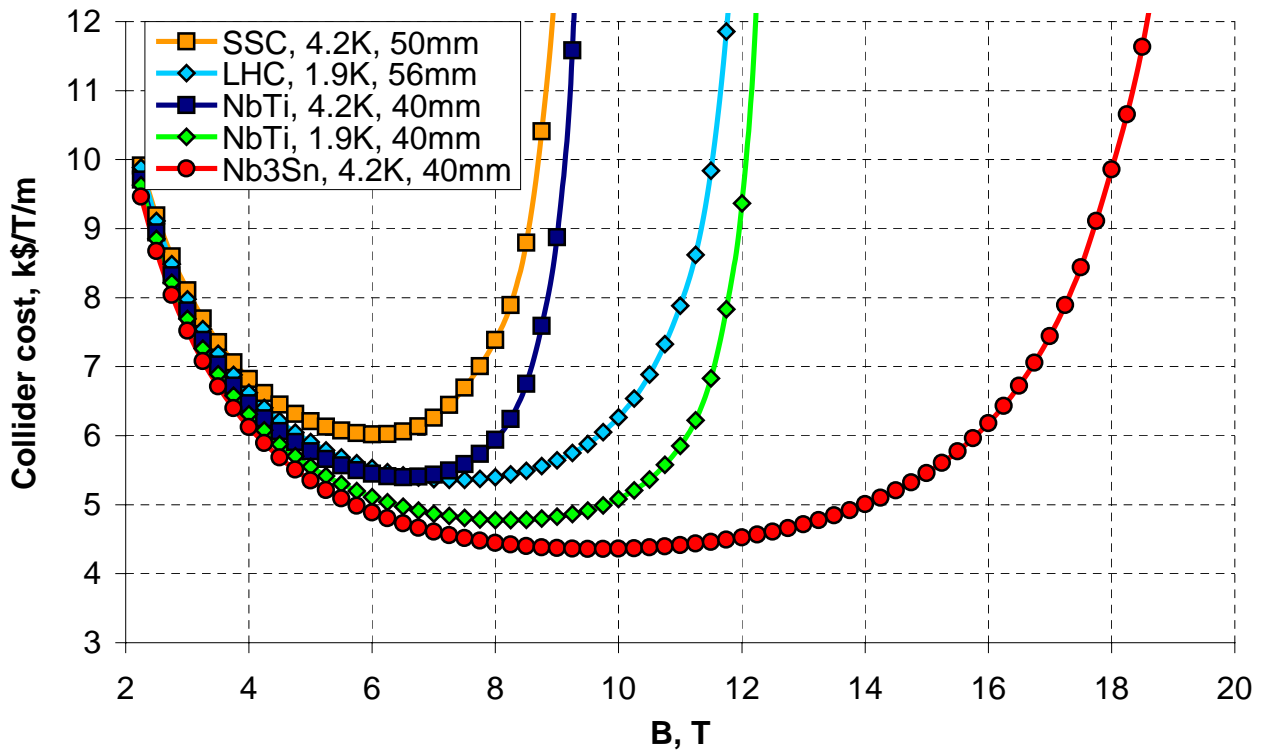
Figure A.2.2. Collider costs as functions of the field in FY2001 dollars.

A.3 Analysis of the magnet design parameters

Results of the previous paragraph demonstrated the cost dependencies for machines with different superconductor properties and aperture sizes. It was interesting to separately analyze effect of each particular parameter on the machine cost and optimum field. For this purpose the critical current density in superconductor was fixed at $J_c(12 \text{ T}, 4.2 \text{ K}) = 3000 \text{ A/mm}^2$, copper to non-copper ratio in the coil at 0.85 and the coil bore diameter was consequently varied within 30-50 mm with 5 mm increment. Figure A.3.1 shows the collider cost as a function of the field for different bore diameters and Figure A.3.2 derives minimum cost and optimum field as functions of the bore diameter. One can notice that decreasing of the coil bore diameter from the "proven-to-be-feasible" 40 mm to somewhat "close-to-the-limit" 30 mm (or by 33 %) leads to decreasing of the collider cost by only 2 %. However, inevitable growth of the beam screen, cryogenics and the magnet alignment system cost (not included in this model) may very likely eliminate advantage of the smaller aperture option, if not to make it more costly at all. In fact, larger than 40 mm aperture may turn out to be more effective, especially for higher than 10 T field magnets, when synchrotron radiation starts playing a significant role in the magnet design. The optimum field depends nearly inversely proportional on the bore diameter and changes from 9.64 T to 9.9 T for the 40 mm to 30 mm aperture change.

Influence of the second parameter – critical current density was analyzed for the coil bore diameter fixed at 40 mm and copper to non-copper ratio in the coil of 0.85. Figure A.3.3 shows the collider cost as a function of the field for different critical current densities in superconductor at 12 T and 4.2 K and Figure A.3.4 derives minimum cost and optimum field as functions of the critical current density. It is noticeable that the collider cost and the optimum field changes significantly within the range of 1000-3000 A/mm^2 but starts to "saturate" for higher values. Thus, the cost drops by 16 % for the first 2000 A/mm^2 and only by 4 % for the second one. It explains by the fact that the coil area and therefore its contribution to the cost decrease at a higher critical current density, while the rest of components contribute nearly constant amount. Obviously, reaching of higher critical current densities requires additional investments to the superconducting technology (at least at the R&D stage) that reduces benefits of conductors with high critical current density even more.

The last parameter necessary to analyze was the copper to non-copper ratio. Since it is in direct correlation with the current density in superconductor, a new copper to non-copper ratio can be calculated as:

$$K_{cusc}^{new} = \frac{J_c^{new}}{J_c^{old}}\left(1 + K_{cusc}^{old}\right) - 1,$$

under assumption that the current in the coil (and so the bore field) remains constant.

Having fixed the critical current density at 3000 A/mm^2, one can easy derive the minimum collider cost and the optimum field as functions of the copper to non-copper ratio from the previous plot. Figure A.3.5 presents the minimum cost and the optimum field as functions of the copper to non-copper ratio. Changing of the copper to non-copper ratio from 0.85 (short models) to 1.2 (necessary for the quench protection of a long magnet) increases the minimum collider cost by 2 % that is a fairly small but necessary price of a safe machine operation.
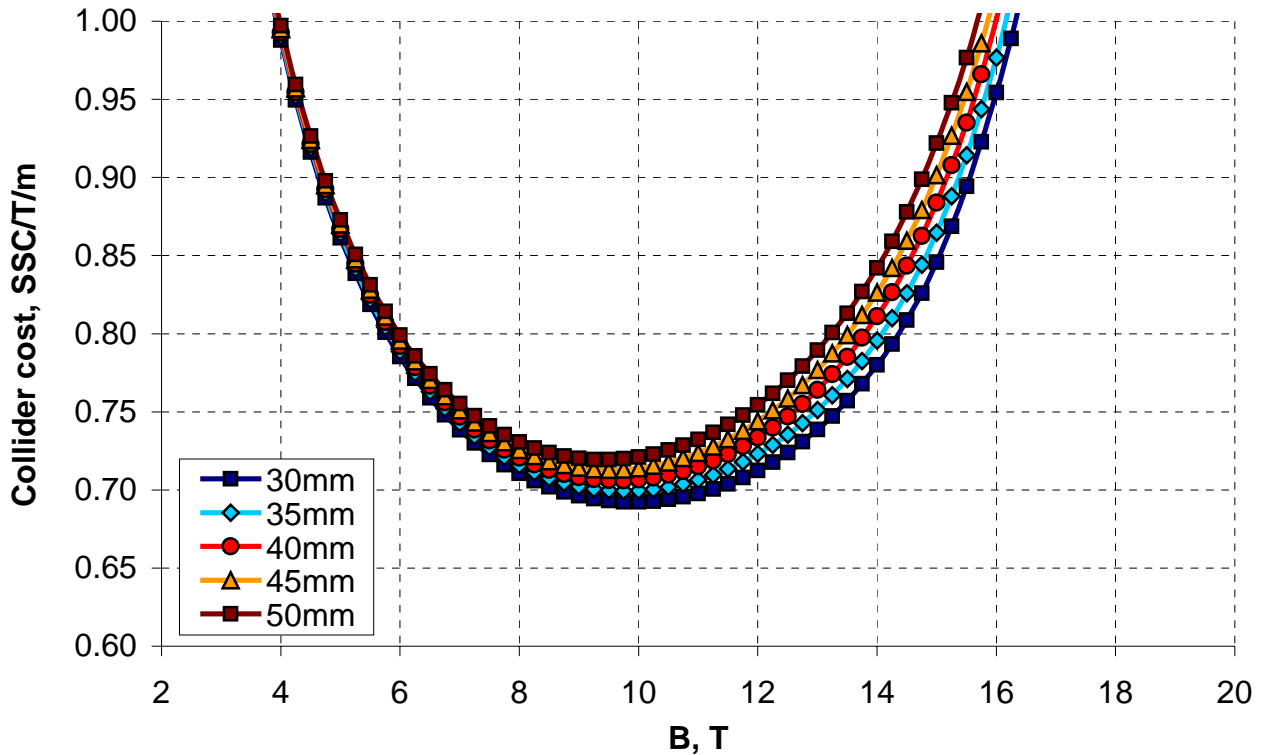
Figure A.3.1. Collider cost as a function of the field in SSC units for different coil apertures.

208
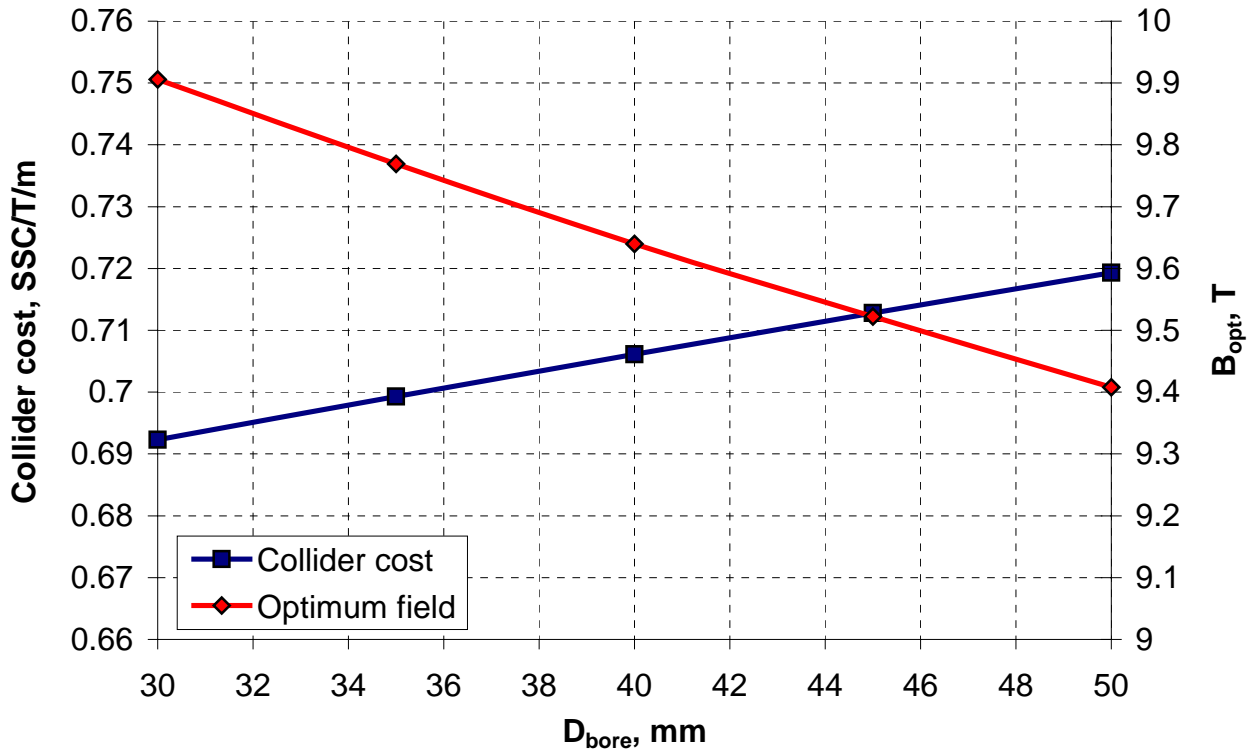
Figure A.3.2. Minimum collider cost and optimum field as functions of the bore diameter.
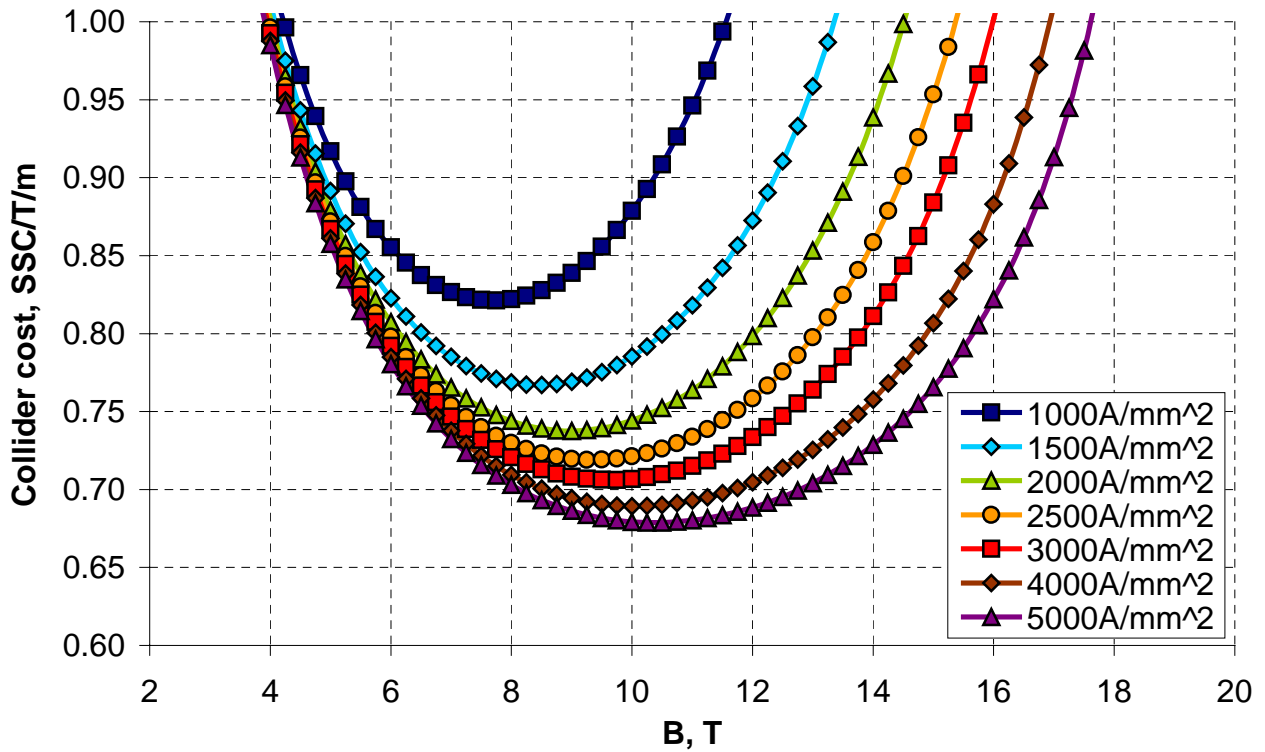
Figure A.3.3. Collider cost as a function of field in SSC units for different critical current densities.
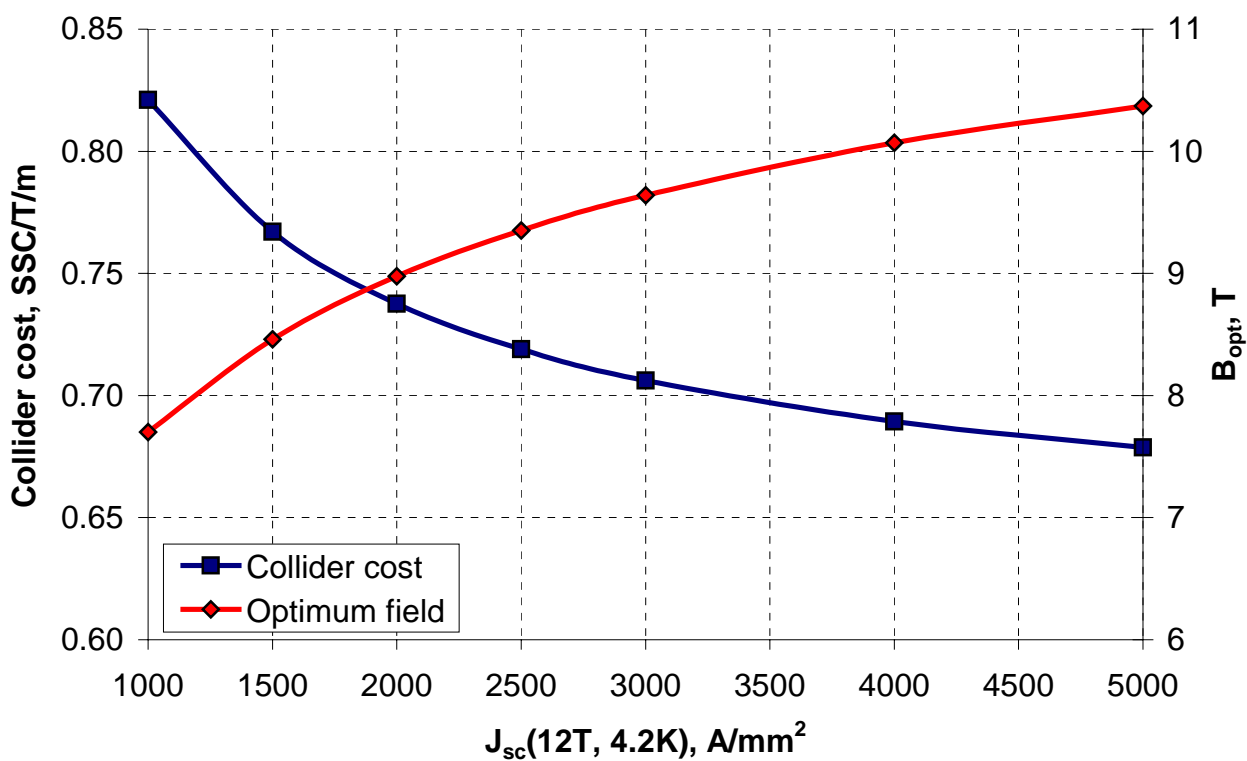
Figure A.3.4. Minimum collider cost and optimum field as functions of critical current density.
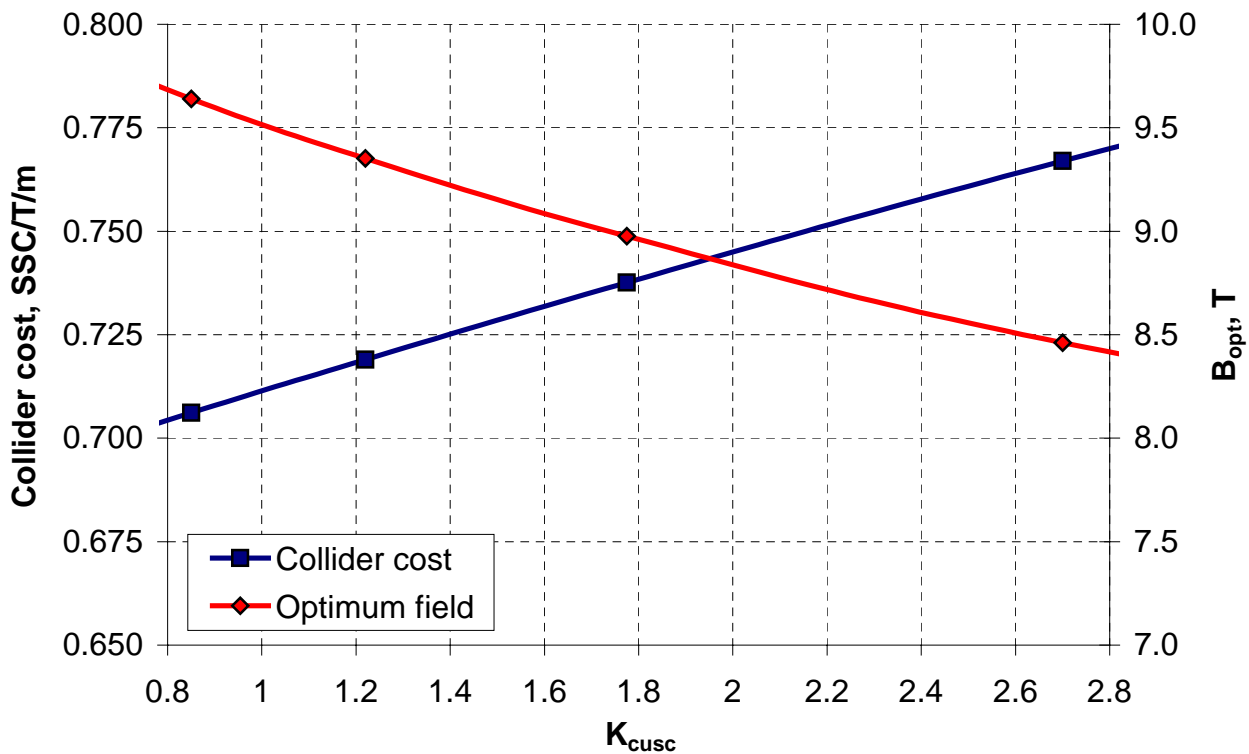
Figure A.3.5. Minimum collider cost and optimum field as functions of the copper to non-copper ratio.

A.4 Economical justification of a Nb$_3$Sn collider

In order for a collider based on Nb$_3$Sn superconductor to be economically effective, its cost should be less than that of a NbTi based collider. The model considered in previous paragraphs did not take the difference in cost between NbTi and Nb$_3$Sn superconductors into account. It can be easily accomplished by adding the corresponding term in (A.1.4):

$$C^{'}_{mag}(R_{bore}, B) \sim S_{coil}(R_{bore}, B) K_{coil} K_{Nb_3Sn/NbTi} + R_{bore}{}^2 B^2 K_{cm} + R_{bore} B K_{cr},$$

where $K_{Nb3Sn/NbTi}$ is the ratio of prices per unit of volume between Nb$_3$Sn and NbTi superconductors. Consequently repeating all the necessary steps, one can find the price ratio that renders cost of Nb$_3$Sn collider being equal to NbTi collider.

The ratio is 4.7 for the Nb$_3$Sn collider with 40-mm bore magnets and the critical current density of 3000 A/mm^2 at 12 T and 4.2 K. Figure A.4.1 shows the cost distribution of corresponding NbTi and Nb$_3$Sn colliders. The optimum field for the NbTi collider is 6.5 T. The optimum field for the Nb$_3$Sn collider with the price ratio of 4.7 is 7.5 T and for the Nb$_3$Sn collider with the price ratio of 1.0 is 10 T.
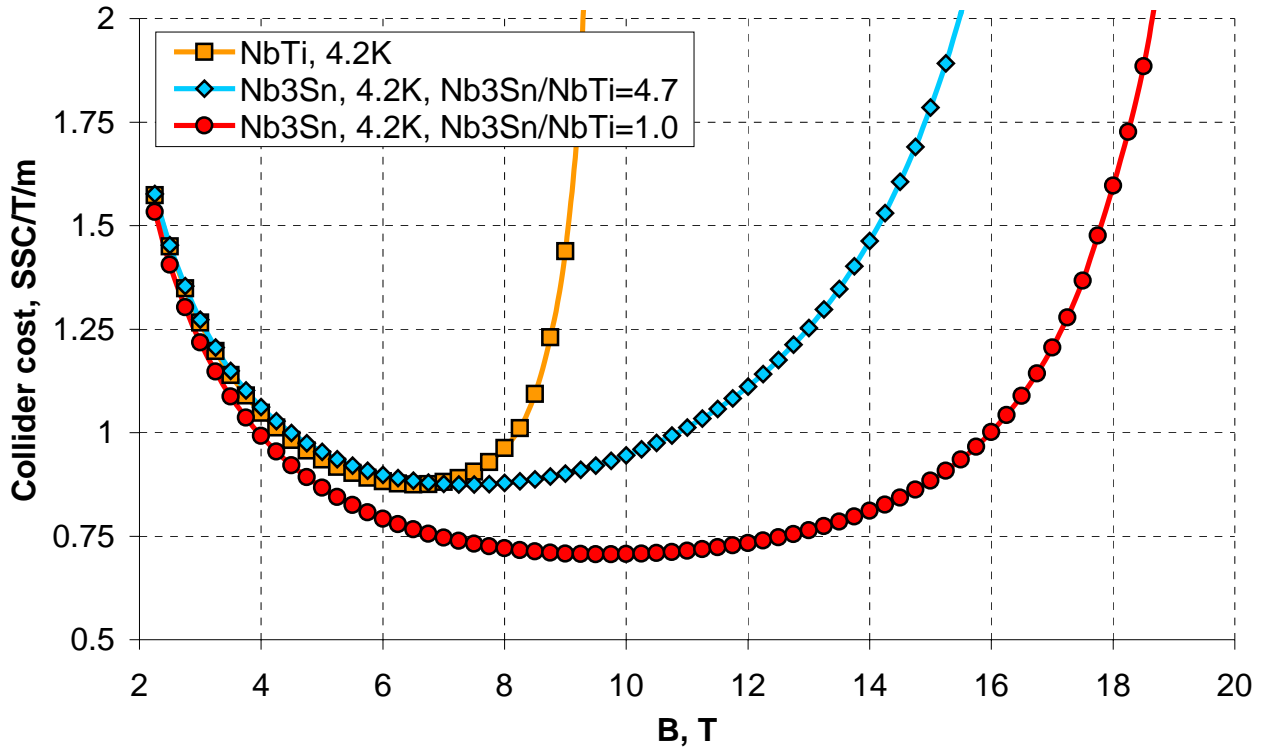
Figure A.4.1. Collider cost as a function of the field in SSC units.

A.5 Summary

The considered cost model based on reasonable assumptions allowed cost comparison between colliders based on the high field magnets with different parameters. Comparison between SSC, LHC and VLHC colliders shows consequent growth of the optimum operating field and reduction of the machine cost per T·m. Thus, fully equipped tunnel of VLHC with justified during the design study parameters [10] and the center-mass energy of 175 TeV would cost 3.1 times the SSC (40 TeV), when the same energy SSC would cost 1.4 times more under assumption of equal prices for the Nb_3Sn and NbTi conductors. Minimum on the cost curve, corresponding to the optimum field for VLHC is ~10 T, which is essentially smaller than fields practically achievable with modern Nb_3Sn conductors. Shallowness of the minimum, in fact, allows defining the optimum field range of 8-11 T. However, contribution of the synchrotron radiation (not included in the model) would cut the optimum range at the high field side, presumably to 8-10 T.

Analyzed influence of the magnet design parameters on the machine cost allows concluding:

- Decreasing of the magnet aperture has a weak effect on the machine cost. Taking into account cost contribution of the beam screen, cryogenics and the magnet alignment, the optimum aperture is unlikely to be smaller than 40 mm. In fact, it may be even larger, especially for more than 10 T field magnets, where synchrotron radiation makes a significant cost contribution.

- Increasing of the critical current density in superconductor from 1000 A/mm^2 to 3000 A/mm^2 makes a noticeable machine cost reduction (16 %). Further increasing of the critical current density however, has a relatively small effect and may not be economically justified at all, due to necessity of significant investments in superconducting technology. Taking into account cabling and other types of critical current degradations, one would define the ultimately wanted critical current density in superconductor at 3500 A/mm^2.

- Variation of the copper to non-copper ratio within the reasonable limits has a weak effect on the machine cost. Thus changing of the copper to non-copper ratio from 0.85 to 1.2, necessary for the quench protection of a long (>15 m) magnet, increases the collider cost by 2 % that seems to be unavoidable price of a safe operation, unless a sophisticated quench protection system is developed.

Economical justification of the Nb_3Sn collider shows that the price of Nb_3Sn conductor may be as large as 4.7 times the price of NbTi for the collider to be economically effective. This price difference is virtually achieved for small quantities of Nb_3Sn superconductor and may be reduced even more after assessment of a large machine.

Further reduction of the collider cost per T·m is possible during R&D program. Using of high field magnets with the "warm" iron yoke [49], for instance, allows reduction of the cryostat size by factor of ~2, while keeping other parameters uniform. Thus, depending on the design of the coil support structure, the cold mass cost can be reduced by a factor of 3-4 and the cryostat ("warm" yoke) cost by at least factor of two. Other improvements leading to reduction of the labor part during coil production by implementing coils with the minimum number of turns are also beneficial [53].

APPENDIX B. COIL DESIGN PARAMETERS

This appendix summarizes design parameters of three types of coils with circular shell, elliptical shell and block type geometry. The coil bore size was varied from 30 to 45 mm for every type of coil. Some steps of the optimization are described in [156], [157].

The block numbering for all the designs starts from the midplane block of the outer coil layer. Since all the coils have horizontal and vertical symmetry with respect to coordinate axes, only coordinates of blocks in I quadrant are presented. The naming convention for the polar coordinates in the shell type coils (positioning and inclination angles φ and α) and Cartesian coordinates in the block type coils are given by Figure B.1. All the coordinates include cable insulation. There are 0.125 mm of the cable insulation and 0.5 mm of the interlayer insulation assumed in all the designs.
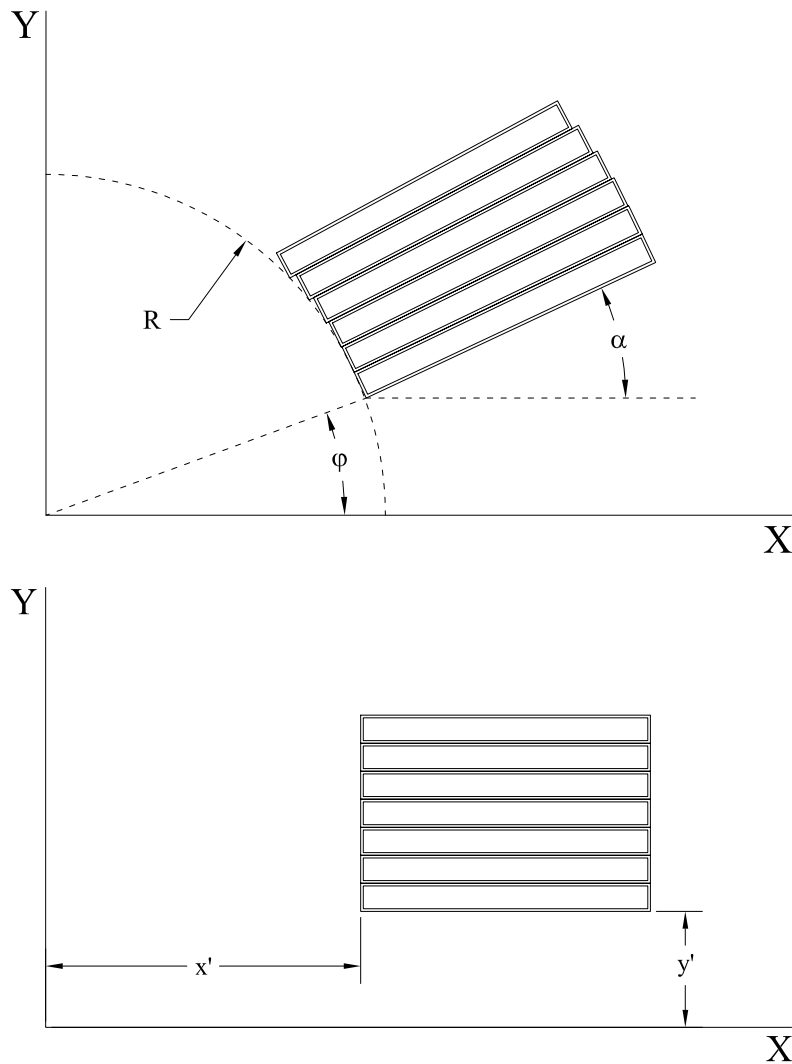
Figure B.1. The naming convention for a shell (top) and block (bottom) type coils.

B.1 Shell type coils with a circular aperture

Coils of this type were optimized in assumption of circular supporting cylinder for inner coil layer. Designs with 30-40 mm bore have 5 block per quadrant, design with 45 mm bore has 6 block per quadrant. Figure B.1.1 presents coil geometry with field quality diagram and Table B.1.1 summarizes coil block coordinates for every optimized design.

Figure B.1.1 Geometry and field quality in shell type coils with circular bore. Bore diameter is written above each coil.

Table B.1.1. Coordinates of the coil blocks in shell type coils with circular bore.

Bore size, mm	Parameter	Block #					
		1	2	3	4	5	6
30	N cables	9	9	4	6	4	-
	R, mm	29.615	29.615	15	15	15	-
	φ, deg	0.000	24.294	0.000	20.000	53.978	-
	α, deg	0.000	32.834	0.000	25.000	51.000	-
35	N cables	9	9	4	6	4	-
	R, mm	30.907	30.907	17.500	17.500	17.500	-
	φ, deg	0.000	25.000	0.000	20.734	55.885	-
	α, deg	0.000	25.269	0.000	26.036	46.000	-
40	N cables	8	7	4	7	4	-
	R, mm	33.608	33.608	20.000	20.000	20.000	-
	φ, deg	0.000	24.903	0.000	19.400	54.300	-
	α, deg	0.000	27.198	0.000	25.906	62.756	-
45	N cables	7	5	4	3	5	3
	R, mm	36.309	36.309	36.309	22.500	22.500	22.500
	φ, deg	0.000	23.553	45.078	0.000	19.600	54.081
	α, deg	0.000	30.017	46.063	0.000	30.769	65.000

B.2 Shell type coil with an elliptical aperture

Coils of this type were optimized in assumption of elliptical supporting cylinder for inner coil layer. Designs with 30-40 mm bore have 5 block per quadrant; design with 45 mm bore has 6 block per quadrant. Figure B.2.1 presents coil geometry with field quality diagram and Table B.2.1 summarizes coil block coordinates for every optimized design.

30 mm

35 mm

40 mm

45 mm
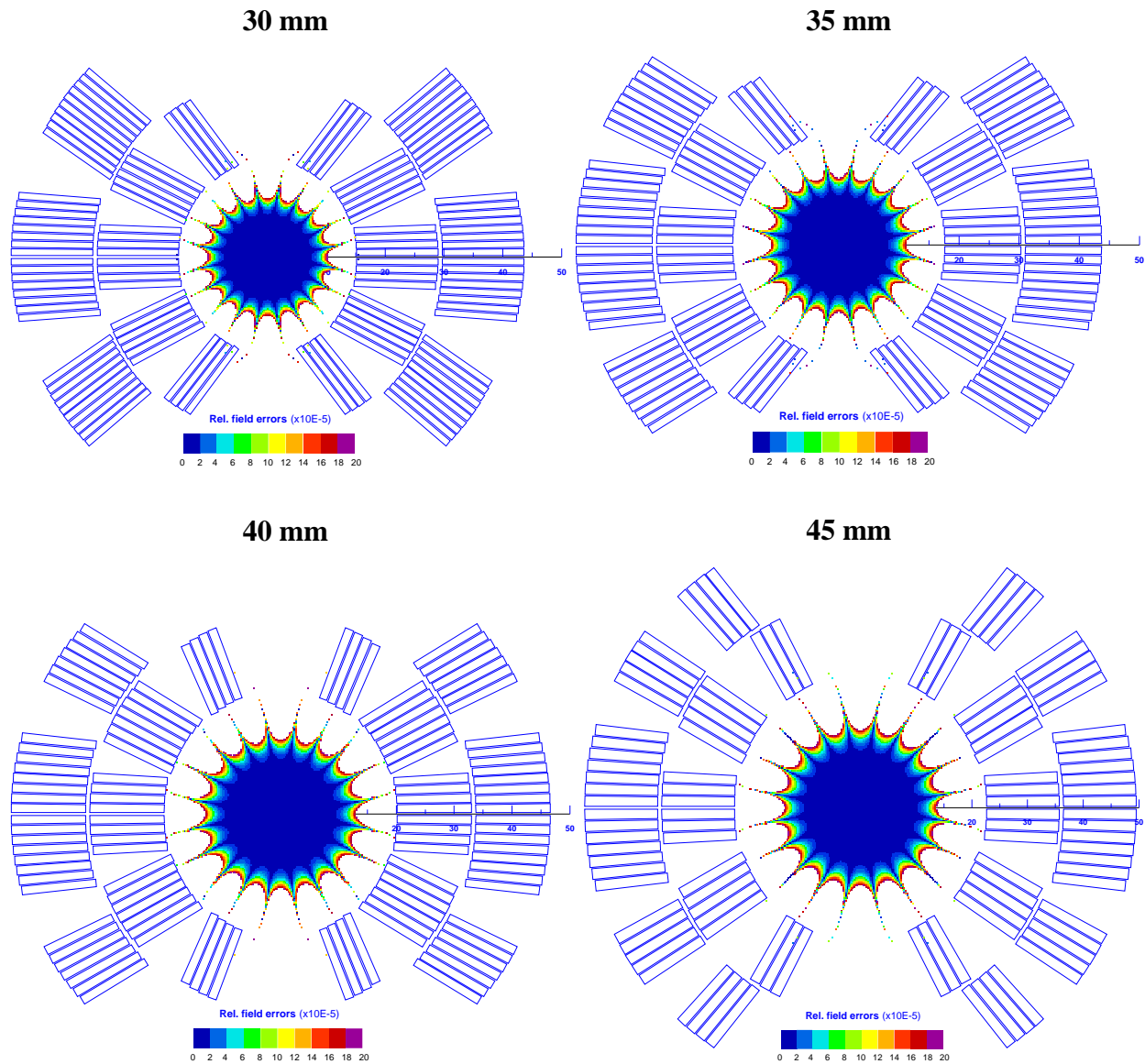
Figure B.2.1 Geometry and field quality in shell type coils with elliptical bore. Bore diameter is written above each coil.

Table B.2.1. Coordinates of the coil blocks in shell type coils with elliptical bore.

Bore size, mm	Parameter	Block #					
		1	2	3	4	5	6
30	N cables	9	9	4	6	4	-
	R, mm	29.615	29.615	15.000	15.000	15.000	-
	φ, deg	0.000	25.896	0.000	20.828	55.448	-
	α, deg	0.000	34.982	0.000	25.333	51.263	-
35	N cables	9	9	4	6	4	-
	R, mm	30.907	30.907	17.500	17.500	17.500	-
	φ, deg	0.000	26.881	0.000	20.953	56.000	-
	α, deg	0.000	25.689	0.000	26.540	48.488	-
40	N cables	8	7	4	7	4	-
	R, mm	33.608	33.608	20.000	20.000	20.000	-
	φ, deg	0.000	30.293	0.000	19.603	54.239	-
	α, deg	0.000	25.854	0.000	25.897	66.304	-
45	N cables	7	5	4	3	5	3
	R, mm	36.309	36.309	36.309	22.500	22.500	22.500
	φ, deg	0.000	26.311	49.186	0.000	19.894	54.991
	α, deg	0.000	28.634	47.625	0.000	29.72	60.076

B.3 Block type coils with square aperture

Coils of this type were optimized in assumption of square supporting cylinder for inner coil layer and auxiliary coils. All the designs have 5 block per quadrant. Figure B.3.1 presents coil geometry with field quality diagram and Table B.3.1 summarizes coil block coordinates for every optimized design.
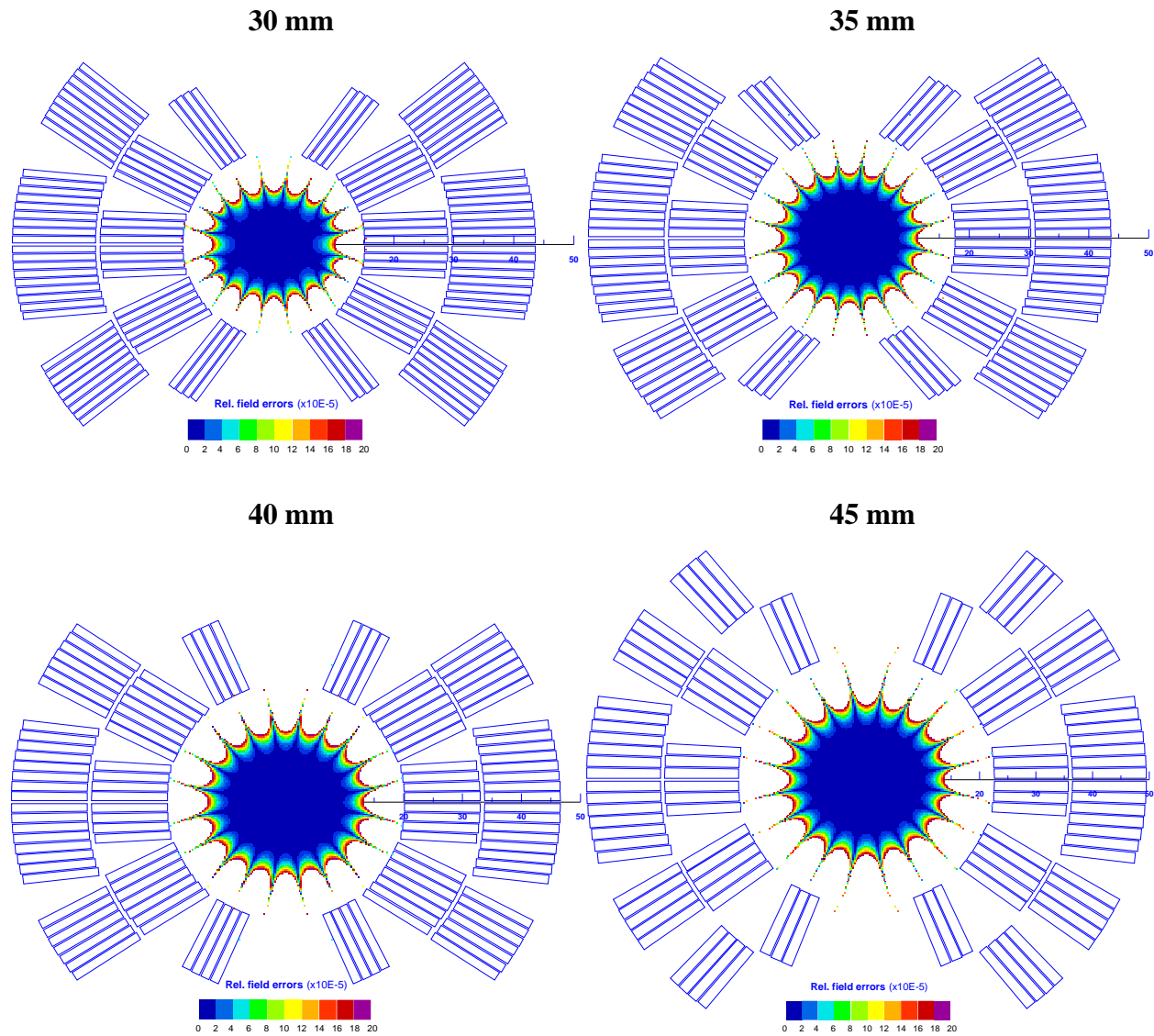
30 mm

35 mm

40 mm

45 mm
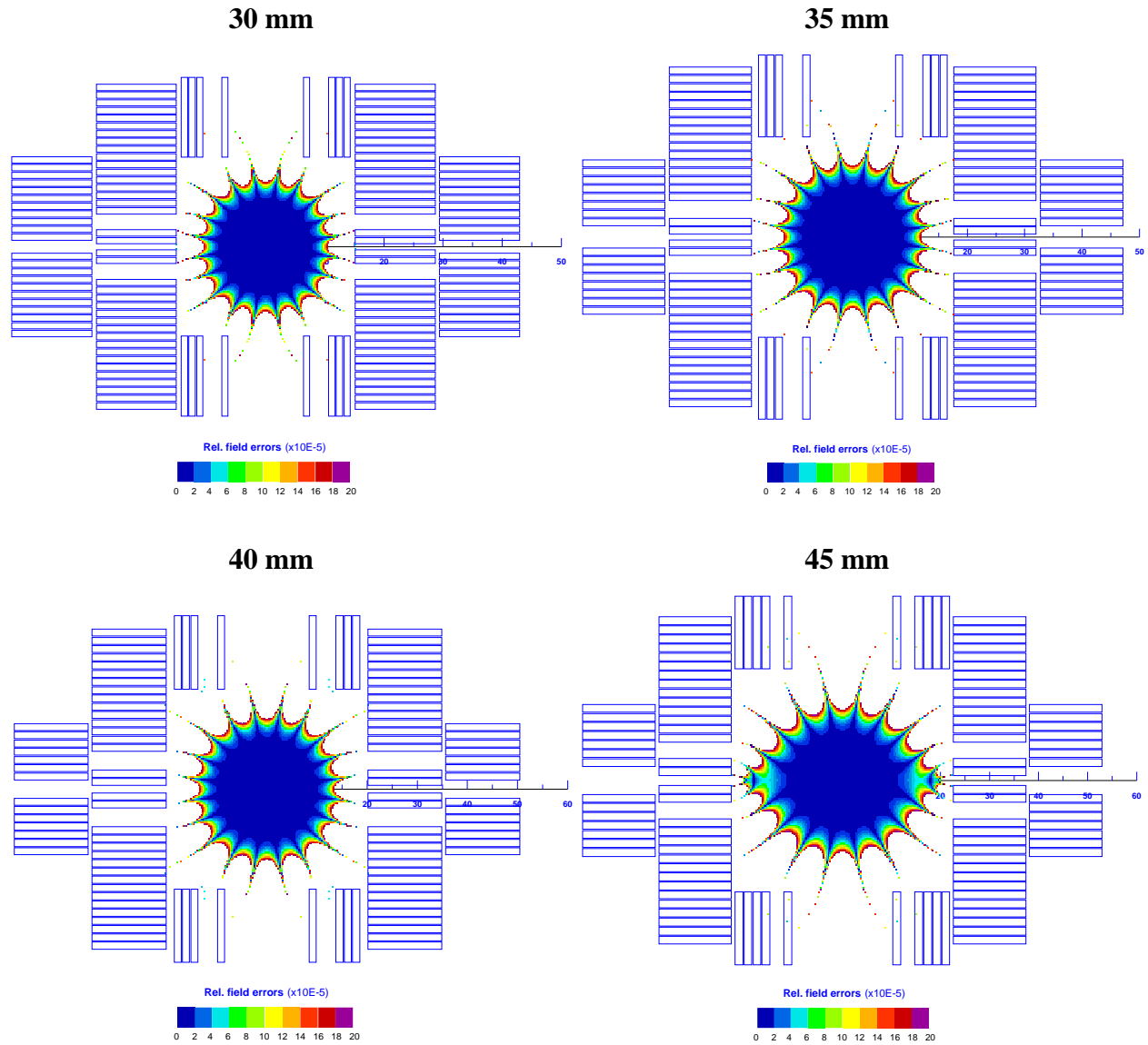
Figure B.3.1 Geometry and field quality of block type coils with square aperture. Bore diameter is written above each coil.

Table B.3.1. Coordinates of the coil blocks in block type coils with square aperture.

Bore size, mm	Parameter	Block #				
		1	2	3	4	5
30	N cables	11	2	17	3	1
	x', mm	29.290	15.000	15.000	10.509	6.257
	y', mm	0.971	0.376	5.407	15.000	15.000
35	N cables	8	2	16	3	1
	x', mm	32.614	17.500	17.500	12.132	7.334
	y', mm	1.839	0.407	6.270	17.500	17.500
40	N cables	7	2	15	3	1
	x', mm	35.524	20.000	20.000	13.654	8.314
	y', mm	1.718	0.632	7.464	20.000	20.000
45	N cables	7	2	14	4	1
	x', mm	38.024	22.500	22.500	14.662	10.185
	y', mm	2.707	0.900	7.642	22.500	22.500

REFERENCES

1. D. W. Kerst, F. T. Cole, H. R. Crane, L. W. Jones, L. J. Laslett, T. Ohkawa, A. M. Sessler, K. R. Symon, K. M. Terwilliger, and Nils Vogt Nilsen, Attainment of Very High Energy by Means of Intersecting Beams of Particles, Physical Review 102, 1956, pp.590-591.

2. A. Wu Chao, M. Tinger, Handbook of accelerator physics and engineering, World Scientific, 1999.

3. E.A. Abramyan et. al., Work on Colliding Electron-Electron, Positron-Electron, Proton-Proton Beams at the Institute of Nuclear Physics, Proceedings of the IV International Conference on High Energy Accelerators, Dubna, 1963, p.274.

4. K. Johnsen, Design Study of ISR, Proceedings of 8th International Conference on High Energy Accelerators, 1971, p.79.

5. Design report Tevatron 1 project, Fermilab, AAA-8131, 1984.

6. HERA facility at DESY, DESY HERA 81/10, 1981.

7. Conceptual Design of the Relativistic Heavy Ion Collider, BNL 52195, 1989.

8. The LHC study group "yellow" book, The Large Hadron Collider, Conceptual design, CERN/AC/95-05(LHC), 1995.

9. SSC central design group, Conceptual design of superconducting super collider, SSC-SR-2020, 1986.

10. The VLHC Design Study Group, Design Study for a Staged Very Large Hadron Collider, Fermilab preprint, Fermilab-TM-2149, June 2001.

11. A. Asner, R. Perin, S. Wenger, F. Zerobin, First Nb_3Sn Superconducting Dipole Model Magnets for the LHC break the 10 Tesla Field Threshold, Proceedings of 11th Conference on Magnet Technology, Tsukuba 1989, Elsevier Applied Science, 1990, pp.36-41.

12. A. den Ouden and H. ten Kate, Quench Characterization of the 11 T Nb_3Sn model dipole magnet MSUT, Proceedings of the 15th International Conference on Magnet Technology, Beijing, 1997.

13. A. McInturff, R. Benjegerdes, P. Bish, S. Caspi, K. Chow, D. Dell'Orco, D. Dietderich, R. Hannaford, W. Harnden, H. Higley, A. Leitzke, L. Morrison, R. Scanlan, J. Smithwick, C. Taylor, J. van Oort, Test Results for a High Field (13 T) Nb_3Sn Dipole, Proceedings of the 1997 Particle Accelerator Conference, Vancouver, 1997, pp.3212-3214.

14. B. Benjegerdes, P. Bish, D. Byford, S. Caspi, D. Dietderich, S. Gourlay, R. Hafalia, R. Hannaford, H. Higley, A. Jackson, A. Lietzke, N. Liggins, A. McInturff, J. O'Neill, E. Palmerston, G.L. Sabbi, R. Scanlan, J. Swanson, Fabrication and Test Results of a High Field, Nb3Sn Superconducting Racetrack Dipole Magnet, Proceedings of 2001 Particle Accelerator Conference, Chicago, June 2001.

15. M. Anerella, J. Cozzolino, J. Escallier, G. Ganetis, A. Ghosh, R. Gupta, M. Harrison, A. Marone, J. Muratore, B.L. Parker, W. Sampson, P. Wanderer, Technology Development for React and Wind Common Coil Magnets, Proceedings of 2001 Particle Accelerator Conference, Chicago, June 2001.

16. I. Akimov, I. Bogdanov, S. Kozub, K. Myznikov, A. Seletsky, A. Shikov, P. Shcherbakov, P. Slabodchikov, V. Sytnik, L. Tkachenko, V. Zubko, Dipole with Coil Based on High Temperature Superconductor, Proceedings of 2001 Particle Accelerator Conference, Chicago, June 2001.

17. R. Perin, Field, forces and mechanics of superconducting magnets, CERN Accelerator School on Superconductivity in Particle Accelerators, CERN 96-03, Geneva, 1996, pp.71-92.

18. S.C. Snowdon, Magnetic field considerations in superferric dipole, Fermilab Internal Note, TM-1210, March 1983.

19. Fermi National Accelerator Laboratory, The Fermilab Main Injector technical design handbook, Batavia, IL, Fermilab Main Injector Department, AAD-6126, 1994.

20. G.W. Foster, V.S. Kashikhin, I. Novitski, Design of a 2 Tesla Transmission Line Magnet for the VLHC, MT-16, IEEE Transactions on Applied Superconductivity, Vol. 10, No. 1, March 2000, pp.202-205.

21. K.-H. Mess, P. Schmuser, S. Wolff, Superconducting Accelerator Magnets, World Scientific Publishing Co. Pte. Ltd, 1996.

22. I.N. Bronshtein, K.A. Semendiaev, Handbook on mathematic, Nauka, Moscow, 1967.

23. H. Brechna, Superconducting magnet systems, Springer, Berlin, 1973.

24. G. Danby, Panel discussion of magnets for a big machine, Proceedings of the 12th International Conference on High Energy Accelerators, Fermilab, 1983.

25. S. Russenschuck, ROXIE – the routine for the optimization of magnets X-sections, inverse field computation and coil end design, Proceedings of the First International ROXIE Users Meeting and Workshop, CERN, Geneva, Switzerland, 1998, CERN-99-01, pp.1-5.

26. S. Russenschuck, C. Paul, S. Ramberger, F. Rodriguez-Mateos, R. Wolf, Integrated design of superconducting accelerator magnets, Proceedings of the First International ROXIE Users Meeting and Workshop, CERN, Geneva, Switzerland, 1998, CERN-99-01, pp.18.30.

27. S. Russenschuck, Mathematical optimization techniques, Proceedings of the First International ROXIE Users Meeting and Workshop, CERN, Geneva, Switzerland, 1998, CERN-99-01, pp.60-72.

28. V. Pareto, Manual of political economy, The Macmillan Press, 1971.

29. A.M. Geoffrion, Proper efficiency and the theory of vector maximization, Journal of Mathematical Analisys and Applications, 1968.

30. G. Zoutdendijk, Methods of feasibly directions: a study in linear and non-linear programming, Elsevier, 1960.

31. A.V. Fiacco, G.P. McCormick, Sequential unconstrained minimization techniques, Wiley, 1968.

32. R.T. Rockafellar, The multiplier method of Hestenes and Powell applied to convex programming, Journal of Optimization Theory and Applications, Vol. 12, 1973.

33. K.M. Ragsdell, A. Ravindran, G.V. Reklaitis, Engineering optimization. Methods and applications, John Willey and Sons, 1983.

34. K. Halbach, A program for inversion of system analysis and its application to the design of magnets, MT2, Proceedings of the international conference on magnet technology, The Rutherford laboratory, 1967.

35. A.G.A.M. Armstrong, M.W. Fan, J. Simkin, C.W. Trowbridge, Automated optimization of magnet design using the boundary integral method, IEEE Transactions on Magnetics, Vol. MAG-18, No.2, March 1982, pp.620-623.

36. P. Girdinio, P. Molfino, G. Molinari, A. Viviani, A package for computer aided design for power electrical engineering, IEEE Transactions on Magnetics, Vol. MAG-19, No.6, November 1983, pp.2659-2662.

37. J.A. Nelder, R. Mead, A simplex method for function minimization, Computer Journal, Vol. 7, 1964.

38. Design study of the Large Hadron Collider (LHC): a multiparticle collider in the LEP tunnel, CERN 91-03, 1991.

39. J. McDonald, E. Barzi, A model for J_c in granular A-15 superconductors, IEEE Transactions on Applied Superconductivity, Vol. 11, No. 1, March 2001, pp.3884-3887.

40. V.V. Kashikhin, P.J. Limon, Cost optimization of a hadron collider, Fermilab Internal Note, Fermilab-TM-2160, September 2001.

41. P. Bauer, M. Dietrich, G.W. Foster, V.V. Kashikhin, P.J. Limon, V. Shiltsev, N. Solyak, The Influence of Accelerator Physics on the Magnet Design of a Very Large Hadron Collider, Proceedings of 17th International Conference on Magnet Technology, Geneva, Switzerland, September 2001.

42. G. Ambrosio, N. Andreev, T. Arkan, E. Barzi, S. Caspi, D. Chichili, V.V. Kashikhin, P.J. Limon, T. Ogitsu, J. Ozelis, I. Terechkine, J.C. Tompkins, M. Wake, S. Yadav, R. Yamada, V. Yarba, A.V. Zlobin, Conceptual design of the Fermilab Nb_3Sn high field dipole model, Proceedings of the 1999 Particle Accelerator Conference, New York, 1999, pp.174-176.

43. A.D. McInturff, Quench protection for high field magnets (>12T), VLHC magnet technologies workshop, Fermilab May 24-26, 2000.

44. G. Ambrosio, S. Caspi, V.V. Kashikhin, P.J. Limon, T. Ogitsu, I. Terechkine, M. Wake, R. Yamada, A.V. Zlobin, Conceptual design study of high field magnets for very large hadron collider, MT-16, IEEE Transactions on Applied Superconductivity, v. 10, No. 1, March 2000, pp.310-313.

45. T.T. Arkan, D. Chichili, J.A. Rice, I. Terechkine, Niobium-Tin Magnet Technology Development at Fermilab, Proceedings of the 1999 Particle Accelerator Conference, New York, 1999, pp. 3242-3244.

46. V.V. Kashikhin, First High Field Magnet Cross-Section Design, Fermilab Internal Note, TD-99-027, April 6, 1999.

47. N. Andreev, G. Ambrosio, P. Bauer, V.V. Kashikhin, I. Novitski, A.V. Zlobin, Design and mechanical analysis of a single layer common coil dipole for VLHC, ASC2000, IEEE Transactions on Applied Superconductivity, Vol. 11, No. 1, March 2001, pp.2276-2279.

48. R. Gupta, Common Coil Magnet System for VLHC, Proceedings of 1999 Particle Accelerator Conference, New York, 1999, pp. 3239-3241.

49. V.V. Kashikhin, A.V. Zlobin, Magnetic designs of 2-in-1 Nb_3Sn dipole magnets for VLHC, ASC2000, IEEE Transactions on Applied Superconductivity, Vol. 11, No. 1, March 2001, pp.2176-2179.

50. L. Imbasciati, G. Ambrosio, P. Bauer, V.V. Kashikhin, A. Zlobin, Quench Protection of the Common Coil Test Facility-Results of Adiabatic Model Calculations, Fermilab Internal Note, TD-00-056, September 18, 2000.

51. T. Ando, T. Isono, K. Hamada, G. Nishijima, H. Tsuji, A. Tomioka, T. Bohno, Y. Yasukawa, M. Konno, T. Uede, Design of a 60-kA HTS Current Lead for Fusion Magnets and its R&D, IEEE Transactions on Applied Superconductivity, Vol. 11, No. 1, March 2001, pp.2535-2538.

52. G.W. Foster, S. Hays, H. Pfeffer, Design of a Compact 100 kA Switching Power Supply for Superconducting Magnet Tests, Fermilab Internal Note, TD-01-045, June 1, 2001.

53. V.V. Kashikhin, A.V. Zlobin, Single-Layer High Field Dipole Magnets, Proceedings of 2001 Particle Accelerator Conference, Chicago, June 2001.

54. V.V. Kashikhin, A.V. Zlobin, Magnetic Design and Field Quality of Nb_3Sn Accelerator magnets, Proceedings of 17th International Conference on Magnet Technology, Geneva, Switzerland, September 2001.

55. V.V, Kashikhin, A.V. Zlobin, Conceptual Design of 2-in-1 Nb3Sn Arc Quadrupole Magnets for VLHC, Fermilab Internal Note, TD-01-019, April 3, 2001.

56. V.V. Kashikhin, A.V. Zlobin, Nb_3Sn Arc Quadrupole Magnets for VLHC, Proceedings of 2001 Particle Accelerator Conference, Chicago, June 2001.

57. E. M. Purcell, Electricity and magnetism, Berkeley physics course, Volume 2, McGraw Hill, 1971.

58. K. Halbach and R. F. Holsinger, SUPERFISH - A Computer Program for Evaluation of RF Cavities with Cylindrical Symmetry, Particle Accelerators 7, 1976, pp.213-222.

59. OPERA-2D/3D User Guide, VF-09-99-A3, Vector Fields Limited, England.

60. ANSYS 5.7 Users Manual, ANSYS Inc., Canonsburg PA, USA.

61. J. Simkin, C.W. Trowbridge, On the use of total scalar potential in the numerical solution of field problems in electromagnetics, International Journal on Numerical Methods, 14, 1979.

62. G. Parzen, K. Jellett, Computation of high field magnets, Particle accelerators, Vol. 2, 1971.

63. C.J. Carpenter, Theory and application of magnetic shells, IEE Proceedings, Vol. 114, No. 7, 1967, pp. 995-1000.

64. N.I. Doinikov, E.A. Lamzin, A.S. Simakov, S.E. Sytchevsky, Features of 3-D magnetostatic

field simulation, Proceedings of 5th International Conference on Mathematical Simulation, Programming and Mathematical Approaches for Physical Problems, Dubna, JINR, 1985, pp. 166-168.

65. N.I. Doinikov, E.A. Lamzin, S.E. Sytchevsky, On computation of 3-D magnetostatic fields of electrophysical apparatus magnet systems, IEEE Transactions on Magnetics, Vol. 28, No. 1, 1992, pp. 908-911.

66. O. Biro, K. Preis, G. Vrisk, K.R. Ritcher, I. Ticar, Computation of 3D magnetostatic fields using a reduced scalar potential, IEEE Transactions on Magnetics, Vol. 29, No. 2, 1993, pp.1329-1322.

67. J.P. Webb, B. Forgani, A single scalar potential method for 3D edge elements using edge elements, IEEE Transactions on Magnetics, Vol. 25, No. 5, 1989, pp.4126-4128.

68. N.I. Doinikov, A.S. Simakov, Modified scalar potential in boundary-value problems in magnetostatics, Soviet Physics – Technical Physics Vol. 16, No. 4, 1971, pp.658-660.

69. V.S. Kashikhin, Programs SCALAR, VECTOR, FESS of numerical simulation electromagnetic systems in electrophysical devices, Preprint NIIEFA B-0598, 1982.

70. N.I. Doinikov, A.S. Simakov, Computer solution of two-dimensional nonlinear magnetostatic problems (strong saturation case), Soviet Physics – Technical Physics Vol. 14, No. 8, 1970, pp.1097-1103.

71. O. Biro, K. Preis, C. Paul, The use of a reduced vector potential formulation for the calculation of iron induced field errors, 1st International Roxie Users Meeting and Workshop, CERN, Geneva, Switzerland, CERN-99-01, 1999.

72. C. Paul, K. Preis, S. Russenschuck, N. Siegel, Saturation Induced Field Errors in the LHC Main Dipoles, 15th International Conference on Magnet Technology - MT-15, Beijing, China, 1997.

73. Ch. Iselin, A Scalar Integral Equation for Magnetostatic Fields, Compumag, 1976, pp.15-18.

74. M.T. Newman, C.W. Trowbridge, L.R. Turner, GFUN: An interactive program as an aid to magnetic design, Proceedings of 4th International Conference on Magnet Technology, BNL, 1972, pp. 617-626.

75. G.H. Morgan, A Computer Program for the 2-D Magnetostatic Problems Based on Integral Equations for the Field of the Conductors and Boundary Elements, IEEE Transactions on Magnetics, Vol. 28, No. 1, 1992, pp. 912-915.

76. V. Amoskov, A. Belov, V.V. Kashikhin, V. Kukhtin, E. Lamzin, Yu. Severgin, N. Shatil, S. Sytchevsky, Numerical Simulation of 3-D Field of Systems Using Permanent Magnets, Proceedings of 1996 European Particle Accelerator Conference, 1996, Vol. 3, pp.2161-2163.

77. V.T. Bauchev, S.V. Vorozhtsov, On the Computation of Three-dimensional Magnetostatic Fields by the Integral Equation Method, Compumag, 1976, pp.82-85.

78. P. Bauer, J. DiMarco, H. Glass, V.V. Kashikhin, G. Sabbi, P. Schlabach, G.Velev, Magnetic Field Measurements of HGQ009 - Test Summary Report, Fermilab Internal Note, TD-00-053, September 13, 2000.

79. A.V. Tollestrup, Superconducting magnets, Physics of High Energy Accelerators, AIP Conference Proceedins, No. 87, 1982, pp.699-804.

80. B.H. Wiik, The status of HERA, Proceedings of the 1991 Particle Accelerator Conference, 1991, pp.2905-2909.

81. R. Meinke, Superconducting magnet system for HERA, IEEE Transactions on Magnetics, 1991, pp.1728-1734.

82. V.I. Balbekov and G.G. Gurov, IHEP accelerating and storage complex: status and possibility of B-factory, Nuclear Instruments and Methods in Physics Research, A333, 1993, pp.189-195.

83. A.V. Zlobin, UNK superconducting magnet development, Nuclear Instruments and Methods in Physics Research, A333, 1993, pp.196-203.

84. P. Schmuser, Field quality issues in superconducting magnets, Proceedings of 1991 particle accelerator conference, Vol.1, San Francisco, 1991, pp.37-41.

85. C. Vollinger, Estimate of saturation induced multipole errors in the LHC main dipoles, Proceedings of the First International ROXIE Users Meeting and Workshop, CERN, Geneva, Switzerland, 1998, CERN-99-01, pp.93-109.

86. J.P. Blewett, Iron shielding for air core magnets, Proceedings of 1968 summer study on superconducting devices and accelerators, BNL, 1968.

87. J.H. Coupland, Dipole, quadrupole and higher order fields from simple coils, Nuclear instruments and methods, Vol. 78, 1978.

88. G.H. Morgan, Use of an elliptical aperture to control saturation in closely-coupled cold iron superconducting magnets, IEEE Transactions on Nuclear Science, Vol. NS-32, No. 5, 1985, pp.3695-3697.

89. G.H. Morgan, Shaping of magnetic fields in beam transport magnets, The physics of particle accelerators, AIP conference proceedings 249, 1990.

90. P.A. Thompson, R.C. Gupta, S.A. Kahn, H. Hahn, G.H. Morgan, P.J. Wanderer, E. Willen, Iron saturation control in RHIC dipole magnets, Proceedings of 1991 particle accelerator conference, Vol. 4 San-Francisco, California, 1991, pp.2242-2244.

91. D. Dell'Orco, S. Caspi, O'Neill, A. Leitzke, R. Scanlan, C.E. Taylor, A. Wandesforde, A 50 mm bore superconducting magnet with a unique iron yoke structure, IEEE Transactions on Applied Superconductivity, Vol. 3, No. 1, March 1993, pp.637-641.

92. S. Zannella, Biological effects of magnetic fields, Cern Accelerator School, Measurement and Alignment of Accelerator and Detector Magnets, CERN 98-05, 1998.

93. G. Ambrosio, E. Barzi, P. Bauer, V.V. Kashikhin, G. Sabbi, R. Yamada, A.V. Zlobin, Superconductor Requirements for the HFM Program at Fermilab, Fermilab Internal Note, TD-99-073, December 15, 1999.

94. G. Ambrosio, N. Andreev, T.T. Arkan, E.A.Z. Barzi, S. Caspi, D.R. Chichili, K. Chow, V.V. Kashikhin, P.J. Limon, A. Makarov, J.P. Ozelis, I. Terechkine, J.C. Tompkins, M. Wake, S. Yadav, R. Yamada, V. Yarba, A.V. Zlobin, Development of the 11 T Nb_3Sn dipole model at Fermilab, MT-16, IEEE Transactions on Applied Superconductivity, v. 10, No. 1, March 2000, pp.298-301.

95. N. Andreev, T.T. Arkan, S. Caspi, D.R. Chichili V.V. Kashikhin, A. Makarov, I. Terechkine, M. Wake, S. Yadav, R. Yamada, A.V. Zlobin, Fabrication and testing of high field dipole mechanical model, MT-16, IEEE Transactions on Applied Superconductivity, v. 10, No. 1, March 2000, pp.314-317.

96. G. Ambrosio, N. Andreev, S. Caspi, K. Chow, V.V. Kashikhin, I. Terechkine, M. Wake, S. Yadav, R. Yamada, A.V. Zlobin, Magnetic design of the Fermilab 11 T Nb_3Sn short dipole model, MT-16, IEEE Transactions on Applied Superconductivity, v. 10, No. 1, March 2000, pp.322-325.

97. E. Barzi, P.J. Limon, R. Yamada, A.V. Zlobin, Study of Nb_3Sn Strands for Fermilab's High Field Dipole Model, IEEE Transactions of Applied Superconductivity, Vol. 11, No. 1, March 2000, pp. 3595-3598.

98. V.V. Kashikhin, A.V. Zlobin, Iron Yoke Optimization in the Double Aperture Nb_3Sn Dipole Magnet for VLHC, Fermilab Internal Note, TD-00-009, February 4, 2000.

99. V.V. Kashikhin, A.V. Zlobin, Conceptual Magnetic Design of the Fermilab 2-in-1 Nb_3Sn

Dipole Magnet for VLHC, Fermilab Internal Note, TD-00-008, February 4, 2000.

100. P. Bauer, L. Imbasciati, V.V. Kashikhin, M. Lamm, A. Zlobin, Quench Protection of High Field Nb_3Sn Magnets for VLHC, G. Ambrosio, Proceedings of 2001 Particle Accelerator Conference, Chicago, June 2001.

101. G. Ambrosio, P. Bauer, L. Imbasciati, V.V. Kashikhin, M. Lamm, A.V. Zlobin, Quench Protection Calculations for Fermilab's Nb_3Sn High Field Magnets for VLHC - Part I, Fermilab Internal Note, TD-01-003, February 9, 2001.

102. D. R. Chichili, G. Ambrosio, Mechanical and Sensitivity Analysis of 43.5 mm Bore Nb_3Sn Dipole Model, Fermilab Internal Note, TD-99-035, July 19, 1999.

103. D.R. Chichili, V.V. Kashikhin, A.V. Zlobin, Mechanical design and analysis of Fermilab 2-in-1 shell type Nb_3Sn dipole models, ASC2000, IEEE Transactions on Applied Superconductivity, Vol. 11, No. 1, March 2001, pp.2288-2291.

104. V.V. Kashikhin, A.V. Zlobin, Conceptual Design of the Double Aperture Nb_3Sn Dipole Magnet for VLHC with Warm Iron Yoke, Fermilab Internal Note, TD-00-012, February 4, 2000.

105. V.V. Kashikhin, A.V. Zlobin, Compensation of Quadrupole Field Component in the VLHC Double Aperture Nb_3Sn Dipole Magnet with Warm Iron Yoke, Fermilab Internal Note, TD-00-036, May 19, 2000.

106. D.R. Chichili, A.V. Zlobin, Mechanical Design and Analysis of 2-in-1 Warm Iron Yoke Dipole Magnet: Version 2, Fermilab Internal Note, TD-01-032, May 3, 2001.

107. S. Caspi, S. Gourlay, R. Hafalia, A. Leitzke, J. Oneill, C. Taylor, A. Jackson, The Use of Pressurized Bladders for Stress Control of Superconducting Magnets, IEEE Transactions on Applied Superconductivity, Vol. 11, No. 1, March 2001, pp. 2272-2275.

108. G. Ambrosio, P. Bauer, V.V. Kashikhin, S.W. Kim, A. Zlobin, Quench Protection of the Single Layer Common Coil Dipole Magnet, L. Imbasciati, Fermilab Internal Note, TD-00-057, September 18, 2000.

109. G. Ambrosio, P. Bauer, L. Imbasciati, V.V. Kashikhin, M. Lamm, A.V. Zlobin, Quench Protection Calculations for Fermilab's Nb_3Sn High Field Magnets for VLHC - Part 2, Fermilab Internal Note, TD-01-004, February 9, 2001.

110. G. Ambrosio, N. Andreev, E. Barzi, P. Bauer, D. Chichili, K. Ewald, L. Imbasciati, V.V. Kashikhin, S.W. Kim, P. Limon, I. Novitski, J.P. Ozelis, R. Scanlan, G. Sabbi, A. Zlobin,

Development of react & wind common coil dipoles for VLHC, ASC2000, IEEE Transactions on Applied Superconductivity, Vol. 11, No. 1, March 2001, pp.2172-2175.

111. G. Ambrosio, N. Andreev, E. Barzi, P. Bauer, D. Chichili, K. Ewald, L. Imbasciati, V.V. Kashikhin, P. Limon, I. Novitski, J-M. Rey, R. Scanlan, S. Yadav, R. Yamada, A. Zlobin, Design and Development of Nb_3Sn Single-Layer Common Coil Dipole Magnet for VLHC, Proceedings of 2001 Particle Accelerator Conference, Chicago, June 2001.

112. G. Ambrosio, N. Andreev, E. Barzi, P. Bauer, C. Carcagno, D.R. Chichili, K. Ewald, S. Feher, L. Imbasciati, V.V. Kashikhin, P.J. Limon, L. Litvinenko, I. Novitski, D. Orris, J.M. Rey, R.M. Scanlan, C. Silvester, M. Tartaglia, J.C. Tompkins, S. Yadav, R. Yamada, A.V. Zlobin, Development of a Single-Layer Nb_3Sn Common Coil Dipole Using React-and-Wind Fabrication Technique, Proceedings of 17th International Conference on Magnet Technology, Geneva, Switzerland, September 2001.

113. G. Ambrosio, N. Andreev, E. Barzi, D. Chichili, V.V. Kashikhin, I. Terechkine, S. Yadav, R. Yamada, A.V. Zlobin, Development of Cos-theta Nb_3Sn Dipole Magnets for VLHC, Proceedings of 2001 Particle Accelerator Conference, Chicago, June 2001.

114. V.V, Kashikhin, A.V. Zlobin, 2-in-1 Arc Dipole and Quadrupole Magnets for VLHC Based on the Shell-type Coils and Vertical Bore Arrangement, Fermilab Internal Note, TD-01-034, May 11, 2001.

115. R. Bossert et al., "Fabrication of the First Short Model of a High Gradient Quadrupole for the LHC Interaction Regions", Proceedings of the 15th International Conference on Magnet Technology, Beijing, 1997.

116. D. Chichili, Mechanical Analysis of FF Arc-Quadrupole for VLHC Stage-2, Fermilab Internal Note, TD-01-012, March 5, 2001.

117. D. Chichili, An Alternate Mechanical Design and Analysis of FF Arc-Quadrupole for VLHC Stage-2, Fermilab Internal Note, TD-01-021, April 5, 2001.

118. V.V. Kashikhin, I. Terechkine, Superconducting Straight Section Quadrupole Magnet for Low Field VLHC, Fermilab Internal Note, TD-01-008, February 27, 2001.

119. E. Willen, Superconducting magnets, INFN Eloisatron Project 34th Workshop, Erice, Sicily, November 4-13, 1996.

120. B. C. Brown, H.E. Fisk and R. Hanft, Persistent current fields in Fermilab Tevatron magnets, IEEE Transactions on Magnetics, Vol. MAG-21, No. 2, March 1985, pp.979-982.

121. M. A. Green, Control of fields due to superconductor magnetization in the SSC magnets, IEEE Transaction on Magnetics, Vol. MAG-23, No.2, March 1987, pp.506-509.

122. M. A. Green, "Passive superconductor a viable method of controlling magnetization multipoles in the SSC dipole", IISSC Supercollider 1, Plenum Press, NY, 1989, p.351.

123. B. Holzer, C. Montag, Reproducibility and predictability of persistent current effects in the HERA proton storage ring, Proceedings of EPAC 2000, Vienna, Austria, 2000, p.2142.

124. L. Bottura, M. Schneider, L. Walkiers, R. Wolf, Cable magnetization effects in the LHC main dipole magnets, Advances in cryogenic engineering, Vol. 43A, 1998, pp. 451-458.

125. M. Aleksa, S. Russenschuk, C. Vollinger, Calculation of persistent currents in superconducting magnets, Proceedings of 6th International Conference on Computational Accelerator Physics, Vol.3, 122402, Darmstadt, Germany, September 2000.

126. E. W. Collings et al., "Design of multifilamentary strands for SSC dipole magnets", IISSC Supercollider 2, Plenum Press, NY, 1990, p.581.

127. H. Gurol, G.W. Albert, R. Simon, M. Marietta, Passive persistent current correctors for accelerator magnets, Proceedings of IEEE Transactions on Applied Superconductivity, Vol. 5, No. 2, June 1995, pp.861-865.

128. A. Asner, A Novel, Elegant Method for Passive Compensation of Magnetization-current-induced Field Errors in the CERN LHC 10 T Superconducting Dipole Magnets by Permanent Multipole Magnets, IEEE Transactions on Magnetics, Vol. MAG-23, No. 2, March 1987, pp.514-517.

129. S. Caspi, W.S. Gilbert, M. Helm, L.J. Laslett, The effects of filament magnetization as calculated by POISSON, IEEE Transactions on Magnetics, Vol. MAG-23, No. 2, March 1987, pp.510-513.

130. C. Boffo, "Magnetization measurements at 4.2 K of multifilamentary superconducting strands", thesis of University of Udine (Italy), December 1999.

131. C.P. Bean, Magnetization of high-field superconductors, Review of Modern Physics, Vol. 36, No. 1, 1964, pp. 31-39.

132. V.V. Kashikhin, A.V. Zlobin, Calculation of Coil Magnetization Effect in Superconducting Accelerator Magnets, Fermilab Internal Note, TD-00-010, February 4, 2000.

133. M.N. Wilson, Superconducting magnets, Clarendon Press, Oxford, 1983.

134. V.V. Kashikhin, A.V. Zlobin, Correction of the persistent current effect in Nb_3Sn dipole magnets, ASC2000, IEEE Transactions on Applied Superconductivity, Vol. 11, No. 1, March 2001, pp.2058-2061.

135. C. Battle, N. Diaczenko, T. Elliott, R. Gaedke, D. Gross, E. Hill, W. Henchel, M. Johnson, P. McIntyre, A. Ravello, A. Sattarov, R. Soika, D. Wind, Optimization of block-coil dipoles for hadron colliders, Proceedings of the 1999 Particle Accelerator Conference, NY, 1999, p.2936-2938.

136. R. Gupta, M. Anerella, J. Cozzolino, J. Escallier, G. Ganetis, A. Ghosh, M. Harrison, G. Morgan, J. Muratore, B. Parker, W. Sampson, P. Wanderer, Common Coil Magnet Program at BNL, ASC2000, IEEE Transactions on Applied Superconductivity, Vol. 11, No. 1, March 2001, pp.2168-2171.

137. R. Gupta, S. Ramberger, Field quality optimization in a common coil magnet design, MT-16, IEEE Transactions on Applied Superconductivity, Vol. 10, No. 1, March 2000, pp.326-239.

138. V.V. Kashikhin, A.V. Zlobin, Correction of Coil Magnetization Effect in Nb_3Sn High Field Dipole Magnet Using Thin Iron Strips, Fermilab Internal Note, TD-99-048, October 15, 1999.

139. S. Russenschuk, C. Vollinger, Compensation of the Persistent Current Multipoles in the LHC Dipoles by making the Coil Protection Sheet from Soft Magnetic Material, LHC-PROJECT-NOTE-228, CERN, Switzerland, 2000.

140. S. Caspi, Reduction of Magnetization Induced Harmonics in Superconducting Magnets, SC-MAG-691, LBNL Internal Note, October 12, 1999.

141. V.V. Kashikhin, A.V. Zlobin, Comparison of Correcting Capability of Passive Correctors Based on a Thin Pipe and Thin Strips, Fermilab Internal Note, TD-99-049, October 15, 1999.

142. V.V. Kashikhin, A.V. Zlobin, Compensation of Strand Magnetization of Superconducting Rutherford Cables with Thin Iron Core, Fermilab Internal Note, TD-00-011, February 4, 2000.

143. V.V. Kashikhin, A.V. Zlobin, Sensitivity of Field Harmonics in Nb_3Sn Dipole Magnet to the Correction Strip Position, Fermilab Internal Note, TD-99-068, December 7, 1999.

144. J. M. Cook, Strain energy minimization in SSC magnet winding, IEEE Transactions on Magnetics, Vol. 27, March 1991, pp.1976-1980.

145. S. Yadav, D. Chichili, I. Terechkine, Coil end parts design and fabrication issues for the high field dipole at Fermilab, IEEE Transactions of Applied Superconductivity, Vol. 11, No. 1, March 2000, pp.2284-2287.

146. D.R. Chichili, G. Ambrosio, N. Andreev, E. Barzi, S. Caspi, V.V. Kashikhin, P.J. Limon, R. Scanlan, I. Terechkine, J. Tompkins, M. Wake, S. Yadav, R. Yamada, V. Yarba, A.V. Zlobin, Fabrication of the shell type Nb_3Sn dipole magnet at Fermilab, ASC2000, IEEE Transactions on Applied Superconductivity, Vol. 11, No. 1, March 2001, pp.2160-2163.

147. D. R. Chichili, N. Andreev, E. Barzi, V.V. Kashikhin, I. Terechkine, S. Yadav, R. Yamada, A.V. Zlobin, Nb_3Sn Cos(theta) Dipole Magnet, Nb_3Sn Dipole Magnet, HFDA-02 Production Report, Fermilab Internal Note, TD-01-036, May 25, 2001.

148. D. Chichili, Nb_3Sn Cos-Theta Dipole Magnet, HFDA-03 Production, Fermilab Internal Note, TD-01-064, August 10, 2001.

149. D. Chichili, T.T. Arkan, J.P. Ozelis, I. Terechkine, Investigation of cable insulation and thermo-mechanical properties of Nb_3Sn composite, MT-16, IEEE Transactions of Applied Superconductivity, Vol. 10, No. 1, March 2000, pp. 1317-1320.

150. N. Andreev, D. Chichili, C. Christensen, J. DiMarco, V.V. Kashikhin, P. Schlabach, C. Sylvester, I. Terechikine, J. Tompkins, G. Velev, A. Zlobin, Field Quality of the Fermilab Nb_3Sn High Field Dipole Model, Proceedings of 2001 Particle Accelerator Conference, Chicago, June 2001.

151. N. Andreev, G. Ambrosio, E. Barzi, R. Carcagno, D.R. Chichili, J. DiMarco, S. Feher, L. Imbasciati, V.V. Kashikhin, M. Lamm, P.J. Limon, D. Orris, P. Schlabach, C. Sylvester, M. Tartaglia, I. Terechkine, J.C. Tompkins, S. Yadav, R. Yamada, A.V. Zlobin, Development and Test of Single-Bore Cosϑ Nb_3Sn Dipole Models With Cold Iron Yoke, Proceedings of 17th International Conference on Magnet Technology, Geneva, Switzerland, September 2001.

152. A. den Ouden, S. Wessel, E. Krooshoop, H. ten Kate, Application of Nb_3Sn Superconductors in High-field Accelerator Magnets, IEEE Transaction on Applied Superconductivity, Vol. 7, No. 2, June 1997, pp.733-738.

153. D.A. Finley, D.A. Edwards, R.W. Hanft, R. Johnson, A.D. McInturff, J. Strait, Time Dependent Chromaticity Changes in Tevatron, Proceedings of 12th Particle Accelerator Conference, Vol. 1, March 1987, pp.151-153.

154. L. Bottura, L. Walckiers, R. Wolf, Field Errors Decay and "Snap-Back" in LHC Model

Dipoles, IEEE Transactions on Applied Superconductivity Vol. 7, 1997, pp. 602-605.

155. P.J. Limon, The Study of a Staged-Energy VLHC at Fermilab, Accelerator Physics and Technology Seminar, Fermilab, May 2001.

156. G. Ambrosio, V.V. Kashikhin, 40-mm Bore HFM Cross-Section Design with 0.8 mm Strand Diameter Nb_3Sn Cable, Fermilab Internal Note, TD-99-010, February 3, 1999.

157. V.V. Kashikhin, I. Terechkine, 40-mm Bore Dipole Cross-Section Using Cable Made of 1-mm-Diameter Nb_3Sn Strand, Fermilab Internal Note, TD-99-014, April 3, 1999.